

Probing surface properties at the nanoscale: effects of physicochemical  
heterogeneity on membrane wettability

By

Md Farhad Ismail

A thesis submitted in partial fulfillment of the requirements for the degree of  
Doctor of Philosophy

Department of Mechanical Engineering  
University of Alberta

© Md Farhad Ismail, 2020

# Abstract

Water purification by polymeric membranes has been abundantly applied to address global challenges of water scarcity and pollution of aquatic environments. Polymeric membranes are excellent candidates for low cost and energy-efficient high-quality water purification process. However, progress in polymeric membranes has been constrained due to their fouling propensity during the filtration process. It is anticipated that next-generation membranes will be highly selective and fouling-resistant. These two parameters can be controlled by three surface parameters, i.e., wettability, roughness, and surface charge due to surface functional groups. Given that, the development of novel materials and proper surface modification approaches are imperative to substantially advance the water purification technology. Thus, proper characterization and tuning of the surface properties are paramount to develop novel material for next-generation membrane.

This work aims at developing novel methodologies to study the membrane surface physicochemical properties through wettability analysis at room and elevated temperature. It is worth noting that techniques to measure the physicochemical properties at the interfacial region with high sensitivity are significantly limited, considering the number of new materials being developed. Such measurement and characterization techniques include contact angle ( $\theta$ ), X-ray photoelectron spectroscopy (XPS), and Atomic force microscopy (AFM). Each of these available techniques provides information about the constitution of a layer of different thicknesses at the polymer surface, which is known as interphase. For example, " $\theta$ -interphase" may refer to the outer  $\sim 1$  nm of a solid surface that contributed to the surface wettability. Likewise, the "XPS interphase" may refer to the outer  $\sim 10$  nm of a solid surface, which is accessible to the XPS measurement technique. In some cases, surface functional group does not influence wetting as it remains outside of the  $\theta$ -interphase and thus nevertheless accessible to reagents in solution. The portion

of the solid where these types of interfacial interactions are possible can be referred to as the "sub-  $\theta$  interphase". This interphase is less well-defined than those associated with the available characterization techniques. A detailed understanding of the solid-liquid interfacial interactions at the "sub-  $\theta$  interphase" can be useful in evaluating the permeation properties of membranes such as selectivity and rate of fouling.

The initial phase of this thesis will study how the wettability analysis determines the physical and chemical heterogeneity. Theoretical frameworks have been developed to predict the physical and chemical heterogeneity based on the quantification of interfacial energy. This further provides useful insights on the membrane permeation properties, e.g., perm-selectivity, and rate of fouling. AFM and streaming potential methods were also employed to compare the obtained results from the wettability analysis. Our experimental results reveal that the wettability method can provide fast and appropriate understandings on the effects of physical and chemical heterogeneity over membrane permeation properties. The second phase of the study is focused on the surface adaptation and responsive behavior due to the change of the surrounding medium. Many polymeric surfaces reversibly change their properties due to the contact and molecular interaction with another liquid. The developed theoretical framework can predict the experimental observation of solid-liquid-liquid wettability within  $\pm\sim 15\%$  deviation. The experimental data reveal that solid surface tension cannot be an intrinsic property which may alter due to the change of the surrounding liquid. Finally, the role of the surrounding medium temperature over the solid surface tension has been studied systematically. The outcome of this study reveals that surface tension of the polymeric surfaces alters due to the increase of surrounding medium temperature. This alteration becomes significant if all the three phases (solid-liquid-liquid) exhibit some polarity.

Overall, the specific goal of this research is to provide a detailed insight regarding the effect of membrane surface heterogeneity in air and aqueous media on membrane wettability, and its subsequent impacts on membrane performance. This work further provides a novel methodology for fast and accurate characterization of

polymeric membranes by wettability analysis. The outcome of the present research can also be readily extended to many other related engineering processes. With the relationship between interfacial energy and permeation properties, this work paves the way for designing novel materials with desired transport properties for the efficient separation process.

**Keywords:** Thin-film composite membranes, wettability, surface heterogeneity, surface tension, adaptive wetting, temperature dependency.



# Preface

This thesis is the original work by Md Farhad Ismail. Some parts of this research chapter 1 and 2 and 3 and 4 and 5 and 6 of this thesis works have been published or prepared for publications or presentations as:

1. Md Farhad Ismail, Behnam Khorshidi, and Mohtada Sadrzadeh. Characterization of membrane surface and permeation properties by contact angle measurements: quantification strategies and applications. *Advances in colloid and interface science* (submission in progress).  
Author Contributions: Md Farhad Ismail (I) was responsible for literature work. All authors contributed to the manuscript composition.
2. Md Farhad Ismail, Behnam Khorshidi, and Mohtada Sadrzadeh. New insights into the impact of nanoscale surface heterogeneity on the wettability of polymeric membranes. *Journal of Membrane Science* 590: 117270, 2019.  
Author Contributions: Md Farhad Ismail (I) was responsible for the concept formation, experimental execution, data analysis, and manuscript composition. Behnam Khorshidi was involved in concept formation, data analysis, and manuscript edits. Mohtada Sadrzadeh was the supervisory author and was involved in concept formation, data analysis and manuscript edits.
3. Md Farhad Ismail, Muhammad Amirul Islam, Behnam Khorshidi, and Mohtada Sadrzadeh. Quantification of surface potential by wettability measurements. *Applied Physics Letters* (submission in progress).

Author Contributions: Md Farhad Ismail (I) was responsible for the concept formation, experimental execution, data analysis, and manuscript composition. Muhammad Amirul Islam and Behnam Khorshidi were involved in concept formation, data analysis, and manuscript edits. Mohtada Sadrzadeh was the supervisory author and was involved in concept formation, data analysis, and manuscript edits.

4. Md Farhad Ismail, Behnam Khorshidi, and Mohtada Sadrzadeh, New insights into the predication of adaptive wetting of a solid surface under a liquid medium. *Journal of Colloid and Interface Science* (under revision).

Author Contributions: Md Farhad Ismail (I) was responsible for the concept formation, experimental execution, data analysis, and manuscript composition. Behnam Khorshidi was involved in concept formation, data analysis, and manuscript edits. Mohtada Sadrzadeh was the supervisory author and was involved in concept formation, data analysis and manuscript edits.

5. Md Farhad Ismail, Behnam Khorshidi, and Mohtada Sadrzadeh. New insights into the role of surrounding medium temperature on the under-liquid wetting of solid surfaces. *Langmuir* (accepted).

Author Contributions: Md Farhad Ismail (I) was responsible for the concept formation, experimental execution, data analysis, and manuscript composition. Behnam Khorshidi was involved in concept formation, data analysis, and manuscript edits. Mohtada Sadrzadeh was the supervisory author and was involved in concept formation, data analysis, and manuscript edits.

6. Md Farhad Ismail, Behnam Khorshidi, and Mohtada Sadrzadeh. Impact of roughness on the wettability of the TFC membrane. *North American*

Membrane Society 28th Annual Meeting (NAMS 2019), Pittsburgh, PA, USA, May 11-15, 2019.

7. Md Farhad Ismail, Behnam Khorshidi, and Mohtada Sadrzadeh. Toward accurate prediction of adaptive wetting of a solid surface under a liquid medium. International Congress on Membranes & Membrane Processes, London, UK, July 12-17, 2020 (in progress).

*Dedicated to my parents, my wife, and my son  
for their unconditional love and inspiring support*

# Acknowledgment

It was an incredible journey for me to finish my Ph.D. program as a member of the Advanced Water Research Lab (AWRL) at the University of Alberta. Without the continuous help and support of a number of amazing people, it was never possible for me to finish this journey. First and foremost, I would like to express my deepest respect and gratitude to my supervisor Dr. Mohtada Sadrzadeh for his guidance, understanding, encouragement, patience, and numerous hours spent helping me complete my research activity. He was always available for discussion not only as my academic supervisor but also as a great life mentor. I am grateful and honored to be a Ph.D. student in his research group. I would also like to express my gratitude to Dr. Behnam Khorshidi, whose knowledge and experience were an invaluable resource for me to successfully finish my research projects. I would also like to thank my supervisory committee members, Dr. Morris Flynn and Dr. Cagri Ayranci for their valuable comments in different parts of the journey.

I would like to express my sincere appreciation to Drs. Ishita Biswas and Abu Hasan Khondoker for their unconditional help in different stressful situations of this research program. I would like to thank my colleagues Dr. Amin Karkooti, Laleh Shamaeighahfarokhi, Pooria Karami, Simin Shabani, Ali Mohammadtabar, Farshad Mohammadtabar, Dr. Hadi Nazariipoor, Dr. Nandini Debnath, Dr. Muhammad Islam, Asad Asad, Sadaf Naomani, Masoud Rastgar, Adham Riad, Sadegh Aghapour for providing me helpful suggestions, helping in experiments, idea discussion, and necessary training. My appreciation is also extended to Mohammad Ullah, Zayed Pavel, Nushrat Jahan, Niema Afroze, Monisha Alam, Nitish Ranjan Sarker, Ikhtair Hossain Soiket, Walid Bin Khaled, Mohib Khan, Md Ashker Ibney Rashid, Dr. Sourayon Chanda, and Shabab Bin Karim.

I would like to thank my wife Nusrat Helali, without who's rigorous support, critics, and understanding I could not be successful in facing the ups and downs of

my journey. No words can fully express my gratitude to my parents and sister, who unconditionally support me in any and every possible way throughout my life.

Finally, I appreciate the financial support from the following funding agencies that helped me to finish my Ph.D. research: Natural Sciences and Engineering Research Council of Canada (NSERC), Alberta innovates technology futures (AITF), Canada's Oil Sands Innovative Alliance (COSIA), ConocoPhillips Corporation, Alberta Graduate Excellence Scholarship from the government of Alberta.

# Contents

<b>Chapter 1<sup>†</sup> Introduction .....</b>	<b>1</b>
<b>1.1 Water demand and membrane technology .....</b>	<b>2</b>
<b>1.2 Membrane characterization and next-generation membrane materials</b>	<b>3</b>
<b>1.3 Methods for measuring the contact angle of membrane surfaces .....</b>	<b>5</b>
<b>1.4 Scope and objectives.....</b>	<b>10</b>
<b>1.5 Thesis Structure.....</b>	<b>12</b>
<b>1.6 Thesis Contributions .....</b>	<b>13</b>
<b>Chapter 2<sup>*</sup> Literature Review: Membrane Characterization by Contact Angle Analyzer.....</b>	<b>19</b>
<b>2.1 Characterization of membrane surface properties using contact angle</b>	<b>20</b>
2.1.1 Characterization of surface wettability .....	20
2.1.2 Characterization of surface tension and hydrophilicity .....	21
2.1.3 Characterization of surface oleophobicity .....	26
2.1.4 Characterization of surface physical heterogeneity .....	28
2.1.5 Characterization of surface charge and zeta potential .....	31
<b>2.2 Analyzing membrane performance parameters using contact angle.</b>	<b>37</b>
2.2.1 Analyzing fouling propensity of membrane materials.....	38
2.2.2 Analyzing scaling propensity of membrane materials.....	39
2.2.3 Development of novel interfacial materials with special wettability for next-generation polymeric membranes.....	41
<b>2.3 Summary .....</b>	<b>42</b>
<b>Chapter 3<sup>§</sup> New Insights into the Impact of Surface Heterogeneity on the Wettability of Polymeric Membranes .....</b>	<b>56</b>

<b>3.1</b>	<b>Surface physical heterogeneity.....</b>	<b>57</b>
3.1.1	Materials .....	61
3.1.2	Theoretical background for wettability analysis.....	61
3.1.3	Measurement of the wettability of the membranes.....	64
3.1.4	Characterization of surface topography of the membranes .....	64
3.1.5	Characterization of fouling propensity of the membranes.....	65
3.1.6	Results and discussion .....	65
3.1.6.1	Characterization of surface morphology by FESEM and AFM .	65
3.1.6.2	Assessing nanoscale heterogeneity by wettability analysis.....	67
3.1.6.3	Implication for membrane development.....	69
<b>3.2</b>	<b>Determination of surface potential .....</b>	<b>71</b>
3.2.1	Materials and methods .....	73
3.2.2	Results and discussions.....	76
<b>3.3</b>	<b>Summary .....</b>	<b>79</b>
<i>Chapter 4<sup>‡</sup> New insights into the predication of adaptive wetting of a solid surface under a liquid medium.....</i>		<b>95</b>
<b>4.1</b>	<b>Introduction .....</b>	<b>96</b>
<b>4.2</b>	<b>Theoretical approach .....</b>	<b>98</b>
4.2.1	Determination of solid surface tension in the air .....	99
4.2.2	Determination of solid surface tension under-liquid .....	100
4.2.3	Determination of oil surface tension components underwater .....	102
<b>4.3</b>	<b>Experimental details .....</b>	<b>102</b>
4.3.1	Materials .....	102
4.3.2	Wettability analysis.....	103
4.3.3	Measurement of interfacial tension of the probe liquids .....	103
<b>4.4</b>	<b>Results and discussions .....</b>	<b>104</b>
4.4.1	Surface topography of solid surfaces.....	104
4.4.2	Evaluation of solid surface tension components in air .....	104
4.4.3	Determination of solid surface tension components underwater .....	105
4.4.4	Validation of underwater wettability and comparison with previous models	106



4.4.5	Determination of electron-acceptor and electron-donor surface tension components .....	109
4.4.6	Effects of surrounding medium interfacial tension on solid wettability	110
<b>4.5</b>	<b>Summary .....</b>	<b>111</b>
<i>Chapter 5<sup>̄</sup> New insights into the role of surrounding medium temperature on the under-liquid wetting of solid surfaces.....</i>		
<b>5.1</b>	<b>Introduction .....</b>	<b>122</b>
<b>5.2</b>	<b>Experimental methodology.....</b>	<b>124</b>
5.2.1	Materials .....	124
5.2.2	Characterization of surface wettability of solid samples .....	125
5.2.3	Measurement of interfacial tension (IFT) of the probe liquids.....	125
<b>5.3</b>	<b>Theoretical model to predict solid surface tension at elevated temperature.....</b>	<b>126</b>
<b>5.4</b>	<b>Results and discussions .....</b>	<b>128</b>
5.4.1	Characterization of surface topography by AFM .....	128
5.4.2	Determination of interfacial tension of the probe liquids at elevated temperatures.....	128
5.4.3	Impact of temperature on under-water wettability of solid surfaces	129
5.4.4	Impact of temperature on under-water solid surface tension components .....	130
5.4.5	Prediction of under-water solid wettability and comparison with previous models:.....	132
5.4.6	Effects of interfacial interactions at elevated temperature on underwater wettability .....	133
<b>5.5</b>	<b>Summary .....</b>	<b>134</b>
<i>Chapter 6 Conclusions and future work.....</i>		
<b>6.1</b>	<b>Conclusions .....</b>	<b>146</b>
<b>6.2</b>	<b>Future work .....</b>	<b>150</b>
<b>6.3</b>	<b>List of contributions .....</b>	<b>153</b>
6.3.1	Journal papers .....	153

6.3.2	Conference publications and presentations.....	154
<i>References</i>	.....	<i>155</i>
<i>Appendix</i>	.....	<i>181</i>
<b>A1.1</b>	<b>Brief literature review on the reported surface properties of TFC membrane .....</b>	<b>182</b>
<b>B1.1</b>	<b>Supplementary information on the surface potential quantification</b>	<b>186</b>
B1.1.1	Characterizations of surface physical heterogeneity.....	186
B1.1.2	Evaluation of Gibbs adsorption equation.....	187
<b>C1.1</b>	<b>Supplementary information for under-liquid wettability analysis</b>	<b>188</b>
C1.1.1	Probe liquids used in wettability analysis.....	188
C1.1.2	Characterizations of surface physical heterogeneity.....	188
C1.1.3	Evaluation of previous theoretical models.....	189
C1.1.4	Influence of surrounding medium on drop wettability .....	192
C1.1.5	Evaluation of equation of state (EQS) model [221–223].....	195
<b>D1.1</b>	<b>Supplementary information for under-liquid wettability analysis</b>	<b>197</b>
D1.1.1	Probe liquids used in wettability analysis.....	197
D1.1.2	Characterizations of surface physical heterogeneity.....	198
D1.1.3	Evaluation of solid total surface tension at different temperature ...	199
D1.1.4	Effect of temperature on solid-medium interfacial interaction.....	200
D1.1.5	Evaluation of previous theoretical models.....	201
D1.1.6	Influence of surrounding medium on drop wettability .....	203

# List of Tables

Table 2.1: Criteria for surface hydrophilicity. ....	53
Table 2.2: Criteria for surface oleophobicity (non-polar oil, e.g., Hexadecane) .....	55
Table 3.1: Properties of the probe liquids .....	94
Table 4.1: Interfacial tension along with surface tension components of the probe liquids. For comparison, the surface tension of the liquids was also reported based on the correlation in the literature at 20 °C [210,211]. .....	119
Table 4.2: Measurement of electron acceptor and electron donor surface tension components of solid samples underwater. The represented data is based on the $\pm 10\%$ standard deviation of the probe droplet wettability. ....	120
Table 5.1: Interfacial tension along with surface tension components of the probe liquids at room temperature. ....	143
Table 5.2 Surface roughness parameters of the solid samples from the AFM analysis (scan size 10 $\mu\text{m}$ $\times$ 10 $\mu\text{m}$ ). SAD is the surface area difference due to the presence of nano-scale features on the surface and was obtained using the Nanoscope Software 1.40. ....	144

# List of Figures

Figure 1.1: Overview of water treatment process and membrane characterization parameters. (a) Global scenario of high-quality water production capacity by different processes [6]. (b) A statistical overview of the characterization of hydrophilicity of TFC membrane from the Scopus literature search. Here, HP: Hydrophilicity, CA: Contact angle, R: Roughness, SFT: surface tension. (c) The sensitivity of the different membrane characterization techniques. Contact angle and AFM provide the highest sensitivity to quantify the surface physiochemical properties [18,19]. (d) Important surface properties and their range observed in the TFC membranes..... 15

Figure 1.2: Various method to determine the contact angle of membrane surface. (a) Static, advancing, and receding contact angle measurements to characterize the wettability with the sessile drop on the dry sample (top) and the captive bubble technique on a fully wet sample (bottom) [55]. (b) Wilhelmy technique is used a thin rectangular plate of the sample to measure the contact angle. The force ( $F$ ) acting on the plate due to wetting and the wetted perimeter ( $2d+2w$ ) are then utilized to determine the contact angle [32]. (c) Contact angle ( $\theta_Y$ ) on smooth surface alters to apparent contact angle ( $\theta_{ap}$ ) due to surface roughness ( $r$ ). ..... 16

Figure 1.3: Membrane surface topography characterization by AFM with different scanning mode. Contact mode operates only in the repulsive zone, non-contact mode operates in attractive zone but tapping mode operates both in the repulsive and attractive zone [28,48]. ..... 17

Figure 1.4: Effects of anisotropic height variation and scan size over the AFM measurements. AFM images of two polymeric surfaces with different topography but similar RMS roughness, (a) 38.5 nm and (b) 36.1 nm [47]. Fractal surface such as XLE RO membrane exhibits roughness dependent of scan size, (c) 5  $\mu\text{m}$ , and (d)

30  $\mu\text{m}$  [14]. A scan size of 5  $\mu\text{m}$  provides  $r_{AFM} = 1.45$ , and 10  $\mu\text{m}$  scan size provides  $r_{AFM} = 1.16$ . ..... 18

Figure 2.1: Connection of contact angle to the solid-liquid adhesion [82]. The long-range attractive forces (hydrophobic) between a surface and water diminish if the contact angle is less than  $\sim 65^\circ$ . The corresponding adhesion force is  $\sim 30 \text{ dyne/cm}$ . The decay of attractive and the increment of repulsive force are observed between water adhesion force 20 and 40  $\text{dyne/cm}$ , which is known as ‘Berg limit’. (b) Every liquid has a specific surface (solid) independent intrinsic wetting threshold (IWT), which is the boundary of partial-wetting and partial non-wetting, e.g., for water,  $\theta_{IWT} \approx 65^\circ$ . The IWT decreases with decreasing liquid surface tension..... 43

Figure 2.2: (a) Four different wetting states for a liquid on a structurally heterogeneous surface. By introducing physical heterogeneity (such as re-entrant profile in a metastable state), the intrinsically hydrophilic surface can be turned into hydrophobic surface [101]. (b) Surface free energy based on wetting state on a physical heterogeneous surface [101]. We observe that the impregnation state stays in the lowest energy minima and thus the most stable state. (c) Wetting states for a liquid on a fractal surface proposed by Tsujii et al. [53,54]. ..... 44

Figure 2.3: (a)-(c) Evidence of self-affinity in a TFC membrane surface [14]. (a) FESEM image of the NF 90 at two different magnification level shows different topography of the surface. (b) AFM analysis at different scan size exhibit significant variation specifically for the membranes having a higher magnitude of roughness. (c) Wenzel roughness factor ( $r$ ) determination through contact angle analysis ( $r_{CA}$ ) exhibits higher magnitude than that obtained by AFM ( $r_{AFM}$ ) at different scan size. .... 45

Figure 2.4: (a) A typical representation of a contact angle titration curve due to acid-base interaction of two different polyamide films containing free carboxylic and amine monomers on the surface [117–119]. (b) Comparison of surface potential measurement from contact angle titration and streaming potential technique [21]. (b)

Surface tension components as a function of pH and NaCl ionic concentration. The inset image shows a conceptual illustration of the influence of NaCl ionic concentration on membrane wettability [21]. .....46

Figure 2.5: (a) Commercial membranes BW 30 and SW 30HR exhibit greater uniformity of surface features thus less contact angle hysteresis. Surface physical and chemical heterogeneity increases (b) colloidal and (c) organic fouling propensity. This fouling behavior is directly related to the surface contact angle hysteresis ( $\Delta\theta$ ) [22,124]. .....47

Figure 2.6: (a) A Synthesis of biofouling resistant membrane by incorporating graphine oxide (GO), and metal (silver, Ag) organic framework (MOF). The GO-AG-MOF exhibits lowest magnitude of contact angle and zeta potential. This ensures (b) high normalized flux for this membrane for both sodium alginate and E. Coli feed water solution [125]. .....48

Figure 2.7: (a) Different stages of biofilm formation over membrane surface [126]. ‘Baier curve’ indicates that surface tension of any material should be greater than 60 mN/m [127]. (b) From the interfacial energy analysis, it is evident that 9-FAS membranes are less hydrophobic than 17- FAS coated membrane. Humic acid fouling clearly shows that less hydrophobic membrane provides better performance. Interestingly, the oil fouling shows different trend. It is due to the higher oleophobicity of 17-FAS coated membrane [128]. .....49

Figure 2.8: (a) Top panel: Evolution of a typical nucleation process. After the formation of critical nuclei, the crystallization process emerges to grow through coalescence [138]. Bottom panel: Scale formation mechanism (silica scaling with hydroxyl group) on the TFC membrane due to heterogeneous nucleation [132]. (b) Surfaces having less adhesion towards silica particle, i.e., cellulose acetate (CA) shows better flux recovery than the polyamide (PA) one. (c) Surface engineered membranes can be an excellent option for scaling resistivity. Dual scale roughness

features (SINP) can shift the membrane surface from pinned to rolling zone which results in higher normalized flux in membrane distillation process [133].....50

Figure 2.9: (a) Schematic of the fabrication of a TFC membrane with as poly(acryloyl hydrazide) star (PAH-SP) polymer via interfacial polymerization reaction. PAH-SP having multiple linear polymer arms showed a globular shape with a uniform size. This globular structure can form interstitial spaces between the close-packed neighboring star polymers, and act as ‘effective’ water channels [135]. This ensures high foulant resistivity. (b) SEM image of the top surface and cross-section morphologies at different magnifications for pristine and surface modified micropatterned membranes prepared using phase separation micro-molding approach [137]. Pattern membranes showed better perm-selectivity than the flat membranes. (c) Fabrication of anti-fouling membranes: fouling resistance and release strategy. Hydrophilic surfaces only exhibit fouling resistant property. But the fouling release strategy includes the incorporation of both hydrophilic and hydrophobic non-polar low surface energy segments. The low surface-energy segments ensure foulant release in the presence of surface turbulence (e.g., high cross-flow) [10].....51

Figure 3.1: Illustration of (a) a sessile droplet over a smooth and chemically homogeneous (ideal) solid surface.  $\theta_Y$  is the equilibrium contact angle based on Young’s equation; (b) equilibrium static contact angle ( $\theta_S$ ) of a liquid droplet over a real surface with physical and chemical heterogeneity; (c) advancing contact angle of liquid droplet while spreading over a real surface; and (d) receding contact angle of a liquid droplet while retreating from a real surface. ....81

Figure 3.2: FESEM images of (a) BW30, (b) X201, (c) XLE, (d) TS 80 and (e) NF90. All the membranes have a polyamide selective layer with a ridge-and-valley structure. The BW30, XLE, and X201 exhibit conservatively a more uniform surface morphology compared to the NF90 and TS80 membranes. ....82

Figure 3.3: AFM surface topography of the polymeric membranes. The horizontal axis represents the scan size (30  $\mu\text{m}$ ), and the vertical scale represents the feature height ( $\mu\text{m}$ ). ..... 83

Figure 3.4: Variation of (a) average surface roughness ( $R_{avg}$ ) and (b) RMS roughness ( $R_{rms}$ ) with scan size. The roughness of BW30 and X201 varied slightly at different scan sizes. In contrast, a higher magnitude of surface roughness was quantified for XLE, TS80, and NF90 at larger scan sizes. .... 84

Figure 3.5: (a) Variation of the roughness-ratio obtained by AFM at different scan sizes. The roughness-ratio decreased as the scan size expanded; (b) Variation of fractal dimension ( $D_{\text{Fractal}}$ ) exponents at different scan sizes. The fractal dimension of the membranes varied up to the scan size of  $\sim 20 \mu\text{m}$ , and then remains steady higher scanned area..... 85

Figure 3.6: Surface wettability plots of polymeric membranes. Linear correlation of  $\gamma L \cos\theta$  versus  $\gamma L$  is observed for both equilibrium and advancing contact angles. The slope and y-axis intersection in panel (a) provide the  $rCAW$  and  $\gamma SD$ , respectively. Similarly, the slope of the linear fit and the intersection with the y-axis in panel (b) gives the  $rCAAd$  and the  $F\gamma L$  of the polymeric surface..... 86

Figure 3.7: (a) validation of experimentally extracted  $rCAAd$  and  $F\gamma L$  with theoretical relation to predict the advancing contact angle ( $\cos\theta Ad$ ). All the calculated contact angles were in good agreement with the theoretical prediction (grey map); (b) validation of experimentally extracted  $\gamma SD$  with theoretical relation to predict the advancing contact angle ( $\cos\theta Ad$ ). The calculated contact angles were within the range (grey map) predicted by theoretical relation. .... 87

Figure 3.8: (a) The comparison of the roughness-ratio obtained by AFM and contact angle analysis. The results reveal the presence of 10% to 25% discrepancies between the roughness-ratio predicted by AFM and the wettability analysis. (b) Variation of dispersive surface tension components due to the variation of roughness factor ( $r_{\text{AFM}}$ ) obtained at different scan size from the AFM analysis..... 88



Figure 3.9: (a) Normalized flux decline versus time for three different membranes: BW30, XLE, and NF90. We observe strong dependency of flux decline with respect to surface morphology; (b) Correlation between the normalized flux ( $J/J_0$  after 6 hr filtration) and surface roughness-ratio ( $r$ ). Correlation between the roughness-ratio of the membranes, evaluated by conventional AFM test and the proposed CA-based methods. ....89

Figure 3.10: (a) Phase diagram of the wettability of the membrane surface with water. Among the tested membranes, NF90 and XLE membrane were close to the non-wetting region while the BW30, X201, and TS80 were in the partial wetting region. (b) Wettability envelope of five different membranes. BW 30 shows larger wettability envelope which indicates better wettability profile toward contact liquid. NF90 shows the lowest wettability envelope which agrees with its higher fouling propensity.....90

Figure 3.11: Schematic diagram and experimental methodology. (a) Conceptual demonstration of adsorbed cation and electric double layer (EDL) formation due to the surface functional groups containing negative charge. Due to EDL formation, two different planes can be identified namely stern plane, and shear plane. The thickness of the electric double layer (also known as inverse Debye length) is solely the function of the solution, more specifically ionic concentration of the solution. For contact angle titration experiments, this layer should be controlled in such a way so that ionic strength effects over the over the contact angle ( $\theta_c$ ) and liquid interfacial tension ( $\gamma_L$ ) is insignificant. (b) Experimental evidence of the under-oil (Hexadecane) pH dependency over contact angle for a polyamide sample. ....91

Figure 3.12 Quantification of surface potential and comparison between the streaming potential and wettability method for (a) glass, and (b) BW 30. We observe reasonable accuracy for Holmes-Farley [175] and Gibbs equation [170]. Young-Lippmann equation[37,182] deviates more than 80% for surfaces having complex surface chemistry such as polyamide BW 30 sample. Under-oil contact angle titration experiments exhibit better accuracy in comparison with the in-air measurement...92

Figure 3.13 Wettability of buffered and unbuffered solutions for (a) in-air, and (b) under-oil measurement. In-air experiments exhibits lower contact angle for both Glass, and BW 30 samples. A likely explanation is the evaporation effects or a thin layer of oil layer over the solid samples. However, despite change of surrounding medium, we observe similar types pH dependency over the contact angle for all the cases. (c) Wettability of buffered solution for hydrophobic polypropylene sample. We did not observe any significant variation for any cases; however, we observe a maximum contact angle at pH ~4. Zeta potential results from the inset image leads us to correlate this point to the surface IEP (pH ~3.5).....93

Figure 4.1. Outline of under-liquid wetting of solid surfaces: (a) A liquid drop (D) spreads over the solid surface (S) under-liquid medium (M). The contact angle ( $\theta_{SMD}$ ) is the resultant of three different surface tensions, drop-medium ( $\gamma_{DM}$ ), solid-drop ( $\gamma_{SD}$ ), and solid-medium ( $\gamma_{SM}$ ); (b) A liquid drop spreading over the thin layer of the medium created on the top of the solid surface; (c) Molecular rearrangement of the solid surface due to the surrounding medium and the drop contact. .... 112

Figure 4.2 Scheme of wettability measurement of solid surface in air and under-liquid. (a) Wetting of a solid surface (S) by a liquid droplet (D) in air (A); (b) Wetting of a solid surface by a liquid droplet in another liquid medium. Due to the formation of a thin layer of surrounding medium on the surface, and/or possible molecular rearrangement at the solid-medium interface, the solid surface tension under-liquid will be different from that in air..... 113

Figure 4.3 AFM surface topography of glass, PMMA and PTFE solid samples. For all the cases, the scan size was  $10\ \mu\text{m} \times 10\ \mu\text{m}$ . The height variation of Glass and PMMA is within about  $5 \pm 0.5\ \text{nm}$ , but PTFE shows a higher variation within about 60 nm. Thus, we observe uniform surface morphology for all the cases. .... 114

Figure 4.4 Dispersive, polar, and total surface tension of glass, PMMA and PTFE samples, (a) in air, and (b) underwater cases. We observe higher polarity of solid-

water interfacial system than in solid-air case. The represented data is based on the  $\pm 10\%$  standard deviation of the probe droplet wettability..... 115

Figure 4.5 Optical images of various probe droplets over PTFE, Glass, and PMMA surfaces underwater. For all the cases, PTFE shows lower underwater contact angle ( $< 90^\circ$ ). This indicates the water repellency of PTFE in a solid-liquid-liquid system. We also observe a similar trend of polar and non-polar oil wettability. In both cases, oil droplets having lower oil-water interfacial tension show lower contact angle, e.g., oleic acid for polar oil and 1,4- Dibromobutane for non-polar oil. .... 116

Figure 4.6 The comparison of theoretical prediction with experimental contact angle observations underwater for (a) PMMA, (b) glass, and (c) PTFE surfaces. The proposed theoretical model in this work exhibited good agreement with the experimental observations within  $\sim \pm 15\%$  deviation. In contrast, a large deviation ( $> \pm 30\%$ ) between the theoretical predictions and experimental values was observed in case of PMMA and Glass based on the previously available theories [90,194,200] In case of PTFE, Trinavee et al.'s [200] theory exhibits deviations more than  $\pm 50\%$ . Moreover, Bartel-Osterhof equation [90,194] cannot predict underwater wettability of PTFE..... 117

Figure 4.7 Effects of oil-medium interfacial tension on the wettability for  $\gamma_S * D = 50$  mN/m,  $\gamma_S * P = 0$  mN/m,  $\gamma_{OD} = 50$  mN/m,  $\gamma_{OP} = 0$  mN/m. We observe that a higher oil-water interfacial tension results in lower wettability. This indicates that from lower to higher (from 10 mN/m to 100 mN/m for this case) oil-water interfacial tension the solid wettability shifts towards the non-wettability region. .... 118

Figure 5.1. Schematic of the experimental setup for analysis of under-liquid wettability at elevated temperature. Here, HRC: High resolution camera, LS: Light source, TCC: Temperature controlled environment chamber, TCU: Temperature control unit..... 136

Figure 5.2. Variation of drop-medium interfacial tension ( $\gamma_{DM}$ ) with temperature. We observe an increasing trend for (a) polar, and decreasing trend for (b) non-polar

probe liquids with the increase of medium temperature. The data presented here are based on the  $\pm 5\%$  standard deviation..... 137

Figure 5.3. Variation of surface tension components at various temperature for (a) polar, and (b) non-polar probe liquids. We observe decrement of polarity with the increased temperature. The dispersive surface tension components are nearly constant for polar liquids but decreases with temperature for non-polar liquids. The data presented here are based on the  $\pm 5\%$  standard deviation of drop ( $\gamma_D$ ), medium ( $\gamma_M$ ), and drop-medium interfacial tension ( $\gamma_{DM}$ ). ..... 138

Figure 5.4. Variation of wettability for different probe liquids at different temperature for (a) glass, and (b) silicon wafer, (c) PMMA, and (d) PTFE. We observe increment (Glass and Wafer), decrement (PMMA), and nearly constant (PTFE) trend for these cases. For PMMA, the decreasing trend continues up to  $60\text{ }^\circ\text{C}$  (with an exception of comparatively highly polar DEP drop), and then nearly constant wettability is observed. For PTFE, no specific trend was observed for all the prob liquids. .... 139

Figure 5.5. Variation of surface tension components at various temperature for various solid surfaces, (a) glass and silicon wafer, and (b) PTFE and PMMA. We observe nearly constant magnitude of surface tension for non-polymeric samples, e.g., glass and silicon wafer. However, we observe no specific trend for polymeric surfaces. The data presented here are based on the  $\pm 10\%$  deviation of the wettability of probe liquids. .... 140

Figure 5.6. The comparison of underwater wettability prediction at different elevated temperature for (a) non-polymeric, and (b) polymeric samples. Present theoretical framework exhibits good agreement with the experimental observations within  $\sim \pm 25\%$  deviation. In contrast, a large deviation ( $> \pm 35\%$ ) between the theoretical predictions and experimental values was observed in case of previously available theories [234]. Moreover, previous theories deviated more when the solid surface

exhibit higher polarity ( $\gamma_{SP} > 30 \text{ mN/m}$ ) with a sharp increasing trend, e.g., glass and wafer..... 141

Figure 5.7. Effects of temperature on the non-polymeric solid wettability with the increasing trend, (a) glass, (b) silicon wafer. We observed three different zones for two different temperature conditions. Due to the increment of temperature, the wetting to non-wetting transition blue line shrank towards right. Partial non-wetting zone I in turn increased to Zone I and II. Furthermore, the interfacial tension of the polar probe liquids moved away (shifts towards left) from the transition lines. The combined effects confirmed the steeper increase of contact angle. The experimental data presented in the figure were based on the 5% standard deviation. .... 142

Figure 6.1. Overview of the characterization of membrane surface and permeation properties using contact angle analyzer. It is evident from the literature that contact angle can provide a wide variety of information: surface properties such as wettability [82,239], roughness and fractal characteristics [14,240], surface charge and zeta potential [21], and permeation properties such as perm-selectivity [13,241], and anti-fouling property [11] for novel material development [10,123]......53

# Chapter 1 †

## Introduction

---

†The material of this chapter has been prepared for submission as Md Farhad Ismail, Behnam Khorshidi, and Mohtada Sadrzadeh. Characterization of membrane surface and permeation properties by contact angle measurements: quantification strategies and applications. *Advances in Colloid and Interface Science*, 2020.

## 1.1 Water demand and membrane technology

The dwindling supply of clean freshwater is one of the world's most severe problems, aggravated by the increased population and contamination of the limited water resources [1,2]. With the growing demand for more pure water, it has become essential to develop innovative water treatment technologies or to improve the existing techniques. Conventional water purification techniques, e.g., thermal distillation (TD) and multi-stage flash, rely on the natural water cycle of evaporation and condensation to produce water with very low salt concentration. Membrane separation processes have become a viable alternative to these conventional methods primarily due to their lower energy consumption, more compact design, simpler operation procedures, and comparable treated water quality [3,4]. **Figure 1.1a** compares the global capacity of high-quality water production processes [5,6]. As can be observed, water purification by membrane process (reverse osmosis) is the leading technology for high-quality water production.

Membranes are semipermeable barriers, which moderate the transport of various species selectively. The driving force for transportation can be pressure (e.g., reverse osmosis), concentration (e.g., gas separation), temperature (e.g., membrane distillation), and electric potential (e.g., electrodialysis). Pressure driven membrane separation units, widely used to produce high-quality water globally, can be divided into four major classes based on the ability of different sized particle rejection [4], such as Microfiltration (MF) a minimum of  $\sim 100$  nm, ultrafiltration (UF) a minimum of  $\sim 1$  nm, nanofiltration (NF) a minimum of  $\sim 0.5$  nm and reverse osmosis (RO) a minimum of  $\sim 0.1$  nm. Nanofiltration and reverse osmosis membranes are considered as the non-porous dense TFC membrane among these classifications. The invention of the TFC membrane provided the opportunity to reduce the thickness of the NF/RO membranes down to nanoscale ( $< 300$  nm). The separation process by membranes is essentially a surface phenomenon. An ideal TFC membrane should have high and stable permeability, high selectivity, and low fouling [7–9]. However, the next-

generation membrane materials will focus on high selectivity and fouling propensity at a constant permeation rate [10]. Fouling is generally caused by the non-specific interaction of foulants and membrane surface which includes hydrogen bonding, van der Waals, hydrophobic, and electrostatic interactions [11].

## **1.2 Membrane characterization and next-generation membrane materials**

One can overcome the limitation of the membrane processes by introducing novel interfacial materials with special wettability [9,12,13]. Notwithstanding, accurate characterization of a membrane is important to understand the underlying science for ensuring high separation efficiency, anti-fouling properties, and the applicability of the fabricated membrane. It is generally accepted that membranes with lower roughness and high water wettability characteristics (with contact angle less than  $45^\circ$ ) are less susceptible to fouling [14–16]. The surface properties of membranes are characterized by quantifying the surface wettability (contact angle measurement), surface topography and morphology (atomic force and scanning electron microscopy), surface chemistry (X-ray photoelectron spectroscopy and Fourier transform infrared), and surface charge (zeta potential measurement). Contact angle measurement is widely used for membrane characterization and can be considered as a first simple step to quantify the membrane surface properties, such as surface wettability, surface tension (and surface free energy), hydrophilicity [17]. Generally, to determine the surface hydrophilicity, in addition to contact angle measurements, it is required to measure surface roughness, and surface tension (free energy) of the material, while only ~1% of the membrane literature measured all the three parameters (**Figure 1.1b**).

Furthermore, one can relate the surface charge and functional groups to the membrane surface tension parameters, which are responsible for altering the surface hydrophilicity. Only a single analytical parameter, i.e., the contact angle can give a



wide variety of useful information. Interestingly, our recent literature survey on the surface properties of TFC membranes (**Table A1.1**) indicates a wide variation of contact angle data of the same membrane surface. This indicates that measurement technique, measurement accuracy, and data reproducibility should be ensured for contact angle analysis.

It is worth noting that each of the analytical techniques provides a varying degree of information at different depths of the surfaces [18,19]. This depth can be referred to as ‘interphase depth’ based on the analytical technique. For example, we can define  $\theta$ -interphase (for contact angle measurement), XPS-interphase (for X-ray photoelectron spectroscopy), and so forth (**Figure 1.1c**). However, surface functional groups remain at different depth of the surface; in some cases remain so deep that there would not be any influence over the interfacial interactions [18]. Ferguson et al. [18] referred the portion of the solid as sub- $\theta$  interphase where interfacial interaction would happen. This sub- $\theta$  interphase is not well defined with respect to the ‘interphase depth’ of the available analytical techniques. Permeability, pore structure, and liquid-solid interactions are the three decisive factors to approximate this.

**Figure 1.1d** depicts a brief overview of the thin-film composite membrane's surface properties. Recent studies over membrane surfaces indicate that the contact angle measurement can be a useful tool to directly quantify not only the surface physical-chemical properties but also can be a powerful tool to analyze the membrane performance parameters [15,20–23]. Off late, several review articles were published on the surface characterization techniques of water treatment polymeric membranes [19,24–30]. These reviews mostly focused on either generalized characterization techniques without detailed illustration. For instance, it is proven that membrane surfaces exhibit fractal characteristics [15,31], with a variety of irregular, rough and fragmented structures. A specific procedure is, therefore, required to determine both the wettability and roughness of such fractal surfaces. Furthermore, surface charge and functional groups are also related parameters with the hydrophilicity, which can also be accessed through contact angle measurement [21,32–36]. Thus, a comprehensive illustration is still required to elucidate the wide range of parameters obtained from contact angle measurements of polymeric membranes and employ them towards novel material development for the efficient separation process. This chapter will highlight different techniques to measure the contact angle of the membrane surface with a focus on accurate characterization and consistency of the results.

### **1.3 Methods for measuring the contact angle of membrane surfaces**

Surface wettability, often characterized by contact angle measurement techniques, is believed to have a direct impact on membrane performance parameters. TFC non-porous membranes generally consist of three layers: a top thin selective layer, porous interlayer support, and base support layer[14]. The support layer provides mechanical stability to the membrane structure to operate under high pressure while the top selective layer plays a vital role in the separation process.

Hence, various surface modification approaches over the top selective layer have been carried out to tune the membrane surface properties [37,38]. Thus, proper and accurate characterization of the surface physical-chemical properties is crucial to understand the outcome of surface modification as well as the development of novel material. This section will focus on the contact angle measurement techniques of ideal, and real surfaces applied for membrane surface characterization.

In general, three different techniques have been employed to measure the contact angle of polymeric membranes, i.e., sessile drop, captive bubble, and Wilhelmy plate method [39,40]. Sessile drop and captive bubble measurement techniques (**Figure 1.2a**) are based on optical analysis of the drop/bubble over the surface, and the Wilhelmy plate method (**Figure 1.2b**) is based on the force balance due to contact of the surface with the liquid [39]. The sessile drop technique can be applied to both dry (e.g., in the air) and wet (e.g., under liquid) samples [41], while the captive bubble technique is only limited to measuring the contact angle only for wet surfaces. The Wilhelmy plate method is used to measure surface tension at an air-liquid or liquid-liquid interface and is only applicable for surfaces that have similar composition and morphology on both sides of the surface [42]. Roux et al. [43] first measured the contact angle of polymeric membrane surfaces using the Wilhelmy plate method. Due to the complexity of the experimental procedure and sample preparation, this method is not utilized widely to determine the membrane contact angle. Zhang et al. [44] conducted a comparative wettability study of ultrafiltration membranes using the sessile drop and captive bubble techniques. They observed different contact angles from these two different measurement techniques for the same sample. They reported that surface reconstruction due to under-liquid measurement is one of the probable reasons for this discrepancy. Baek et al. [45] conducted a comparative study of contact angle measurements over the TFC membranes. They observed more reliable and reproducible results from the captive bubble technique as compared to the sessile drop one. However, the straightforward nature of the sessile drop technique along with advantages, such as the capability to investigate liquid drop spreading and impact, phase change (e.g., evaporation and

solidification), surface heterogeneity, and liquid sliding angle for wetting cases ( $\theta < 90^\circ$ ) and roll-off angle for non-wetting cases ( $\theta > 90^\circ$ ), made this method the most popular one to analyze the wettability of membranes [42]. In the present study, we will mainly focus on the contact angle measurements using the sessile drop technique.

From the contact angle measurement, three different data can be obtained: static, advancing, and receding contact angle. Static contact angle ( $\theta_e$ ) is the angle obtained over a smooth, rigid, and chemically homogeneous surface. This contact angle is also known as static equilibrium or Young contact angle ( $\theta_Y$ ). In equilibrium, the contact angle between the liquid and the ideal solid surface (i.e., atomically smooth, chemically homogeneous, nonreactive, and rigid) can be defined using Young's equation (**Figure 1.2c**) [46]:

$$\cos \theta_Y = \frac{\gamma_{SV} - \gamma_{SL}}{\gamma_{LV}}, \quad (1.1)$$

where,  $\gamma_{SV}$ (or  $\gamma_S$ ),  $\gamma_{LV}$  ( $\gamma_L$ ) and  $\gamma_{SL}$  are the solid-vapor, liquid-vapor, and solid-liquid interfacial tension, respectively. Eq. 1.1 indicates that an ideal solid surface with high surface tension tends to show a low contact angle and vice versa. The highest contact angle observed over a surface due to the increment of drop volume is known as advancing contact angle ( $\theta_{ad}$ ). In contrast, the lowest contact angle observed over a surface due to the decrement of drop volume is known as the receding contact angle ( $\theta_{re}$ ). Both of these two contact angles also represent equilibrium states at two different metastable conditions. These three contact angle values should be the same for an ideal case scenario, although in reality, it hardly occurs. In reality, membrane surfaces have physical (e.g., roughness), and chemical (e.g., functional groups) heterogeneity. The contact angle over a real surface can be considered as an apparent contact angle ( $\theta_{ap}$ ) (also known as macroscopic contact angle). Thus, the contact angle obtained from different techniques over membrane surfaces is actually apparent contact angle (bottom panel of **Figure 1.2c**). However, for determining the wettability related parameters such as surface free energy, and

hydrophilicity, it is required to measure the equilibrium contact angle from the observed apparent contact angle. To account for the effect of different heterogeneity, two theories, namely Wenzel equation [47,48] (for physical heterogeneity), and Cassie-Baxter equation [49,50] (for chemical heterogeneity) are commonly utilized. A detailed description of these two equations will be discussed in the next section.

The next step to determine the equilibrium contact angle is to measure the surface roughness factor ( $r$ ), which is also known as the Wenzel roughness factor. This parameter is related to the surface area difference due to the roughness and generally characterized by the atomic force microscopy (AFM) technique [51,52]. Polymeric membrane surfaces exhibit average nanoscale roughness, mostly between 10 nm to more than 200 nm. It is believed that a root mean squared (RMS, will be discussed later) roughness of less than ~80 nm does not influence the wettability and thus, this value can be considered as the transition between smooth and rough surface [53]. However, a recent study [15] indicates that for a membrane surface this limit should be ~50 nm. Thus, the surface roughness factor ( $r$ ) plays a vital role in determining the equilibrium contact angle. There are different ways to measure the surface roughness factor such as optical profilometry, and atomic force microscopy (AFM) [52,54–56]. However, the AFM measurement technique provides better accuracy for the surfaces having nanoscale roughness [55,56]. The Wenzel roughness factor ( $r$ ) from the AFM analysis can be obtained using Eq. 1.2 [57] :

$$r_{AFM} = \frac{\sum_{j=1}^{N-1} \sum_{i=1}^{M-1} A_{i,j}}{(M-1)(N-1) \Delta x \Delta y} \times 100\% \quad (1.2)$$

where, M is the number of points per sampling profile, N is the number of sampling profile,  $A_{ij}$  is the actual surface area, and  $\Delta x \Delta y$  is the geometric cross-sectional area.

However, the accuracy and reliability of the AFM measurement largely depend on the scan size, scan mode, and scan speed [15,58,59]. AFM provides three significant modes of measurement: contact mode, non-contact mode, and tapping mode (**Figure 1.3**). Contact mode operates in the repulsive interaction regime

(constant force/height between the sample and the probe), non-contact mode operates in the attractive regime (based on intermolecular forces), and tapping mode operates in both regimes while maintaining lower interactions with the surface (**Figure 1.3**). Tapping and non-contact modes demonstrate the surface topography to a greater extent compared to the contact mode. Moreover, the operation in contact mode may damage the sample surface due to the lateral dragging interactions between the probe tip and surface [60]. Tapping mode response time is more than three times faster than the contact mode due to their variation of resonance frequency [58]. Though many researchers utilized different modes, however, the tapping mode measurement is recommended due to a wide range of advantages, e.g., better response time [28,58,60,61].

Given the above discussion, the accurate determination of the surface roughness is equally essential to determine the wettability of any physically heterogeneous surface. Surface roughness is the variation of the height along the surface, which can be uniform patterns or random ridge and valley structures. This variation is generally quantified by average roughness ( $R_a$ ), and the root mean squared (RMS) surface roughness ( $R_q$ ) [28,62,63]. Average roughness is the mean height variation due to the heterogeneity, and RMS roughness is the standard deviation of the height variation. It is to be noted that these two commonly used parameters extracted from AFM do not always provide the anisotropy in the topography or the distance between the features on the surface. For example, surfaces with different morphologies may have the same magnitude of RMS through their response with regards to tribology, or adhesion will be different (**Figure 1.4a,b**). However, in the case of randomly distributed heterogeneous surfaces, such as TFC membranes, the roughness parameters also change in a lateral direction, i.e., AFM scan size-dependent [15,31]. These types of characteristics are commonly observed in fractal surfaces. Fractal surfaces display different topography up to a specific magnification level (self-affinity) and after that, show self-similar characteristics (**Figure 1.4c,d**). So, for membrane surfaces, in addition to surface roughness, which measures the vertical distribution of heterogeneity, it is worth evaluating the lateral

distribution of the irregularities. In this context, it is necessary to distinguish between self-affine and self-similar fractal surfaces. The former exhibits invariant surface features at different spots, while the latter shows surface structures that vary over the translation and scaling [64]. The roughness parameters of these types of surfaces follow a power-law relationship as follows [31,65]

$$R = AL^{3-D_f} \quad (1.3)$$

where,  $R$  is the roughness related parameter such as RMS roughness,  $L$  is the AFM scan size, and  $D_f$  is the fractal dimension.

There are different methods to determine the fractal dimension  $D_f$ , such as the slope ( $m$ ) of power spectral density (PSD) plot of the height variation [65]. The relationship between the fractal dimension and slope of the plot is given by as follows:  $D_f=3+0.5 \times m$ . Tsujii et al. [66,67] reported that this fractal dimension ( $D_f$ ) is directly related to the roughness factor  $r_{fractal} = \left(\frac{L}{l}\right)^{D_f-2}$ , where ‘ $L$ ’ is the upper (maximum), and ‘ $l$ ’ is the lower (minimum) length scale of the heterogeneity observed on the fractal surface. More detail description on this topic will be described in the next chapter.

## 1.4 Scope and objectives

The immense potential of incorporating the interfacial materials with special wettability in the membrane-based separation process prompts the necessity for an in-depth understanding of the underlying science that governs the membrane separation process. More specifically, the ability to tailor surface wettability is now a key challenge to develop novel membrane materials in real-world applications [10,13,14,68]. The primary goal to incorporate novel materials with special wettability in the membrane process is to increase the hydrophilicity with reduced heterogeneity. Thus in an effort to fundamentally understand the permeation properties of the membrane materials, several attempts have been carried out to

incorporate new characterization techniques for evaluating the wettability related parameters [20–22,69–75]. However, a comprehensive effort is still required to bridge the gap between theoretical assumptions and experimental applications. For example, the fractal behavior [31] and under-liquid wettability adaptation [76,77] of polymeric membrane surfaces still require special attention. Based on the comprehensive literature review provided in Chapter 2 on analysis of membrane surface properties, several specific questions yet to be answered are:

(a) How does the membrane heterogeneity (e.g., roughness) affect the wettability and surface tension?

(b) What are the effects of surface polarity on underwater membrane wettability?

(c) How do feed water and environmental conditions (e.g., temperature) affect the membrane wettability and anti-fouling property?

Given that, the main objectives of this thesis that defines the scope of the work are as follows:

1. Probe the nanoscale heterogeneity of membrane surface by contact angle analyzer and its impact on the membrane surface tension and fouling propensity.
2. Develop a theoretical framework and experimental validation of the model to correlate under-liquid adaptive wetting of the membrane surface.
3. Quantify the interfacial interaction in harsh environmental conditions, e.g., at elevated temperatures. The developed theoretical framework will be applied to investigate the surface wettability adaptation at elevated temperatures.



## 1.5 Thesis Structure

Chapter 1 introduces the advantages and limitations of membrane technology, the importance of membrane characterization for novel material development to improve the limitation, usefulness of contact angle to understand the membrane surface properties and performance analysis. The scope and objectives of this thesis are also presented.

Chapter 2 presents a detailed literature review on the quantification of membrane surface properties and evaluating the permeation properties using contact angle analyzer.

Chapter 3 demonstrates the theoretical and experimental approach to probe the membrane nanoscale heterogeneity, which includes determination of surface roughness and surface charge distribution using contact angle analyzer. A detailed comparison with the other available analytical techniques such as atomic force microscopy (AFM) and streaming potential analyzer are also provided.

Chapter 4 illustrates the approach to evaluate under-liquid wettability adaptation of a solid surface, which is essential for assessing the membrane surface properties under real environmental conditions.

Chapter 5 investigates the impact of surrounding medium temperature over membrane wettability. The developed theoretical framework and experimental technique are applied to characterize the stability of membrane surfaces in harsh environmental conditions such as an elevated temperature up to 90 °C.

Chapter 6 summarizes the significant findings and major conclusions of this thesis. The suggestions for future work are also provided.

## 1.6 Thesis Contributions

This work provided the first feasible methodologies to quantify all the three membrane influential surface properties, i.e., surface tension, roughness, and surface charge in complex and harsh environmental conditions using only one single analytical parameter, e.g., contact angle. The proposed nanoscale characterization technique indicates the fractal behavior of membrane surfaces. The outcome of the contact angle characterization technique suggests that conventional AFM measurement requires special types of assessment to quantify the surface heterogeneity of the fractal surfaces. Furthermore, surface charge and surface potential are also quantified using the contact angle analyzer. It is worth noting that reducing the degree of surface charge heterogeneity is important to synthesize new materials for anti-fouling membranes. The contact angle characterization technique provides the information on local surface charge distribution, whereas conventional streaming potential technique indicates the average surface charge density and surface potential over the sample surface.

Polymeric membrane surfaces exhibit wettability adaptation due to the change of surrounding medium conditions. The current in-air wettability characterization technique is inadequate to understand the membrane surface properties for underwater application. Underwater super-oleophobic and anti-fouling membranes require specific interfacial interaction to withstand harsh environmental conditions. Experimental validation of the proposed theoretical framework for the under-liquid characterization confirms the influence of surrounding medium over the surface wettability. The novel under-liquid characterization technique can provide the dispersive, polar, and acid-base surface tension parameters, which play a crucial role in foulant-surface interfacial interaction. High-temperature membrane separation processes are advantageous for the membrane-based water treatment due to their increased water wettability and fouling resistivity. However, the thermal stability of the polymeric membranes is a severe concern in this regard. Present research work also provides the theoretical framework to characterize the polymeric

surfaces at an elevated temperature. This also provides a novel pathway to evaluate the permeation properties and thermal stability of the membrane surfaces at elevated temperatures.

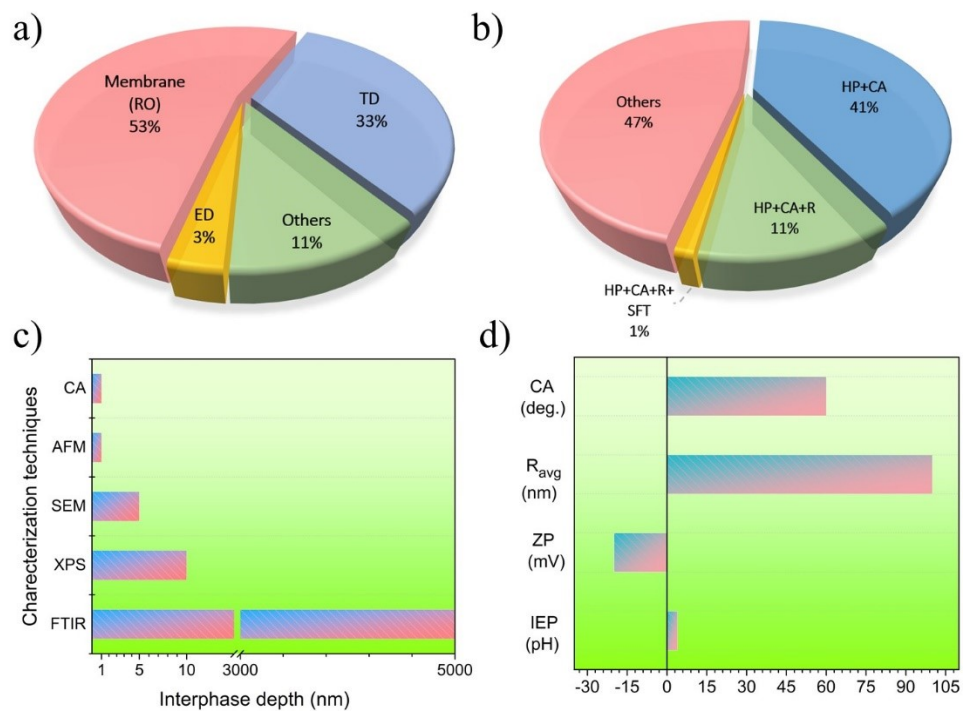


Figure 1.1: Overview of the water treatment processes and membrane characterization parameters. (a) Global scenario of high-quality water production capacity by different processes [6]. Here, RO: reverse osmosis, TD: thermal distillation, ED: electro dialysis. (b) A statistical overview of the characterization of hydrophilicity of TFC membranes from the Scopus literature search (conducted in August 2019). Here, HP: Hydrophilicity, CA: Contact angle, R: Roughness, SFT: surface tension. (c) The sensitivity of the different membrane characterization techniques [18,19]. (d) Surface properties of TFC membranes [14,78]. The zeta potential is shown for a pH of 7. Here, CA: contact angle,  $R_{avg}$ : average surface roughness, ZP: zeta potential, IEP: iso-electric point.

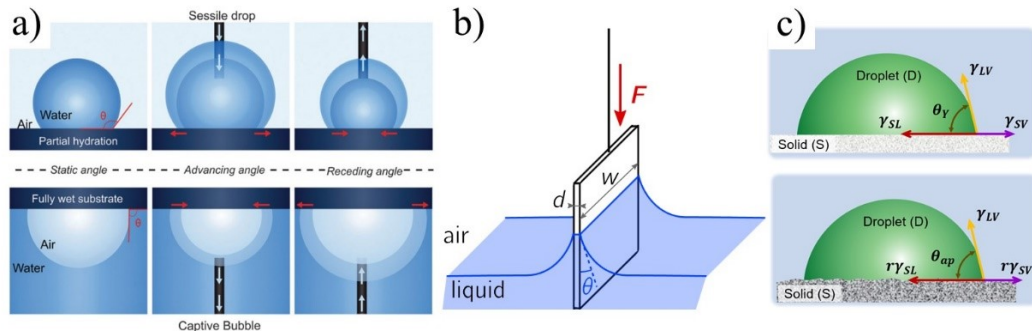


Figure 1.2: Various methods to determine the contact angle of the membrane surface. (a) Static, advancing, and receding contact angle measurements to characterize the wettability with the sessile drop on the dry sample (top panel) and the captive bubble technique on a thoroughly wet sample (bottom panel) [79]. (b) Wilhelmy technique is used a thin rectangular plate of the sample to measure the contact angle. The force ( $F$ ) acting on the plate due to wetting and the wetted perimeter ( $2d+2w$ ) are then utilized to determine the contact angle [40]. (c) The contact angle ( $\theta_y$ ) on a smooth surface (top panel) alters to the apparent contact angle ( $\theta_{ap}$ ) due to surface roughness (bottom panel). The factors of physical heterogeneity affecting the wettability is known as Wenzel roughness factor ( $r$ ).

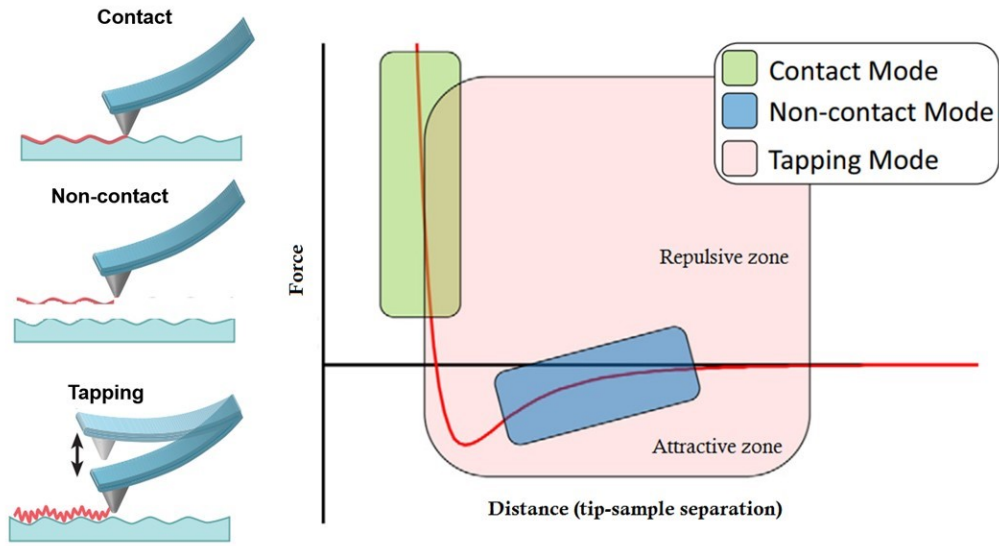


Figure 1.3: Membrane surface topography characterization by AFM with different scanning modes. Contact mode operates only in the repulsive zone, non-contact mode operates in an attractive zone, but tapping mode operates both in the repulsive and attractive zone [28,61].

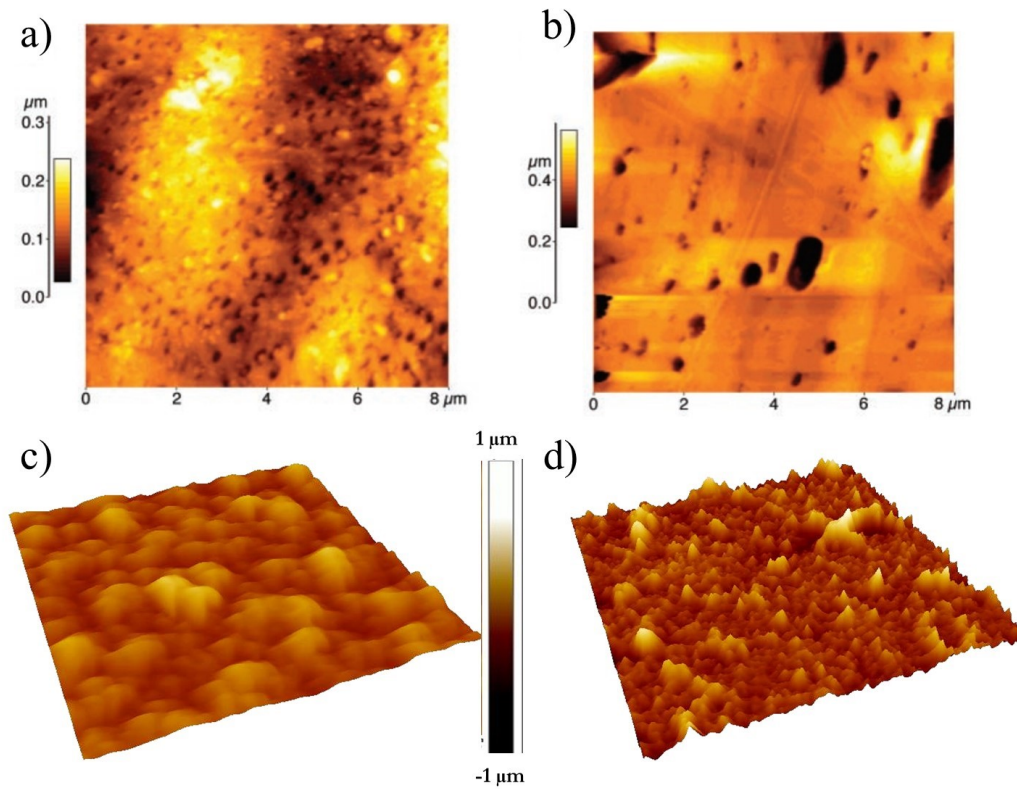


Figure 1.4: Effects of anisotropic height variation and scan size over the AFM measurements. AFM images of two polymeric surfaces with different topography but similar RMS roughness, (a) 38.5 nm, and (b) 36.1 nm [60]. Fractal surfaces such as the XLE RO membrane exhibits roughness dependent on scan size, (c) 5  $\mu\text{m}$ , and (d) 30  $\mu\text{m}$  [15]. A scan size of 5  $\mu\text{m}$  provides  $r_{AFM} = 1.45$ , and 10  $\mu\text{m}$  scan size provides  $r_{AFM} = 1.16$ .

## **Chapter 2** ※

# **Literature Review: Membrane Characterization by Contact Angle Analyzer**

---

※ The material of this chapter has been prepared for submission as Md Farhad Ismail, Behnam Khorshidi, and Mohtada Sadrzadeh. Characterization of membrane surface and permeation properties by contact angle measurements: quantification strategies and applications. *Advances in Colloid and Interface Science*, 2020.



## **2.1 Characterization of membrane surface properties using contact angle**

### **2.1.1 Characterization of surface wettability**

The terms “wettability”, “hydrophilicity” and “hydrophobicity” have been widely used in the membrane science community and are commonly used to describe the spreading behavior of liquids over a solid membrane surface. Wettability defines the spreading behavior of any liquid over a surface, while the terms hydrophilicity and hydrophobicity refer to the affinity and repellency of surface towards the water, respectively. In most of the membrane literature studies (refer to **Table A1.1**) the terms “hydrophilicity” and “hydrophobicity” are defined only based on the three-phase contact angle ( $\theta$ ), determined by observing the spreading of a water droplet over the membrane surface, i.e.,  $\theta < 90^\circ$  (partial and complete wetting) for a hydrophilic case and  $\theta > 90^\circ$  (partial and complete non-wetting). However, this simple interpretation of contact angle data in terms of hydrophilicity/phobicity is not complete as the contact angle is the combined effect of liquid affinity towards the surface, as well as the surface physicochemical heterogeneity [47,80]. Wettability measurement through contact angle includes two significant steps, as discussed in the previous study [42,81,82], (i) measurement of apparent contact angle, and (ii) measurement of surface roughness. Two more essential parameters control the wettability of a surface: the rate and extent of wetting [40]. The rate of wetting specifies how fast a liquid can spread over the surface, which depends on several factors, e.g., capillary force, liquid viscosity, thermal/chemical condition of the system. The extent of wetting is described by the so-called contact angle formed at the three-phase meeting line and the plane of a solid surface where liquid resides or moves [83].

In many cases, the single magnitude of the static contact angle fails to provide the required information about solid-liquid interaction [42]. The Young's equilibrium contact angle corresponds to the lowest state of the energy for the system. However, due to heterogeneity, there exist several metastable energy levels, e.g., the highest metastable energy level corresponds to an advancing contact angle, and the lowest one corresponds to a receding contact angle. Nevertheless, most of the reported contact angles in the literature are the static contact angles [81], i.e., determined from the stationary three-phase contact line. The static contact angle corresponds to any metastable energy level in between the advancing and receding ones, and thus it is not necessarily reproducible. Hence, the static contact angle becomes meaningless and unreliable if the advancing and receding contact angles are not mentioned [83]. A systematic approach to determine the most stable contact angle is to apply external energy (e.g., vibrations) to overcome the intermediate metastable state [84]. However, this technique is currently unavailable in commercially available devices [42]. A common method to obtain reproducible results is to determine the advancing and receding contact angles measured respectively by increasing and decreasing the drop volume over the sample surfaces. The most stable contact angle can be approximated by a proper average between the advancing and receding contact angles [84]. The difference between advancing and receding contact angles is contact angle hysteresis ( $\Delta\theta$ ) [39], which also gives useful insights not only about the surface chemical and/or physical inhomogeneities but also membrane performance parameters. The usefulness of contact angle hysteresis to determine the membrane performance parameters will be discussed in the next section.

### **2.1.2 Characterization of surface tension and hydrophilicity**

Surface tension is an important parameter to elucidate the interfacial interaction of a solid surface with another material, e.g., hydrophilicity, oleophobicity. It can be considered the intrinsic property of a material at a given condition. Generally, for solids this term can be expressed as surface free energy,

and for liquids this term is widely used as interfacial tension. In this review paper, in general, we consider all these parameters as surface tension.

Surface hydrophilicity can be quantified by two parameters: solid surface free energy of cohesion and solid-water free energy of adhesion. Dupré et al. [85] introduced the concept of free energy of cohesion ( $\Delta G_{ii}^{coh}$ ) and adhesion ( $\Delta G_{ij}^{ad}$ ) in terms of the surface tension ( $\gamma_i$ ) of any condensed-phase material (e.g., solid or liquid). They stated that the free energy of cohesion and adhesion can be expressed as follows:  $\Delta G_{ii}^{coh} = -2\gamma_{ii}$ ,  $\Delta G_{ij}^{ad} = \gamma_{ij} - \gamma_i - \gamma_j$ , where  $i$  and  $j$  refer to the phase of two dissimilar materials (e.g., solid/liquid). By combining the Young and Dupré equations we can obtain the Young-Dupré equation of adhesion:  $\Delta G_{ij}^{ad} = -\gamma_L(1 + \cos \theta)$ .

In the case of liquid materials, a pendant drop approach is a widely applied method to determine the surface tension (details of the liquid surface tension measurement technique can be found elsewhere [40,86]). However, in the case of solid materials, the surface tension cannot be determined directly. Instead, it is determined by the types of molecular interaction of different liquids with the solid surface. Fowkes proposed [87–89] the surface tension of any condensed phase material (solid/liquid) is the sum of components resulting from various intermolecular interaction, e.g.,  $\gamma_i = \sum \gamma_i^j$ , where  $j$  represents specific molecular interactions such as dispersion, polar/acid-base, and hydrogen bonding. Owens and Wendt [90] specified this interaction in terms of dispersion and hydrogen-bonding components. Rabel [91] and Kaelbe [92] also stated a similar expression for the surface tension calculation, i.e., dispersion ( $\gamma_i^D$ ) and polar components ( $\gamma_i^P$ ). They also stated that the surface tension between two condensed phase materials, e.g., a solid ( $\gamma_S$ ) and a liquid ( $\gamma_L$ ), can be expressed as:  $\gamma_{SL} = \gamma_S + \gamma_L - 2\sqrt{\gamma_S^D \gamma_L^D} - 2\sqrt{\gamma_S^P \gamma_L^P}$ . This expression is known as the OWRK method of determining the surface tension of any condensed phase material. By combining this method with Young and Dupré et al. expression we can obtain,  $\gamma_L(1 + \cos \theta) = 2\sqrt{\gamma_S^D \gamma_L^D} + 2\sqrt{\gamma_S^P \gamma_L^P}$ .

van Oss et al. [93–99] extended the surface tension concept and introduced long-range Lifshitz-van der Waals ( $\gamma_i^{LW}$ ) and short-range acid-base interaction ( $\gamma_i^{AB}$ ) components, i.e.,  $\gamma_i = \gamma_i^{LW} + \gamma_i^{AB}$  and  $\Delta G_{ij}^{ad} = \Delta G_{ij}^{LW} + \Delta G_{ij}^{AB}$ . They stated that the Lifshitz-van der Waals component includes the sum of the dispersion, dipole-dipole, and induced dipole-dipole interactions. On the contrary, the acid-base component includes the interaction of electron acceptor (Lewis acid) and electron donor (Lewis base) components. van Oss et al. demonstrated that the acid-base interaction of any condensed phase material is:  $\gamma_i^{AB} = 2\sqrt{\gamma_i^+ \gamma_i^-}$ . This can be extended for two different condensed phase material as:  $\gamma_{ij}^{AB} = 2(\sqrt{\gamma_i^+ \gamma_i^-} + \sqrt{\gamma_j^+ \gamma_j^-} - \sqrt{\gamma_i^+ \gamma_j^-} - \sqrt{\gamma_i^- \gamma_j^+})$ . Thus, the final expression for the interfacial interaction of two different condensed phase materials, e.g., a solid ( $\gamma_S$ ) and a liquid ( $\gamma_L$ ) becomes:  $\gamma_{SL} = \gamma_S + \gamma_L - 2\sqrt{\gamma_S^{LW} \gamma_L^{LW}} - 2\sqrt{\gamma_S^+ \gamma_L^-} - 2\sqrt{\gamma_S^- \gamma_L^+}$ .

By combining this method with the Young- Dupré equation the following expression can be established:

$$-\Delta G_{SL}^{ad} = \gamma_L(1 + \cos \theta) = 2 \left( \sqrt{\gamma_L^{LW} \gamma_S^{LW}} + \sqrt{\gamma_L^+ \gamma_S^-} + \sqrt{\gamma_L^- \gamma_S^+} \right). \quad (2.1)$$

From the above expression, it is obvious that at least three probe liquids are needed to obtain the three unknown surface tension components of a solid. van Oss et al. recommended that of these three probe liquids, two must be polar, and the surface tension of the three liquids should be greater than the solid to avoid the complete wetting scenario [100]. However, for all of these approaches, the results largely depend on the choice of the probe liquids [101,102]. To obtain reliable and consistent results, Holländer [103] introduced the importance of the ratio of the acid-base surface tension components ( $Q_\gamma = \frac{\gamma^-}{\gamma^+}$ ) and suggested that the difference of this ratio for the two polar liquids should be as large as possible, e.g.,  $\Delta Q_\gamma > \sim 15$ . Such a combination can be selected as follows: water and formamide and the other non-

polar probe liquid can be diiodomethane. To avoid a complete wetting scenario, liquids having a higher surface tension are recommended. van Oss et al. [93–97,99,100,104,105] also extended the Dupré equation for two dissimilar condensed-phase material, 1 and 2 interact while immersed in a liquid, 3, which can be expressed as follows:  $\Delta G_{132} = \gamma_{12} - \gamma_{13} - \gamma_{23}$ . Finally, this equation can be written in the following terms of polar and apolar interaction of various surface tension components:

$$\Delta G_{132} = 2 \left( \sqrt{\gamma_3^{LW}} - \sqrt{\gamma_1^{LW}} \right) \left( \sqrt{\gamma_2^{LW}} - \sqrt{\gamma_3^{LW}} \right) + 2\sqrt{\gamma_3^+} (\sqrt{\gamma_1^-} + \sqrt{\gamma_2^-} - \sqrt{\gamma_3^-}) + 2\sqrt{\gamma_3^-} (\sqrt{\gamma_1^+} + \sqrt{\gamma_2^+} - \sqrt{\gamma_3^+}) - 2\sqrt{\gamma_1^+ \gamma_2^-} - 2\sqrt{\gamma_1^- \gamma_2^+}. \quad (2.2)$$

From this expression, van Oss et al. defined the term hydrophobicity and hydrophilicity. If  $\Delta G_{132} < 0$ , then the interaction between material ‘1’ and ‘3’ considered to be hydrophobic attraction (cohesive interaction) and if  $\Delta G_{132} > 0$ , then this interaction will be hydrophilic repulsion (non-cohesive interaction). However, if the surfaces ‘1’ and ‘2’ are the same material (1=2) then the free energy of the interactions can be called the free energy of cohesion ( $\Delta G_{131}$ ) which can be expressed as follows:

$$\Delta G_{131} = -2 \left( \sqrt{\gamma_1^{LW}} - \sqrt{\gamma_3^{LW}} \right)^2 - 4 \left( \sqrt{\gamma_1^+ \gamma_1^-} + \sqrt{\gamma_3^+ \gamma_3^-} - \sqrt{\gamma_1^+ \gamma_3^-} - \sqrt{\gamma_1^- \gamma_3^+} \right) \quad (2.3)$$

van Oss et al. [93–97,99,100,104,105] further extended the definition of hydrophilicity by proposing two more conditions considering  $\Delta G_{131} = 0$ : (1) the electron donor surface tension parameter ( $\gamma_S^-$ ) should be higher than  $28.3 \text{ mJ/m}^2$ ; and (2) the free energy of hydration for solid-water interface ( $\Delta G_{SL}^{ad}$ ) should be lower than  $-113 \text{ mJ/m}^2$ . For most biological and many other organic materials the apolar Lifshitz-van der Waals surface tension ( $\gamma_S^{LW}$ ) is  $\sim 40 \text{ mJ/m}^2$ , and the electron acceptor surface tension parameter ( $\gamma_S^+$ ) is  $\sim 0 \text{ mJ/m}^2$ . Further, from the free energy

of cohesion equation, in the case of water ( $\gamma_L^{LW} = 21.8 \text{ mJ/m}^2$  and  $\gamma_L^+ = \gamma_L^- = 25.5 \text{ mJ/m}^2$ ) the electron donor surface tension parameter is calculated to be  $\gamma_S^- = 28.3 \text{ mJ/m}^2$ . Having all of these known parameters, we can further extend the hydrophilicity in terms of surface free energy of adhesion,  $\Delta G_{SL}^{ad} \approx -113 \text{ mJ/m}^2$ . From the free energy of adhesion equation, we can determine the equilibrium contact angle criteria for the hydrophilicity. If the free energy of adhesion is  $113 \text{ mJ/m}^2$ , then the equilibrium contact angle criteria for surface hydrophilicity is given by,  $\theta < \sim 55^\circ$ .

This theoretical analysis is consistent with the equilibrium contact angle criteria for the hydrophilicity reported by Vogler [106]. Vogler showed that solid-water long-range attractive interaction (hydrophobic) can only be detected if the water adhesion tension ( $\tau = \gamma_L \cos \theta_{IWT}$ ) is less than 30 mN/m, from which the contact angle of the intrinsic wetting threshold (IWT) can be determined (**Figure 2.1a**). More specifically there exist a range where the long-range intermolecular interaction is minimum which is known as ‘Berg limit’ [107,108]. For water having the interfacial tension of  $\gamma_L = 72 \text{ mN/m}$ , this range varies from  $\sim 56^\circ$  to  $\sim 74^\circ$ . Vogler [106] approximated this wetting threshold as follows:  $\theta_{IWT} \approx 65^\circ$ . This wetting threshold is very important while designing wettable and non-wettable surfaces using any kind of surface modification [108,109]. It is anticipated that any kind of surface physical modification (roughness, pattern) of the polymeric surfaces enhances the hydrophobicity if the contact angle over the base smooth surface is greater than  $65^\circ$  (not the commonly used contact angle value of  $90^\circ$ ) [108,109]. The threshold limit should be strictly followed while fabricating robust super-wettable or super liquid-repellent surfaces for harsh environment applications [108–110]. The magnitude of the wetting threshold varies with the magnitude of the interfacial tension of the contacting liquid, **Figure 2.1b** indicates that this limit is increased with the increment of liquid interfacial tension.

In addition to the equilibrium contact angle, there are also some other definitions of hydrophilicity available in the literature in terms of advancing or receding contact angle (**Table 2.1**). Law et al. [111,112] defined the hydrophilicity

in terms of receding contact angle. They reported that the surfaces that exhibit a receding contact angle of less than  $90^\circ$  require a high pull-off force to detach the water droplet from the surface. They considered this as another alternative approach to determine solid-liquid adhesion to determine the surface hydrophilicity. **Table 2.1** provides a brief overview of the criteria to determine the surface hydrophilicity available in the literature. However, from the membrane literature (**Table A1.1**), it is observed that a very few researchers reported the interfacial free energy of interactions ( $\Delta G_{SL}^{ad}$  or  $\Delta G_{131}$ ), as well as the advancing/receding contact angle to determine the hydrophilicity of a membrane surface. Though most of the literature utilized the wetting to non-wetting transition ( $\theta_e = 90^\circ$ ) as a measure of hydrophilicity, but the above discussion makes this assumption inappropriate.

### 2.1.3 Characterization of surface oleophobicity

In addition to the hydrophilicity, it is important in some membrane research works to measure the underwater oleophobicity or oil repellency, such as for the oil-water separation processes [113–115]. The underwater superoleophobic surfaces can be observed in nature on the skin of marine animals [116], e.g., fish skin, which is superoleophobic underwater though superoleophilic in air. A double-layered skin structure facilitates the superoleophobic behavior underwater, which serves the same purpose that air bubbles do in superhydrophobic surfaces. From Young's equation, it can be demonstrated that when the liquid surface tension decreases ( $\gamma_l$ ), the spreading tendency of any liquid over a surface also increases as contact angle decreases. Hence, any solid that wets water ( $72.8 \text{ mN/m}$ ) also wets most of oils ( $\gamma_l < 35 \text{ mN/m}$ ). For this reason, it is challenging to generate in-air hydrophilic but oleophobic membranes. Moreover, most of the oleophobic surfaces show underwater oleophobicity. As most of the oils are non-polar liquids, in underwater conditions, it is necessary to enhance the surface polarity to facilitate the hydrogen bonding for making the surface hydrophilic but superoleophobic (highly oil repellent). To achieve such different types of oleophobicity at different conditions, significant

efforts have been made to tune the wettability of the surface by introducing different surface modification approaches. Surface coating and surface grafting can be such types of modification approach [11]. It is to mention that the wetting threshold limit should be followed while selecting the base membrane to obtain the maximum impact of these types of modifications. Similar to hydrophilicity, different theories have been proposed based on Young's and Fowke's equation to determine the criteria for oleophobicity. We can also extend the hydrophilicity/phobicity concept of van Oss et al. [93–97,99,100,104,105] to determine the criteria for oleophobicity (**Table 2.2**). Some other criteria for oleophobicity are also available in the literature. Jung et al. [117] proposed the following modification of Young's equation for underwater oleophobicity:

$$\cos \theta_{ow} = \frac{\gamma_o \cos \theta_{oA} - \gamma_w \cos \theta_{wA}}{\gamma_{ow}}, \quad (2.4)$$

where, the subscripts 'o', 'A' and 'w' denote oil, air, and water, and 'ow', 'oA' and 'wA' refer to the oil-water, oil-air, and water-air interface, respectively. Schultz et al. [118] proposed a different theory for under liquid wettability combining the Young's and OWRK methods. The following equation can be helpful to measure the surface oleophobicity underwater [118]:

$$\gamma_o - \gamma_w + \gamma_{ow} \cos \theta_{swO} = 2\sqrt{\gamma_S^D} \left( \sqrt{\gamma_o^D} - \sqrt{\gamma_w^D} \right) + 2\sqrt{\gamma_S^P \gamma_o^P} - 2\sqrt{\gamma_S^P \gamma_w^P}, \quad (2.5)$$

where, the subscript 'S' refers to solid and 'SWO' is the oil contact angle over the solid surface underwater. Similarly, as the hydrophilicity, in addition to the equilibrium contact angle, Law et al. [111,112] defined the oleophobicity in terms of receding contact angle. It is worth noting that various criteria have been developed based on different applications, in air or under-water. The membrane researcher should follow these criteria while fabricating the oleophobic membrane. All of the



criteria for oleophobicity proposed by different researchers are highlighted in Table 2 (the data showed for the case of Hexadecane).

#### 2.1.4 Characterization of surface physical heterogeneity

Surface morphology and topography of membranes largely depends on the type of materials utilized during the fabrication process and synthesis conditions [68,119]. For example, TFC membranes have a roughness ranging from 50 nm to 100 nm. This range is significant enough to alter the wettability and interfacial property [15]. This, in turn, increases the membrane foulant interactions and increases fouling propensity by altering the membrane adhesion properties [14,120,121]. On the other hand, roughness increases the surface area, which provides greater opportunity to interact with water molecules and ultimately increases the permeability [122,123]. Thus, a proper combination of physical and chemical modification can ensure the maximum separation performance. In the performance characterization section, a detail explanation of this phenomenon will be provided. This section will focus on characterizing membrane physical heterogeneity by contact angle measurements. In this regard, the effect of physical heterogeneity over the contact angle is essential to explain.

Based on the wetting ( $\theta_e < 90^\circ$ ), and non-wetting cases ( $\theta_e \geq 90^\circ$ ), two important theories can be employed to understand the effects of surface physical heterogeneity. For the wetting cases when the surface is favorable the contacting liquid to spread over the surface, the well-known Wenzel equation [48] is given by

$$\cos \theta_w = r \cos \theta_Y, \quad (2.6)$$

where  $r$  is the ratio of actual surface area to geometric surface area (also refer to the previous section for detail),  $\theta_w$  is the apparent contact angle (can also be denoted as  $\theta_{ap}$ ),  $\theta_Y$  is the Young's contact angle (can also be denoted as  $\theta_e$ ). From this equation, we indicate that for partially wetting cases ( $\theta_e < 90^\circ$ ), introducing

roughness ( $r>1$ ) will enhance the wettability. This enhancement will be more impactful less than the wetting threshold ( $\theta_{IWT}$ ) limit (also refer to the previous section).

However, in the case of non-wetting scenario ( $\theta_Y \geq 90^\circ$ ), roughness increases the resistance to the spread of liquid (e.g., water) molecules over the surface. In this case, the droplet sits on top of the asperities, and air is trapped underneath. This phenomenon is also known as chemical heterogeneity, which depends on the interfacial interaction of two different contacting fluids (liquid and trapped air). However, in this review article, we indicated chemical heterogeneity as non-uniform charge distribution over the membrane surface. For non-wetting case, introducing roughness is known as the Cassie–Baxter state, with Young’s equation which can be written in terms of solid-liquid surface area fraction ( $\phi_s$ ) as follows (Cassie-Baxter equation) [49,50]:

$$\cos \theta_{CB} = -1 + \phi_s (1 + \cos \theta_Y) \quad (2.7)$$

where,  $\theta_{CB}$  is the apparent contact angle proposed by Cassie-Baxter.

However, in reality, often, Wenzel and Cassie-Baxter mixed states are observed due to partial penetration of the liquid inside the air pockets formed due to the roughness (**Figure 2.2a**). Conversely, there is another state in the Wenzel region (**Figure 2.2a**) known as the impregnation state. This state can be useful for the impregnated membrane cases, which is beyond the scope of the present study. Curious authors may find more detail elsewhere [124–126]. The following equations are introduced for the mixed Wenzel-Cassie-Baxter and impregnation wetting states, respectively [127].

$$\cos \theta_{MCB} = -1 + \phi_s (1 + r \cos \theta_Y) \quad (2.8)$$

$$\cos \theta_{IMP} = 1 - \phi_s (1 - \cos \theta_Y) \quad (2.9)$$

In addition to the Wenzel and Cassie-Baxter states, another theory is available specifically applicable to the fractal surfaces proposed by Tsujii et al. (**Figure 2.2b**) [66,67]. In the previous section, we mention that the membrane surface exhibits fractal behaviors, and thus, this equation needs special attention for designing membrane surfaces. Wenzel roughness factor obtained from any general rough surfaces is lower than the fractal surfaces. Ismail et al. [15] from their proposed contact angle method also reported that the Wenzel roughness factor obtained from the conventional AFM analysis (as mentioned in the previous section) is lower than the TFC membrane surfaces, which show fractal behavior. Tsujii et al. [66,67] reported that this parameter is rather the function of fractal dimension,  $r_{fractal} = \left(\frac{L}{l}\right)^{D_f - 2}$ , where ‘L’ is the upper (maximum), and ‘l’ is the lower (minimum) length scale of the heterogeneity observed on the fractal surface, and  $D_f$  is the fractal dimension ( $2 < D_f < 3$ ). Moreover, the applicability of the Tsujii et al.’s model [66,67] to membrane surfaces still awaits clarification for membrane surfaces. **Figure 2.3a** provide the evidence that TFC membrane surfaces (NF 90 as an example) exhibit different types of heterogeneity at different magnification level of FESEM images. AFM analysis at different scan size can also shows the evidence of fractal characteristics (**Figure 2.3b**) as the roughness factor varies significantly with the scan size.

Ismail et al. [15] and Han et al. [20] proposed different approaches to determine the roughness factor using contact angle analysis. However, the approach proposed by Ismail et al. [15] is specifically developed for a generalized approach to determine the roughness factor of the fractal surfaces. They combined Young equation [46], Wenzel equation [47,48], and Fowkes Equation [88] for the non-polar probe liquids as follows:

$$\sqrt{\gamma_L} \cos \theta_W = -r\sqrt{\gamma_L} + 2r\sqrt{\gamma_S^D} \quad (2.10)$$

$$\sqrt{\gamma_L} \cos \theta_{Ad} = -\sqrt{\gamma_L} \left[ r + \frac{F}{\gamma_L} \right] + 2r \sqrt{\gamma_S^D} \quad (2.11)$$

where  $\theta_W$  is the apparent contact angle based on the Wenzel model,  $r$  is called surface roughness factor,  $\frac{F}{\gamma_L}$  indicates the resistive frictional force due to the surface physical heterogeneity, the superscripts  $D$  denotes the dispersive intermolecular interaction.  $\sqrt{\gamma_L} \cos \theta$  vs.  $\sqrt{\gamma_L}$  plot can be obtained for a wide range of non-polar probe liquids. The slope and interception will provide the information on the roughness factor. **Figure 2.3c** shows the comparison between the roughness factor obtained from the conventional AFM analysis and contact angle analysis. The obtained roughness from the contact angle analysis was compatible with the fractal roughness factor proposed by Tsujii et al. [66,67].

### 2.1.5 Characterization of surface charge and zeta potential

Membrane surfaces contain surface charge (mostly negative) and functional groups to obtain better hydrophilicity (hydrogen bonding) and anti-fouling property. Polyamide membranes have both weak acidic carboxyl groups ( $-\text{COOH}$ ) and basic amine groups ( $-\text{NH}_2$ ) that allow the membrane surface to acquire either a positive or negative charge based on pH and concentration of the contact solution [128–130]. This, in turn, controls the selectivity of the membrane and also in some cases, the fouling phenomena. Before presenting the surface potential characterization method using contact angle analysis, we first discuss the conventional zeta potential measurement technique and origin of surface charge.

When an aqueous solution comes in contact with a membrane surface, a charged layer is formed, which is known as the electric double layer (EDL). This causes higher counterion concentration near the membrane surface than that in the bulk solution. From this, two different regions can be identified near the membrane surface: the immobile stern layer where ions bind at the solid-liquid interface, and the diffuse layer where ions can move freely. The electrical potential at the stern

layer is difficult to measure directly, but at the diffuse layer, it is called the zeta ( $\zeta$ ) potential and can be measured experimentally. The thickness of EDL depends on the ionic concentration and electrical properties of the liquid, which may vary from a few nanometers for high ionic concentration to several micrometers for distilled water and pure organic liquids [131–133]. The boundary between the stern layer and diffuse layer is known as the shear plane where zeta potential is measured. The total thickness of the stern layer and the shear layer of EDL is known as Debye length ( $\kappa^{-1}$ ), which is a characteristic parameter of the electrolyte solution which can be obtained as following [132,133]:

$$\kappa^{-1} = \sqrt{\frac{\varepsilon\varepsilon_0RT}{2Mz^2e^2}} \quad (2.12)$$

where  $M$  is the molar concentration of the solution,  $z$  is the valence of the ions,  $\varepsilon\varepsilon_0$  is the dielectric coefficients of the solution,  $e$  is the charge of the electron,  $R$  is the molar gas constant,  $T$  is temperature. Zeta potential is a property of the solid-liquid pair and can be measured generally in four ways by the relative motion of an electrolyte solution and a charged solid, (1) electrophoresis, (2) electro-osmosis, (3) sedimentation potential, or (4) streaming potential [133]. Electroosmosis and streaming potential methods are utilized to determine the zeta potential on a flat surface. However, due to the lack of sensitivity for the surfaces having low potential, streaming potential techniques is more convenient than the electroosmosis [130,134,135]. Streaming potential measurements can be further classified into transverse (especially for porous samples) and tangential streaming potential methods (**Figure 2(d)**) [136]. Transversal streaming potential (also known as filtration streaming potential) is measured by flowing the solution through the pores of the membrane during the filtration process. In this case, the membrane is mounted between a pair of electrodes. This method is advantageous as it provides more realistic results when zeta potential measurement is conducted during the filtration process. However, it is difficult to measure the streaming potential for multilayer

membranes due to different electrostatic properties at different layers. The tangential streaming potential is an alternate option to measure the zeta potential at the separating layer. For this measurement, a flow of solution passes along the active surface of the membrane under applied hydrostatic pressure, usually through a fabricated capillary or a slit microchannel. Elimelech and coworkers [137] performed initial experiments on the feasibility of using a streaming potential analyzer to determine the zeta potential of RO and NF membranes. The advantages of this method include (i) adjustable channel height to avoid EDL overlap due to the charge distribution inside the pore and the active layer, (ii) insignificant concentration polarization phenomena as no filtration takes place, (iii) applicability for a wide range of pore sizes from MF to RO membranes, (iv) determination of the streaming potential of the active layer, and (v) simplistic interpretation of the results as the contribution of the support layer is excluded [138–140]. The functional groups on a membrane surface can be dissociated upon contact with an aqueous solution and can form charged functional groups, i.e., amino, carboxyl, and sulfonates [131–133]. Depending on the pH of the solution, the surface can acquire a positive or negative charge. For example, PA TFC membranes contain carboxylic ( $\text{R-COO}^-$ ) and amine ( $\text{R-NH}_3^+$ ) ionizable functional groups which are responsible for development of surface charge [129,130,141,142]. The equilibrium dissociation reactions of these groups are as follows [130]:



According to these reactions, the surface charge is dependent on the degree of ionization, and obviously, the pH of the solution [130]. At high pH values,  $\text{H}^+$  in reaction (1) reacts with  $\text{OH}^-$  and reaction progress to the right. Higher  $\text{R-COO}^-$  on the surface makes the membrane negatively charged. In contrast, at low pH values, reaction (2) moves backward, and the resulting membrane becomes positively charged. The charge on the membrane surface causes electrostatic attraction or

repulsion with the charge of the constituents present in the contact solution. Thus, this may affect the separation process and control the concentration polarization and fouling phenomena. One can have the information on surface charge density by measuring its zeta potential. Zeta potential depends on different parameters, e.g., the solution viscosity, ion diffusivities, ionic strength of the solution, and the surface charge density [131–133]. In general, zeta potential ( $\zeta$ ) can be calculated by the following Helmholtz-Smoluchowski equation [132,133]:

$$\zeta = \frac{\Delta E}{\Delta P} \frac{\eta}{\varepsilon \varepsilon_0} \frac{L}{A} \frac{1}{\Omega} \quad (2.15)$$

where,  $\frac{\Delta E}{\Delta P}$  is the ratio of electrical potential to pressure drop,  $\eta$  is the solution viscosity,  $\varepsilon \varepsilon_0$  is the dielectric coefficients of the solution,  $L$  and  $A$  are the cross-section of the channel, and  $\Omega$  is the electrical resistance of the channel. Helmholtz-Smoluchowski further approximated the equation by assuming electrical conductivity as follows:  $\lambda = \frac{L}{A} \frac{1}{R}$ . Thus, the final equation can be expressed as [132,133]-

$$\zeta = \frac{\Delta E}{\Delta P} \frac{\eta}{\varepsilon \varepsilon_0} \lambda \quad (2.16)$$

It is worth noting that though, in literature, electrical conductivity is demoted by  $\sigma$ , in this review article, this symbol signifies surface charge density.

Membrane surfaces contain acidic or basic functional groups, which undergo acid-base reactions in aqueous media. For any dissociation reaction, the mass action reaction can be written as follows:  $SH \rightleftharpoons S^- + H^+$  [132]. The maximum possible proton concentration at the surface can be written as  $[H^+]_0$ . The concentration of negative sites,  $[S^-]_0$ , is related to the maximum possible surface charge density ( $\sigma_0$ ),  $\sigma_0 = -e[S^-]_0$ . Here,  $e$  is the magnitude of the fundamental charge of an electron ( $1.602 \times 10^{-19}$  C). The maximum possible surface charge density is required to

calculate the surface charge at any specific pH, i.e.,  $\sigma = \sigma_0\alpha$ , where,  $\alpha$  is the degree of ionization of the acidic groups:

$$\alpha = \frac{[S^-]}{[S^-] + [SH]} \quad (2.17)$$

By measuring the surface potential ( $\psi_s$ ) at the stern plane, it is possible to calculate the surface charge ( $\sigma$ ) from the Grahame equation [132]. For a 1:1 electrolyte solution (e.g., NaCl and HCl) we can write:

$$\sigma = \sqrt{8RT\epsilon\epsilon_0([NaCl] + [HCl])} \sinh\left(\frac{-e\psi_s}{2RT}\right), \quad (2.18)$$

where  $R$  is the molar gas constant,  $T$  is the absolute temperature, and  $[NaCl]$  and  $[HCl]$  refer to the concentration of salt and acid, respectively.

Now, we will present the characterization of surface potential using the contact angle method. **Figure 2.4a** depicts that based on the pH of the electrolyte drop, surface wettability alters. There are clearly two distinct plots for the carboxylic- and amine-rich surfaces [33,143]. Hurwitz et al. [21] utilized this concept determined the surface potential at the stern plane and compared their results with the zeta potential obtained at the shear plane using the conventional streaming potential method (**Figure 2.4b**). They observed comparable results between these two methods, especially in the negative surface potential zones. They further extended their analysis for different molar concentrations and reported that solid surface tension components also alter due to the variation of surface pH (**Figure 2.4c**). The surface potential measurement from the wettability analysis is developed based on the non-covalent interactions between the solid surface and the probe liquids [21,32–35]. van Oss [93–99] simplified the non-covalent interactions as follows: (i) Lifshitz-van der Waals (LW) electrodynamic interactions due to van der Waals forces; (ii) polar or Lewis acid-base interactions due to attractive (‘hydrophobic interaction’) and repulsive (‘hydration pressure’) forces; (iii) electrostatic interactions; and (iv)



interactions due to Brownian movement forces. If a solid surface exhibits Lewis acid-base interaction with the liquid, the solid-liquid interfacial tension ( $\gamma_{SL}$ ) changes as a function of pH. Holmes-Farley et al. [33,143] developed the contact angle titration technique based on three assumptions: (i) the surface free energy of the solid-liquid interface ( $\gamma_{SL}$ ) consists of the total contributions of all functional groups present at the solid surface; (ii) there is no reconstruction of the surface, e.g., variation of surface properties is observed only due to pH variations; and (iii) change in the wettability of the surface due to change in pH are mainly due to the variation of the solid-liquid interfacial tension ( $\gamma_{SL}$ ). Applying these assumptions along with Young's equation, the degree of ionization ( $\alpha$ ) is obtained which is an important part of the surface potential calculation from contact angle measurement. Surface extent of ionization is given by **(Figure 2.4a)** [33,143]

$$\alpha = \frac{\gamma_{LS}(pH1) - \gamma_{LS}(pH)}{\gamma_{LS}(pH1) - \gamma_{LS}(pH13)} = \frac{\cos \theta_{pH} - \cos \theta_{pH1}}{\cos \theta_{pH13} - \cos \theta_{pH1}} \quad (2.19)$$

where all the contact angle data can be obtained from the contact angle titration curve **(Figure 2.4a)**.

The next step to determine surface potential is to calculate the maximum charge density ( $\sigma_0 = -e[S^-]_0$ ). We can further determine the concentration of reactive groups  $[S^-]_0$  as follows:

$$[S^-]_0 = \frac{10^{-(14-pH_{bp})} (V)(N)}{rA_s} \quad (2.20)$$

Here,  $pH_{bp}$  is the pH where the titration curve breaks from horizontal, N is the Avogadro's number,  $r$  is Wenzel roughness factor,  $A_s = \left[ \pi^{1/3} V^{2/3} \sin^2 \theta \right] \left[ \frac{2}{3} - \cos \theta + \frac{\cos^3 \theta}{3} \right]^{-2/3}$  is the actual area under the drop, and V is drop volume.

## **2.2 Analyzing membrane performance parameters using contact angle**

In the previous sections, we present a detailed description of the characterization of membrane influential surface parameters using contact angle analysis. This section will focus on the characterization of membrane performance parameters using contact angle analysis and their connection towards the solid-liquid interfacial properties. Researchers have employed both chemical modification (e.g., grafting) and physical modification (e.g., coating) to improve the separation performance [11,14,113,115]. More importantly, to ensure increased selectivity at a constant permeability and anti-fouling property, interfacial material with special wettability can be an excellent option [13,144]. Synthesis of oil-removing materials is an example of successfully introducing special wettability into the field of oily wastewater treatment [113]. However, many of these membranes are readily fouled, or even blocked up, by oils because of their intrinsic oleophilicity or even hydrophobicity. The synthesis of membrane materials having both superhydrophilic and superoleophobic properties is very challenging since a material whose surface energy is simultaneously greater than that of the water and smaller than that of oil is hardly found. Hence, these types of materials are fabricated through surface engineering for the desired application with the incorporation of new functionalities to the polymer surface. For example, superhydrophilicity and underwater superoleophobicity arise from the synergistic effect of hierarchical micro-/nano-scale surface features and the hydrophilic chemistry of the grafted materials. The grafted hydrophilic groups increase the hydrogen bonding capability of the membrane surface, which ensures the creation of the hydration layer at the membrane-water interface and incorporates fouling resistivity. Membrane researchers have extensively quantified and connected the wettability parameters with the membrane performance parameters. We will provide a few of those which can be the starting point of the novel material development for membrane processes.

## 2.2.1 Analyzing fouling propensity of membrane materials

Inspired by naturally occurring surfaces, researchers have developed surface engineered materials with special wettability, which can provide an effective solution to challenging environmental problems. In many cases, surface engineered membrane surfaces exhibit undesirable physical and chemical heterogeneity since it is difficult to control all the synthesis parameters. However, these types of surface heterogeneities also alter the membrane performance, which can be determined by contact angle analysis and related interfacial parameters. Ismail et al. and Sangyoun et al. [22,71] reported that colloidal and organic fouling is directly related to the contact angle hysteresis (**Figure 2.5**). Not only the surface physical heterogeneity, but even non-uniform distribution of surface charge can also initiate fouling.

In addition to colloidal and organic fouling, biofouling is also another type of undesired phenomenon which often occurs. Membrane biofouling can be defined as the accumulation of microorganisms over the membrane surface. These types of fouling are more complex in nature since microorganisms can grow, multiply, and relocate over the membrane surface [5]. Biofouling can also be directly related to membrane surface properties, more specifically contact angle and surface zeta potential. Firouzjaei et al. [145] synthesized different types of thin-film nanocomposite membranes (TFN) utilizing metal-organic frameworks (**Figure 2.6**). The lowest contact angle and lowest zeta potential of the surface ensure maximum performance (**Figure 2.6 a,b**).

The formation of biofilm over the membrane surface is a complex process. The microorganisms stay over the surface, forming extracellular polymeric substances (EPS). **Figure 2.7a** depicts the complex procedure of biofilm formation [146]. This formation is mainly governed by the adhesion process between the EPS and membrane surface with hydrophobic and hydrogen bonding interactions. **Figure 2.7a** also provides the interrelation between the membrane surface tension and degree of biofouling, which is known as the 'Baier curve' [147]. From this plot, we observe that there remain two different states where the 'fouling release'

phenomenon exists, solid surface tension in between 20 mN/m and 30 mN/m, and greater than 60 mN/m. Most of the hydrophilic membrane surfaces have a surface tension of 40 mN/m or greater. Thus, to obtain the ‘fouling release’ surfaces, it is required to increase the membrane surface tension so that they can reach the 60 mN/m criteria. **Figure 2.7b** shows another example of the characterization of membrane performance parameters (humic acid and oil fouling) with the interfacial properties [148]. As mentioned in the previous section, the hydrophilic surfaces surface free energy should be close to zero. We can observe this phenomenon from the humic acid fouling, 9-FAS coated PVDF membrane provides better performance (**Figure 2.7c**). Interestingly, oil fouling plots provide different information. Though both of the membranes are hydrophobic underwater, the 17-FAS membrane exhibits a higher oil contact angle, which indicates the oleophobicity of the material. This, in turn, reduces the oil fouling, as shown in the figure (**Figure 2.7c**).

### 2.2.2 Analyzing scaling propensity of membrane materials

Scaling is another type of membrane fouling which is observed due to inorganic depositions of the dissolved salt in the feed solution. The salt deposition includes Calcium carbonate ( $\text{CaCO}_3$ ), barium sulfate ( $\text{BaSO}_4$ ), silica ( $\text{SiO}_2$ ), and calcium sulfate ( $\text{CaSO}_4$ ) [5]. This type of fouling strongly depends on the solubility and the concentration in the feed solution. Generally, any dissolved material may start to deposit over the surface by two types of nucleation (or crystallization in general) process: homogeneous and heterogeneous (**Figure 2.8a**). Nucleation is generally the process of phase change of a material, e.g., crystal generation from a solution. Homogeneous nucleation happens from the bulk of the solution surface, but heterogeneous nucleation occurs at any interface of another surface or due to surface heterogeneity. Heterogeneous nucleation starts with forming a nucleus of a critical radius,  $r_c = f(\gamma_{ls}, \Delta G_v)$ , where,  $\gamma_{ls}$  is the solid-liquid interfacial area  $A_{ls}$  and  $\Delta G_v$  is the free energy change associated with the volume of phase change from liquid to

solid ( $V_s$ ) [149,150]. The critical free energy for heterogeneous nucleation can be calculated as follows [149,150]:

$$\Delta G_{cri}^{het} = \frac{(2 + \cos \theta_{cri})(1 - \cos \theta_{cri})^2}{4} \Delta G_{cri}^{hom}, \quad (2.21)$$

where,  $\Delta G_{cri}^{hom} = V_s \Delta G_v + \gamma_{ls} A_{ls} = \frac{\pi r_c^3}{3} \Delta G_v + 4\pi r_c^2 \gamma_{ls}$ ,  $f(\theta_{cri}) = \frac{(2 + \cos \theta_{cri})(1 - \cos \theta_{cri})^2}{4}$  is the wettability parameter and  $\theta_{cri}$  denotes the contact angle at the nucleus-surface interface. The magnitude of  $f(\theta_{cri})$  varies between 0 and 0.5. This magnitude should be as large as possible to avoid nucleation and material deposition phenomenon. Tong et al. [151] conducted a study to relate silica scaling in reverse osmosis (RO) process with the heterogeneous nucleation, surface charge, hydrophilicity, and surface free energy. With some exceptions, they reported that lower magnitude of  $f(\theta_{cri})$  increases silica scaling possibility. They concluded that silica scaling is the combined effect of surface charge distribution and surface free energy ( $\Delta G_{cri}^{het}$ ). Mi et al. [152] reported that silica scaling in forward osmosis (FO) is mainly governed by the heterogeneous nucleation process (**Figure 2.8a,b**). From the adhesion force analysis, they concluded that membrane having low adhesion tendency with silica might exhibit better scaling resistant behavior. For example, silica-scaled cellulose acetate (CA) membrane recovered a higher amount of flux after the DI water rinse than the polyamide (PA) membranes. In addition to the FO and RO processes, interfacial materials have also been utilized in the membrane distillation (MD) process to prevent scaling (**Figure 2.8c**). Xiao et al. [153] introduced dual scale surface roughness features over the membrane surface to shift the surface from the pinning state to the rolling state and reported better scaling resistant performance. Thus, in a nutshell, we can conclude that though a single value of contact angle does not provide a direct quantification of membrane scaling; however, the parameters derived from the contact angle analysis (e.g., surface free energy, and adhesion force) can provide valuable insights on membrane scaling resistivity.

### 2.2.3 Development of novel interfacial materials with special wettability for next-generation polymeric membranes

Nature-inspired interfacial materials with special wettability have drawn specific attention towards novel membrane material development [13]. These applications can be utilized for the oil-water separation process, membrane-based water treatment, and fouling control strategy. Moreover, in many cases, surfaces with special wettability are required for harsh environment applications, e.g., high-temperature water purification. Such modification towards novel material development includes attachment of block copolymer on the selective layer and introducing micropattern over the membrane surface. Numerous examples can be found in the literature to employ materials with special wettability [11,113,115,154]. In this study, we only present two of such efforts, which can be the starting point for the implication of interfacial materials for water treatment.

Jeon et al. [155] reported that introducing new material such as poly(acryloyl hydrazide) star (PAH-SP) polymer can improve the permselectivity and anti-fouling properties (**Figure 2.9a**) simultaneously. This is due to the high-density reactive functional groups resulting from highly crowded chain architecture and enhanced polymer chain mobility (**Figure 2.9a**). Maruf et al. [156] first introduced topography modification of the TFC membrane incorporating micro-scale features over the selective layer. They observed reduced gypsum scaling for the patterned membrane in comparison with the unpatterned one. They reported that the pattern introduced a secondary flow at the membrane water interface, which is advantageous to prevent concentration polarization and scaling. El Sherbiny et al. [157] reported that micro-patterned TFC membranes have superior permselectivity and anti-fouling properties than the flat ones. They developed bio-inspired superhydrophilic micro-patterned TFC membranes with stimuli-responsive characteristics (**Figure 2.9b**). The combination of surface micro-patterns and the responsive hydrogel coating enabled the ‘smart’ wettability switching of the membrane surface and thus controlled the permselectivity.

Another important application of interfacial materials can be the anti-fouling membranes. The effective anti-fouling membranes not only exhibit fouling-resistant phenomenon but also provide fouling release characteristics (**Figure 2.9c**) [68]. One of the ways to achieve this goal is to introduce amphiphilic molecules over the membrane selective layer. Amphiphilic materials contain both hydrophobic and hydrophilic segments. Hydrophilic segments ensure the fouling resistivity, while, in contrast, the hydrophobic segments provide fouling release.

## 2.3 Summary

Polymeric membranes are excellent candidates for low cost and energy-efficient water purification processes. However, their performance is greatly affected due to fouling during filtration. The membrane separation process is substantially a surface phenomenon, i.e., the membrane's surface properties, such as wettability, roughness, and surface charge, play a crucial role in the membrane performance. Proper surface modification can be employed to improve the membrane permeation properties, e.g., water flux and anti-fouling property. Surface roughness and surface functional groups may alter due to the surface modification, which in turn affects the wettability of the membrane. It is anticipated that proper quantification and application of surface wettability and related parameters may enable meticulous design and parameterize of the membranes. In this review, we survey the techniques to quantify the membrane surface and permeation properties using contact angle analyzer. The contact angle can be such an important parameter through which one can access the information of surface wettability, hydrophilicity, free energy, adhesion, roughness, and zeta potential with high sensitivity. All these parameters can be further utilized to elucidate and qualitatively analyze the membrane permeation properties. **Figure 2.10** represents a brief overview of the membrane surface and performance parameters, which can be evaluated by contact angle analyzer. This review study mainly highlights the quantification and analyzing technique of membrane parameters by contact angle analysis.

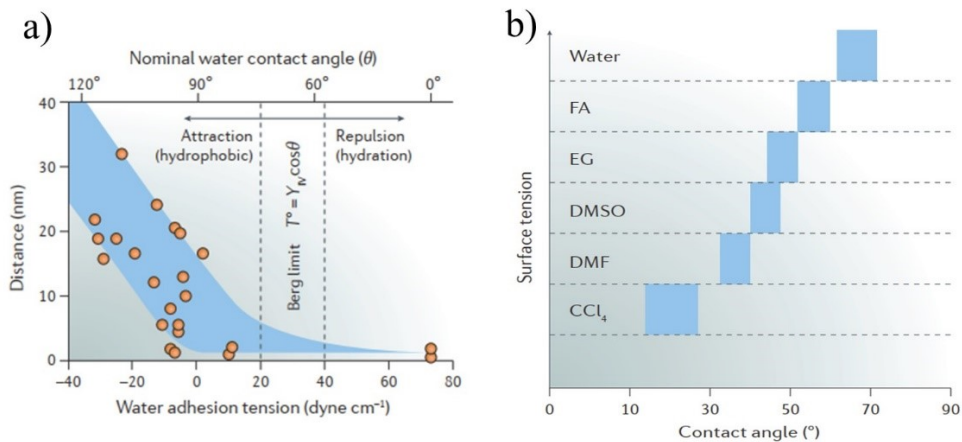


Figure 2.1: (a) Connection of contact angle to the solid-liquid adhesion. If the contact angle is less than  $\sim 65^\circ$ , the attractive long-range forces between a surface and water diminish, and the surface can be considered as hydrophilic [107]. The decay of attractive and the increment of repulsive force are observed between water adhesion force 20 and 40 *dyne/cm*, which is known as ‘Berg limit’. (b) Every liquid has a specific surface (solid) independent intrinsic wetting threshold (IWT), which is the boundary of partial-wetting and partial non-wetting, e.g., for water,  $\theta_{IWT} \approx 65^\circ$ . The IWT decreases with decreasing liquid interfacial tension.



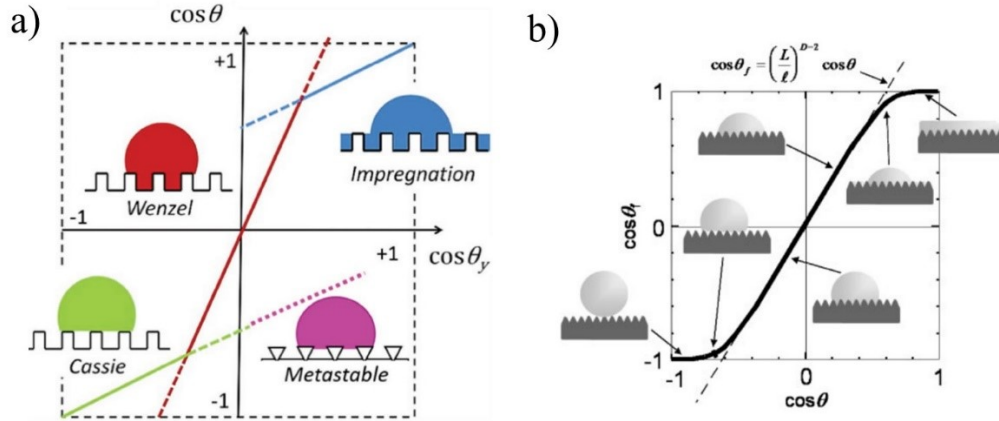


Figure 2.2: (a) Four different wetting states for a liquid on a structurally heterogeneous surface. By introducing physical heterogeneity (such as re-entrant profile in a metastable state), the intrinsically hydrophilic surface can be turned into hydrophobic surface [127]. (b) Surface free energy based on wetting state on a physical heterogeneous surface [127]. We observe that the impregnation state stays in the lowest energy minima and thus the most stable state. (c) Wetting states for a liquid on a fractal surface proposed by Tsujii et al. [66,67].

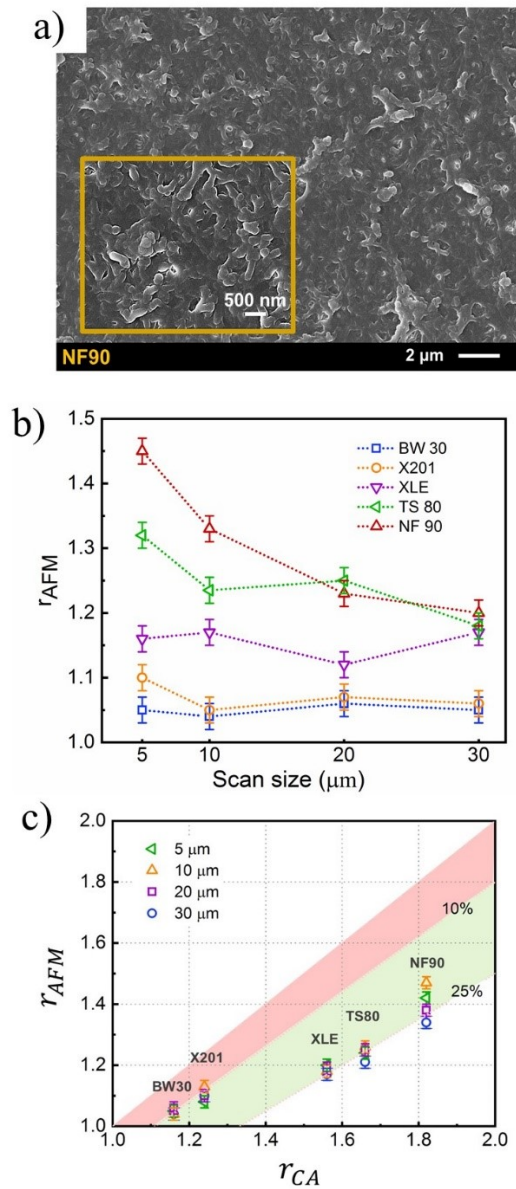


Figure 2.3: (a)-(c) Evidence of self-affinity in a TFC membrane surface [15]. (a) FESEM image of the NF 90 at two different magnification levels shows different topography of the surface. (b) AFM analysis at different scan size exhibit significant variation specifically for the membranes having a higher magnitude of roughness. (c) Wenzel roughness factor ( $r$ ) determination through contact angle analysis ( $r_{CA}$ ) exhibits higher magnitude than that obtained by AFM ( $r_{AFM}$ ) at different scan size.

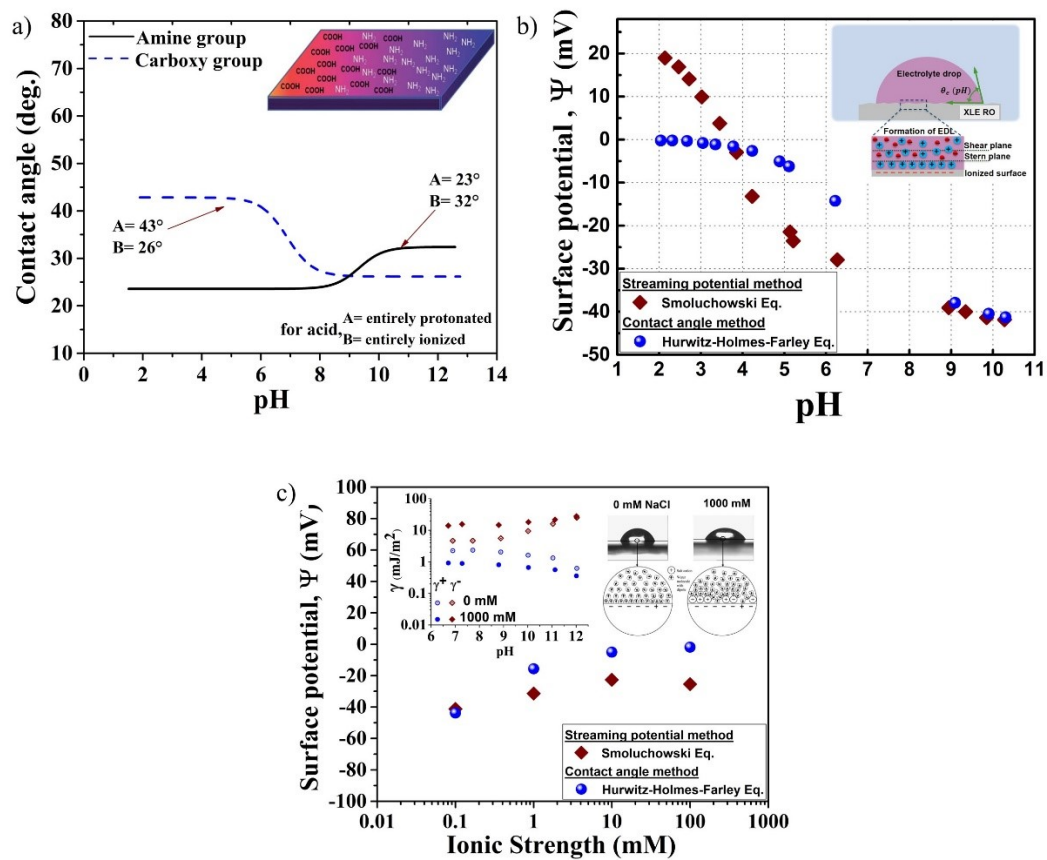


Figure 2.4: (a) A typical representation of a contact angle titration curve due to acid-base interaction of two different polyamide films containing free carboxylic and amine monomers on the surface [33,35,143]. (b) Comparison of surface potential measurement from contact angle titration and streaming potential technique [21]. (b) Surface tension components as a function of pH and NaCl ionic concentration. The inset image shows a conceptual illustration of the influence of NaCl ionic concentration on membrane wettability [21].

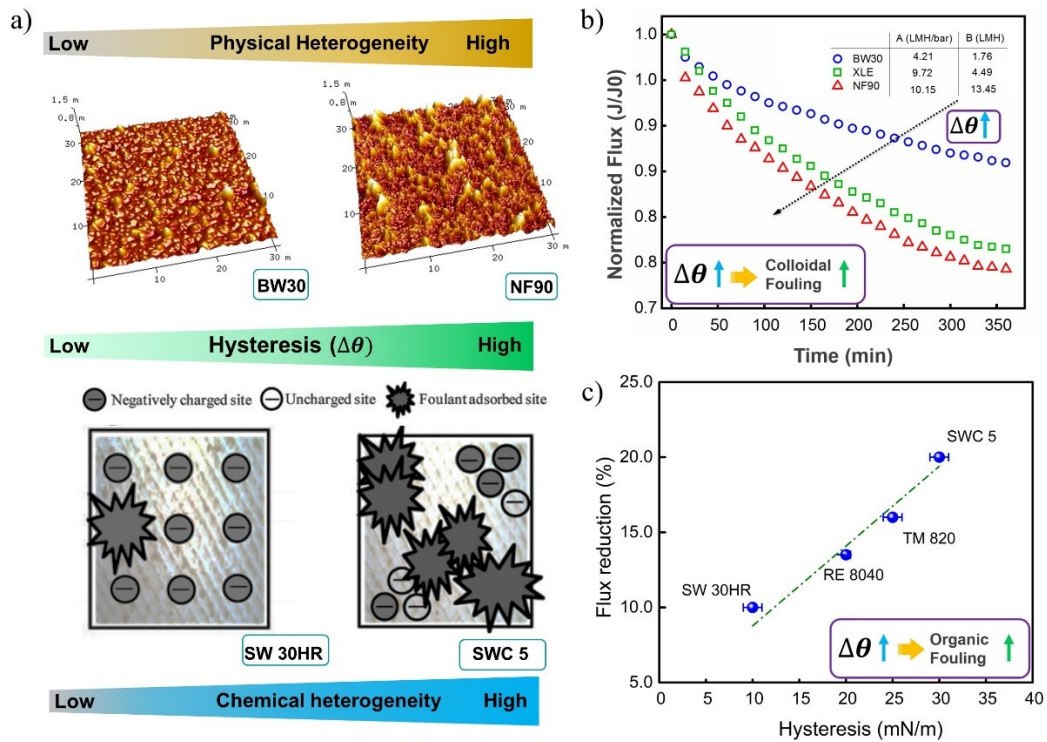


Figure 2.5: (a) Commercial membranes BW 30 and SW 30HR exhibit greater uniformity of surface features thus less contact angle hysteresis. Surface physical and chemical heterogeneity increases (b) colloidal and (c) organic fouling propensity. This fouling behavior is directly related to the surface contact angle hysteresis ( $\Delta\theta$ ) [22,71].

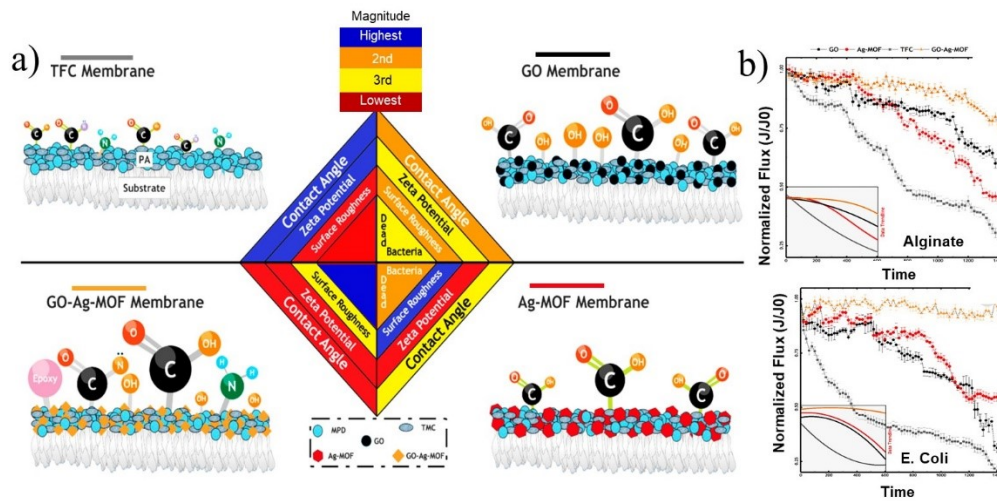


Figure 2.6: (a) A Synthesis of biofouling resistant membrane by incorporating graphene oxide (GO), and metal (silver, Ag) organic framework (MOF). The GO-AG-MOF exhibits the lowest magnitude of the contact angle and the zeta potential. This ensures (b) high normalized flux for this membrane for both sodium alginate and E. Coli feed water solution [145].

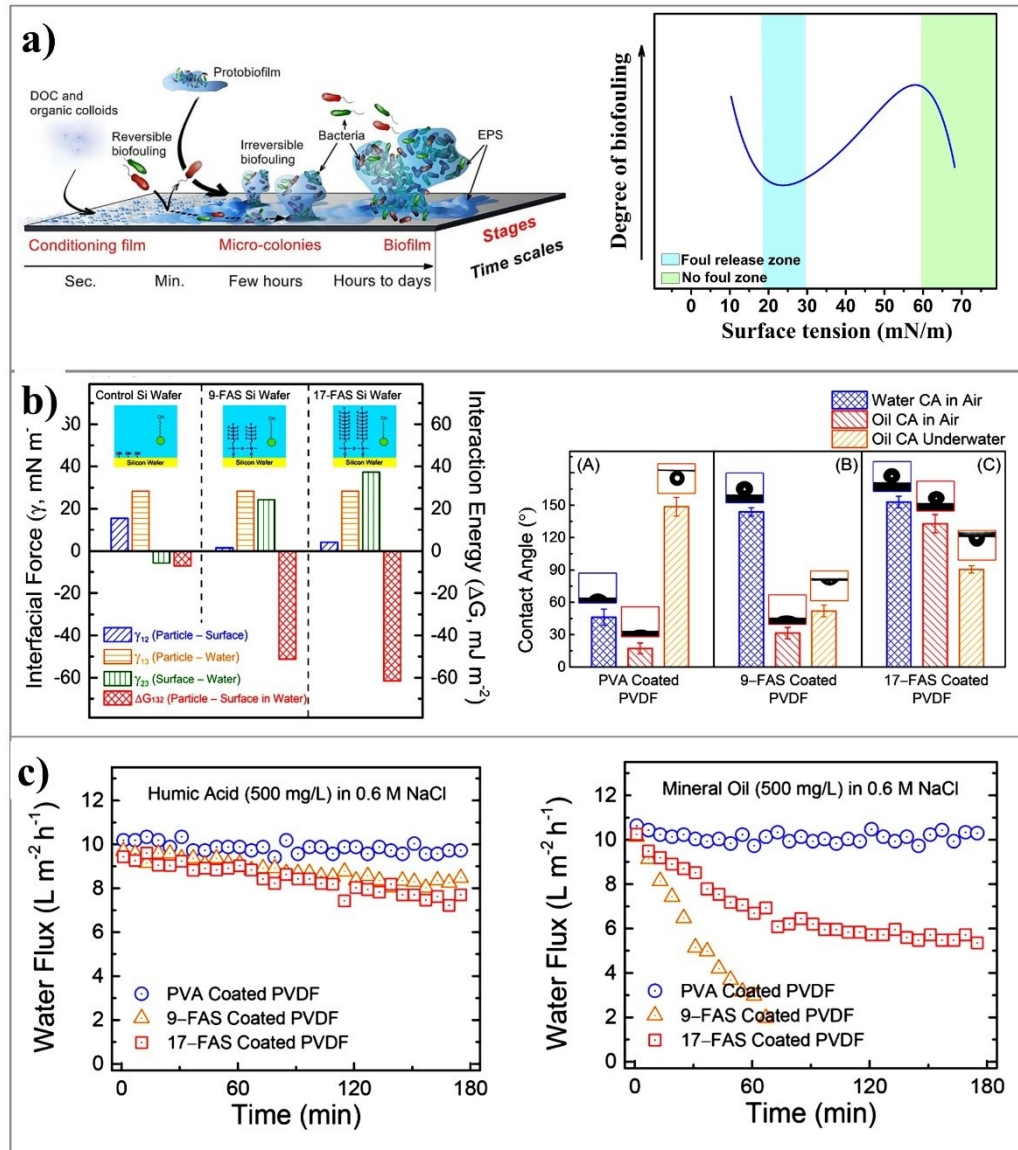


Figure 2.7: (a) Different stages of biofilm formation over membrane surface [146]. ‘Baier curve’ indicates that the surface tension of any material should be greater than 60 mN/m [147]. (b) From the interfacial energy analysis, it is evident that 9-FAS membranes are less hydrophobic than 17-FAS coated membrane. Humic acid fouling clearly shows that less hydrophobic membrane provides better performance. Interestingly, the oil fouling shows a different trend. It is due to the higher oleophobicity of 17-FAS coated membrane [148].



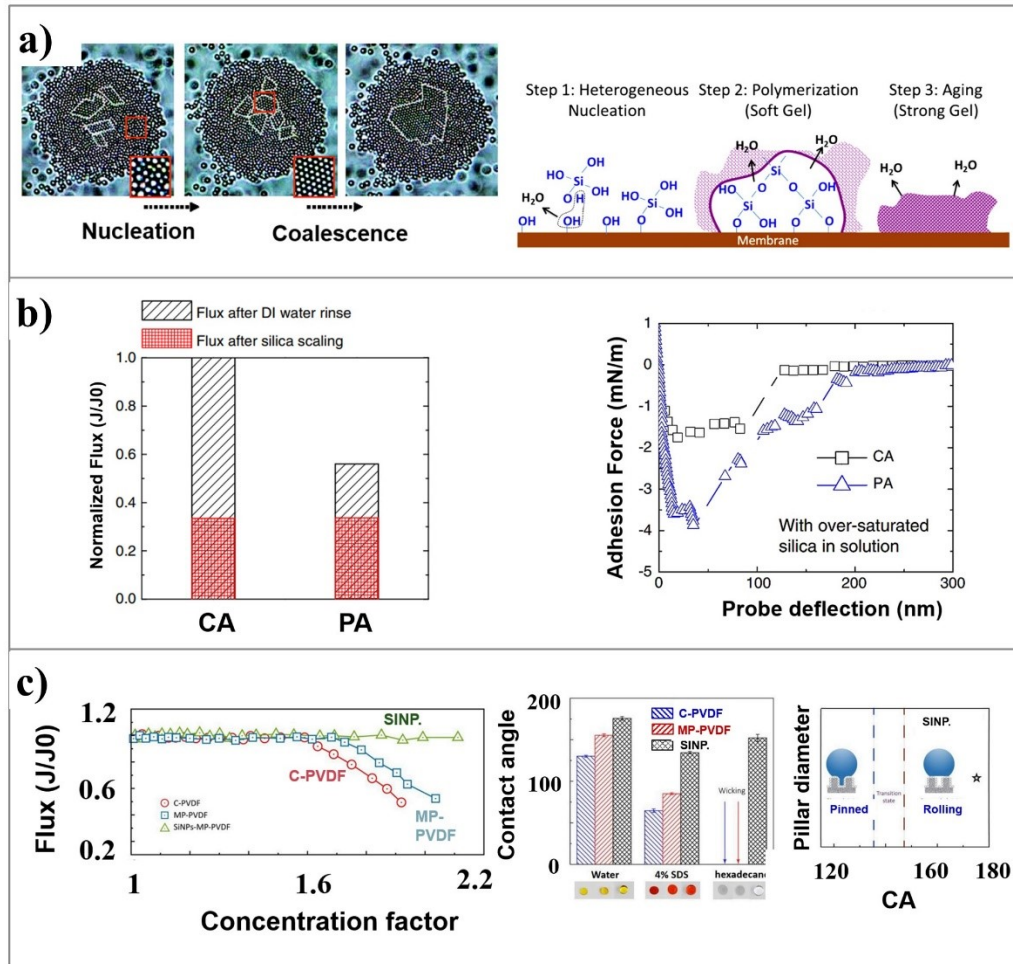


Figure 2.8: (a) Top panel: Evolution of a typical nucleation process. After the formation of critical nuclei, the crystallization process emerges to grow through coalescence [158]. Bottom panel: Scale formation mechanism (silica scaling with hydroxyl group) on the TFC membrane due to heterogeneous nucleation [152]. (b) Surfaces having less adhesion towards silica particle, i.e., cellulose acetate (CA) shows better flux recovery than the polyamide (PA) one. (c) Surface engineered membranes can be an excellent option for scaling resistivity. Dual scale roughness features (SINP) can shift the membrane surface from pinned to a rolling zone which results in higher normalized flux in the membrane distillation process [153].

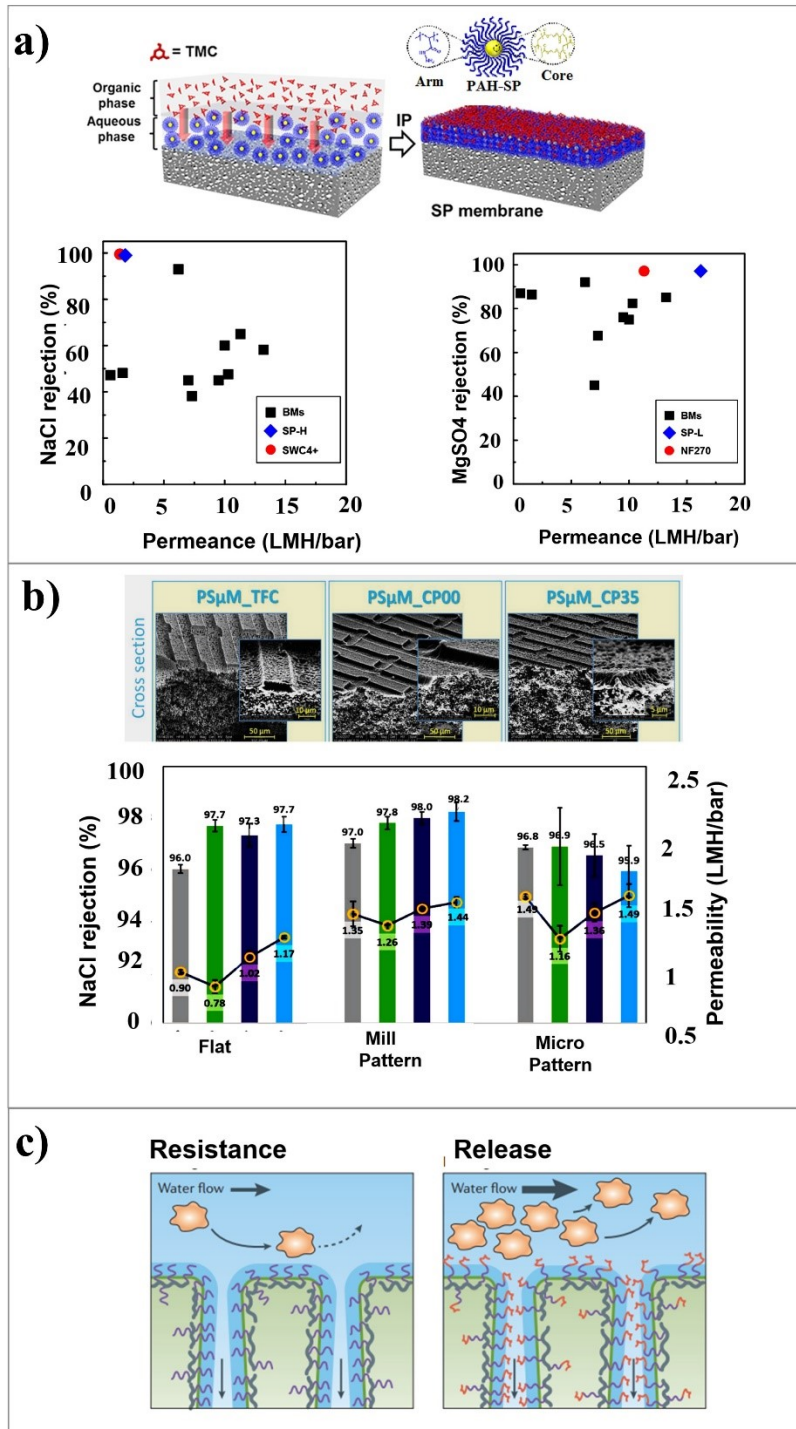


Figure 2.9: (a) Schematic of the fabrication of a TFC membrane with as poly(acryloyl hydrazide) star (PAH-SP) polymer via interfacial polymerization reaction. PAH-SP having multiple linear polymer arms showed a globular shape with a uniform size. This



globular structure can form interstitial spaces between the close-packed neighboring star polymers, and act as 'effective' water channels [155]. This ensures high foulant resistivity. (b) SEM image of the top surface and cross-section morphologies at different magnifications for pristine and surface modified micropatterned membranes prepared using phase separation micro-molding approach [157]. Pattern membranes showed better perm-selectivity than the flat membranes. (c) Fabrication of anti-fouling membranes: fouling resistance and release strategy. Hydrophilic surfaces only exhibit fouling resistant property. But the fouling release strategy includes the incorporation of both hydrophilic and hydrophobic non-polar low surface energy segments. The low surface-energy segments ensure foulant release in the presence of surface turbulence (e.g., high cross-flow) [68].

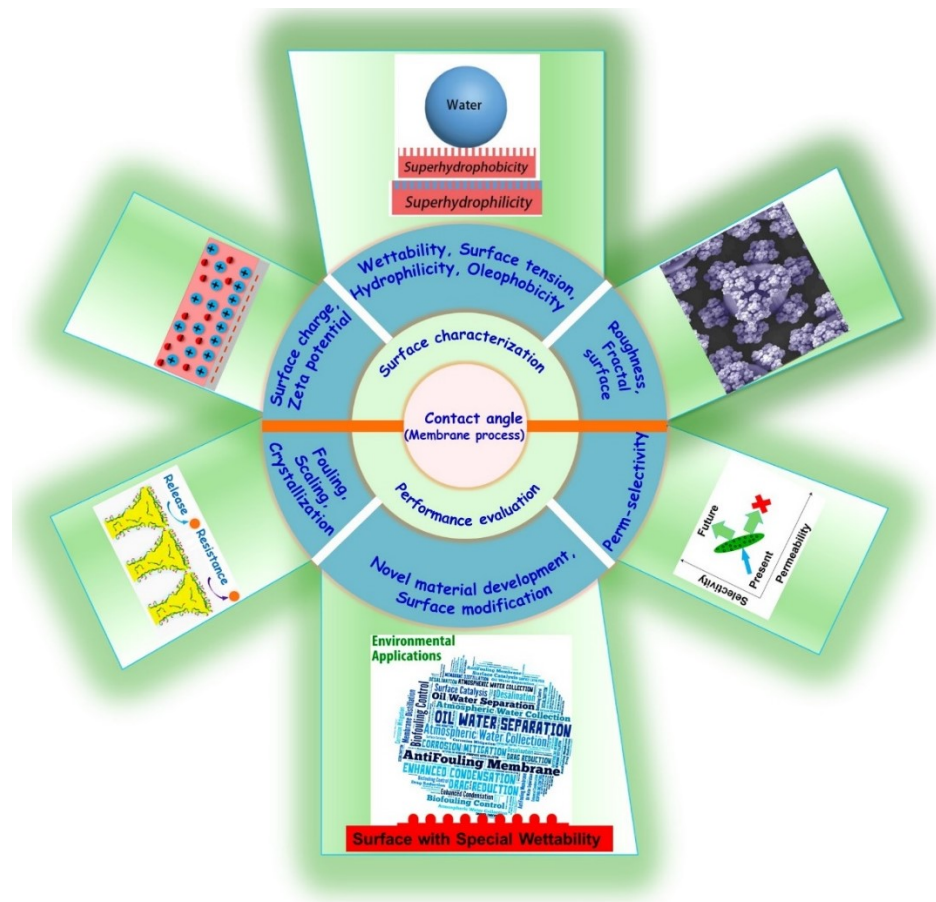


Figure 2.10. Overview of the characterization of the membrane surface and permeation properties using contact angle analyzer. It is evident from the literature that contact angle can provide a wide variety of information: surface properties such as wettability [107,159], roughness and fractal characteristics [15,160], surface charge and zeta potential [21], and permeation properties such as perm-selectivity [10,14], and anti-fouling property [11] for novel material development [13,68].

Table 2.1: Criteria for surface hydrophilicity.

Parameter	Condition	Literature
Free energy of cohesion	$\Delta G_{SW} > 0$	van Oss et al. [100]
Electron donor surface tension parameter	$\gamma_s^- < 28.3 \text{ mJ/m}^2$	Extension of van Oss et al. [100]
Free energy of adhesion	$\Delta G_{SW}^{ad} < -113 \text{ mJ/m}^2$	Extension of van Oss et al. [100]
Equilibrium contact angle (theoretical analysis)	$\theta_Y < \sim 55^\circ$	Combined van Oss et al. [100] and Young-Dupre equation [46,85]
Equilibrium contact angle (experimental analysis)	$\theta_Y < \sim 65^\circ$	Vogler [106]
Receding contact angle	$\theta_{rec} < 90^\circ$	Law et al. [111,112]

\*S=solid, W=water, ad=Adhesion

Table 2.2: Criteria for surface oleophobicity (non-polar oil, e.g., Hexadecane)

Parameter	Condition	Literature
Free energy of interaction underwater	$\Delta G_{SWO} > 0$	van Oss et al. [100]
Free energy of interaction in air condition	$\Delta G_{SOS} < 0$	van Oss et al. [100]
Polar surface tension parameter underwater condition	$\sqrt{\gamma_S^+ \gamma_S^-} > 27 \text{ mJ/m}^2$	Calculated from van Oss et al. [100]
Receding contact angle in air	$\theta_{OA_{receding}} > 124^\circ$	Law et al. [111,112]
Equilibrium contact angle	$\theta_{SWO} > 158^\circ$	Combined van Oss et al. [100]-Schultz et al. [118]
In air hydrophilic and oleophilic surfaces ( $\gamma_{SA} > \gamma_{SW}$ and $\gamma_{SA} > \gamma_{SO}$ )	$\gamma_{OA} \cos \theta_O < \gamma_{WA} \cos \theta_W$	Jung et al. [117]
In air hydrophobic and oleophobic surfaces ( $\gamma_{SA} < \gamma_{SW}$ and $\gamma_{SA} < \gamma_{SO}$ )	$\gamma_{OA} \cos \theta_{OA} > \gamma_{WA} \cos \theta_{WA}$	Jung et al. [117]

## Chapter 3 §

# New Insights into the Impact of Surface Heterogeneity on the Wettability of Polymeric Membranes

---

§Material of this chapter has been published/prepared for submission as *i.* Md Farhad Ismail, Behnam Khorshidi, and Mohtada Sadrzadeh. New insights into the impact of nanoscale surface heterogeneity on the wettability of polymeric membranes. *Journal of Membrane Science* 590: 117270, 2019. 3. *ii.* Md Farhad Ismail, Muhammad Amirul Islam, Behnam Khorshidi, and Mohtada Sadrzadeh. Quantification of surface potential by wettability measurements. *Applied Physics Letters*, 2020 (in progress).

### 3.1 Surface physical heterogeneity

Membrane technology is currently utilized in a broad range of applications, from industrial and residential wastewater treatment to seawater desalination [14,161]. Despite the promising advantages of membrane processes, such as high product quality, low operating costs, and compact design, the susceptibility of membranes to fouling remains one of the most challenging issues, which limits the sustainable application of membrane technology for water treatment [11,162]. Fouling decreases the membrane performance dramatically by reducing the flux and the quality of water and subsequently increases operating costs [163,164]. The physicochemical properties of the membrane surface (e.g., wettability, surface charge, and roughness) are found to be the most influential factors on fouling [37,78,165]. It is generally accepted that membranes with higher water wettability and lower magnitude of roughness are less prone to fouling [14,78,166]. Wettability is typically characterized by measuring the contact angle of a wetting liquid (often water) over a substrate. Surface roughness is commonly measured by atomic force microscopy (AFM) [167].

It is well established that the surface roughness inherently affects the wettability by providing more contact area to the spreading liquid [47]. Busscher et al. [168] studied the influence of surface roughness on the contact angle of five different liquids over twelve polymeric substrates. Their objective was to find out how smooth it should be a surface so that the influence of surface roughness on contact angle can be neglected. They evaluated the wettability by sessile drop technique and the average surface roughness by stylus profilometer. They found that the influence of surface roughness on contact angle is negligible when the average roughness is less than 100 nm. However, no attempt was made to evaluate the root mean square (RMS) roughness, Wenzel roughness-ratio [47], as well as the impact of surface chemical heterogeneity on the contact angle. The invention of AFM in the 1980s provided more opportunities for surface scientists to evaluate the surface topography of the solid materials with higher resolution down to micron and

nanoscale [52]. Miller et al. [53] conducted a similar study to clarify the effect of nano-sized surface asperities on the water contact angle over polytetrafluoroethylene (PTFE). They generated two different types of surfaces having RMS roughness of 8.3 nm and 83.6 nm and employed AFM and contact angle goniometry techniques to quantify the RMS roughness and wetting properties of the PTFE surfaces, respectively. They observed that the advancing and receding contact angle increased with an increase in surface roughness. Accordingly, surface roughness was found to alter the wettability of any surface having RMS roughness of greater than 80 nm. It is worth noting that this study also disregarded the polar interaction between the solid and liquid surfaces. Besides, the AFM measurement was limited to a small scan area of  $5 \times 5 \mu\text{m}^2$ , which may not adequately represent the surface heterogeneity. Good et al. [169] performed a study to determine the surface roughness of fluorinated ethylene propylene (FEP) and poly(methyl methacrylate) (PMMA). They created a wide range of roughness on these substrates by using different silicon carbide papers. They have utilized different polar and non-polar test liquids and reported that wettability could alter due to physical (roughness) and chemical (functional groups) heterogeneities. They qualitatively compared the roughness factor of their samples with the smoothest surface and found good agreement only for non-polar FEP surfaces. Kuna et al. [170] and Voitchovsky et al. [171] investigated the effect of nanoscale physical heterogeneity on the solid surface tension of self-assembled monolayers, coated with binary mixtures of 1-octanethiol and 6-mercaptohexan-1-ol (MHol). They have generated comparatively smooth and rough surfaces by coating multi-layer films of nanoparticles. They evaluated the work of adhesion using AFM and wettability analyses and reported a monotonic dependence of the work of adhesion on the MHol composition for the smooth surface. In contrast, a non-monotonic trend is observed for the rough surface due to the effect of nanoscale physical heterogeneity. They also realized that the work of adhesion is higher when it is obtained by contact angle analysis compared to AFM. They proposed that the AFM results need calibration with a known reference surface to provide accurate results. However, no comment was provided about the influence of polar interaction

of the solid-liquid interface on the contact angle analysis. Another shortcoming of these studies is that the wettability analysis was merely based on the static contact angle while evaluation of advancing or receding contact angles is required for a reliable wettability analysis of heterogeneous surfaces [42]. Furthermore, the AFM measurements were limited to a small scan size of 5  $\mu\text{m}$ , which may provide misleading information by skipping the scattered surface features. A recent study of Johnson et al. [31] illustrated that the AFM characterization depends on the selected scan size due to the self-affine fractal characteristics of the sample surface. They used four polymeric membranes and carried out the AFM analysis at different scan sizes ranging from 1  $\mu\text{m}$  to 80  $\mu\text{m}$ . Calculating the fractal dimension and roughness exponent from the AFM power spectral density (PSD) plot, they reported that the RMS roughness of the polymeric membranes increased sharply with the increase in scan size from 1  $\mu\text{m}$  up to 10  $\mu\text{m}$ , followed by a slight rise at larger scan sizes.

Taniguchi et al. [172] developed an experimental model to correct the contact angle measurement for the surface roughness of porous ultrafiltration polyethersulfone (PES) membranes. They used the captive bubble technique for the contact angle, and contact mode for AFM roughness measurement. They compared the corrected advancing, receding and equilibrium contact angles of porous PES membranes with a nonporous PES film. Except for high-porosity membranes, they found reasonable agreement between the corrected advancing and equilibrium contact angles of low-porosity PES membranes with a nonporous PES film. In contrast, the corrected receding contact angle of the porous membranes were not comparable with that of nonporous PES film. They suggested that the discrepancy was due to the surface restructuring and molecular rearrangement of the functional groups. This study would be more comprehensive if the effect of surface porosity and scan size (larger than 5  $\mu\text{m}$ ) was considered in the proposed model. Tröger et al. [173] suggested a theoretical modification to correct the contact angles due to porosity. They have utilized the sessile drop contact angle measurement technique to measure the contact angle of seven microporous PTFE membranes with the pore size ranging from 0.2 to 5  $\mu\text{m}$ . The experimental observations were compared with the



contact angle obtained from non-porous PTFE surfaces and reasonable agreement was obtained. This study indicated that not only roughness but also the surface porosity needs to be considered while correcting the contact angle of porous surfaces. Han et al. [20] proposed a method to simultaneously quantify the surface energy and Wenzel surface roughness of nonporous polymeric membranes. Based on the surface tension measurement proposed by Good and co-workers [100,169], they employed a combination of four polar and non-polar probe liquids to characterize the apparent (equilibrium) contact angle of commercial NF90 and ESPA1 membranes. While conventional AFM measurement provided higher surface area difference for ESPA1 than NF90, their proposed wettability method showed exactly the opposite result. Conducting a sensitivity analysis, they concluded that surface roughness propagates the error and amplifies the magnitude of the predicted surface energy. A potential weakness of this study is the combination of employed polar/nonpolar probe liquids for wettability analysis of polar polymeric membrane surfaces, which might result in the reported discrepancies. Furthermore, this study could be more interesting if the advancing contact angle was employed in addition to the static contact angle in the wettability analysis. It was suggested by Good et al. [169] to consider only nonpolar liquids to minimize polar interactions when determining the physical heterogeneity from contact angle-based analysis.

In this work, a systematic study has been conducted to assess the impact of surface nanoscale physical heterogeneity over surface wettability. Five polymeric membranes having different surface roughness are selected and a new experimental approach is developed to quantify the non-polar surface tension component, as well as the surface roughness-ratio (e.g., Wenzel roughness factor) of the polymeric membranes. The proposed approach includes evaluation of the equilibrium static and advancing contact angles of different non-polar liquids over the surface of the membrane. To compare the outcomes with the conventional characterization approach, the surface topography of the membranes using AFM has also been measured. This study is believed to be the first study to evaluate all the surface

wettability related parameters of polymeric membranes by solely using contact angle analyzer.

### 3.1.1 Materials

Five commercially available polymeric membranes were selected as a solid surface in this study: NF90 (NF, FILMTEC™), TS80 (NF, TriSep™), BW30 (RO, FILMTEC™), XLE (RO, FILMTEC™) and X201 (RO, TriSep™). All these membranes have a thin film composite structure with a polyamide film as their topmost selective surface. Colloidal silica (SiO<sub>2</sub>) particles (SNOWTEX 20L, 40–50 nm, 20-21 wt.% suspension in water) were purchased from Nissan Chemical Corporation (USA) and were used for fouling tests. Several non-polar liquids were purchased from Fisher Scientific and were used without further purification as probe liquids in contact angle tests. **Table 3.1** presents the name and the main physicochemical properties of these probe liquids.

### 3.1.2 Theoretical background for wettability analysis

The contact angle is defined as the tangential angle formed at the liquid-solid interface when a liquid droplet is in contact with a solid surface. The contact angle can also be defined as a mechanical equilibrium of three surface tension forces: solid-air ( $\gamma_{SA}$  or  $\gamma_S$ ), liquid-air ( $\gamma_{LA}$  or  $\gamma_L$ ), and solid-liquid ( $\gamma_{SL}$ ) interfacial tensions, as shown in **Figure 3.1a**. Considering a sessile liquid droplet over a surface, three different contact angles can be defined, namely equilibrium static ( $\theta_S$ ), advancing ( $\theta_{Ad}$ ) and receding ( $\theta_{Re}$ ) contact angles which are illustrated in **Figure 3.1(b-d)** [83]. The advancing and receding contact angles are defined as the maximum and minimum angles of the liquid droplet over the solid surface during the wetting and de-wetting processes, respectively. These contact angles are measured by a steady increment and decrement of the drop volume over the surface.

For a liquid droplet sitting over a flat, smooth and chemically homogeneous (ideal) surface, the correlation between the surface tension forces and the static equilibrium contact angle can be presented by Young's equation [46]:

$$\gamma_L \cos \theta_Y = \gamma_S - \gamma_{SL} \quad (3.1)$$

where  $\theta_Y$  is the Young's contact angle. However, real surfaces contain both physical and chemical heterogeneities, which affect their wettability toward contacting liquids. For a rough surface without chemical heterogeneity, the Wenzel model [47] correlates the static (apparent) contact angle with the surface physical heterogeneity as [174]:

$$\gamma_L \cos \theta_W = r(\gamma_S - \gamma_{SL}) \quad (3.2)$$

where  $\theta_W$  is the equilibrium contact angle based on the Wenzel model. The parameter  $r$  is called surface roughness-ratio and is defined as the ratio of the actual surface area over the projected area. According to extended Fowkes' model, the interfacial surface tension between a solid surface and a contacting liquid can be presented in terms of the polar and non-polar components of surface tension [88,90,100] :

$$\gamma_{SL} = \gamma_S + \gamma_L - 2 \left( \sqrt{\gamma_L^P \gamma_S^P} + \sqrt{\gamma_L^D \gamma_S^D} \right) \quad (3.3)$$

where the superscripts  $P$  and  $D$  denote the polar and dispersive interactions, respectively. Polar interactions, also known as Lewis acid-base interactions, originate from electron-donating and electron-accepting interactions such as hydrogen bonding [100]. The non-polar dispersive interactions account for Lifshitz-van der Waals (LW) interactions [100]. The substitution of  $\gamma_{SL}$  from Eq. (3.3) into Eq. (3.2) provides the correlation between the surface tension components of a rough surface and a wetting liquid as follows:

$$\gamma_L \left(1 + \frac{\cos \theta_W}{r}\right) = 2 \left( \sqrt{\gamma_L^P \gamma_S^P} + \sqrt{\gamma_L^D \gamma_S^D} \right) \quad (3.4)$$

Equation (3.4) simplifies more if a non-polar liquid is used for wettability analysis ( $\gamma_L^P = 0, \gamma_L = \gamma_L^D$ ):

$$\sqrt{\gamma_L} \cos \theta_W = -r \sqrt{\gamma_L} + 2r \sqrt{\gamma_S^D} \quad (3.5)$$

It is worth noting that the wettability analysis solely based on static contact angle fails to provide the complete information of the solid-liquid interaction for the case of rough surfaces [42]. It is because the liquid droplet may entrap at different heterogeneous spots (metastable states) during spreading over the surface and exhibit a contact angle in between the advancing and receding contact angles. Therefore, the evaluation of advancing or receding contact angles is necessary to provide a reliable set of information on the wetting characteristics of a solid surface.

Accordingly, extending the Wenzel model to consider the advancing contact angle yields [174]:

$$\gamma_L \cos \theta_{Ad} = r (\gamma_S - \gamma_{SL}) - F \quad (3.6)$$

where  $F$  indicates the resistive frictional force due to the surface physical heterogeneity [174]. For the case of a non-polar wetting liquid, employing Eq. (3.3) into Eq. (3.6) results in:

$$\sqrt{\gamma_L} \cos \theta_{Ad} = -\sqrt{\gamma_L} \left[ r + \frac{F}{\gamma_L} \right] + 2r \sqrt{\gamma_S^D} \quad (3.7)$$

where  $F/\gamma_L$  is termed as a non-dimensional pinning force and depends on the molecular interaction between the liquid and solid surfaces. Equations (3.5) and (3.7)

are the key expressions that are used in the present study to evaluate the surface wettability characteristics. The slopes and the intersections of the linear plots of  $\sqrt{\gamma_L} \cos\theta$  versus  $\sqrt{\gamma_L}$  using Eqs. (3.5) and (3.7) provide the roughness-ratio ( $r_{CA}$ ), the non-dimensional pinning force ( $F/\gamma_L$ ), and the dispersive component of the solid surface tension ( $\gamma_S^D$ ).

### **3.1.3 Measurement of the wettability of the membranes**

The surface wettability of the membranes was evaluated by measuring the equilibrium and advancing contact angles using a drop shape analyzer (Krüss DSA 100E, Hamburg, Germany). For each sample, five different positions on the membrane surface were tested, and the average value of the contact angles was reported. The equilibrium contact angle was recorded after 25s to ensure the stability of the liquid droplet over the membrane surface. The advancing contact angle was measured by forming a small drop ( $\sim 3 \mu\text{L}$ ) and gently increasing its volume to 15  $\mu\text{L}$ .

### **3.1.4 Characterization of surface topography of the membranes**

The surface morphology of the membranes was evaluated using AFM (Bruker Dimension Edge instrument, model, city, country) and FESEM (Zeiss Sigma 300 VP, city, country). The AFM measurements were carried out in tapping mode in air. The AFM cantilever had a nominal resonant frequency and spring constant of 300 Hz and 42 N/m, respectively. The AFM measurements were conducted at four scan sizes: 5  $\mu\text{m}$ , 10  $\mu\text{m}$ , 20  $\mu\text{m}$ , and 30  $\mu\text{m}$ . For FESEM, the samples were coated by carbon and tested at an accelerating voltage of 10.0 kV using an in-lens detector.

### 3.1.5 Characterization of fouling propensity of the membranes

Permeation performance of the membranes was evaluated using a crossflow filtration setup (Sterlitech Co., USA). The permeation flux ( $J_w$ ) of the TFC membranes was calculated at steady state by  $J_w = \Delta m / (\rho \times A_m \times \Delta t)$ , where  $\Delta m$  is the mass of the permeate passed through the membrane effective surface area ( $A_m$ ) over the sample collection period ( $\Delta t$ ). The hydraulic permeability ( $A$ ) of the membranes was obtained based on the slope of the linear plot of permeate flux versus transmembrane pressure ( $A = \Delta J_w / \Delta P$ ). The apparent salt rejection ( $R$ ) of the membranes was evaluated by  $R = (1 - C_p / C_f) \times 100$ , where  $C_p$  and  $C_f$  are the salt concentration in the permeate and feed (2000 ppm NaCl) solutions. The salt permeability ( $B$ ) of the membranes was calculated by  $B = J_w(1 - R) / R$ . The fouling tests were conducted at a crossflow feed velocity of 0.085 m/s, using 200 ppm of SiO<sub>2</sub> colloids and 2000 ppm NaCl solution at pH 6.8-7.0 and 25 °C. The initial permeate flux ( $J_0$ ) of the membranes was set to  $1.583 \times 10^{-5}$  m/s ( $57 \text{ Lm}^{-2}\text{h}^{-1}$ , LMH) by adjusting the transmembrane pressure.

### 3.1.6 Results and discussion

#### 3.1.6.1 Characterization of surface morphology by FESEM and AFM

AFM and FESEM characterization techniques provide the visual and quantitative information of the surface morphology. **Figure 3.2** shows the top surface FESEM images of the studied polymeric membranes. All these membranes exhibit the so-called ridge-and-valley structure, which is a typical characteristic of the polyamide layer of the TFC membranes [175,176]. A qualitative comparison based on the distribution of the surface features suggests that the BW30, X201, and XLE have almost a uniform morphology. In contrast, the NF90 and TS80 membranes

possess several random protrusions, which make their surface more heterogeneous than the other membranes. The nanoscale surface features of the membranes are more noticeable in AFM images in **Figure 3.3**. The AFM 3D topographies illustrate that BW30 and X201 have a nearly homogeneous surface morphology with the RMS roughness of 50 nm and 64 nm, respectively. In contrast, the ridges and valleys are distributed heterogeneously at the surface of XLE, TS80, and NF90, resulting in RMS roughness of 90 nm, 91, nm and 101 nm, respectively, at the surface of these membranes.

The random distribution of the physical heterogeneity on the surface of the membranes in **Figure 3.3** implies a strong dependency of the AFM quantifications on the size of the tested area. To evaluate this hypothesis, the AFM measurements were also carried out at different scan sizes of 5  $\mu\text{m}$ , 10  $\mu\text{m}$ , 20  $\mu\text{m}$ . **Figure 3.4** illustrates the variation of surface average roughness ( $R_{avg}$ ) and RMS roughness ( $R_{rms}$ ) of the membranes with scan size. Both surface roughness values increased when a larger area of the membranes was mapped by AFM. The roughness of BW30 and X201 showed small variation, particularly at scan sizes of 20  $\mu\text{m}$  and 30  $\mu\text{m}$ , implying the presence of a uniform and self-similar structure on the surface of these membranes. The variation of  $R_{avg}$  and  $R_{rms}$  for these membranes is found to be within  $\pm 5$  nm for the range of scan sizes studied. In contrast, the roughness values of XLE, TS80, and NF90 increased consistently as the scanned area expanded which reveals the self-affinity of the nanoscale features at the surface of these membranes.

**Figure 3.5a** demonstrates the variation of roughness-ratio ( $r_{AFM}$ ) at different scan sizes. Consistent with the roughness variation in **Figure 3.5**, BW30 and X201 showed a small variation of  $r_{AFM}$  when the scan size expanded from 5  $\mu\text{m}$  to 30  $\mu\text{m}$ . In contrast, the roughness factor of XLE, TS80 and NF90 slightly decreased at higher scan sizes. In addition to surface roughness, which measures the vertical distribution of heterogeneity, it is worth evaluating the lateral distribution of the irregularities. This information is valuable for the characterization of fractal surfaces, which exhibits a variety of irregular, rough and fragmented structures. In this context, it is necessary to distinguish between self-similar and self-affine fractal surfaces. The

former exhibits invariant surface features at different spots, while the latter has surface structures that varies over translation and scaling [64]. Fractal geometries can be characterized by scaling factors, known as the fractal dimension ( $D_{\text{Fractal}}$ ) and roughness exponent ( $H$ ). For these geometries, the roughness characteristics (e.g.,  $R_{rms}$ ) follow a power law correlation with the measurement length (scan size,  $L$ ), i.e.,  $R_{rms} \sim L^H$  [65]. Victor et al. [65] reported that the AFM power spectral density (PSD) analysis can be used to evaluate the surface fractal dimension ( $D_{\text{Fractal}}$ ). The PSD plot typically represents the roughness amplitude as a function of spatial frequency. For a 2D isotropic PSD plots, the fractal dimension and roughness exponents are correlated as  $H = 2 - D_{\text{Fractal}}$  [65]. The fractal dimension can be obtained using  $D_{\text{Fractal}} = 3 + \frac{1}{2} \frac{d \log P(f)}{d \log f}$ , where  $P(f)$  is the power spectrum and  $f$  is the spatial frequency [177]. **Figure 3.5b** depicts the variation of fractal dimension of the polymeric membranes at different scan sizes. The fractal dimension varied continuously up to a scan size of  $\sim 20 \mu\text{m}$ . However, after that a steady data has been observed. This observation implies that, the transition from self-affine to a self-similar structure occurs at a scan size of  $20 \mu\text{m}$  or higher. Therefore, care must be taken to interpret the AFM results that are obtained at a small scan size, e.g.  $< 20 \mu\text{m}$ .

### 3.1.6.2 Assessing nanoscale heterogeneity by wettability analysis

**Figure 3.6** presents the surface wettability plots of the polymeric membranes. The wettability data were obtained by measuring the equilibrium and advancing contact angles of different non-polar liquids over the membrane surface and  $\sqrt{\gamma_L} \cos \theta$  was plotted against  $\sqrt{\gamma_L}$ . Consistent with the predicted trend by Eqs. (3.5) and (3.7), the plotted data are linearly correlated for both equilibrium and advancing contact angles. The slope of the fitted lines in **Figure 3.6a** gives the roughness-ratio based on the equilibrium contact angle ( $r_{CAW}$ ) and the intersection with the y-axis provides the dispersive surface tension components ( $\gamma_S^D$ ). Similarly, the slope of the



regression lines in **Figure 3.6b** provides roughness-ratio based on advancing contact angle ( $r_{CAAd}$ ), as well as the magnitude of non-dimensional pinning force ( $\frac{F}{\gamma_L}$ ).

The validity of the extracted surface wettability parameters from the wettability plots in **Figure 3.6** can be examined by calculating the advancing contact angle using experimental and theoretical roughness-ratio, dispersive surface tension component, and the non-dimensional surface pinning force using Eq. (3.7) and the following relation [174]:

$$\cos \theta_{Ad} = r_{CAAd} \cos \theta_Y - \frac{F}{\gamma_L} \quad (3.8)$$

**Figure 3.7** illustrates that the calculated  $\cos \theta_{Ad}$  values, based on experimentally evaluated surface wettability parameters, were in a good agreement ( $\pm 15\%$  deviation) with the theoretical prediction. The theoretical map (grey region) were plotted for the minimum and maximum roughness-ratio of 1 to 2.5 and the non-dimensional pinning force between 0.05 to 0.35. These values are very close to the experimentally extracted roughness-ratio (1.16-1.82) and non-dimensional pinning force (0.05-0.17) which are presented in the inner panel of **Figure 3.7a**. Both the roughness-ratio and the non-dimensional pinning force increase with the increase of the surface heterogeneity. Among the studied membranes, BW30 and X201 exhibited lower pinning force which can be due to their smooth surface morphologies. TS80 and XLE membranes showed similar pinning force and NF90 demonstrated the highest magnitude of pinning force. It is worth noting that, although the roughness-ratio of all membranes is in the same order of magnitude, the non-dimensional pinning force of XLE, TS80, and NF90 is one order of magnitude higher than that of BW30 and X201. This observation implies a more significant influence of nanoscale heterogeneity on the non-dimensional pinning force compared to surface roughness-ratio of the polymeric membranes.

**Figure 3.8** compares the values of measured roughness-ratio and dispersive surface tension component using AFM ( $r_{AFM}$  and  $\gamma_S^D (AFM)$ ) at different scan sizes

versus the same parameters based on advancing contact angle analysis ( $r_{CAAd}$  and  $\gamma_S^D(CA)$ ). **Figure 3.8a** illustrates a discrepancy between 10% to 25% among the  $r_{AFM}$  and  $r_{CA}$ . In all measurements, AFM provided a lower value of surface roughness-ratio. **Figure 3.8b** demonstrates the values of AFM-based dispersive surface tension components influenced significantly by scan size, particularly for NF90 and TS80, which had larger surface heterogeneity compared to other membranes. There are two likely causes for the discrepancies between the results of AFM and the contact angle analysis. First, the radius of the AFM tip used in the characterization tests was in the same order of the surface roughness ( $\sim 10$  nm). In this case, the tip could not possibly reach every gap inside the ridge-and-valley structure, specifically at the sub-10 nm scale. Second, the wet area of the liquid droplet in contact angle test is considerably larger than the AFM scanned area. Therefore, the contact angle-based wettability analysis provides more reliable information on surface properties particularly for the self-affine surfaces with large surface heterogeneity.

### 3.1.6.3 Implication for membrane development

In order to correlate the antifouling propensity of the membranes with the proposed model in this study, the colloidal fouling behavior of three membranes, which possessed the highest (NF90), lowest (BW30), and middle range (XLE) surface heterogeneity was evaluated using SiO<sub>2</sub> nanoparticle suspension. **Figure 3.9a** presents the normalized flux ( $J/J_0$ ) of the membranes over 6 hr filtration test. A strong correlation between the surface heterogeneity and flux decline of the membranes was observed. NF90 membrane, which had the largest roughness-ratio, based on both AFM and CA measurement, showed a 25.7% flux decline due to the deposition of silica particles on its surface. In contrast, the smoothest membrane, BW30, exhibited a low flux decline of 14% under similar test conditions. The XLE membrane resulted in a 23.5% flux decline, consistent with the order of its surface heterogeneity as compared to BW30 and NF90. **Figure 3.9b** illustrates the correlation between the normalized flux (after 6 hr filtration) and the roughness-ratio measured by the

conventional AFM ( $r_{AFM}$ ) analysis and the proposed contact angle-based ( $r_{CA}$ ) technique. It was found that the contact angle analysis provided a more reliable trend of variation ( $R^2=0.99$ ) compared to AFM tests ( $R^2\sim 0.81-0.9$ ) between the surface roughness-ratio and the normalized flux. It is also worth noting the AFM tests, which were conducted at a larger scan size (e.g., 30  $\mu\text{m}$ ), provided higher precision results as compared to lower scan sizes (10  $\mu\text{m}$ ).

**Figure 3.10a** depicts a theoretical phase diagram for a solid surface such as a polymeric membrane in contact with water. The phase diagram maps three regions of non-wetting ( $\theta_W = 90^\circ$ ), partial, and complete wetting ( $\theta_W = 0^\circ$ ) for an arbitrary solid surface with known polar and apolar surface tension components. The phase plot was generated using Equation (3.4) for a solid surface in contact with water ( $\gamma_L = 72.8 \frac{mN}{m}$ ,  $\gamma_L^D = 21.8 \frac{mN}{m}$ ,  $\gamma_L^P = 51 \text{ mN/m}$ ). The phase diagram demonstrates that the five membranes are in the partial wetting region. Among them, NF90 and XLE are close to the non-wetting region and thus show greater fouling propensity compared to BW30. **Figure 3.10b** displays the wettability profile, also known as the wettability envelope, of the membranes. The wetting envelope provides the complete wettability condition ( $\theta_W = 0^\circ$ ) of the membrane for an arbitrary probe liquid with known polar and apolar interfacial tension components. The area enclosed by the axes and the individual curve indicates the complete wetting of the liquid over that particular membrane. The outside region indicates a wetting contact angle greater than  $0^\circ$ . Therefore, a surface having a higher enclosed area shows better wettability toward the contact liquid. Among the membranes, NF90 and XLE had the lowest wettability envelope and thus showed greater fouling propensity. The phase diagram and wettability envelope can provide useful guidelines for the fabrication of membrane with tuned surface wettability and antifouling propensity for the particular applications of interest.

## 3.2 Determination of surface potential

Surface potential at the solid-liquid interfacial layer has emerged as an important parameter to quantify in numerous surface and interface phenomena such as adhesion, wetting, coating, colloidal stability, and particle separation process[178–183]. Experimental techniques to determine the surface charge and zeta potential have been explored for more than 60 years[134,184–186]. Surface charge properties at the solid-liquid interfaces are conventionally measured by streaming potential techniques. However, zeta potential obtained from the streaming potential technique is not equal to the surface potential at the solid-liquid interface and this method can be sensitive to specific ion adsorption [187–189]. Contact angle titration is an alternative approach through which one can access the surface charge and potential information at different pH [21,36,190–192]. To date, the contact angle titration has been widely applied to determine the surface charge density, surface isoelectric point, specific ion adsorption, functional group dissociation, and degree of ionization[18,21,193,32,36,143,179,189–192]. Hurwitz et al.[21] demonstrated a unified approach to quantify the negative charge distribution at the interfacial layer, and acid-base properties of the hydrophilic surfaces using contact angle titration method. The observed surface potentials were in qualitative agreement with the data obtained from their streaming potential measurements. However, more comprehensive clarification still requires regarding the surface isoelectric point for both hydrophilic and hydrophobic samples which leads us to determine the transition between the positive and negative surface charge distribution. Isoelectric point (IEP) or point of zero charge (PZC) can be defined at that stage of the pH titration experiments where surface charge density is considered as zero due to the existence of a similar number of negative and positive charges[187].

An ionizable solid surface acquires a certain amount of charge due to the adsorption or desorption of a certain number of protons or electrons because of the contact with an aqueous electrolyte solution. For a small drop size ( $\sim 2 \mu\text{l}$ ), two different information can be obtained based on the type of electrolyte

solution[32,143]. Buffered solution provides the extent of ionization ( $\alpha$ ), and unbuffered one provides the information on the available surface functional groups to interact with the hydroxide ions available in the electrolyte drop. Contact angle titration experiments often provide the information of IEP where a maximum magnitude of contact angle can be observed[191–193]. However, each of the previous works either focused on hydrophobic[194,195] or hydrophilic[21,190] surfaces. The contact angle measurement techniques were also varied, e.g., either sessile drop or captive bubble measurement techniques. However, for a complete understanding of the contact angle titration experiments, and proper comparison between the results it is required to perform similar measurement techniques. The outcome of these contact angle titration experiments over the same sample might be disparate if different measurement method has been followed [196]. Furthermore, the characteristics of the solution, and the surface are also essential since the experimental results highly depend on the drop shape (drop-solid interfacial contact area), surface roughness, and solution ionic strength. The ionic strength of the electrolyte solution should be in the order of  $\sim 50$  mM to avoid the effects of the electric double layer [32,190]. It is worth noting that even though all the experiments are required to be performed under saturated vapor conditions, it is not possible to completely neglect the effect of evaporation which results in a decrease of the contact angle despite the repeatability of the experimental data[32,197,198]. To circumvent this problem, under-liquid (non-polar oil) contact angle titration can be an alternative. One can argue are there any significant variation between the under-liquid and in-air contact angle titration experiment while quantifying the surface potential?

In this section, an attempt has been made to establish the methodology for the quantification of surface potential by contact angle titration technique. The experiments have been performed for three different surfaces hydrophilic ( $\theta_e < 65^\circ$ ), weakly hydrophilic ( $65^\circ < \theta_e < 90^\circ$ ), and weakly hydrophobic ( $\theta_e \approx 90^\circ$ ) cases for in-air and under-liquid conditions. Three different theoretical frameworks have been explored namely Holmes-Farley[32], Lippmann[199], and Gibbs adsorption[189]

equation with appropriate modifications. All the obtained contact angle titration results are also with the zeta potential data using Smoluchowski equation[188]. For all the cases, the observed in-air measurement deviates more than the under-liquid measurements. The results of this study demonstrate that the physicochemical property of the solid-liquid interface can be meticulously estimated using a single analytical parameter, *e.g.*, contact angle measurement.

**Figure 3.11** shows a conceptual illustration of the contact angle titration technique in air and under-oil condition. The contact angle of the electrolyte drop depends on the ionization state of the surface functional groups. Due to the ionic concentration of the electrolyte solution, and the presence of surface functional groups, an electric double layer (EDL) will be formed. The EDL consists of two different planes namely stern plane, and shear plane [188,189]. The potential at the stern plane can be considered as surface potential, and at the shear plane can be termed as zeta potential. Here, we demonstrate that under-oil contact angle titration can provide better accuracy to characterize the surface potential which can be comparable with other available measurement techniques.

### **3.2.1 Materials and methods**

The surface wettability of the samples (microscopic glass slide, Fisher Scientific, Canada, Polyamide-BW30, RO, FILMTEC™, USA, and Polypropylene film, Anton Paar, GmbH, Austria) was evaluated by measuring the equilibrium contact angles using a drop shape analyzer (DSA 100E, KRÜSS GmbH, Germany). A distortion-free glass cuvette (SC-02, KRÜSS GmbH, Germany) was used to generate a saturated environment. The cuvette was partially prefilled with DI water (for in-air measurement) with placing the sample inside on a holder. This cuvette was then sealed with Parafilm to create a saturated environment [81]. We further kept the cuvette sealed no less than 24 hours and assumed that a saturated environment was obtained. For under-oil measurement, the cuvette was filled with oil (n-Hexadecane, 99% purity, Fisher Scientific, Canada) instead of the electrolyte solution. For each

experiment, a  $\sim 2 \pm 0.1$   $\mu\text{L}$  droplet was placed on the surface, and the equilibrium contact angle was recorded after 1 m to ensure the stability and equilibrium of the liquid droplet over the sample surface. All the presented experimental data are repeatable as every data point corresponds to an average of more than three different events within a 10% deviation. We measured the surface tension of the electrolyte drops using pendant drop techniques [200]. The concentration of buffered and buffered solutions were 50 mM and the preparation procedure can be found elsewhere[18,21,32]. We performed the streaming potential measurements using an Electro-kinetic Analyzer (SurPASS<sup>TM</sup> 3, Anton-Paar KG, Austria). The solution pH was adjusted by the addition of NaOH or HCl to the DI water (Milli-Q Synthesis, Millipore, Germany) or NaCl solutions. We measured the surface roughness using the atomic force microscopy technique (AFM). The surface morphology of the samples was evaluated using the atomic force microscopy (AFM) technique (BRUKER Dimension Edge<sup>TM</sup>, USA). The AFM measurements were carried out in tapping mode in air with a nominal resonant frequency and spring constant of 300 Hz and 42 N/m, respectively (refer to section B 1.1.1 of the Appendix).

We initially quantify the surface charge density ( $\sigma$ ) at different pH from all the three theoretical approaches explored in this study. The surface potential ( $\psi_s$ ) can then be calculated from the Grahame equation as follows[187,188]

$$\sigma = 0.117\sqrt{c} \sinh \frac{\psi_s}{51.4} \quad (3.9)$$

where  $c$  is the concentration of the electrolyte solution,  $\psi_s$  is the surface potential at the stern plane of the diffuse double layer.

Surface functional groups can undergo ionization or dissociation based on pH of the solution. The samples considered in this study contain different types of functional groups. For example, glass contains silanol ( $-\text{SiOH}$ ) groups, and the polyamide membrane sample mostly contains free carboxylic acid groups ( $\text{R-COOH}$ ) with a mixture of amides and free amines ( $-\text{NH}_2$ ). In contrast with these two

samples, the polypropylene sample mostly contains nonionizing surface groups ( $-\text{CH}_2\text{CH}-$ ). Holmes-Farley et al.'s [32] and Hurwitz et al.'s [21] unified approach can be utilized to obtain the correlation between surface ionization states and surface charge density from the contact angle titration experiment.

$$\sigma = \sigma_{max}\alpha = \left( \frac{-e[R - O^-]}{r} \right) \left( \frac{\cos \theta_{pH} - \cos \theta_{pH1}}{\cos \theta_{pH13} - \cos \theta_{pH1}} \right) \quad (3.10)$$

where  $\sigma$  is the surface charge density,  $\alpha$  is the extent of ionization,  $e$  is the electronic charge,  $[R - O^-]$  is the concentrations (per unit area) of surface acidic groups,  $r$  is the Wenzel roughness ratio, and  $\theta$  is the contact angle at different pH. The subscript 'max' denotes as 'maximum.' It is worth noting that this method utilizes both the buffered and unbuffered contact angle titration plots. The buffered solution can provide the information of the surface ionization state ( $\alpha$ ), and the unbuffered one provides the information on the concentration of the surface acidic groups. The exact concentration of the acidic groups can be calculated from the solid-liquid interfacial contact area.

We assume that the liquid interfacial tension and solid surface tension do not alter due to the variation of pH. This can further allow us to apply combined Gibbs adsorption[189] and Young equation[46] as follows

$$\sigma = \frac{d(\cos \theta_{pH})}{d(pH)} \frac{F\gamma_{DM}}{2.303 RT} \quad (3.11)$$

where  $F$  is the Faraday constant ( $96500 \text{ C}\cdot\text{mol}^{-1}$ ),  $R$  is the molar gas constant,  $T$  is the system temperature, and  $\gamma_{DM}$  is the interfacial tension between the drop and the surrounding medium. It is worth noting that for this study we experimentally obtained the term  $\frac{d(\cos \theta_{pH})}{d(pH)}$  directly from the contact angle titration experiments of the buffered solutions (**Figure B 1.2** of the Appendix).



Furthermore, we can employ the Young-Lippmann[46,199] equation to quantify the surface potential as follows

$$\gamma_{DM}(\cos \theta_{pH} - \cos \theta_{IEP}) = 0.006\sqrt{c} \left( \cosh \frac{\psi_s}{51.4} - 1 \right) \quad (3.12)$$

where  $\theta_{IEP}$  is the maximum contact angle observed during the unbuffered contact angle titration experiments.

We can also add that for all the above theories, the surface charge is considered positive or negative based on the surface ionization state due to the adsorption of protons or electrons from the electrolyte solution. The IEP leads us to determine this process where one can observe the maximum contact angle. Conversely, the streaming potential technique provides us the information on the surface potential at the shear plane of the EDL which is known as surface zeta potential. This can be obtained using Smoluchowski equation as follows[188]

$$\zeta = \frac{\Delta U_{str}}{\Delta P} \frac{\eta \kappa}{\epsilon \epsilon_0} \quad (3.13)$$

where  $\zeta$  is the surface (zeta) potential at the shear plane,  $\frac{\Delta U_{str}}{\Delta P}$  is the streaming potential coefficient due to the applied pressure in the cell,  $\eta$  is the dynamic viscosity of the electrolyte solution,  $\epsilon \epsilon_0$  is the dielectric constant, and  $\kappa$  is the electrical conductivity of the solution.

### 3.2.2 Results and discussions

Surface potential ( $\psi_s$ ) at the stern plane and zeta potential at the shear plane are not exactly the same in magnitude, but they can be correlated. **Figure 3.12** depicts that the magnitude of the surface potential varies based on different calculations. We

observe that the Holmes-Farley equation provides better approximation while comparing it with the Smoluchowski equation (~30% variation). Young-Lippmann equation deviates more than 80% for all the cases. It is worth noting that Holmes-Farley (Eq. 3.10) and Gibbs equations (Eq. 3.11) are based on the concentration of the available surface functional groups to interact with the electrolyte drop. We calculate the surface charge density considering the exact solid-liquid interfacial contact area in case of Holmes-Farley equation, while in case of the Gibbs equation, we determine this from a sigmoidal fit approximation fitting of the  $\cos \theta_{pH}$  vs.  $pH$  curve (refer to section B1.1.2 of the Appendix). This curve leads us to determine the approximate surface ionization state ( $\alpha$ ), *i.e.*, we can write  $\frac{d(\alpha)}{d(pH)} \approx A \frac{d(\cos \theta_{pH})}{d(pH)}$ , where  $A = \frac{1}{\cos \theta_{pH13} - \cos \theta_{pH1}}$ . Conversely, Young-Lippmann equation determines the surface charge density based on the maximum contact angle observed at the surface IEP. Hence, the obtained surface potential deviates based on the approximation of the derived parameters. Gibbs equation and Young-Lippmann equation deviates even more in the case of BW 30 polyamide samples (**Figure 3.12b**) which contains complex surface chemistry than the glass surface (**Figure 3.12a**). However, we observe that under-oil contact angle titration experiments provide better accuracy than the in-air measurements. A likely explanation can be the effects of drop evaporation at the initial stage of the in-air, *i.e.*, saturated vapor experiment.

We observe nearly constant drop-medium interfacial tension at different pH. The obtained interfacial tension was 72.3 mN  $\pm$ 0.5 mN in air, and 50 mN  $\pm$ 0.3 in hexadecane medium. The streaming potential measurement of the polypropylene film showed that (**Figure 3.13c**) the surface zeta potential varied from 9 mV to -58 mV with an isoelectric point at pH 3.5. However, the contact angle titration experiments of the polypropylene film did not show any significant variation at different pH in both cases, *i.e.*, in-air, and under-oil measurements (refer to supplementary information). Interestingly, we obtain a slightly higher contact angle at pH ~3 which may correspond to the surface isoelectric point. Thus, the contact

angle titration experiment cannot provide surface potential information ionizing surface groups are absent.

The contact angle variation due to pH is shown in **Figure 3.13** for in-air and under-oil measurements. We observe similar types of pH dependency over contact angles though there are significant variations in magnitude. The contact angle generally decreases due to the evaporation effects [197,198]. Even though the saturated condition has been maintained, still a certain decrease is inevitable which can be demonstrated from the previous contact angle titration experiments[32,190]. Moreover, under-oil experiments are performed based on the assumption that the electrolyte drop completely removes the surrounding oil from the solid surfaces which might not be strictly maintained. These can be the likely explanation of observed higher under-oil contact angle. Contact angle experiments of the unbuffered solutions show that the breakpoint of the curves is at pH  $\sim 7.5$ . This indicates that at this point the number of surface acidic functional groups are equal to the number of solution hydroxide ions. We did not observe any significant variation for the hydrophobic polypropylene samples (**Figure 3.13c**) for both in-air and under-oil measurements. Interestingly, we observed a maximum contact angle at  $\sim$ pH 4 for both cases which can be identified as IEP. The streaming potential measurement also indicates a similar IEP ( $\sim$  pH 3.5). We observe a large variation of zeta potential from the streaming potential measurements ranging from 10 mV to -60 mV. This may be attributed to the adsorption and accumulation of higher hydroxide ions ( $\text{OH}^-$ ) over the surface during the streaming potential measurements.

Similar cases for other hydrophobic material (e.g., Teflon) was observed in previous literature [194,195]. These observations support that we can only obtain the IEP for the hydrophobic cases or surfaces having lower reactivity with water. Relation between wettability and surface charge distribution at different pH of the hydrophobic surfaces is still a disputable topic in recent years [194,195,201,202]. It is worth noting that different analytical techniques give information on different layers of thickness of the solid surface. Sometimes surface functional groups remain

such layer of thickness that no considerable effects over wetting has been observed, and thus inaccessible to reagents in the solution [18]. The portion of the solid where these types of interactions are observed can be termed as ‘sub- $\theta$ ’ interphase. This interfacial layer is less well-defined compared to those layers associated with the available analytical techniques. Thus, much caution should be undertaken while comparing the similar parameters obtained from different analytical techniques.

### 3.3 Summary

The impact of surface nanoscale physical heterogeneity on the wettability of polymeric membranes is still elusive. Conventional wettability analysis includes quantifying the membrane surface roughness using AFM followed by measuring the apparent equilibrium contact angle of DI water over the membrane surface. Here, a novel experimental approach is presented, solely based on contact angle analysis, to elucidate the impact of surface heterogeneity on the wettability of polymeric membranes. The proposed approach involves the evaluation of equilibrium and advancing contact angles of at least three non-polar liquids over the membrane surface. Using this information, the wettability parameters including the surface roughness-ratio, frictional pinning force, and the dispersive surface tension component of the polymeric membranes were successfully quantified. The comparison with the conventional approach showed that there are 10% to 20% discrepancies between the AFM-based and contact angle-based wettability parameters. The results revealed that the AFM measurements strongly depend on the size of the scanned area, particularly for samples with large surface heterogeneity. Furthermore, the water flux decline due to colloidal fouling was found to be in good agreement with the results of our proposed model. This study can provide new insights into developing advanced membrane materials with desired surface wettability and antifouling property.

This chapter have further demonstrated that surface potential can be quantitatively determined by under-liquid wettability measurements without any

adjusting parameters. This quantification technique is exemplified using three different surfaces containing different surface chemistry, and obtained comparable results considering other analytical techniques, e.g., streaming potential. The experimental results reveal that surfaces containing reactive functional groups are excellent candidates for these types of analyses. The under-oil sessile drop contact angle titration experiments provide the first direct measurement of surface potential with better accuracy than in-air experimentation. This in turn discards the experimental complexity of the captive bubble as well as saturated vapor condition measurements. This study sheds light on the nature of surface specific ion adsorption and its subsequent effects on wettability related parameters such as adhesion, and surface tension.

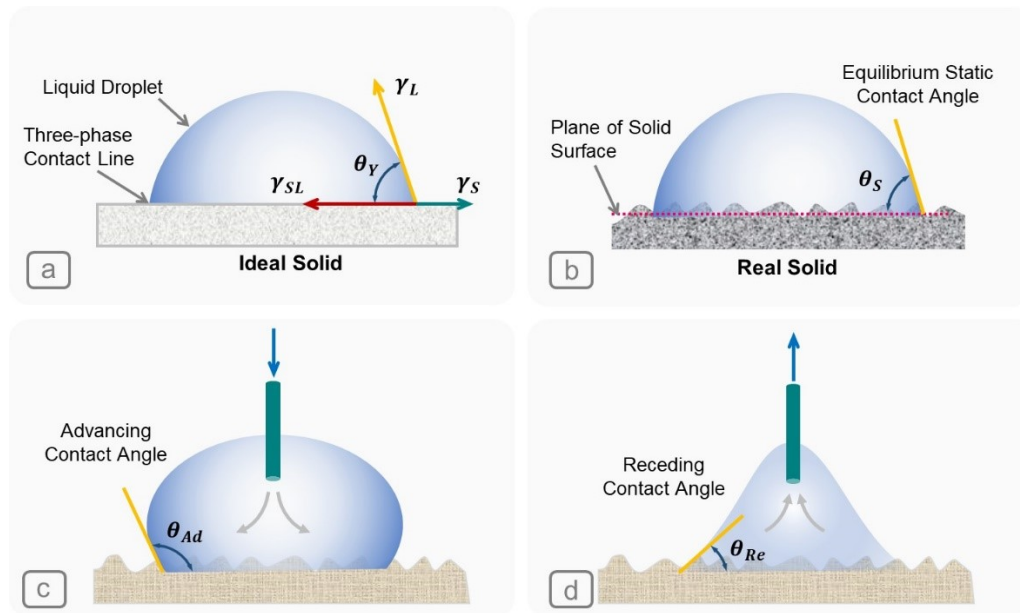


Figure 3.1: Illustration of (a) a sessile droplet over a smooth and chemically homogeneous (ideal) solid surface.  $\theta_Y$  is the equilibrium contact angle based on Young's equation; (b) equilibrium static contact angle ( $\theta_S$ ) of a liquid droplet over a real surface with physical and chemical heterogeneity; (c) advancing contact angle of liquid droplet while spreading over a real surface; and (d) receding contact angle of a liquid droplet while retreating from a real surface.

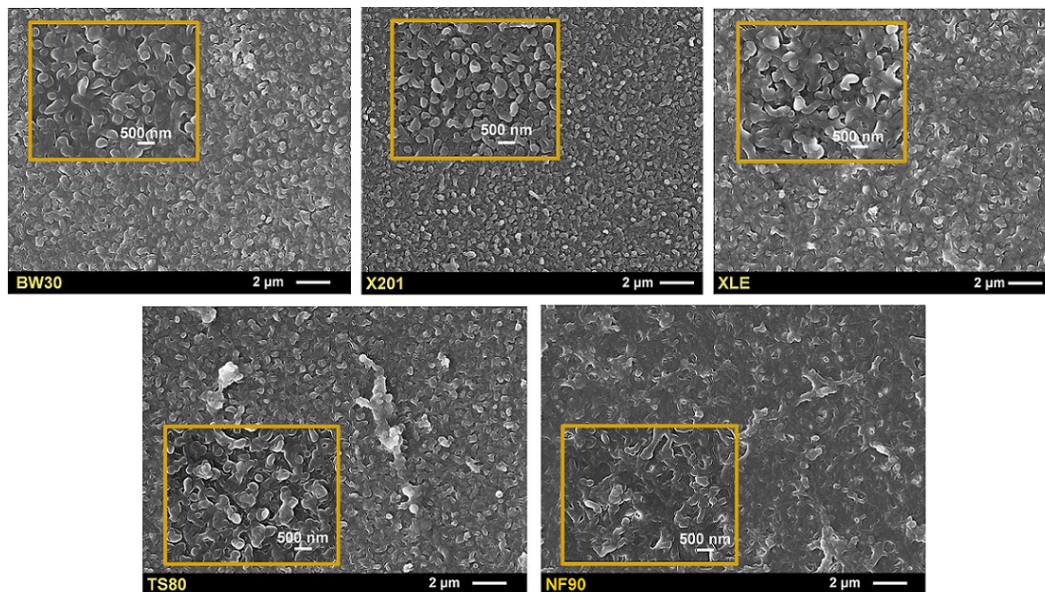


Figure 3.2: FESEM images of (a) BW30, (b) X201, (c) XLE, (d) TS 80 and (e) NF90. All the membranes have a polyamide selective layer with a ridge-and-valley structure. The BW30, XLE, and X201 exhibit conservatively a more uniform surface morphology compared to the NF90 and TS80 membranes.

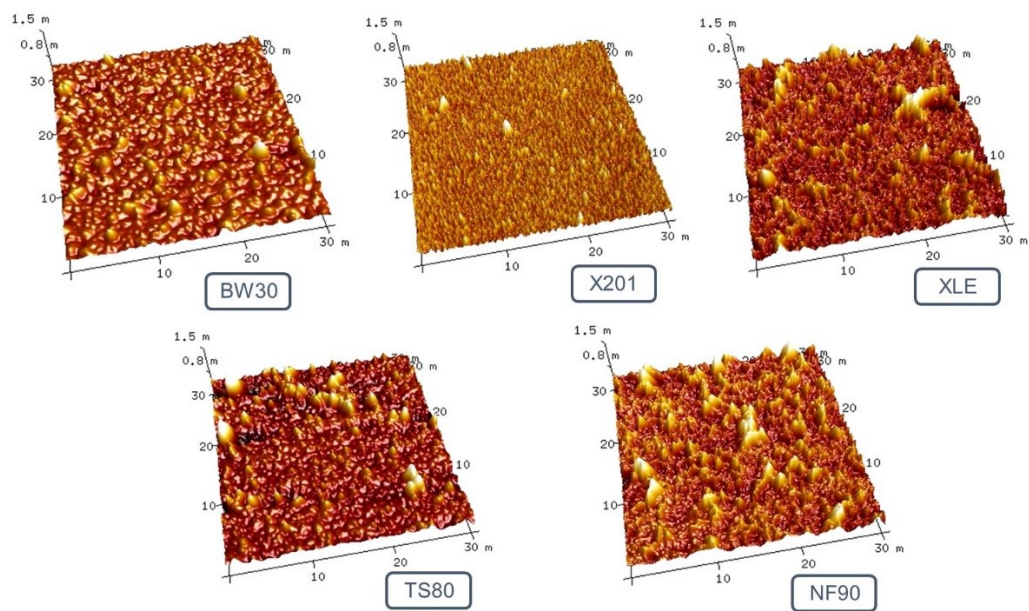


Figure 3.3: AFM surface topography of the polymeric membranes. The horizontal axis represents the scan size (30  $\mu\text{m}$ ), and the vertical scale represents the feature height ( $\mu\text{m}$ ).



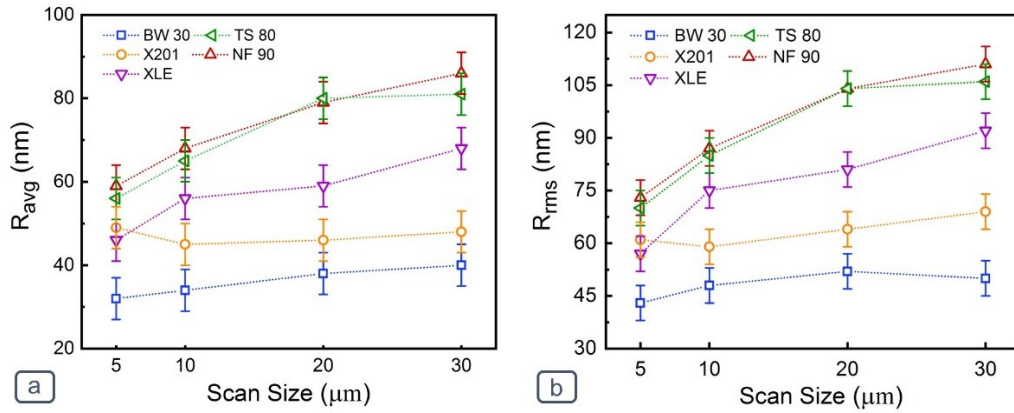


Figure 3.4: Variation of (a) average surface roughness ( $R_{avg}$ ) and (b) RMS roughness ( $R_{rms}$ ) with scan size. The roughness of BW30 and X201 varied slightly at different scan sizes. In contrast, a higher magnitude of surface roughness was quantified for XLE, TS80, and NF90 at larger scan sizes.

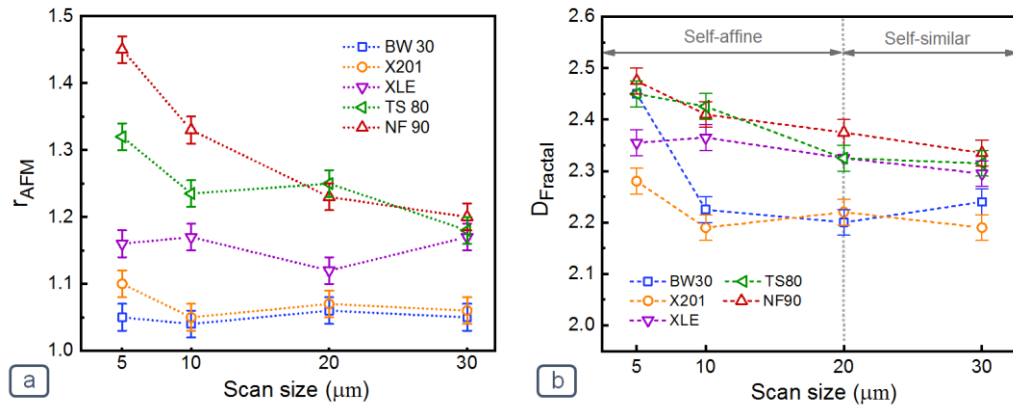


Figure 3.5: (a) Variation of the roughness-ratio obtained by AFM at different scan sizes. The roughness-ratio decreased as the scan size expanded; (b) Variation of fractal dimension ( $D_{\text{Fractal}}$ ) exponents at different scan sizes. The fractal dimension of the membranes varied up to the scan size of  $\sim 20 \mu\text{m}$ , and then remains steady higher scanned area.

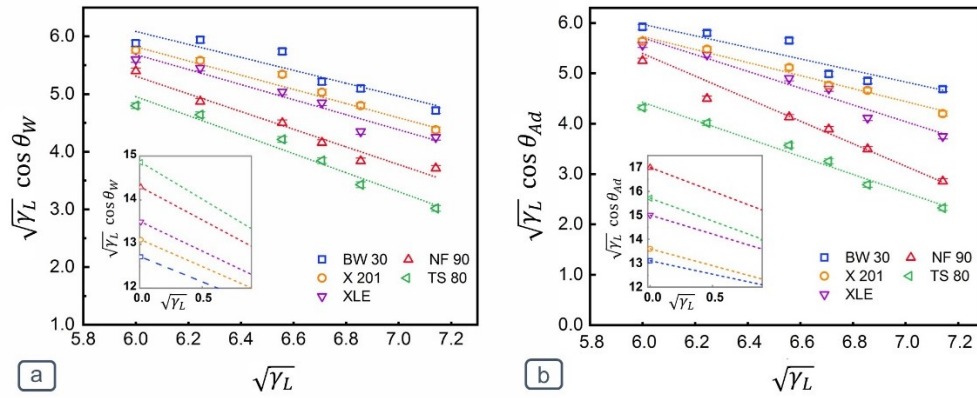


Figure 3.6: Surface wettability plots of polymeric membranes. Linear correlation of  $\sqrt{\gamma_L} \cos \theta$  versus  $\sqrt{\gamma_L}$  is observed for both equilibrium and advancing contact angles. The slope and y-axis intersection in panel (a) provide the  $r_{CA_W}$  and  $\gamma_S^D$ , respectively. Similarly, the slope of the linear fit and the intersection with the y-axis in panel (b) gives the  $r_{CA_{Ad}}$  and the  $F/\gamma_L$  of the polymeric surface.

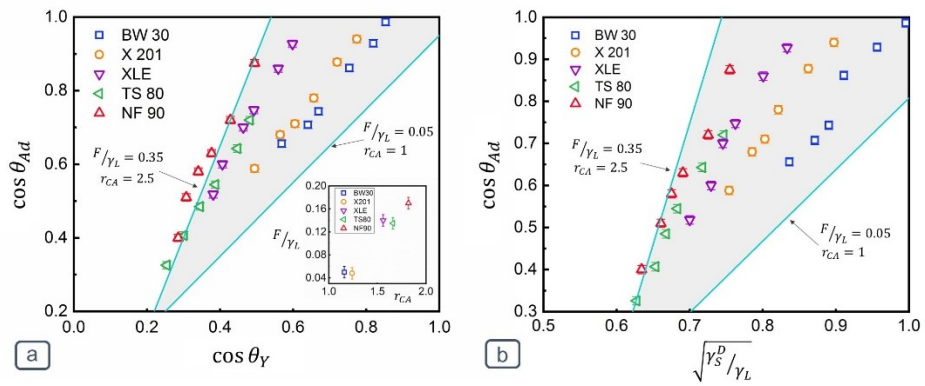


Figure 3.7: (a) validation of experimentally extracted  $r_{CAAd}$  and  $F/\gamma_L$  with theoretical relation to predict the advancing contact angle ( $\cos \theta_{Ad}$ ). All the calculated contact angles were in good agreement with the theoretical prediction (grey map); (b) validation of experimentally extracted  $\gamma_S^D$  with theoretical relation to predict the advancing contact angle ( $\cos \theta_{Ad}$ ). The calculated contact angles were within the range (grey map) predicted by theoretical relation.

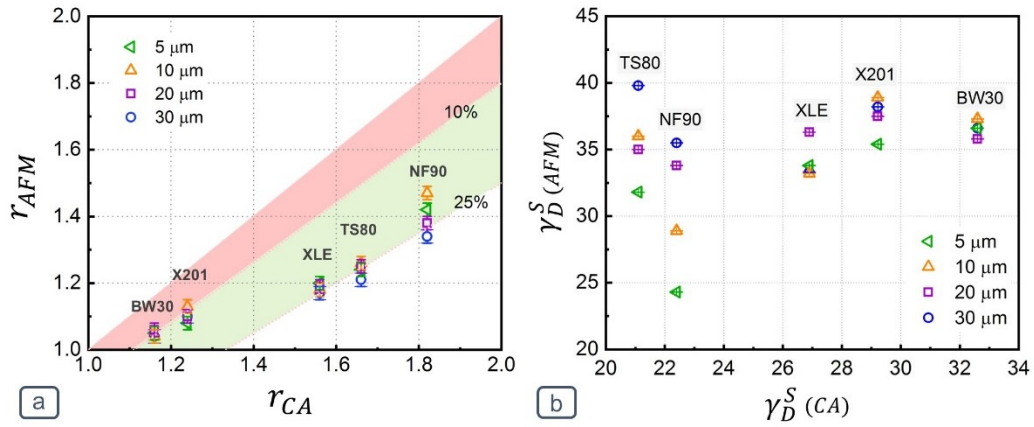


Figure 3.8: (a) The comparison of the roughness-ratio obtained by AFM and contact angle analysis. The results reveal the presence of 10% to 25% discrepancies between the roughness-ratio predicted by AFM and the wettability analysis. (b) Variation of dispersive surface tension components due to the variation of roughness factor ( $r_{AFM}$ ) obtained at different scan sizes from the AFM analysis.

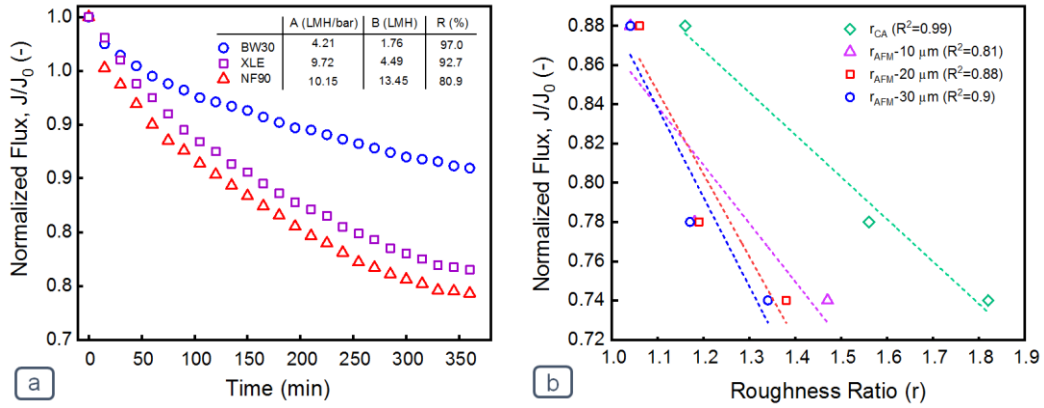


Figure 3.9: (a) Normalized flux decline versus time for three different membranes: BW30, XLE, and NF90. We observe a strong dependency of flux decline with respect to surface morphology; (b) Correlation between the normalized flux ( $J/J_0$  after 6 hr filtration) and surface roughness-ratio ( $r$ ). Correlation between the roughness-ratio of the membranes, evaluated by conventional AFM test and the proposed CA-based methods.

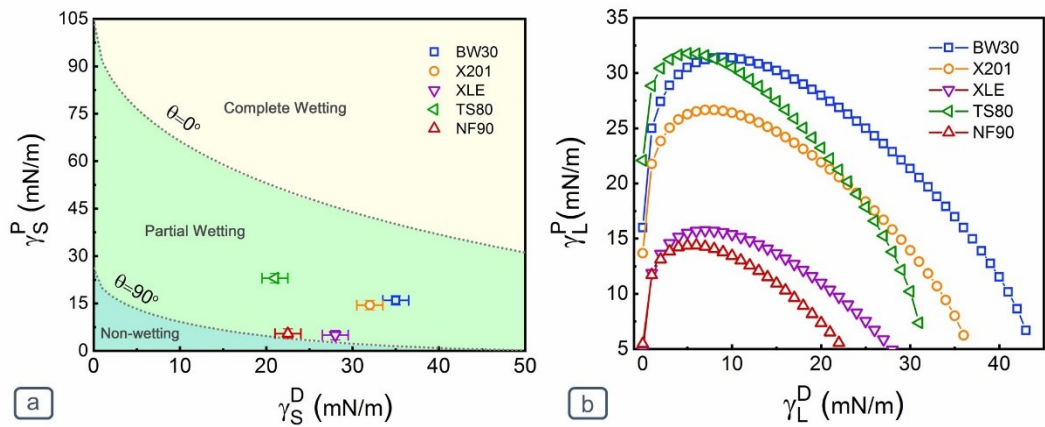


Figure 3.10: (a) Phase diagram of the wettability of the membrane surface with water. Among the tested membranes, NF90 and XLE membrane were close to the non-wetting region while the BW30, X201, and TS80 were in the partial wetting region. (b) Wettability envelope of five different membranes. BW 30 shows a larger wettability envelope which indicates a better wettability profile toward contact liquid. NF90 shows the lowest wettability envelope which agrees with its higher fouling propensity.

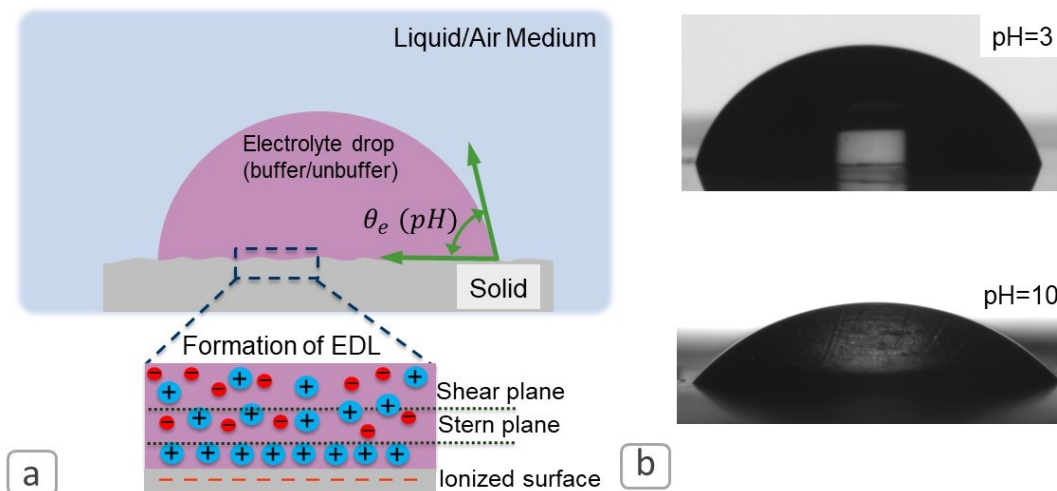


Figure 3.11: Schematic diagram and experimental methodology. (a) Conceptual demonstration of adsorbed cation and electric double layer (EDL) formation due to the surface functional groups containing the negative charge. Due to EDL formation, two different planes can be identified namely stern plane, and shear plane. The thickness of the electric double layer (also known as inverse Debye length) is solely the function of the solution, more specifically ionic concentration of the solution. For contact angle titration experiments, this layer should be controlled in such a way so that ionic strength effects over the contact angle ( $\theta_e$ ) and liquid interfacial tension ( $\gamma_L$ ) is insignificant. (b) Experimental evidence of the under-oil (Hexadecane) pH dependency over contact angle for a polyamide sample.



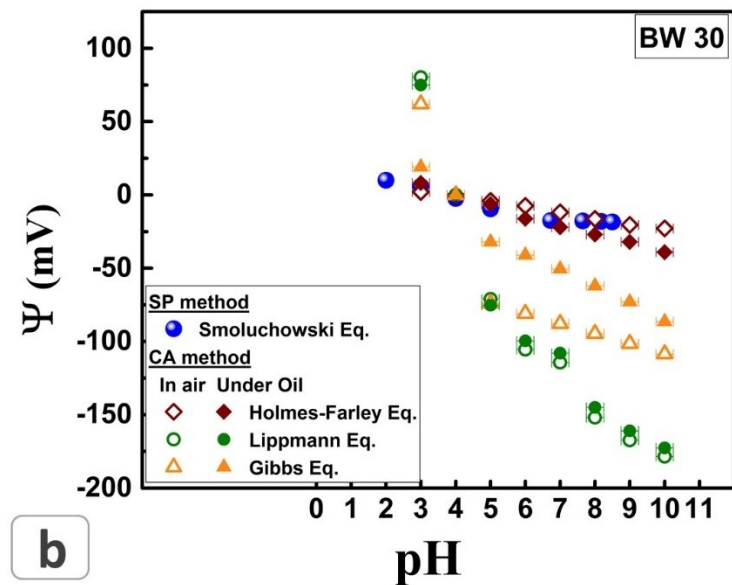
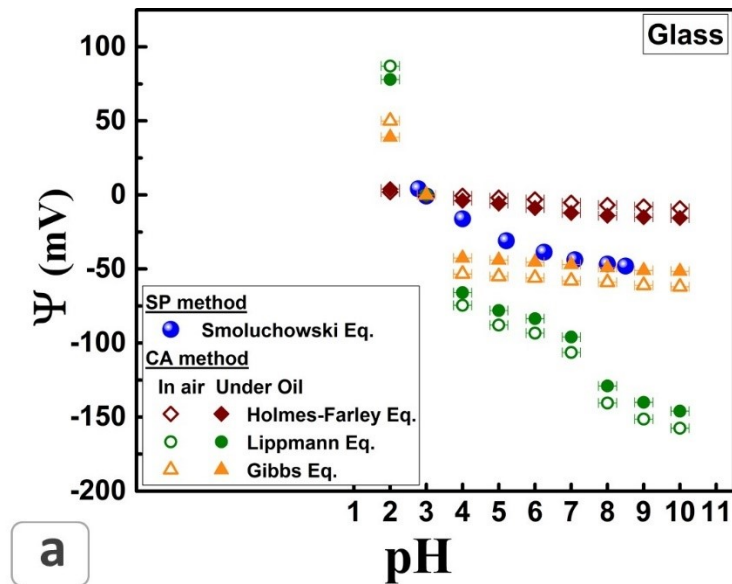


Figure 3.12 Quantification of surface potential and comparison between the streaming potential and wettability method for (a) glass, and (b) BW 30. We observe reasonable accuracy for Holmes-Farley [32] and Gibbs equation [189]. Young-Lippmann equation[46,199] deviates more than 80% for surfaces having complex surface chemistry such as polyamide BW 30 samples. Under-oil contact angle titration experiments exhibit better accuracy in comparison with the in-air measurement.

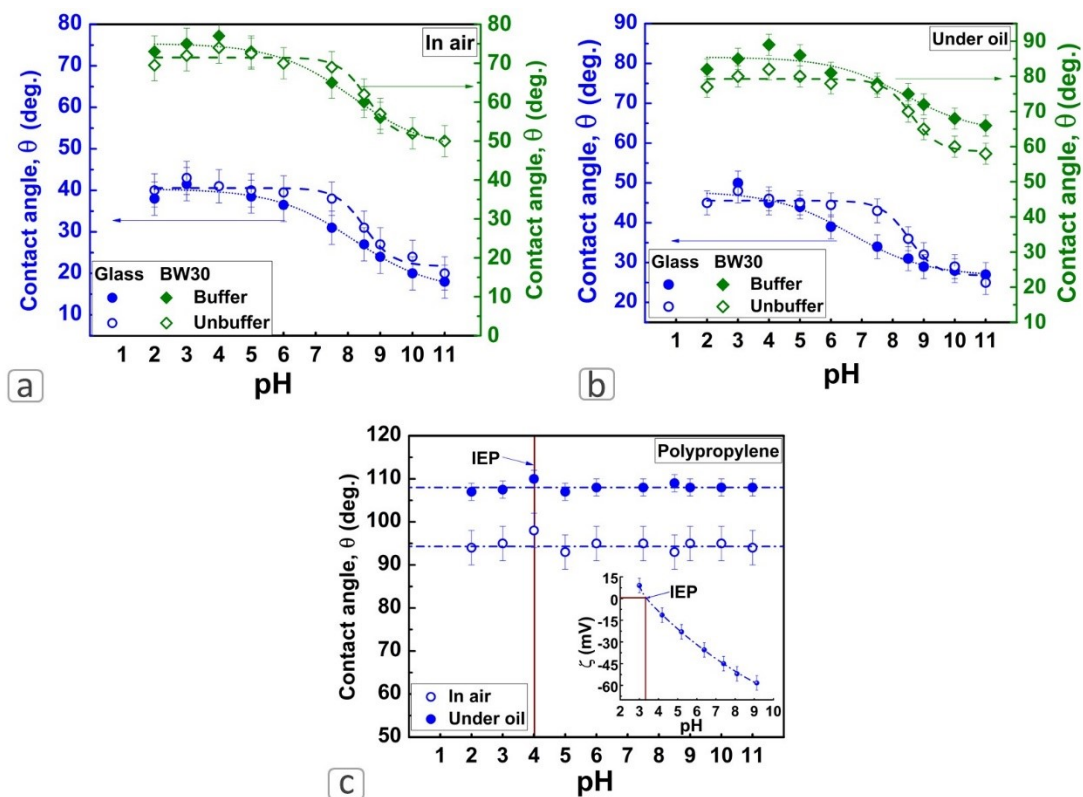


Figure 3.13 Wettability of buffered and unbuffered solutions for (a) in-air, and (b) under-oil measurement. In-air experiments exhibit a lower contact angle for both Glass, and BW 30 samples. A likely explanation is the evaporation effects or a thin layer of oil layer over the solid samples. However, despite the change of the surrounding medium, we observe similar types of pH dependency over the contact angle for all the cases. (c) Wettability of buffered solution for hydrophobic polypropylene sample. We did not observe any significant variation for any cases; however, we observe a maximum contact angle at pH ~4. Zeta potential results from the inset image leads us to correlate this point to the surface IEP (pH ~3.5).

Table 3.1: Properties of the probe liquids

Liquid	Chemical formula	Density (g/mL)	Molecular weight (g/mol)	Surface tension (mN/m)	Measured surface tension (mN/m)	Viscosity (mPa. s)	Solubility in water (g/L)	Boiling point (°C)
1,4-Dibromobutane	C <sub>4</sub> H <sub>8</sub> Br <sub>2</sub>	1.81	215.92	40.86	38.0±0.5	1.91	insoluble	63
1,2-Dibromoethane	C <sub>2</sub> H <sub>4</sub> Br <sub>2</sub>	2.20	187.90	39.79	37.0±0.5	1.78	4.04	131
Diiodomethane	CH <sub>2</sub> I <sub>2</sub>	3.32	267.84	50.80	50.0±0.5	2.77	1.24	181
1,5-Diiodopentane	C <sub>5</sub> H <sub>10</sub> I <sub>2</sub>	2.2	323.94	45.54	36.0±0.5	7.92	insoluble	128
1,4-Diiodobutane	C <sub>4</sub> H <sub>8</sub> I <sub>2</sub>	2.35	309.92	47.00	44.0±0.5	6.46	insoluble	108
1,3-Diiodopropane	C <sub>3</sub> H <sub>6</sub> I <sub>2</sub>	2.58	295.89	47.87	45.5±0.5	5.89	insoluble	111
1,6-diiodohexane	C <sub>6</sub> H <sub>12</sub> I <sub>2</sub>	2.05	337.97	44.49	39.5±0.5	6.76	insoluble	123
1,1,2,2-Tetrabromoethane	C <sub>2</sub> H <sub>2</sub> Br <sub>4</sub>	2.96	345.66	48.71	46.5±0.5	9.16	0.63	119

## **Chapter 4 ‡**

# **New insights into the predication of adaptive wetting of a solid surface under a liquid medium**

---

‡The material of this chapter has been under revision as Md Farhad Ismail, Behnam Khorshidi, and Mohtada Sadrzadeh, New insights into the predication of adaptive wetting of a solid surface under a liquid medium. *Journal of Colloid and Interface Science*, 2020.

## 4.1 Introduction

The interfacial properties, such as wettability and surface tension of a surface, can control many natural and industrial processes which involve coating, adhesion, adsorption, preparation of suspensions and emulsions, flotation, and oil recovery [13,203]. Some of such applications require a good wetting and adhesion between the liquid and the solid surface, whereas some others demand poor adhesion or repellency. The adhesion or repellency is not only limited to the interaction between a single solid and liquid in a dry surrounding system such as air, rather in many cases more than one liquid is involved with the solid surface. Solid wettability towards a liquid in the air can be quantified by the contact angle resulted from the balance of three forces, i.e., the surface tension of solid, liquid, and solid-liquid interface [46]. However, wetting and spreading of a liquid drop (D) over a solid surface (S) under a liquid medium (M) are the consequence of the physiochemical interactions of the two liquids with the surface. However, interfacial interactions between the two liquids themselves must also be accounted for. **Figure 4.1a** illustrates a framework of the under-liquid wetting of a solid surface. The contact angle ( $\theta_{SMD}$ ) is the combined effects of three interfacial tensions: solid-drop ( $\gamma_{SD}$ ), solid-medium ( $\gamma_{SM}$ ), and drop-medium ( $\gamma_{DM}$ ). However, the wetting and spreading scenario in an under-liquid system is more complex than in air medium. For the under-liquid wetting, two different cases can be considered: formation of a thin layer of liquid medium over the solid surface (**Figure 4.1b**), and/or molecular rearrangement of the solid surface (**Figure 4.1c**). Several studies focused on exploring this under-liquid wettability determination utilizing one of these three assumptions, as shown in **Figure 4.1**.

Nevertheless, there are no direct methods to measure the solid surface tension; rather it can be quantified by the interaction of some specific probe liquids with the solid surface. Girifalco-Good [204,205], Fowkes [87,88], Owens-Wendt [90], and van Oss-Chaudhury-Good [40,100] proposed different methods to quantify solid surface tension. The concept underlies all proposed methods includes quantification of the interfacial interactions in terms of various components, such as

dispersive ( $\gamma_s^D$ ), polar ( $\gamma_s^P$ ), electron-acceptor ( $\gamma_s^+$ ), and electron-donor ( $\gamma_s^-$ ) interactions. However, these interpretations are developed based on the contact angle measurements in the air medium. It is more challenging to apply such methods for adaptive surfaces which can change their surface properties based on the external stimuli, e.g., temperature, or the presence of a liquid [76,206–209]. Numerous attempts have been employed to determine the applicability of such techniques in an under-liquid system [210–216]. Bartell and Osterhof [210] first anticipated the wettability of non-polar organic liquids over powdered silica and carbon surfaces immersed in water medium. They employed Young's equation [46] to determine the contact angle and adhesion work between the organic liquid and the solid surface in the water medium. They concluded that in a two-liquid system the solid surfaces had the tendency to interact more with that liquid, which could generate greater work of adhesion. Tamai et al. [211] and Schultz et al. [214] later proposed a new method to determine the under-liquid surface wettability. Both studies used Owens-Wendt equation [90] along with Young's equation to determine the under-liquid surface tension of a solid surface. They reported that solid dispersive surface tension components could vary due to the surrounding medium. However, both studies did not report the polar surface tension components of the solid. To address this issue, El-Shimi et al. [212] later developed a theoretical framework to predict the wettability of polar solid at underwater condition and employed similar theoretical framework as proposed by Tamai et al. [211] and Schultz et al. [214]. Their observed results were in somewhat reasonable agreement only for the non-polar probe liquids. Similar to El-Shimi et al. [212], Schultz et al. [208] also conducted another study considering polar liquid as a surrounding medium. They concluded that surface tension cannot be the intrinsic property of the solid. Binks et al. [215] developed a theoretical framework to determine the contact angle of water drop over polar surfaces under different polar and non-polar oil medium. However, they considered surface tension as the intrinsic property of the material. Their experimental results showed good agreement for a wide range of non-polar oil medium, but they reported more than 30% deviation for the polar oil medium. Under-liquid wettability was

further explored by Jung et al. [117] who investigated the applicability of Wenzel and Cassie-Baxter equation for flat and micro-patterned surfaces. A recent study of Trinavee et al. [216] explored the applicability and modification of Young's and Owens-Wendt equations for a wide range of polar and non-polar oil drops over polar solids. They assumed a thin layer of film over the solid surface (**Figure 4.1b**). They concluded that solid surface wettability is anomalous under-liquid conditions, which requires modifications of current theories with detailed experimentation.

Although extensive research has investigated the under-liquid wettability, no developed theoretical framework can predict the solid-liquid-liquid wettability when all the involved phases exhibit polarity. In this study, we have developed a theoretical framework to determine all the solid surface tension components under-liquid. The proposed theoretical framework considers the influence of the surrounding liquid. We further proposed a new two liquid approach, e.g., one polar and one non-polar liquid to determine the under-liquid solid surface tension components. To validate the outcomes, we compared the predicted results with the experimental ones for various polar and non-polar liquids. Finally, we conducted a parametric study to determine the effects of medium surface tension components on the wettability of any solid. To the best of our knowledge, this is the first study to quantify all the solid surface tension components (dispersive, polar, electron-donor and electron-acceptor) considering the effects of polarity involved in the solid-liquid-liquid wettability conditions.

## 4.2 Theoretical approach

In this section, the theoretical framework for evaluating the underwater wettability of a solid surface is presented. The modeling includes the determination of the surface tension of the solid sample in air and underwater. **Figure 4.2** presents a schematic of the wettability components in different media. It is worth noting that the solid surface tension under a liquid is shown by  $\gamma_{S^*}$  to be distinguished from the solid surface tension measured in air ( $\gamma_S$ ). Due to the formation of a thin layer of

surrounding medium on the solid surface, as well as possible molecular rearrangement at the solid-liquid interface, the surface tension of a solid under a liquid can be different from that in air.

#### 4.2.1 Determination of solid surface tension in the air

When a liquid droplet is placed on a solid surface in air, there will be a balance between the three different interfaces, i.e., solid-air ( $\gamma_{SA}$  or  $\gamma_S$ ), solid-liquid ( $\gamma_{SL}$ ), and liquid-air ( $\gamma_{LA}$  or  $\gamma_L$ ) interfaces (**Figure 4.2a**). These three interfaces come together with an angle at the point of contact which is defined by the well-known Young's equation [46]:

$$\gamma_L \cos \theta_{SAL} = \gamma_S - \gamma_{SL} \quad (4.1)$$

where  $\theta_{SAL}$  is the contact angle between solid-droplet in air medium. To determine the solid surface tension ( $\gamma_S$ ) by Young's equation one needs to obtain the solid-liquid surface tension ( $\gamma_{SL}$ ) [40]. For this, Dupre [85] and Fowkes [40] equations can be utilized. Dupre [85] introduced the concept of free energy of adhesion ( $\Delta G_{SL} = \gamma_{SL} - \gamma_S - \gamma_L$ ) and Fowkes introduced the concept of dispersion ( $\gamma^D$ ) and polar ( $\gamma^P$ ) surface tension components for the solid-liquid interface in air. The generalized Fowkes equation can be written for two different phase  $\alpha$  and  $\beta$  as:

$$\gamma_{\alpha\beta} = \gamma_\alpha + \gamma_\beta - 2 \left( \sqrt{\gamma_\alpha^D \gamma_\beta^D} + \sqrt{\gamma_\alpha^P \gamma_\beta^P} \right) \quad (4.2)$$

The  $\alpha$ - $\beta$  pair can be solid-liquid ( $\gamma_{SL}$ ), liquid-air ( $\gamma_L$ ), and solid-air ( $\gamma_S$ ). For these cases, Fowkes equation can be re-written as follows:

$$\gamma_{SL} = \gamma_S + \gamma_L - 2 \left( \sqrt{\gamma_L^D \gamma_S^D} + \sqrt{\gamma_L^P \gamma_S^P} \right) \quad (4.3)$$



Eq. 4.2 is also known as Owens-Wendt relation [40]. It is worth noting that the total surface tension of solid ( $\gamma_S$ ) is the sum of the surface tension components, i.e.,  $\gamma = \gamma^P + \gamma^D$ . The combination of all these Equations results in a relation between the surface tension components of the solid and liquid as:

$$\gamma_L(1 + \cos \theta_{SAL}) = 2 \left( \sqrt{\gamma_L^D \gamma_S^D} + \sqrt{\gamma_L^P \gamma_S^P} \right) \quad (4.4)$$

There are two unknown solid surface tension components (i.e.,  $\gamma_S^D$  and  $\gamma_S^P$ ) in the above equation, and thus at least two probe liquids are required to determine these parameters. In the present work, we used water and diiodomethane are used as polar and non-polar liquids, respectively, to determine the unknown surface tension components of the solid samples.

## 4.2.2 Determination of solid surface tension under-liquid

Compared to wettability analysis in air, the under-liquid wettability analysis involves additional interactions between the probe liquid and the medium, as well as the medium and the solid surface. When a liquid droplet is placed on a solid surface in a liquid medium rather than air (**Figure 4.2b**), Young's equation can be modified as:

$$\gamma_{DM} \cos \theta_{S^*MD} = \gamma_{S^*M} - \gamma_{S^*D} \quad (4.5)$$

where  $\theta_{S^*MD}$  is the contact angle between solid-droplet in liquid medium,  $\gamma_{S^*M}$ ,  $\gamma_{S^*D}$ , and  $\gamma_{DM}$  are the interfacial tension of solid-medium, solid-droplet, and droplet-medium, respectively. The Dupre equation for the solid-liquid-liquid interface can be modified as follows.  $\Delta G_{S^*MD} = \gamma_{S^*D} - \gamma_{S^*M} - \gamma_{DM}$ . Thus, for a typical wettability case of a solid surface underwater medium (W) with an oil droplet (O), the combination of Eqs. 4.2 and 4.5 can be written as follows:

$$\begin{aligned}
& \gamma_{ow}(1 + \cos \theta_{s^*wo}) \\
& = 2\gamma_w \\
& + 2 \left( \sqrt{\gamma_{s^*o}^D \gamma_o^D} + \sqrt{\gamma_{s^*o}^P \gamma_o^P} - \sqrt{\gamma_{s^*w}^D \gamma_w^D} - \sqrt{\gamma_{s^*w}^P \gamma_w^P} - \sqrt{\gamma_o^D \gamma_w^D} - \sqrt{\gamma_o^P \gamma_w^P} \right) \quad (4.6)
\end{aligned}$$

Eq. 4.6 considers all the possible interactions for the wettability analysis of a solid underwater. Similar to Eq. 4.3, there are two unknown polar and dispersive surface tension components (i.e.,  $\gamma_{s^*}^P$  and  $\gamma_{s^*}^D$ ), which can be obtained by solving two equations. In the present work, we determined the underwater surface tension of the solid samples using two probe liquids and validated the predictions with different pairs of polar and non-polar liquids. A list of the probe liquids with their main properties is presented in **Table 4.1**.

Eq. 4.6 can be further expanded to provide more details on the polar surface tension component. According to Van Oss et al. [100], the polar surface tension component (also can be termed as an acid-base component) can be presented in terms of electron-acceptor ( $\gamma^+$ ), and electron-donor ( $\gamma^-$ ) components as:  $\gamma^P = 2(\sqrt{\gamma^+ \gamma^-})$ .

Therefore, Eq. 4.6 can be modified as:

$$\begin{aligned}
& \gamma_{ow}(1 + \cos \theta_{s^*wo}) \\
& = 2\gamma_w \\
& + 2 \left( \sqrt{\gamma_{s^*o}^D \gamma_o^D} + \sqrt{\gamma_{s^*o}^+ \gamma_o^-} + \sqrt{\gamma_{s^*o}^- \gamma_o^+} - \sqrt{\gamma_{s^*w}^D \gamma_w^D} - \sqrt{\gamma_{s^*w}^+ \gamma_w^-} - \sqrt{\gamma_{s^*w}^- \gamma_w^+} \right. \\
& \quad \left. - \sqrt{\gamma_o^D \gamma_w^D} - \sqrt{\gamma_o^+ \gamma_w^-} - \sqrt{\gamma_o^- \gamma_w^+} \right) \quad (4.7)
\end{aligned}$$

Eq. 4.7 can now be utilized to determine the dispersive, electron-acceptor, and electron-donor components of solid surface tension underwater or any other liquid. To determine the three unknown solid surface tension components (i.e.,  $\gamma_{s^*}^D$ ,  $\gamma_{s^*}^+$ ,  $\gamma_{s^*}^-$ ), three different probe liquids can be utilized to provide three relations for the interactions in the solid-medium-droplet system. It is to be noted that in the

present study we utilized the Young-Dupre equation in combination with the Fowkes[87] approach.

### 4.2.3 Determination of oil surface tension components underwater

The surface tension components of a probe liquid droplet underwater medium can be obtained using the generalized Fowkes equation as:

$$\gamma_{OW} = \gamma_O + \gamma_W - 2 \left( \sqrt{\gamma_O^D \gamma_W^D} + \sqrt{\gamma_O^P \gamma_W^P} \right) \quad (4.8)$$

The oil and oil-water interfacial tensions ( $\gamma_O$  and  $\gamma_{OW}$ ) can be determined experimentally. The dispersive and polar surface tension components of the probe oil droplet can then be written as follows.  $\gamma_O = \gamma_O^D + \gamma_O^P$ . We can now determine the surface tension components of the probe liquid by simultaneously solving these two equations.

## 4.3 Experimental details

### 4.3.1 Materials

In the present work, we evaluated the under-liquid wettability of three substrates: microscopic glass slide (Fisher Scientific, Canada), poly (methyl methacrylate) (PMMA) (Fisher Scientific, Canada), and polytetrafluoroethylene (PTFE) (Thermo Fisher Scientific, Canada). Seven polar and non-polar liquids were purchased from Fisher Scientific and used as probe liquids without further purification. **Table C1.1** presents the name and the main physicochemical properties of the probe liquids.

### 4.3.2 Wettability analysis

The surface wettability of the membranes was evaluated by measuring the equilibrium contact angles using a drop shape analyzer (DSA 100E, KRÜSS GmbH, Germany). Glass and PTFE samples were first cleaned by sonicating in ethanol in an ultrasonic bath, and then washed with deionized water for 5 min. The PMMA substrates were cleaned with hexane and then rinsed with DI water for 5 min. After that, the samples were dried with nitrogen gas. For each experiment, a  $3\pm 0.1$   $\mu\text{L}$  droplet was placed on the surface, and the equilibrium contact angle was recorded after 25s to ensure the stability and equilibrium of the liquid droplet over the sample surface. For all samples, the contact angle at five different positions of the surface was measured and the average value was reported. All the presented experimental data are repeatable as every data point corresponds to an average of more than three different events within a 10% deviation.

### 4.3.3 Measurement of interfacial tension of the probe liquids

In the present work, we measured the polar and non-polar surface tension components of the probe liquids using the pendant drop technique [200]. For the underwater liquid interfacial tension measurements, a cuvette was filled with water and a needle of 1.8 mm diameter was used for the formation of a pendant drop. The reported interfacial tensions are the average of five measurements. **Table 4.1** presents the obtained interfacial tension and the dispersive, and polar surface tension components of the probe liquids.

## 4.4 Results and discussions

### 4.4.1 Surface topography of solid surfaces

Wettability, in general, depends on surface physical topography [15] as well as the surface chemical composition [217,218]. The physical heterogeneities change the surface roughness, and chemical inhomogeneities vary the surface tension [108]. Therefore, it is necessary to evaluate the contribution of surface roughness on wettability before determining the solid surface tension. **Figure 4.3** shows the 2D surface topography of the glass, PMMA, and PTFE surfaces.

All the solid surfaces possess a smooth and uniform surface structure visually. **Table C1.2** presents the average roughness ( $R_{avg}$ ), root mean square roughness ( $R_{rms}$ ), and Wenzel roughness ratio ( $r$ ). Glass and PMMA samples showed sub-10 nanoscale surface roughnesses, whereas the PTFE sample exhibited about one order of magnitude average and RMS roughness values. However, all the surfaces showed similar surface area difference (SAD) of about zero ( $SAD \approx 0$ ) and eventually the Wenzel roughness ratio of about one ( $r \approx 1$ ) with a standard deviation of less than 1%. Therefore, the three solid surfaces can be considered smooth, and thus the effect of roughness on the wettability can be neglected in the present work.

### 4.4.2 Evaluation of solid surface tension components in air

The polar and non-polar surface tension components of the solid surfaces in the air were first evaluated based on Eq. 4.3 using water and diiodomethane as probe liquids. **Figure 4.4a** presents the measured dispersive, polar, and total surface tension of the solid samples. Among the samples, PMMA-air interface possessed the highest total surface tension of 47.88 mN/m, followed by glass (32.22 mN/m), and PTFE (19.27 mN/m). All samples had both polar and non-polar surface tension components. Furthermore, the polar component was smaller than the dispersive

component. This observation was quite significant for PTFE for which the polar component contributed 2.44 % to total surface tension. The contribution of polar components to total surface tension for glass and PMMA surfaces were 9.22% and 17.55%, respectively.

#### 4.4.3 Determination of solid surface tension components underwater

In this section, we utilized Eq. 4.6 to determine the surface tension components of the solid samples underwater using diiodomethane and diethyl phthalate as non-polar and polar probe liquids, respectively. **Figure 4.4b** presents the evaluated surface tension components of the solid surfaces. For all samples, the underwater total surface tension increased with respect to their corresponding in-air values. Compared to glass, polymeric surfaces exhibited more significant variation in their surface tension values with the highest increment of 215% for PTFE-water interface, followed by 80.4% for PMMA-water, and 12.4% for glass-water interface. A likely explanation can be the adsorption of the thin layer of the medium over the solid surface. Due to the polar and apolar interactions at the solid-liquid interface, molecular rearrangement and/or reorientation can also occur [206–208,212,215,219]. Thus, the interfacial tension at the solid-medium interface will be different than in the bulk of the solid. Moreover, a thin film of surrounding medium over the solid surface can influence the contact of the probe droplet over the solid surface. These two phenomena, i.e., molecular rearrangement (and/or reorientation) at solid-medium interface, and the formation of a thin film of medium over the surface can vary the wettability of the solid surface.

Fowkes [87,88] quantified the molecular interaction between two liquid ( $L_1$ - $L_2$ ) interfaces where the interfacial tension of each layer would be  $\gamma_{L_1} - (\gamma_{L_1}^{D,P} \gamma_{L_2}^{D,P})^{0.5}$ . We can further demonstrate these molecular interactions for general solid-liquid-liquid systems. If one condensed phase such as a solid surface S comes

in contact with a liquid  $L_1$  under another liquid medium  $L_2$ , then the spreading of the liquid  $L_1$  over solid  $S$  will be dependent on the work of adhesion ( $W_{SL_2L_1}$ ) between the three interfaces namely  $\gamma_{SL_2}$ ,  $\gamma_{SL_1}$ , and  $\gamma_{L_1L_2}$  [220], where,  $W_{SL_2L_1} = \gamma_{SL_2} + \gamma_{L_1L_2} - \gamma_{SL_1}$ . This adhesion work needs to be positive ( $\gamma_{SL_2} + \gamma_{L_1L_2} > \gamma_{SL_1}$ ) to avoid complete wetting scenario. The molecular interactions (dispersive and polar) at the solid interfacial layer with the contacting liquid also alter accordingly. Hence, from the experimental findings of Trinavee et al. [216], we can demonstrate that the contact angle of oil drop ( $\theta_O$ ) in water medium will not be equal to the complementary contact angle for a water drop under that oil medium ( $180^\circ - \theta_W$ ) over the same solid surface. We quantified this alteration using Eq. 4.6 which differs from the general Fowkes approach (Eq. 4.3) applicable in the air medium.

The variation of the surface tension parameters in **Figure 4.4** demonstrates that the surface tension of a solid is a combined molecular interaction of the solid interface with its surrounding medium, rather than being an intrinsic property of the solid material. Therefore, it is recommended to consider the impact of the surrounding medium for the accurate measurement of solid surface tension parameters.

#### **4.4.4 Validation of underwater wettability and comparison with previous models**

In the previous section, we obtained the underwater surface tension of the solid samples using diiodomethane and diethyl phthalate. In this section, we validated the results with five other polar and non-polar probe liquids, which are immiscible with water, i.e., di-n-butyl phthalate, oleic acid, castor oil, 1,4-dibromobutane, and 1,3-diiodopropane. The probe liquids were selected to include a wide range of densities (0.89 to 3.32 g/mL) and viscosities (1.91 to 100 mPa.s) to ensure the universal applicability of the proposed theoretical model. **Figure 4.5** illustrates the optical images of the equilibrium contact angle of the probe droplets

with the solid surfaces underwater which include both partial wetting ( $0^\circ < \theta_{S^*WO} < 90^\circ$ ) and partial non-wetting ( $90^\circ \leq \theta_{S^*WO} < 180^\circ$ ) regimes. The significant variation of the underwater contact angle confirms the substantial impact of solid/medium molecular interaction on surface tension parameters.

Based on **Figure 4.5**, the solid surface which had less affinity towards the water in the air (more hydrophobic surface, e.g., PTFE) exhibited a lower contact angle with the probe liquids underwater. This indicates that in a solid-droplet-medium system, the drop will be in the partial/complete wetting region if the solid is liquid medium repellent in air and vice versa. We can further classify the medium-droplet interaction in terms of polar and non-polar probe liquids. In both cases, we observe that lower droplet-medium (oil-water) interfacial tension results in a lower contact angle. These observations suggest that the under-liquid wettability is a competition of interactions between solid-medium, solid-droplet, and medium-droplet. For instance, **Figure 4.4** shows that PTFE has the lowest polar surface tension component compared to glass and PMMA. Therefore, PTFE prefers non-polar (or less polar) probe liquids than the surrounding water medium, which consequently gives a lower contact angle for low polarity liquids compared to glass and PMMA. Furthermore, glass and PMMA showed similar wettability towards polar probe droplets such as di-n-butyl phthalate, castor oil, and oleic acid. This observation can be attributed to comparable polar surface tension components of PMMA and glass underwater. However, in the case of non-polar probe droplets, PMMA exhibited lower contact angle than the glass which can be due to the larger dispersive surface tension component of PMMA-water interface. **Figure 4.6** compares the experimental results with the theoretical prediction of underwater contact angle. We also compared the predictions of our model with the results of Trinavee et al.'s [216] and Bartel-Osterhof equation [117,210]. It is to be noted that the study of Trinavee et al. [216] was the first to consider the effect of the surrounding medium for the prediction of under-liquid wettability. They proposed the modified Young's equation (Eq. 4.9) and the modified Owens-Wendt equation (Eq. 4.10) as follows [216]:



$$\gamma_{OW} \cos \theta_{OW} = \gamma_S - \gamma_0 \cos \theta_{OA} - \gamma_{OW} \quad (4.9)$$

$$\gamma_{OW} \cos \theta_{OW} = \gamma_S + \gamma_W - 2\sqrt{\gamma_S^D \gamma_W^D} - 2\sqrt{\gamma_S^P \gamma_W^P} - \gamma_{OW} \quad (4.10)$$

where  $\theta_{OW}$  and  $\theta_{OA}$  are the contact angle between solid-oil droplet in water medium and solid-oil droplet in air medium,  $\gamma_{OW}$ ,  $\gamma_S$ ,  $\gamma_0$ ,  $\gamma_W$  are the interfacial tension of oil-water, solid-air, oil-air, and water-air, respectively.

However, Bartel-Osterhof equation [117,210] includes contact angle measurement of oil and water in the air medium and utilized those in under-liquid cases. This can be written as follows [117,210]:

$$\gamma_{OW} \cos \theta_{OW} = \gamma_{OA} \cos \theta_{OA} - \gamma_{WA} \cos \theta_{WA} \quad (4.11)$$

where  $\theta_{OW}$ ,  $\theta_{OA}$ , and  $\theta_{WA}$  are the contact angle between solid-oil droplet in water medium, solid- oil droplet in air medium, and solid-water droplet in air medium.

It is to be noted that though all these works used under-liquid contact angle as  $\theta_{OW}$ , the present study represents this as  $\theta_{SWO}$ . **Figure 4.6** demonstrates that the predictions of our proposed theory which are within 15% deviation margin of the experimental contact angles of the probe liquids over PTFE, glass, and PMMA surfaces underwater. In contrast, the prediction of the modified Young's equation (Eq. 4.9), modified Owens-Wendt's equations (Eq. 4.10), and Bartel-Osterhof equation [117,210] deviate more than  $\pm 30\%$  for most of the experimental observations for PMMA and glass surfaces (**Figure 4.6a** and **4.6b**). For the case of the PTFE surface, this deviation became even larger and exceeded  $\pm 50\%$  (**Figure 4.6c**). The observed deviation can be explained by the fact that all the previous model did not consider the possible molecular interaction between solid-medium, medium-droplet interface, and utilized the solid-air surface tension results. It is to be noted that among all the previous models, only the model of Trinavee et al. [216] showed

a few considerable results of contact angle in the case of PTFE. Furthermore, we also explored the previous literature based on the equation of state (EQS) approach [77,221–223] for under-water wettability prediction of PTFE (refer to section C1.1.5 of the Appendix). The data measured at the PTFE-air interface (**Figure C1.3a**) is consistent with the present surface tension component (STC) based approach. However, in the case of the PTFE-water interface, no trend has been observed to determine the solid surface tension (**Figure C1.3b**). Stammitti-Scarpone et al. [77] observed similar characteristics for the PTFE-water interface. They proposed that this value would be 55 mN/m by arbitrarily setting the curve fitting parameters. This value is consistent with our present calculation (60.7 mN/m). We reported the wettability prediction of Bartel-Osterhof equation [117,210] in the **Table C1.5** of the Appendix. Though PTFE is hydrophobic in an ideal case scenario, but still it has a small magnitude of polar surface tension component as shown in **Figure 4.4a**. Thus, there can be the existence of a thin layer of water medium on the PTFE surface which was only considered by the model of Trinavee et al. [216].

We also reported the theoretical predictions proposed by El-Shimi et al. [212] for underwater solid wettability case in **Table C1.3** and **Table C1.4** of the Appendix. El-Shimi et al. [212] proposed a theoretical approach, based on two different models, i.e., Fowkes[88] and Wu[224] models, that was used here to predict the underwater wettability of PTFE, glass, and PMMA. We observed that none of the previous theoretical approach can predict the solid wettability underwater.

#### **4.4.5 Determination of electron-acceptor and electron-donor surface tension components**

The developed method of under-liquid wettability analysis was extended to determine the acid-base surface tension components proposed by van Oss et al. [100]. We utilized Eq. 4.7 with three probe liquids (diiodomethane, diethyl phthalate, and Di-n-butyl phthalate). **Table 4.2** presents the electron donor and electron acceptor components of the PTFE, glass, and PMMA surfaces. For all samples, the electron

donor surface tension components are two orders of magnitude larger than the electron acceptor component. Determination of these surface tension components will indicate the interfacial interaction and free energy of adhesion of a solid surface with some other surfaces (e.g., colloid) underwater.

#### **4.4.6 Effects of surrounding medium interfacial tension on solid wettability**

The developed theoretical study (Eq. 4.6) further allows us to observe the influence of surrounding medium over solid wettability. This can be performed by evaluating the change in the solid wettability with varying the surrounding medium surface tension components when all other parameters are fixed. **Figure 4.7** depicts the effects of oil-medium interfacial tension on the wettability of a non-polar oil droplet over a non-polar solid surface. We observed that the wettability region shifts from wetting to the non-wetting region with the increase of oil-medium interfacial tension. For very low oil-medium interfacial tension ( $\gamma_{OM} \leq 10$  mN/m), the complete non-wetting condition is hard to achieve. However, for high oil-medium interfacial tension ( $\gamma_{OM} \geq 100$  mN/m), it will be very difficult to reach even partial wetting region. We can also explain this from **Figure 4.2b**. Since wettability is the resultant of three surface tension, the higher the oil-medium interfacial tension, the higher will be the contact angle and vice versa. We further conducted a parametric study to understand the effects of medium surface tension over polar and non-polar solid wettability. The outcome of this observation is discussed in section C1.1.4 of the Appendix. The surface tension mapping in **Figures 4.7 and C1.1-C1.2** provides valuable insight into the design and fabrication of surfaces possessing a wide range of wettabilities at different surrounding medium. **Figure 4.7** also suggests that for a fixed oil-water interfacial tension there exists a wide range of wettability cases.

## 4.5 Summary

The wetting of a solid surface by a liquid droplet under a liquid medium not only includes the solid-droplet molecular interactions, but also involves the interfacial interaction with the surrounding medium. Such wettability adaptation evolves either due to the formation of a thin film of the surrounding medium over the solid surface, or the interfacial molecular reorientation of the solid surface in contact with the wetting liquids. Here a theoretical framework is developed, and a novel experimental approach is proposed to evaluate the solid surface tension under liquid medium by implicitly involving the adaptation behavior of a solid surface in the presence of another liquid. The wettability of three solid surfaces is investigated, namely glass, poly(methyl methacrylate) (PMMA), and polytetrafluoroethylene (PTFE), for a wide range of polar and non-polar oil droplets underwater. From the proposed two-liquid approach, the polar and non-polar solid surface tension components are measured. The experimental results revealed the significant impact of interfacial tension of both droplet and the surrounding medium on the overall wettability of the solid-droplet-medium system. The predicted results were in  $\pm 15\%$  deviation from that of the experimental observation for all the cases. Previously available theories, by contrast, deviated more than  $\pm 30\%$  for all the cases.

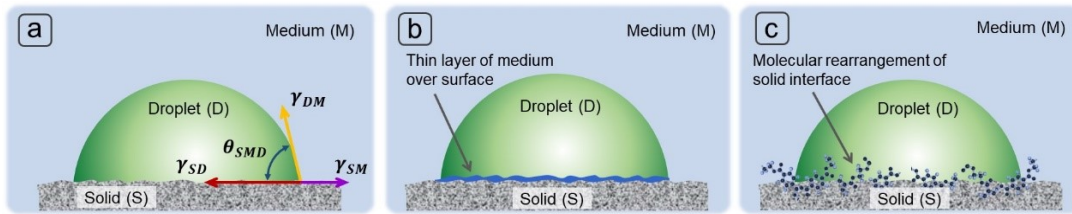


Figure 4.1. Outline of under-liquid wetting of solid surfaces: (a) A liquid drop (D) spreads over the solid surface (S) under-liquid medium (M). The contact angle ( $\theta_{SMD}$ ) is the resultant of three different surface tensions, drop-medium ( $\gamma_{DM}$ ), solid-drop ( $\gamma_{SD}$ ), and solid-medium ( $\gamma_{SM}$ ); (b) A liquid drop spreading over the thin layer of the medium created on the top of the solid surface; (c) Molecular rearrangement of the solid surface due to the surrounding medium and the drop contact.

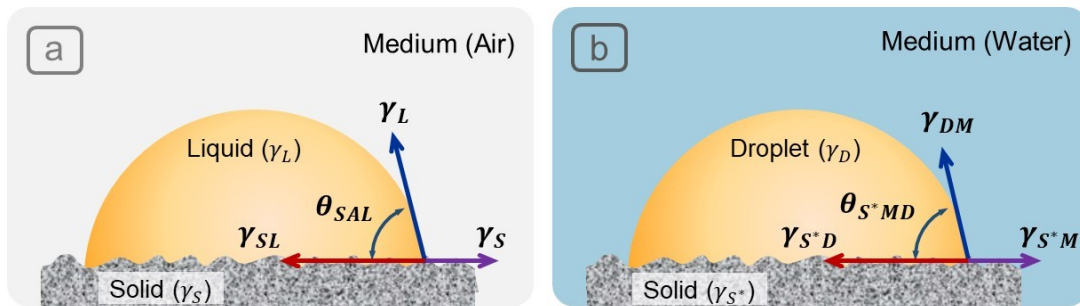


Figure 4.2 Scheme of wettability measurement of solid surface in air and under-liquid. (a) Wetting of a solid surface (S) by a liquid droplet (D) in the air (A); (b) Wetting of a solid surface by a liquid droplet in another liquid medium. Due to the formation of a thin layer of surrounding medium on the surface, and/or possible molecular rearrangement at the solid-medium interface, the solid surface tension under-liquid will be different from that in air.

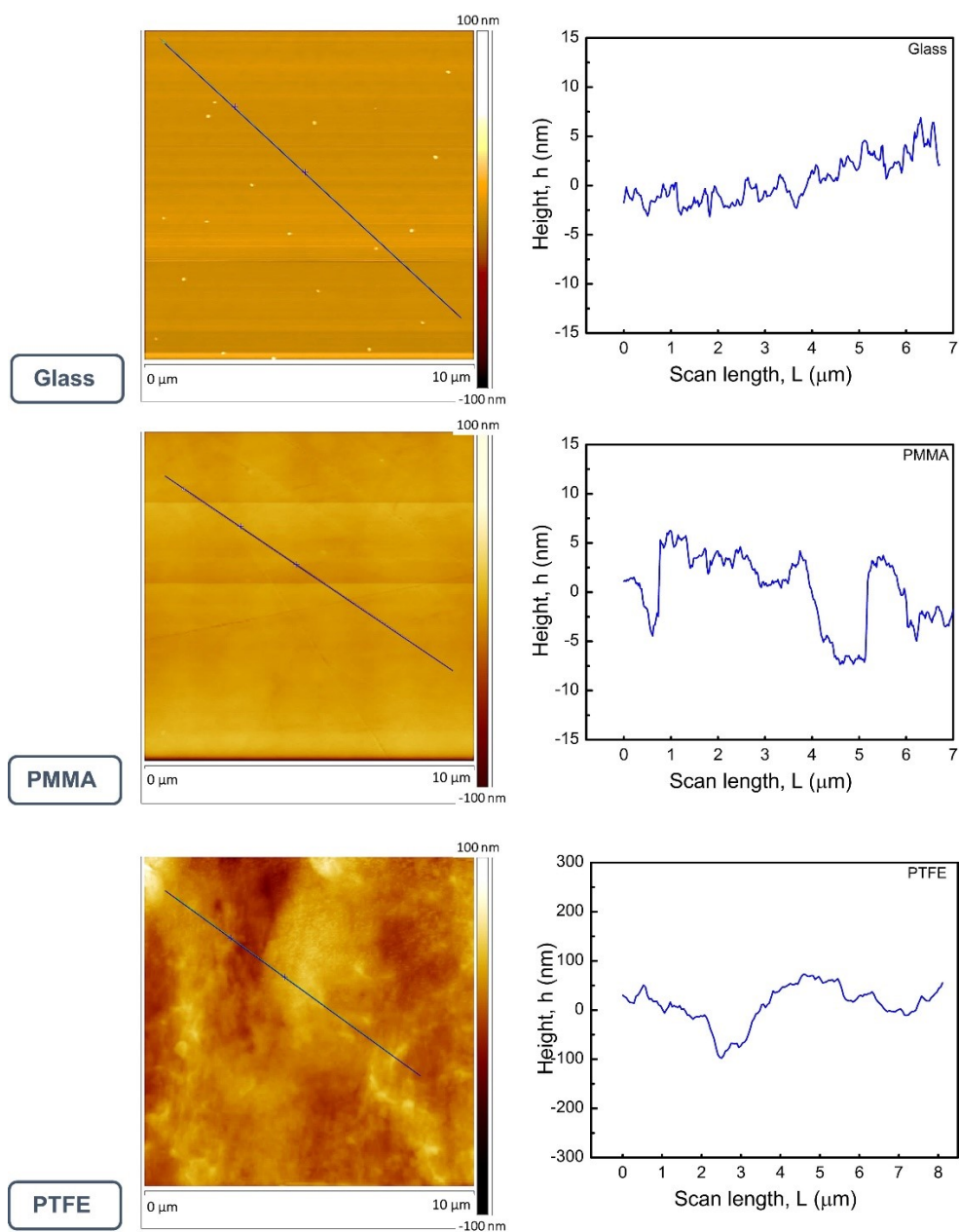


Figure 4.3 AFM surface topography of glass, PMMA and PTFE solid samples. For all the cases, the scan size was  $10\ \mu\text{m} \times 10\ \mu\text{m}$ . The height variation of Glass and PMMA is within about  $5 \pm 0.5\ \text{nm}$ , but PTFE shows a higher variation within about 60 nm. Thus, we observe uniform surface morphology for all the cases.

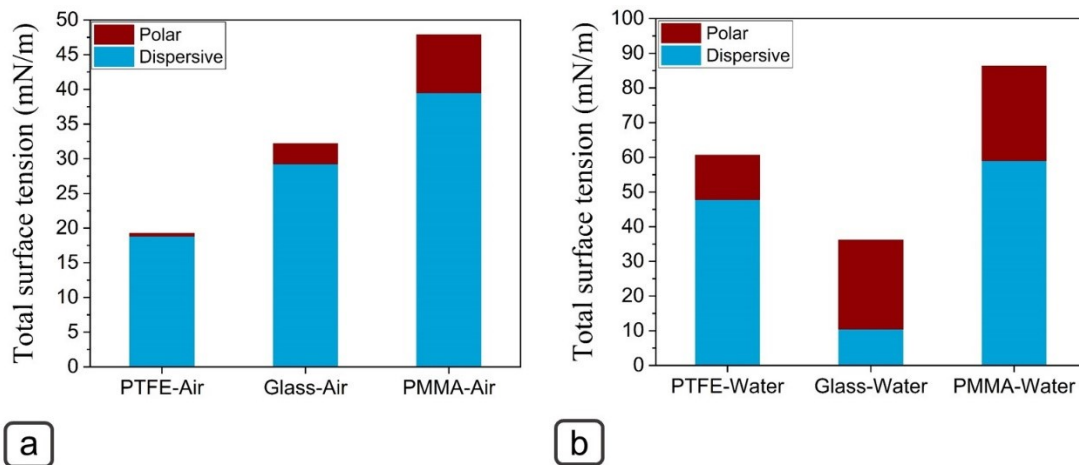


Figure 4.4 Dispersive, polar, and total surface tension of glass, PMMA and PTFE samples, (a) in air, and (b) underwater cases. We observe higher polarity of solid-water interfacial system than in the solid-air case. The represented data is based on the  $\pm 10\%$  standard deviation of the probe droplet wettability.
















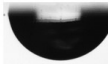

Solid Surface Probe Droplet	Solid Surface		
	PTFE	Glass	PMMA
<b>Di-n-butyl phthalate</b>	 $\theta_{S^*WO} = 47^\circ \pm 2^\circ$	 $\theta_{S^*WO} = 98^\circ \pm 2^\circ$	 $\theta_{S^*WO} = 93^\circ \pm 2^\circ$
<b>1,3-Diodopropane</b>	 $48^\circ \pm 2^\circ$	 $108^\circ \pm 2^\circ$	 $70^\circ \pm 2^\circ$
<b>1, 4-Dibromobutane</b>	 $29^\circ \pm 2^\circ$	 $101^\circ \pm 2^\circ$	 $68^\circ \pm 2^\circ$
<b>Castor Oil</b>	 $54^\circ \pm 4^\circ$	 $88^\circ \pm 4^\circ$	 $100^\circ \pm 4^\circ$
<b>Oleic acid</b>	 $45^\circ \pm 4^\circ$	 $83^\circ \pm 4^\circ$	 $80^\circ \pm 4^\circ$

Figure 4.5 Optical images of various probe droplets over PTFE, Glass, and PMMA surfaces underwater. For all the cases, PTFE shows a lower underwater contact angle ( $<90^\circ$ ). This indicates the water repellency of PTFE in a solid-liquid-liquid system. We also observe a similar trend of polar and non-polar oil wettability. In both cases, oil droplets having lower oil-water interfacial tension show lower contact angle, e.g., oleic acid for polar oil and 1,4-Dibromobutane for non-polar oil.

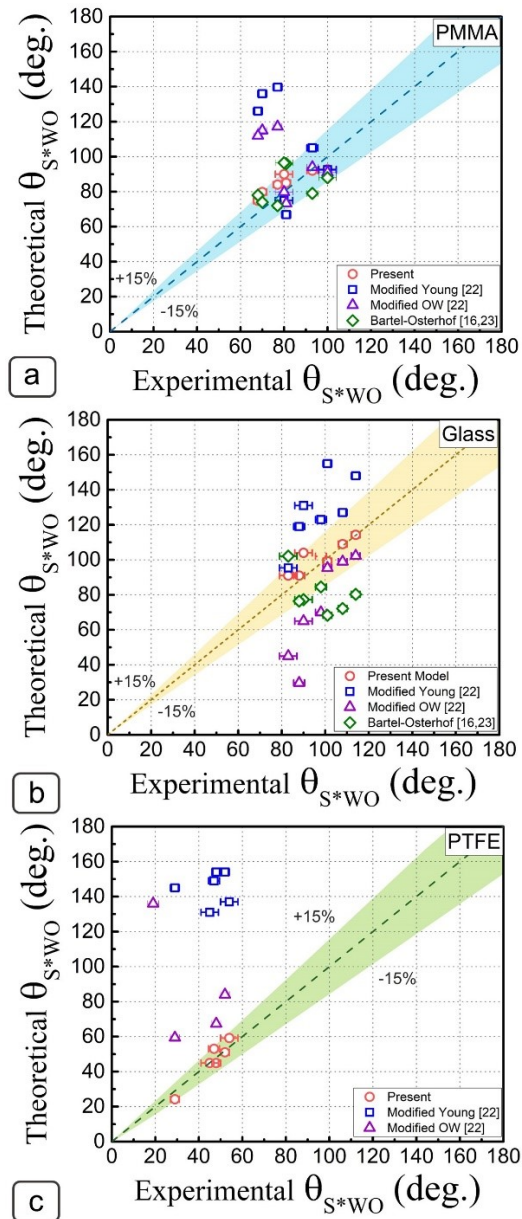


Figure 4.6 The comparison of theoretical prediction with experimental contact angle observations underwater for (a) PMMA, (b) glass, and (c) PTFE surfaces. The proposed theoretical model in this work exhibited good agreement with the experimental observations within  $\sim \pm 15\%$  deviation. In contrast, a large deviation ( $> \pm 30\%$ ) between the theoretical predictions and experimental values was observed in case of PMMA and Glass based on the previously available theories [117,210,216]. In case of PTFE, Trinavee et al.'s [216] theory exhibits deviations more than  $\pm 50\%$ . Moreover, Bartel-Osterhof equation [117,210] cannot predict the underwater wettability of PTFE.

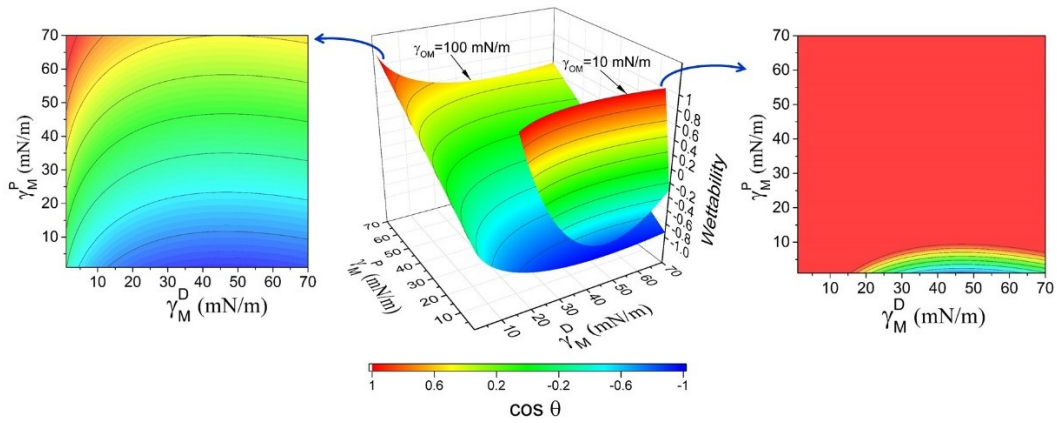


Figure 4.7 Effects of oil-medium interfacial tension on the wettability for  $\gamma_S^D = 50$  mN/m,  $\gamma_S^P = 0$  mN/m,  $\gamma_O^D = 50$  mN/m,  $\gamma_O^P = 0$  mN/m. We observe that a higher oil-water interfacial tension results in lower wettability. This indicates that from lower to higher (from 10 mN/m to 100 mN/m for this case) oil-water interfacial tension the solid wettability shifts towards the non-wettability region.

Table 4.1: Interfacial tension along with surface tension components of the probe liquids. For comparison, the surface tension of the liquids was also reported based on the correlation in the literature at 20 °C [225,226].

Liquid	Surface tension in air based on correlation (mN/m)	Measured surface tension in air (mN/m)	Interfacial tension underwater (mN/m)	Polar component (mN/m)	Dispersive component (mN/m)
1,4-Dibromobutane	40.86	38±0.3	33±0.2	0	38
Diiodomethane	50.80	50±0.3	38±0.2	0	50
1,3-Diiodopropane	47.87	44±0.3	36±0.2	0	44
Diethyl phthalate	36.99	35±0.5	16±0.1	9.95	25.05
Di-n-butyl phthalate	32.76	32±0.5	22.5±0.1	6.1	25.9
Oleic acid	32.8	31±1	17.5±0.5	8.75	22.25
Castor oil	39	35±1	21±0.5	8.7	26.3

Table 4.2: Measurement of electron acceptor and electron donor surface tension components of solid samples underwater. The represented data is based on the  $\pm 10\%$  standard deviation of the probe droplet wettability.

Sample in water	Electron-acceptor ( $\gamma_S^+$ ) (mN/m)	Electron-donor ( $\gamma_S^-$ ) (mN/m)
PTFE/Water	0.16	261.0
Glass/Water	1.17	141.9
PMMA/Water	1.26	149.2

## **Chapter 5 <sup>̅</sup>**

# **New insights into the role of surrounding medium temperature on the under-liquid wetting of solid surfaces**

---

<sup>̅</sup>The material in this chapter has been submitted as Md Farhad Ismail, Behnam Khorshidi, and Mohtada Sadrzadeh. New insights into the role of surrounding medium temperature on the under-liquid wetting of solid surfaces. *Langmuir*, 2020 (under review).

## 5.1 Introduction

Surface wettability, often characterized by contact angle measurements, is central to numerous natural and industrial processes [11,13,203,227–229]. Wettability of a solid surface depends on both surface physiochemical structure and the conditions of the surrounding environment, such as pressure, temperature, and ionic strength [76,117,234,235,206,215,216,219,230–233]. Effect of ambient temperature on solid wettability has attained considerable attention for various practical applications such as boiling, condensation, and evaporation, anti-icing, anti-fogging, anti-fouling, transport and separation processes [73,107,236–239]. Several experimental and numerical studies have been conducted to explore the impact of temperature on surface wettability and surface energy of solids. However, research on the subject has been mostly restricted to the wettability of solid-liquid-vapor (SLV) systems, where the equilibrium contact angle of a probe droplet is evaluated in air or vapor. Since many engineering applications deal with solid-liquid-liquid (SLL) systems, e.g., surface cleaning and enhanced oil recovery, the research would have been more relevant if SLL systems at elevated temperatures had been explored.

The work done by Phillips et al. [240] is among the first experimental efforts to explore the effect of temperature on the partial non-wetting cases ( $\theta_e > 90^\circ$ ) of glass surface in air and under-liquid (paraffin oil) medium. They considered the dispersive solid-drop interfacial interaction as proposed by Fowkes [88] to elucidate the results. For all non-wetting cases, they observed no significant influence of temperature over the contact angle in the air medium. However, under-liquid tests showed a  $15^\circ$  increase in contact angle with a  $50^\circ\text{C}$  temperature increment. Schonhorn [241] later observed a trivial effect of temperature on the wettability of polar drops, including water, formamide, and glycerol on the polyethylene surface. Using the Fowkes approach [88,90], they proposed that high-temperature wettability is merely a function of the interfacial tension of the spreading liquid drop. Petke et al. [242] reported decreasing/increasing trend of advancing/receding contact angle with temperature for polymeric materials having surface tension within 20-50 mN/m.

The study considered several polar and non-polar probe liquids with interfacial tension ranging from 36.5 mN/m to 72.8 mN/m. The outcome of this study indicates that the wettability at higher temperatures is a function of both the interfacial tension of the wetting droplet and the dispersive surface tension of the solid. Baszkin et al. [243] reported the effect of temperature on the dispersive and polar surface tension components of oxidized polyethylene film. They observed a decreasing trend for both dispersive and polar surface tension components of the solid at elevated temperatures. They also showed that solid-liquid interfacial tension increases in the case of polyethylene-water, while it decreases in the case of polyethylene-octane. Yuk et al. [244] investigated the effect of temperature on surface tension components of polymer hydrogels. Using five water-immiscible probe liquids, they reported more than 40% decrease in the surface tension of polymer hydrogels with an increase in temperature from 10 °C to 60 °C. They attributed this result to the variation of polymer chain conformation and mobility of functional groups of the polymer hydrogel surface at elevated temperatures. Aydar et al. [245] studied the effect of temperature on the wettability of polytetrafluoroethylene (PTFE) surface by Canola and olive oils in air and steam medium. They reported a decreasing trend for both cases. A similar decreasing trend of olive oil over metallic and polymeric surfaces was also reported by Ashokkumar et al. [246] for a temperature range of 25 °C to 200 °C. Diaz et al. [247] conducted a theoretical study to evaluate the effects of temperature on the wetting transition of non-polar liquid over a PTFE interface and observed a decrease in contact angle by increasing the temperature. Villa et al. [248] proposed two models, namely decreasing trend model (DTM) and unsymmetric trend model (UTM), based on extended Fowkes approach [88,90], to evaluate solid wettability at elevated temperatures. Their experimental study on water and diiodomethane showed a decreasing trend of contact angle for PTFE, aluminum, and nanoparticle coated glass surface. They concluded that the DTM approach could predict the variation of the contact angle at high temperatures more accurately. Song et al. [249] reported the change of water contact angle on stainless steel over a wide range of temperatures from room temperature to 250 °C. They also observed a



decreasing trend with two distinct regions, i.e., a slight decrement below 120 °C followed by a steeper decline at higher temperatures. They suggested that such a decreasing trend is mainly governed by the change in the interfacial tension of probe water droplets.

Although considerable efforts have been made to evaluate the impact of temperature on wettability and surface tension of solids, the reported studies have been focused on the solid-liquid-vapor system. Less attention was given to solid-liquid-liquid systems where all the three contributors, i.e., solid, probe droplet, and the surrounding medium, may influence the overall wettability at elevated temperatures. The present work aims to investigate the impact of temperature on solid surface tension under a liquid medium. A ‘two-liquid approach’ is employed to measure the surface tension of polar and non-polar solids at elevated temperatures. A theoretical model is also developed to calculate the dispersive and polar components of the solid surface tension under a liquid medium at elevated temperatures. The predicted results are also compared with the proposed models in the literature. This work is believed to be the first study that quantified contact angle and surface tension components of polar and non-polar solid samples under a liquid medium at elevated temperatures.

## **5.2 Experimental methodology**

### **5.2.1 Materials**

In the present work, we evaluated the under-liquid wettability of four solid surfaces, namely microscopic glass slide (Fisher Scientific, Canada), silicon wafer (Silicon Materials Inc., USA), poly (methyl methacrylate) (PMMA) (Fisher Scientific, Canada), and polytetrafluoroethylene (PTFE) (Thermo Fisher Scientific, Canada). The solid samples contained both polar and non-polar (dispersive) functional groups at their surface. Deionized (DI) water was selected as the

surrounding liquid medium for all tests. Four polar and non-polar probe liquids, namely Diiodomethane, 1,3-Diiodopropane, Diethyl phthalate (DEP), and Di-n-butyl phthalate (DBP), were purchased from Fisher Scientific and used without further purification.

### **5.2.2 Characterization of surface wettability of solid samples**

The surface wettability of the samples was evaluated by measuring the equilibrium contact angles using a drop shape analyzer (DSA 100E, KRÜSS GmbH, Germany). A temperature-controlled environmental chamber (SC30, KRÜSS GmbH, Germany) was utilized to control the temperature of the surrounding medium. Before the characterization test, the glass, PTFE, and silicon wafer samples were first cleaned by sonicating in ethanol using an ultrasonic bath and then washed with deionized water for 5 min. The PMMA substrates were cleaned with hexane and then rinsed with DI water for 5 min. After that, the samples were dried with nitrogen gas. For each measurement, a  $3 \pm 0.1 \mu\text{L}$  probe liquid droplet was placed on a solid surface underwater, and the contact angle was recorded after 1 minute to ensure the stability and equilibrium of the liquid droplet over the surface. The contact angle was evaluated at five different locations at the surface, and the average value was reported. **Figure 5.1** illustrates the experimental setup of the under-liquid wettability measurement at elevated temperatures.

### **5.2.3 Measurement of interfacial tension (IFT) of the probe liquids**

The interfacial tension of the probe liquids was evaluated at different temperatures using the pendant drop technique [200]. For each test, the measurement chamber was filled with DI water, and the desired temperature was reached using a temperature control unit (A10 bath circulators, Thermo Scientific™, Canada). A needle of 1.8 mm diameter was used for the formation of a pendant drop. The needle

was kept inside the chamber to assure the thermal equilibrium of the probe liquid and water. The average of five measurements were reported as the IFT of the probe liquids. **Table 5.1** presents the measured IFT, polar and dispersive surface tension components of the probe liquids at room temperature conditions (20 °C). Furthermore, the surface tension of the probe liquids in air was calculated with the proposed correlations in literature [225,226]. The other main properties of the probe liquids were presented in **Table D 1.1** of the appendix.

### 5.3 Theoretical model to predict solid surface tension at elevated temperature

A theoretical model was developed to predict the variation of solid surface tension at elevated temperatures under a liquid medium. The under-liquid wettability involves interactions between the droplet-solid surface, droplet-surrounding medium, as well as the interaction between the solid surface and the surrounding medium. In a SLL system where a liquid droplet is placed on a solid surface in a liquid medium (**Figure 5.1**), the interactions between the three phases can be presented by modified Young's equation as [250]:

$$\gamma_{DM} \cos \theta_{S^*MD} = \gamma_{S^*M} - \gamma_{S^*D} \quad (5.1)$$

where  $\theta_{S^*MD}$  is the contact angle between solid-droplet in liquid medium ( $\theta_{S^*WD}$  for solid-water-drop case),  $\gamma_{S^*M}$ ,  $\gamma_{S^*D}$ , and  $\gamma_{DM}$  are the interfacial tension of solid-medium, solid-droplet, and droplet-medium, respectively, at a given temperature. The solid surface tension under the liquid is denoted as  $\gamma_{S^*}$  to be distinguished from the solid surface tension measured in air ( $\gamma_S$ ). Among the unknown parameters in Eq. (5.1), only  $\gamma_{DM}$ , and  $\theta_{S^*MD}$  can be directly measured by experimental tests. To determine the unknown parameters we need to combine the Dupre equation [85] and extended Fowkes equation [88,90]. The Dupre equation [85] for the solid-liquid-liquid interface can be modified as follows.  $\Delta G_{S^*MD} = \gamma_{S^*D} -$

$\gamma_{S^*M} - \gamma_{DM}$ . The generalized extended Fowkes equation for two different phases of  $\alpha$  and  $\beta$  states [88,90] is given by:

$$\gamma_{\alpha\beta} = \gamma_{\alpha} + \gamma_{\beta} - 2 \left( \sqrt{\gamma_{\alpha}^D \gamma_{\beta}^D} + \sqrt{\gamma_{\alpha}^P \gamma_{\beta}^P} \right) \quad (5.2)$$

where the  $\alpha$ - $\beta$  pair can be solid-medium, solid-droplet, and droplet-medium. Therefore, for a SLL system, Eq. (5.1) can be further expanded as:

$$\begin{aligned} \gamma_{DM}(1 + \cos \theta_{S^*MD}) = 2\gamma_M + 2 \left( \sqrt{\gamma_{S^*}^D \gamma_D^D} + \sqrt{\gamma_{S^*}^P \gamma_D^P} - \sqrt{\gamma_{S^*}^D \gamma_M^D} - \sqrt{\gamma_{S^*}^P \gamma_M^P} - \right. \\ \left. \sqrt{\gamma_D^D \gamma_M^D} - \sqrt{\gamma_D^P \gamma_M^P} \right) \end{aligned} \quad (5.3)$$

where only the polar and dispersive surface tension components (i.e.,  $\gamma_{S^*}^P$  and  $\gamma_{S^*}^D$ ) are the unknown parameters at a given temperature. Eq. (5.3) were used to predict the surface tension components of the solid samples using two probe liquids with known interfacial tensions under the liquid medium. Eq. (5.2) was used to predict the IFT and surface tension components of the probe liquids. The total interfacial tension of the probe and medium liquids ( $\gamma_D$ , and  $\gamma_M$ ), as well as the droplet-medium interfacial tensions ( $\gamma_{DM}$ ) at different temperatures can be measured experimentally using the pendant drop technique. Therefore, the two unknown parameters in Eq. (5.2) can be obtained by considering that the total interfacial tension of a phase ( $\alpha$ ) is the sum of the surface tension components ( $\gamma_{\alpha}^{total} = \gamma_{\alpha}^P + \gamma_{\alpha}^D$ ).

## 5.4 Results and discussions

### 5.4.1 Characterization of surface topography by AFM

Surface nano-scale physical heterogeneity can alter the equilibrium contact angle of a droplet over a surface [15,48]. Therefore, it is necessary to characterize the surface topography of the solids and consider its potential impact on the observed contact angle. **Table 5.2** presents the surface average roughness ( $R_{avg}$ ), root mean square roughness ( $R_{rms}$ ), and Wenzel roughness-ratio ( $r$ ) of the solid samples. Except for PTFE which showed a high magnitude of average surface roughness ( $35.00 \pm 3.0$  nm), the other three solids, i.e., glass, Silicon wafer, and PMMA showed very low surface roughness ( $\leq 6$  nm). Overall, all the samples showed a Wenzel roughness-ratio close to one ( $r \approx 1$ ) which implied that the effect of surface physical heterogeneity was negligible on the variation of equilibrium contact angle. The 2D and 3D AFM images of the solid surfaces were presented in **Figure D1.1** of the Appendix.

### 5.4.2 Determination of interfacial tension of the probe liquids at elevated temperatures

Before studying the variation of the surface wettability of solid samples at elevated temperatures, it is essential to evaluate the impact of temperature on the interfacial tension of the probe liquids and the surrounding water medium. **Figure 5.2** depicts the drop-medium interfacial tension ( $\gamma_{DM}$ ) followed two opposing linear trends with temperature depending on the polarity of the probe liquids. For the polar probe liquids, i.e., DEP and DBP, the interfacial tension increased linearly when the temperature increased from 20 °C to 90 °C. In contrast, for the non-polar liquids, i.e., DIM and DIP, the interfacial tension decreased with the increase of temperature.

The variation of drop-medium interfacial tension ( $\gamma_{DM}$ ) with temperature can be better explained based on the temperature dependency of the surface tension components of each phase. According to extended Fowkes relation [88] (Eq. 5.2), the drop-medium interfacial tension ( $\gamma_{DM}$ ) involves the surface tension of each phase and the interactions exerted by the contacting phases at the interface, and is given by

$$\gamma_{DM} = \left( \gamma_D^P + \gamma_M^P - 2\sqrt{\gamma_D^P \gamma_M^P} \right) + \left( \gamma_D^D + \gamma_M^D - 2\sqrt{\gamma_D^D \gamma_M^D} \right) \quad (5.4)$$

**Figure 5.3** demonstrates how the surface tension components of the probe liquids varied with temperature. For the case of polar probe liquids, the dispersive surface tension component showed small variation over temperature. In contrast, the polar component decreased considerably by the increase of temperature from 20 °C to 90 °C. Therefore, the polar interactions in Eq. (5.4), i.e.,  $(\gamma_D^P \gamma_M^P)^{0.5}$ , approached to zero while the dispersive interaction, i.e.,  $(\gamma_D^D \gamma_M^D)^{0.5}$ , remained approximately constant. As a result, the drop-medium interfacial tension ( $\gamma_{DM}$ ) increased (**Figure 5.2a**) with an elevation of temperature for the case of polar droplets in water (**Figure 5.3a**). In the case of non-polar probe liquids in water, the dispersive surface tension component decreased linearly with an increase in temperature (**Figure 5.3b**). Since there was no contribution from the polar interactions between the non-polar droplets and water, the total interfacial tension of drop-medium decreased at higher temperatures.

### 5.4.3 Impact of temperature on under-water wettability of solid surfaces

**Figure 5.4** illustrates the variation of under-water contact angle ( $\theta_{S*WD}$ ) of solid surfaces with temperature. The contact angle of glass and silicon wafer, which are grouped as non-polymeric surface here, increased with the increase of the temperature for all the probe liquids (**Figure 5.4a** and **5.4b**). A likely explanation

can be the formation of hydration film over the glass and silicon wafer due to the higher wettability of water medium compared to the probe liquids. In an SLL system, the overall wettability depends on the competition of three interfacial interactions between the solid-droplet, solid-medium, and droplet-medium. Water has higher polarity compared to the probe liquids tested for wettability analysis, and its surface tension decreased at elevated temperatures. Therefore, glass and silicon wafer, which also contains highly polar surface functional groups, showed more affinity toward the water medium than the probe liquid droplets.

The polymeric solids, i.e., PMMA and PTFE, exhibited different wettability characteristics than the non-polymeric solids when the temperature varied from 20 °C to 80 °C (**Figure 5.4c** and **5.4d**). PMMA showed the linear decreasing trend up to 60 °C, and then the wettability becomes nearly constant except for a case that the highly polar DEP which was used as a probe droplet. On the other hand, PTFE did not exhibit any specific trend with neither of the probe liquids. We have already observed that all the probe liquids follow a linear trend with the temperature variation. Thus, the non-linear trend of contact angle variation in the case of PTFE can be attributed to the significant non-linear variation of the surface tension at different temperatures. We will quantify this variation in the next section.

#### **5.4.4 Impact of temperature on under-water solid surface tension components**

**Figure 5.5** presents the variation of surface tension components of the solid surfaces underwater at different temperatures. The surface tension components were obtained using Eq. 5.3 by employing one non-polar (DIM) and one polar (DEP) probe liquids. For the case of glass-water and silicon wafer-water interfaces, while the dispersive surface tension components were nearly constant, the polar surface tension components slightly increased at elevated temperatures (**Figure 5.5a**). We also have plotted the total surface tension of all the solid at different temperatures and calculated the average one over the observed temperature (**Figure D1.2** of the

Appendix). The results indicated that the overall surface tension of both surfaces varied less than ~8% with the magnitude of  $64.5 \pm 2.2$  mN/m, and  $60.6 \pm 5.1$  mN/m for the glass and silicon wafer, respectively. For PMMA, we observed a decreasing trend of polar surface tension components up to 60 °C, followed by a nearly constant value for higher temperatures (**Figure 5.5b**). Overall, the total surface tension of PMMA exhibit a ~20% variation ( $20.4 \pm 3.8$  mN/m). PTFE, however, showed a fluctuating trend with a 16% variation in the total surface tension ( $36.5 \pm 5.5$  mN/m). Yuk et al. [244], and Petke et al. [242] also reported a large variation of the total surface tension for the polymeric surfaces in air. The change in the surface tension of polymers with temperature under-liquid cases was found to be more significant. This might be attributed to much greater freedom of polymer molecules in terms of reorientation and conformational change of polymer chains in the water [18]. This phenomenon is driven by the tendency to minimize the interfacial energy and can alter the polymer-water interfacial interaction. Moreover, a thin film of surrounding water medium may form over the surface, which can affect the interfacial properties at different temperatures [216].

It is worth noting that PMMA contains polar functional groups (acryloyl). Hu et al.[251] reported a decreasing trend of the aqueous polymer solutions containing similar functional groups within the temperature range of 20 °C to 60 °C. Our experimental data provided similar evidence of a decreasing trend (**Figure 5.5b**) which is due to the reduced polarity at elevated temperatures. To further elucidate this variation, we calculated the interaction between the solid and the bulk liquid medium. We can calculate the interfacial dispersive and polar interfacial interaction from the Fowkes geometric mean approach [88] as  $\sqrt{\gamma_{S^*}^D \gamma_W^D}$  and  $\sqrt{\gamma_{S^*}^P \gamma_W^P}$ , respectively. This calculation will show the variation of solid-medium interfacial interaction due to temperature variation even before interacting with any probe droplet. **Figure D1.3** of the Appendix indicates a significant temperature dependency of these parameters for the polymeric surfaces.



### 5.4.5 Prediction of under-water solid wettability and comparison with previous models:

In the previous section, we observed different wettability characteristics for the polymeric and non-polymeric surfaces. In this section, we compared our theoretical results with the proposed models by Yuk et al. [244] and Villa et al. [248]. Yuk et al. [244] developed their model based on the extended Fowkes approach [88,90] applicable for non-polar probe liquid cases. On the other hand, Villa et al. [248] considered both trend, i.e., increasing and decreasing variation trend of contact angle with temperature in their study. Their proposed theoretical models, DTM (Eq. 5.5) and UTM (Eq. 5.6) are described as follows:

$$\cos \theta(T) = -1 + 2 \sqrt{\frac{\gamma_D(T_0)(1 + \cos \theta(T_0))^2}{\gamma_D(T)}} \quad (5.5)$$

$$\cos \theta(T) = \frac{\gamma_D(T_0) \cos \theta(T_0)}{\gamma_D(T)} \quad (5.6)$$

where  $T_0$  is a reference temperature (e.g., 25 °C),  $T$  is the elevated temperature at the experimental condition,  $\gamma_D$  is the interfacial tension of the liquid drop, and  $\cos \theta$  is the wettability at the SLL condition.

**Figure 5.6** demonstrates that the DTM and UTM models [248] deviated more than 35% for most of the experimental observations. In the case of glass and silicon wafer, the deviation increased to more than 50% (**Figure 5.6a**). Furthermore, the UTM model predicted a decreasing trend for partial wetting cases ( $\theta < 90^\circ$ ), and an increasing trend for partial non-wetting cases ( $\theta \geq 90^\circ$ ). In contrast, the predictions of our proposed model were within less than 25% of the experimental contact angle data in an SLL system at different temperatures. This evidence confirms the significant effect of surrounding medium temperature on the wettability parameters of the solid surfaces. The observed large deviation of the DTM and UTM models can be due to the assumption of constant solid surface tension over the temperature in Villa et al.'s study [248]. These models showed a more significant deviation for the

surface with higher polarity ( $\gamma_S^P > 30 \text{ mN/m}$ ) such as glass and silicon wafer compared to PMMA and PTFE surfaces. The Yuk et al.'s model [244] also showed more than 50% deviation for all the cases (see **Table D1.2** of the Appendix for details). The large deviation of this model can be ascribed to the disregard of the polarity of the probe droplet, as well as, possible interaction between the probe droplet and the surrounding medium.

#### **5.4.6 Effects of interfacial interactions at elevated temperature on underwater wettability**

Our present experimental observations showed all the possible trends of contact angle variation, including increasing, decreasing, and nearly constant, with temperature. We observed an increasing trend of contact angle for the glass and silicon wafer surfaces. Previous studies deviated more for these two cases as most of the developed theories were based on the decreasing trend model. The steep rise of contact angle with temperature hardly occurs in air medium, however, it is commonly observed under-water specifically for hydrophilic surfaces such as glass and the silicon wafer. Our developed theoretical model (Eq. 5.3) allows us to map the influence of surrounding medium temperature on the solid contact angle and to elucidate this sharp increase of contact angle.

**Figure 5.7** depicts the specific case of glass and silicon wafer underwater wettability for a wide range of probe liquid droplets. The figure represents the transition of the wettability of the probe liquids over the surface under a liquid medium. For both cases, we observed that the partial wettability zone shrank towards the right, from the intersecting blue line of zone I and zone II to the intersecting red line of zone II and zone III due to the temperature increase from 25 °C to 80 °C. This resulted in an extension of the partial non-wetting region (Zone I). Furthermore, the interfacial tension of polar probe liquids such as DBP and DEP, moved from the green zone to the red zone, which is farther away from the transition zone observed at elevated temperature (red line). These two phenomena have eventually led to a

sharp increase in the contact angle. Our theoretical model successfully captured this trend with a ~25% deviation.

We further conducted a parametric study to understand the impact of surrounding medium over polar and non-polar solid wettability (**Figures D1.4-D1.6** of the Appendix). Our analysis indicated that underwater partial wettability would hardly occur for a hydrophilic solid surface at elevated temperatures. This means that an increment of surrounding medium temperature would increase the underwater liquid repellency of the solid.

## 5.5 Summary

The wetting of a solid surface by a liquid droplet under a liquid medium at elevated temperatures not only depends on the solid-drop and drop-medium interfacial tensions but also on the temperature dependency of the interfacial tension of the surrounding medium. Previous studies have shown either decreasing or nearly invariant trend of wettability with an increase in temperature. However, much of the research up to now has only focused on the evaluation of solid wettability in air or vapor, and no model has been proposed to predict the variation of solid wettability at high temperatures under a liquid medium. A theoretical framework and a novel experimental approach are developed in this study to evaluate the high-temperature solid-liquid-liquid wettability. The wettability of different polymeric and non-polymeric surfaces are investigated, namely glass, silicon wafer, poly (methyl methacrylate) (PMMA), and polytetrafluoroethylene (PTFE), for a wide range of polar and non-polar probe droplets underwater (as a liquid medium) at temperatures up to 90 °C. Experimental results revealed that the non-polymeric solid surfaces, i.e., glass and silicon wafer, showed a sharp increase in their contact angle with the probe droplets at elevated temperatures. Between the two polymeric surfaces, PMMA showed a decreasing trend of contact angle over the variation of temperatures, while in the case of PTFE, no specific trend was observed. The predictions of our

theoretical model were in good agreement with the experimental observations with less than  $\pm 25\%$  deviation.

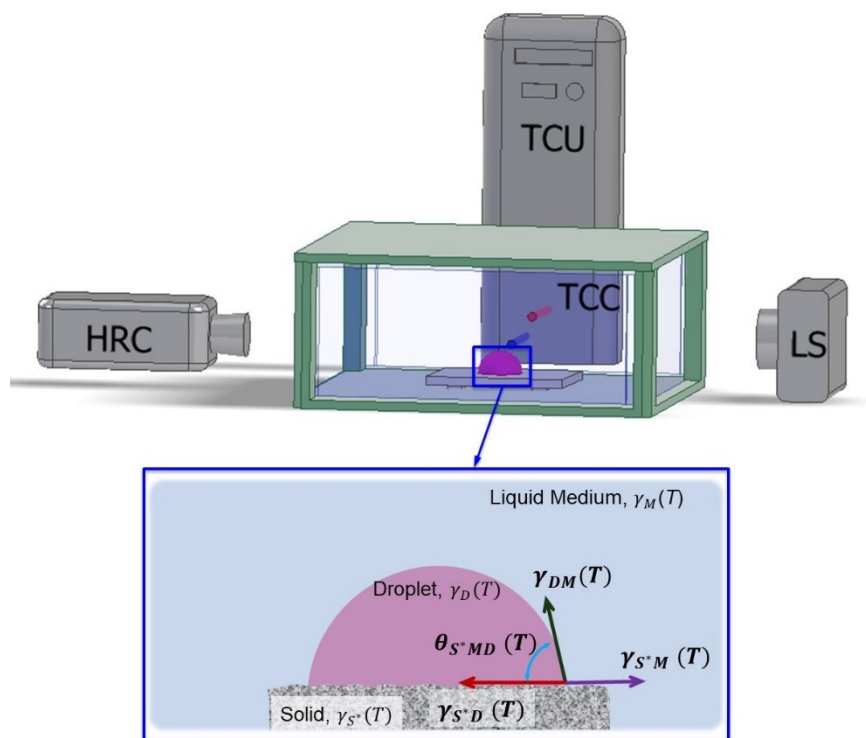


Figure 5.1. Schematic of the experimental setup for analysis of under-liquid wettability at elevated temperature. Here, HRC: High-resolution camera, LS: Light source, TCC: Temperature controlled environment chamber, TCU: Temperature control unit.

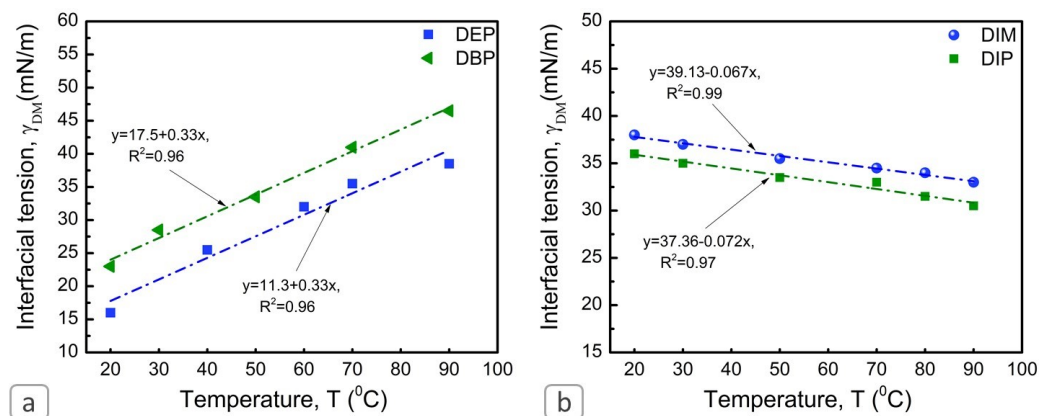


Figure 5.2. Variation of drop-medium interfacial tension ( $\gamma_{DM}$ ) with temperature. We observe an increasing trend for (a) polar, and a decreasing trend for (b) non-polar probe liquids with the increase of medium temperature. The data presented here are based on the  $\pm 5\%$  standard deviation.

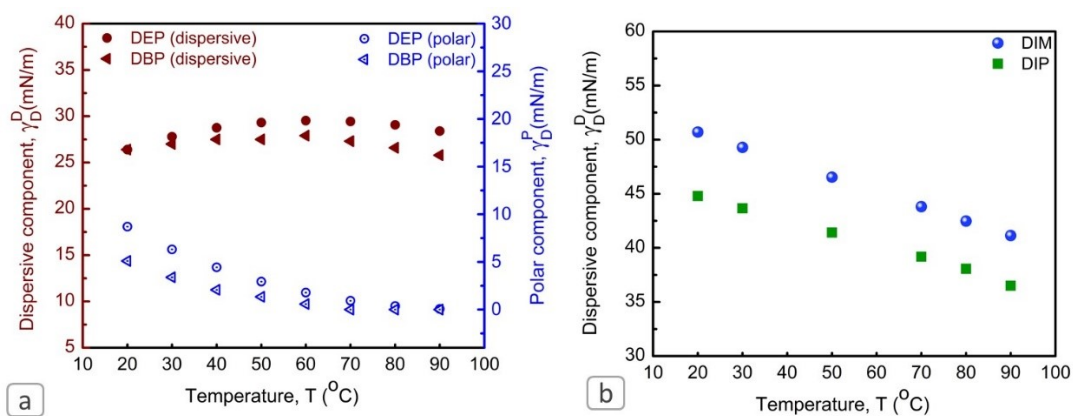


Figure 5.3. Variation of surface tension components at various temperatures for (a) polar, and (b) non-polar probe liquids. We observe the decrement of polarity with the increased temperature. The dispersive surface tension components are nearly constant for polar liquids but decreases with temperature for non-polar liquids. The data presented here are based on the  $\pm 5\%$  standard deviation of drop ( $\gamma_D$ ), medium ( $\gamma_M$ ), and drop-medium interfacial tension ( $\gamma_{DM}$ ).

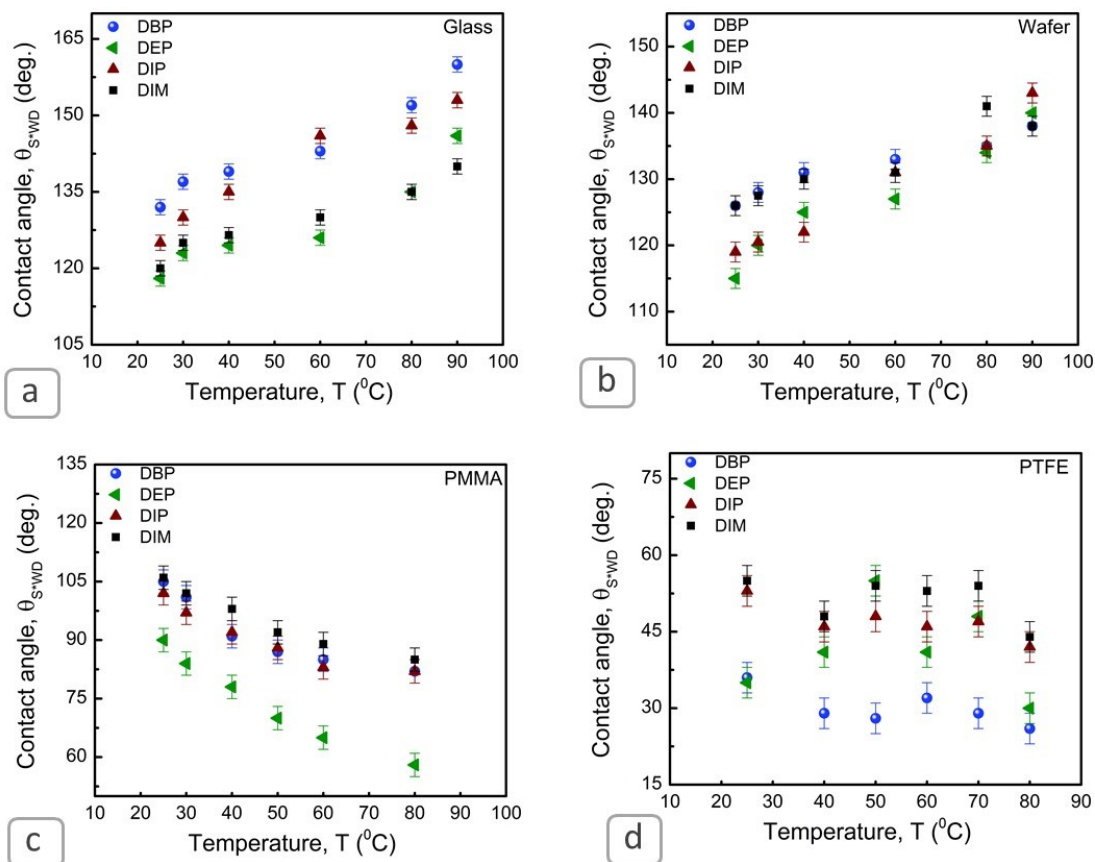


Figure 5.4. Variation of wettability for different probe liquids at different temperatures for (a) glass, and (b) silicon wafer, (c) PMMA, and (d) PTFE. We observe increment (Glass and Wafer), decrement (PMMA), and nearly constant (PTFE) trends for these cases. For PMMA, the decreasing trend continues up to 60 °C (with an exception of comparatively highly polar DEP drop), and then nearly constant wettability is observed. For PTFE, no specific trend was observed for all the prob liquids.



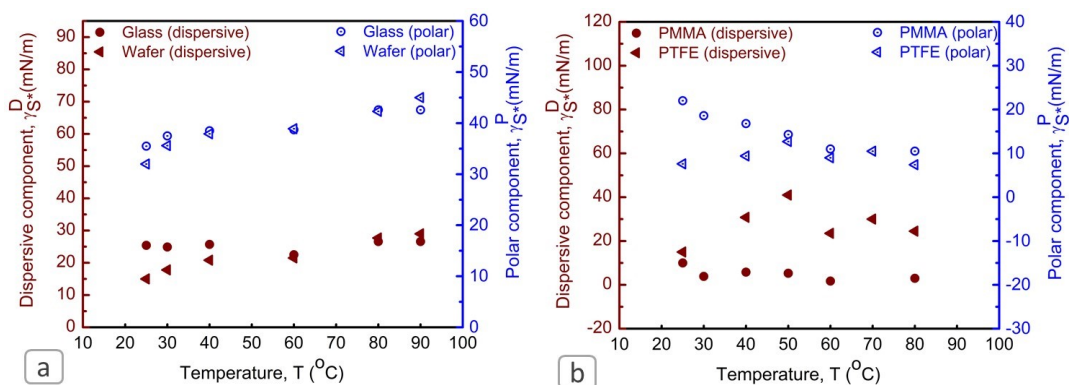


Figure 5.5. Variation of surface tension components at various temperatures for various solid surfaces, (a) glass and silicon wafer, and (b) PTFE and PMMA. We observe nearly constant magnitude of surface tension for non-polymeric samples, e.g., glass and silicon wafer. However, we observe no specific trend for polymeric surfaces. The data presented here are based on the  $\pm 10\%$  deviation of the wettability of probe liquids.

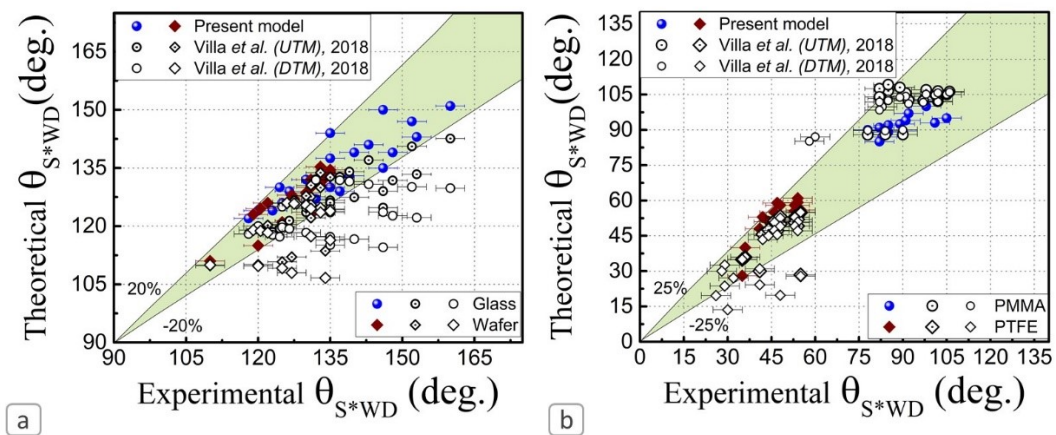


Figure 5.6. The comparison of underwater wettability prediction at different elevated temperatures for (a) non-polymeric, and (b) polymeric samples. The present theoretical framework exhibits good agreement with the experimental observations within  $\sim\pm 25\%$  deviation. In contrast, a large deviation ( $>\pm\sim 35\%$ ) between the theoretical predictions and experimental values was observed in the case of previously available theories [248]. Moreover, previous theories deviated more when the solid surface exhibit higher polarity ( $\gamma_S^P > 30 \text{ mN/m}$ ) with a sharp increasing trend, e.g., glass and wafer.

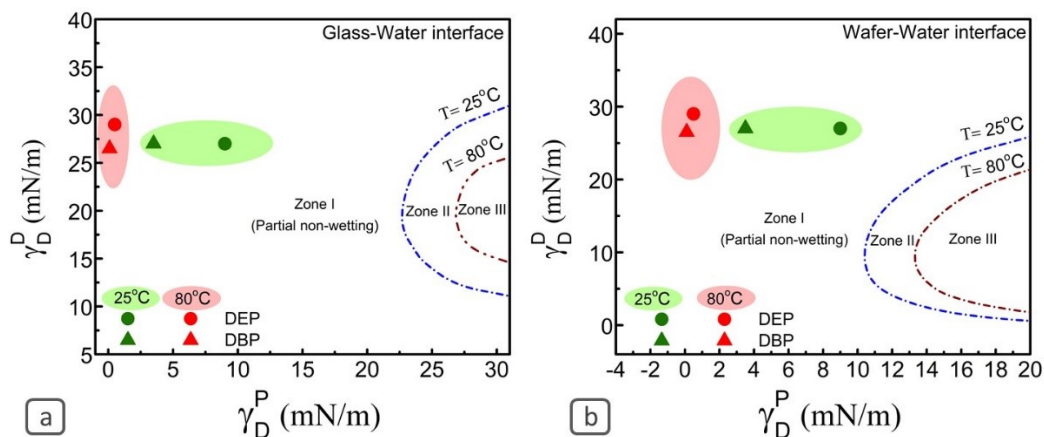


Figure 5.7. Effects of temperature on the non-polymeric solid wettability with the increasing trend, (a) glass, (b) silicon wafer. We observed three different zones for two different temperature conditions. Due to the increment of temperature, the wetting to non-wetting transition blue line shrank towards the right. Partial non-wetting zone I in turn increased to Zone I and II. Furthermore, the interfacial tension of the polar probe liquids moved away (shifts towards left) from the transition lines. The combined effects confirmed the steeper increase of contact angle. The experimental data presented in the figure were based on the 5% standard deviation.

Table 5.1: Interfacial tension along with surface tension components of the probe liquids at room temperature.

Probe Liquid	Surface tension in air based on correlation [225,226] (mN/m)	Surface tension in air (mN/m)	Probe liquid- water interfacial tension (mN/m)	Polar component (mN/m)	Dispersive component (mN/m)
Diiodomethane	50.80	50±0.3	38±0.2	0	50
1,3-Diiodopropane	45.87	44±0.3	36±0.2	0	44
Diethyl phthalate (DEP)	36.99	35±0.5	16±0.1	9.95	25.05
Di-n-butyl phthalate (DBP)	32.76	32±0.5	22.5±0.1	6.1	25.9

Table 5.2 Surface roughness parameters of the solid samples from the AFM analysis (scan size  $10\ \mu\text{m} \times 10\ \mu\text{m}$ ). SAD is the surface area difference due to the presence of nano-scale features on the surface and was obtained using the Nanoscope Software 1.40.

Sample	Average roughness ( $R_{avg}$ )	RMS roughness ( $R_{rms}$ )	Wenzel roughness-ratio ( $r=1+SAD$ )
Glass	$2.01 \pm 0.5\ \text{nm}$	$3.09 \pm 0.5\ \text{nm}$	$1.002 \pm 0.001$
Silicon Wafer	$0.836 \pm 0.2\ \text{nm}$	$1.15 \pm 0.2\ \text{nm}$	$1.0002 \pm 0.0002$
PMMA	$5.75 \pm 0.5\ \text{nm}$	$10.90 \pm 0.5\ \text{nm}$	$1.005 \pm 0.001$
PTFE	$35.00 \pm 3.0\ \text{nm}$	$44.00 \pm 3.0\ \text{nm}$	$1.030 \pm 0.010$

# **Chapter 6**

## **Conclusions and future work**

## 6.1 Conclusions

The present research work provided a novel methodology to probe all the influential surface properties of the membrane using contact angle analyzer under different conditions, aiming to understand the membrane underwater separation performance at room and elevated temperatures. It is well understood that next-generation membrane material requires to fulfill the critical demand of higher selectivity and anti-fouling propensity. To circumvent this challenge, the demand for surfaces with special wettability is increasing over recent years. Membrane researchers tried various methods to tune the wettability of polymeric membranes, which include (1) chemical surface modification methods (chemical grafting, plasma treatment), (2) physical coating of hydrophilic functional materials, and (3) adding micro/nano-patterns to the surface. All of these modifications can be analyzed by only a single analytical tool, i.e., contact angle analyzer. The contact angle can be such a useful parameter through which one can access to the information of other two influential membrane surface parameters, e.g., surface roughness, and surface charge. One should also keep in mind that only a single contact angle value sometimes does not complete to interpret the perm-selectivity data. Instead, many useful parameters derived from the contact angle data, e.g., hydrophilicity, liquid repellency, surface energy, and adhesion work, can be the decisive factors to design novel materials for next-generation membrane. Accomplishing this target can only be possible if accurate characterization and proper utilization of surface wettability properties are ensured.

In Chapters 1 and 2, a detail literature work has been performed and current membrane characterization techniques were presented. It was shown that only 1% of the present literature utilized the accurate characterization technique to determine the surface hydrophilicity and under-water oleophobicity. Based on the available literature and present calculations, a guideline was also provided to determine the criteria for surface hydrophilicity, under-water oleophobicity, and fouling resistivity.

In Chapter 3, surface heterogeneity and surface charge distribution were characterized using a contact angle analyzer. Precise measurement of surface tension of the solid surfaces with nanoscale physical heterogeneity is essential for developing advanced materials with tuned surface wettability. In this research work, a new experimental approach using solely contact angle analysis to quantify the surface roughness-ratio and the dispersive surface tension components of five polymeric membranes with different nanoscale surface physical heterogeneity was determined. To have a comparison with the conventional measurement procedure, the surface wettability parameters were also evaluated using AFM. The results revealed a strong dependency of the AFM data on the size of the scanned area, particularly for the surface with a large degree of physical heterogeneity. In contrast, employing a combination of equilibrium and advancing contact angle analysis provided highly reproducible information regarding the surface roughness-ratio, dispersive surface tension component, and the surface frictional pinning forces. Upon being compatible with the probe liquid, the proposed method can be used to evaluate the surface roughness-ratio, dispersive surface tension component, and the surface frictional pinning force of any solid surface with different scales of physical heterogeneity.

Moreover, an excellent correlation between the flux decline behavior of membranes, due to colloidal fouling, and the obtained roughness of membranes by our proposed model was observed. The results have the implications for designing antifouling membranes where foulants and surface interaction play an important role. This study provides new insight regarding the impact of nanoscale surface heterogeneity on the evaluation of the surface wettability and surface tension components of the solid materials. Another focus of this chapter was to quantify the surface charge density and surface potential for two different environmental conditions in air and under-liquid cases using wettability measurements. This quantification technique was exemplified using three different samples containing different surface chemistry, and the outcome was compared with another measurement technique, namely streaming potential analysis. The experimental results revealed that surfaces containing reactive functional groups, e.g., polymeric



membranes are excellent candidates for these types of studies. The under-liquid sessile drop contact angle titration experiments provided the first direct measurement of surface potential using contact angle analysis with reasonable accuracy. This, in turn, discards the experimental complexity of the captive bubble as well as saturated vapor condition measurements. This study sheds light on the nature of surface-specific ion adsorption and its subsequent effects on wettability related parameters such as adhesion, and surface tension in the air and under-liquid conditions.

In Chapter 4, a theoretical framework and a novel experimental approach were developed to predict the under-liquid wetting behavior of various solid surfaces. There have been a few systematic studies on the quantification of under-liquid solid surface tension and solid-liquid-liquid wettability. None of these previous studies can predict the wettability of solid-liquid-liquid systems accurately. Furthermore, the deviations of these theories are larger (>40%) when all the three phases (solid-liquid-liquid) exhibit polarity. However, many of these studies considered solid surface tension as the intrinsic property. This assumption is not applicable in many practical applications which involve responsive/adaptive surfaces. For such cases, molecular reorientation is mainly governed by the surface tension of the solid because of the fundamental tendency of a system to minimize the interfacial energy between the solid and its surrounding environment. The experimental outcome of this work suggested that solid surface tension could not be the intrinsic property of the solid material. The theoretical predictions of the underwater wetting behavior of the solid surfaces were in good agreement with the experimental observations and showed less than 15% deviation for all the cases. The proposed adhesion work and surface tension mapping indicated that the wettability for a specific solid-droplet combination could only be altered by altering the medium interfacial property. It is worth noting that solid surface tension determination based on surface tension component (STC) approach is an approximate approach. The accuracy of the results is dependent on the proper choice of probe liquids, e.g., one of the probe liquids must be non-polar, which was considered in the present study. On the other hand, another method (equation of state) of solid surface tension determination is also available in the

literature, which relies on the empirical fitting approach. The present study also explored this method for under-liquid application. The experimental results suggested that further modification was required to determine its applicability for under-liquid applications. This study provides valuable guidelines for the design, development, and characterization of under-liquid anti-fouling, super-wettable, and super repellent surfaces. For instance, in membrane separation processes, the development of superhydrophilic and underwater superoleophobic membranes is always challenging. Inspired by the wetting behavior of fish scales, and taking advantage of high-energy materials with water-favoring properties, researchers tried to construct superhydrophilic and underwater superoleophobic surfaces in solid-water-oil interfacial systems. Although a few experimental studies reported the influence of surrounding medium over solid wettability, a theoretical framework for this observation still awaits clarification. The theoretical results of this study can provide this clarification to further explore the influence of the surrounding medium for solid wettability adaptation.

In Chapter 5, a theoretical framework and an experimental approach were utilized to predict under-liquid solid wetting behavior at elevated temperatures in the range of  $25\text{ }^{\circ}\text{C} < T < 90\text{ }^{\circ}\text{C}$ . There have been a few systematic studies on the effects of temperature on the surface tension components and solid-liquid wettability. None of the available models can predict the wettability of solid-liquid-liquid systems at elevated temperatures as they have been developed for the in-air systems. The deviations of the available models become even larger (>50%) when the three involving phases (solid-liquid-liquid) exhibit polarity. The majority of earlier studies have considered solid surface tension to be invariant at elevated temperatures. This assumption is not valid for many practical applications that involve temperature-responsive/adaptive surfaces[76,233]. Here, we proposed a theoretical framework based on the surface tension component approach, which could predict the solid surface tension exposed to different surrounding medium temperatures. Furthermore, our model could capture all the possible trends of contact angle variation, i.e., increasing, decreasing, and nearly constant with increasing temperature. We

observed that the surface properties of polymeric solid surfaces altered due to the change of the surrounding medium temperature. More specifically, polymeric samples exhibited a large variety of surface tension ( $> \sim 16\%$ ) for high-temperature under-water conditions. We proposed a novel experimental technique to quantify the observed alteration. Our theoretical prediction of the underwater wetting behavior was in good agreement with the experimental observations at different temperatures with less than 25% deviation. We observed that partial non-wetting to partial wetting transition would hardly be observed at higher temperatures. The partial non-wetting cases move towards completely non-wetting cases for the hydrophilic surfaces at elevated temperatures. The proposed mapping of adhesion work and surface tension indicated that the surface wettability for a specific solid-droplet combination can be altered from complete wetting to complete non-wetting states by variation of the temperature of the surrounding medium. This study provides valuable guidelines for the design, development, and characterization of under-liquid anti-fouling, super-wettable, and super repellent surfaces for high-temperature applications. For instance, in membrane separation processes, higher temperature operation increases the separation performance and anti-fouling characteristics [236,252].

## 6.2 Future work

This thesis has primarily focused on probing all the membrane influential surface properties with high sensitivity using contact angle analyzer, aiming to elucidate membrane permeation properties in complex and harsh environmental conditions. In summary, the following outlook of the membrane research can be demonstrated. Further studies that can be performed to extend the present contributions are listed below:

- ❖ The present theoretical calculation suggests that surfaces can be considered as strongly hydrophilic if the equilibrium contact angle is less than  $55^\circ$  and oleophobic if the underwater contact angle is greater than  $158^\circ$ . An experimental investigation is worth being conducted in support of these

assumptions. This will further lead the researchers to synthesize superhydrophilic membranes (contact angle  $< 10^0$ ), which can meet the criteria for next-generation membrane.

- ❖ The present study suggested that membrane surfaces exhibit fractal characteristics. It is worth noting that fractal surfaces behave differently than the usual irregular rough surface. It would be interesting to combine the fractal surface characteristics with different types of surface pattern over the membrane surface. Wettability and related surface parameters can be utilized to obtain the design criteria.
- ❖ The present work also indicates that the Wenzel roughness factor obtained from the membrane surfaces is larger than the conventional surface area difference (SAD) based AFM analysis due to the fractal characteristics. Thus, fractal surfaces exhibit different wettability characteristics than the conventional Wenzel and Cassie-Baxter model, which is proposed by Tsuji and coworkers. It is worth evaluating the fractal wettability parameters for the membrane surfaces, specifically having average roughness greater than  $\sim 50$  nm.
- ❖ One of the important wettability related parameters is surface tension. From this literature study, we observe that only 1% of the recent research study reported this parameter. For the anti-fouling membranes, the surface tension should be higher than 60 mN/m. Surface tension parameters can be utilized to tune the membrane surface properties.
- ❖ Contact angle hysteresis is a wettability related parameter which requires further focus to better understand the membrane surface heterogeneity and its connection towards membrane separation efficiency.
- ❖ Membrane surfaces contain various polar and non-polar functional groups. Most of the cases, the reactivity, and effectiveness of these functional groups are evaluated by different analytical tools, e.g., contact angle, streaming potential analyzer, and XPS analysis. The present study provides a pathway to evaluate all the influential parameters with a single analytical tool with

high sensitivity which can ensure the consistency and accuracy of the analysis.

- ❖ The present study indicates that surface oleophobicity can be controlled only by changing the interfacial property of the surrounding medium or even altering the surrounding medium temperature. This further establishes the necessity of evaluating other parameters, e.g., surrounding medium pressure, pH, and ionic concentration.

## 6.3 List of contributions

The present research work is an attempt to establish membrane characterization techniques based on a single analytical tool. The major three contributions of this research work are listed as follows-

1. The present developed theoretical framework can demonstrate the physical heterogeneity of membrane surfaces (self-affine fractals) with less than 25% deviation in comparison with AFM measurement technique.
2. The modification proposed in this thesis to determine the role of surrounding medium pH over the surface potential is based on the low-rate dynamic contact angle experiments. The outcome of this modifications can apprehend the role of surrounding medium pH over surface wettability and the surface potential with less than 30% deviation in comparison with streaming potential technique.
3. Surrounding medium interfacial tension can alter the wettability of any probe liquid. Present research work demonstrated that surface oleophobicity and anti-fouling property can be controlled by merely altering the surrounding medium pH or temperature (without any surface physical/chemical modifications).

The outcomes of this research are published/ prepared for submission, and presented/ prepared for presentation in the following journals and conferences:

### 6.3.1 Journal papers

1. Md Farhad Ismail, Behnam Khorshidi, and Mohtada Sadrzadeh. Characterization of membrane surface and permeation properties by contact angle measurements: quantification strategies and applications. *Advances in colloid and interface science*, 2020 (submission in progress).
2. Md Farhad Ismail, Behnam Khorshidi, and Mohtada Sadrzadeh. New insights into the impact of nanoscale surface heterogeneity on the

wettability of polymeric membranes. *Journal of Membrane Science* 590: 117270, 2019.

3. Md Farhad Ismail, Muhammad Amirul Islam, Behnam Khorshidi, and Mohtada Sadrzadeh. Quantification of surface potential by wettability measurements. *Applied Physics Letters*, 2020 (submission in progress).
4. Md Farhad Ismail, Behnam Khorshidi, and Mohtada Sadrzadeh, New insights into the predication of adaptive wetting of a solid surface under a liquid medium. *Journal of Colloid and Interface Science*, (under revision).
5. Md Farhad Ismail, Behnam Khorshidi, and Mohtada Sadrzadeh. New insights into the role of surrounding medium temperature on the under-liquid wetting of solid surfaces. *Langmuir* (under review).

### **6.3.2 Conference publications and presentations**

1. Md Farhad Ismail, Behnam Khorshidi, and Mohtada Sadrzadeh. Impact of roughness on the wettability of the TFC membrane. North American Membrane Society 28th Annual Meeting (NAMS 2019), Pittsburgh, PA, USA, May 11-15, 2019.
2. Md Farhad Ismail, Behnam Khorshidi, and Mohtada Sadrzadeh. Toward accurate prediction of adaptive wetting of a solid surface under a liquid medium. International Congress on Membranes & Membrane Processes, London, UK, July 12-17, 2020 (in preparation).

# References

- [1] T.G. Crittenden J. C., Trussell R. R., Hand D. W., Howe K. J., *Water Treatment: Principles and Design*, 2nd ed., John Wiley & Sons, Inc., Hoboken, NJ, 2005.
- [2] M. Elimelech, W.A. Phillip, The Future of Seawater and the Environment: Energy, Technology, and the Environment, *Science* (80-. ). 333 (2011) 712–718. doi:10.1126/science.1200488.
- [3] M.A. Shannon, P.W. Bohn, M. Elimelech, J.G. Georgiadis, B.J. Mariñas, A.M. Mayes, Science and technology for water purification in the coming decades, *Nature*. 452 (2008) 301–310. doi:10.1038/nature06599.
- [4] R.W. Baker, *Membrane Technology and Applications*, 3rd ed., John Wiley & Sons, New York, 2012.
- [5] M. Asadollahi, D. Bastani, S.A. Musavi, Enhancement of surface properties and performance of reverse osmosis membranes after surface modification: A review, *Desalination*. 420 (2017) 330–383. doi:10.1016/j.desal.2017.05.027.
- [6] T. Mezher, H. Fath, Z. Abbas, A. Khaled, Techno-economic assessment and environmental impacts of desalination technologies, *Desalination*. 266 (2011) 263–273. doi:10.1016/j.desal.2010.08.035.
- [7] J.R. Werber, A. Deshmukh, M. Elimelech, The Critical Need for Increased Selectivity, Not Increased Water Permeability, for Desalination Membranes, *Environ. Sci. Technol. Lett.* 3 (2016) 112–120. doi:10.1021/acs.estlett.6b00050.
- [8] H.B. Park, J. Kamcev, L.M. Robeson, M. Elimelech, B.D. Freeman, Maximizing the right stuff: The trade-off between membrane permeability and selectivity, *Science* (80-. ). 356 (2017) 1138–1148. doi:10.1126/science.aab0530.
- [9] J.R. Werber, C.O. Osuji, M. Elimelech, Materials for next-generation desalination and water purification membranes, *Nat. Rev. Mater.* 1 (2016). doi:10.1038/natrevmats.2016.18.
- [10] P.J.J. Alvarez, C.K. Chan, M. Elimelech, N.J. Halas, D. Villagrán, Emerging opportunities for nanotechnology to enhance water security, *Nat. Nanotechnol.* 13 (2018) 634–641. doi:10.1038/s41565-018-0203-2.



- [11] R. Zhang, Y. Liu, M. He, Y. Su, X. Zhao, M. Elimelech, Z. Jiang, Antifouling membranes for sustainable water purification: Strategies and mechanisms, *Chem. Soc. Rev.* 45 (2016) 5888–5924. doi:10.1039/c5cs00579e.
- [12] D. Zang, H. Yi, Z. Gu, L. Chen, D. Han, X. Guo, S. Wang, M. Liu, L. Jiang, Interfacial Engineering of Hierarchically Porous NiTi/Hydrogels Nanocomposites with Exceptional Antibiofouling Surfaces, *Adv. Mater.* 29 (2017) 1–7. doi:10.1002/adma.201602869.
- [13] Z. Wang, M. Elimelech, S. Lin, Environmental Applications of Interfacial Materials with Special Wettability, *Environ. Sci. Technol.* 50 (2016) 2132–2150. doi:10.1021/acs.est.5b04351.
- [14] M. Elimelech, W.A. Phillip, The future of seawater desalination: Energy, technology, and the environment, *Science* (80-. ). 333 (2011) 712–717. doi:10.1126/science.1200488.
- [15] M Farhad Ismail, B. Khorshidi, M. Sadrzadeh, New Insights into the Impact of Nanoscale Surface Heterogeneity on the Wettability of Polymeric Membranes, *J. Memb. Sci.* 590 (2019) 1–9. doi:10.1016/j.memsci.2019.117270.
- [16] S. Lee, S. Kim, J. Cho, E.M.V. Hoek, Natural organic matter fouling due to foulant-membrane physicochemical interactions, *Desalination.* 202 (2007) 377–384. doi:10.1016/j.desal.2005.12.077.
- [17] C.J. van Oss, *Interfacial Forces in Aqueous Media*, Taylor & Francis Group, 2006.
- [18] G.S. Ferguson, G.M. Whitesides, *Thermal Reconstruction of the Functionalized Interface of Polyethylene Carboxylic Acid and Its Derivatives*, Springer, Boston, MA, 1992. doi:10.1007/978-1-4899-1176-6\_6.
- [19] and L.-S.W. Xu, Zhi-Kang, Xiao-Jun Huang, Techniques for Membrane Surface Characterization, in: *Surf. Eng. Polym. Membr.*, Springer Science & Business Media, 2009: pp. 6–7.
- [20] B. Han, S. Liang, B. Wang, J. Zheng, X. Xie, K. Xiao, X. Wang, X. Huang, Simultaneous determination of surface energy and roughness of dense membranes by a modified contact angle method, *Colloids Surfaces A Physicochem. Eng. Asp.* 562 (2019) 370–376. doi:10.1016/j.colsurfa.2018.11.059.
- [21] G. Hurwitz, G.R. Guillen, E.M.V. V Hoek, Probing polyamide membrane surface charge, zeta potential, wettability, and hydrophilicity with contact angle measurements, *J. Memb. Sci.* 349 (2010) 349–357. doi:10.1016/j.memsci.2009.11.063.
- [22] E. Lee, S. Lee, S. Hong, A new approach to the characterization of reverse osmosis membrane by dynamic hysteresis, *Desalin. Water Treat.* 18 (2010)

257–263. doi:10.5004/dwt.2010.1782.

- [23] Y. Kim, S. Lee, J. Kuk, S. Hong, Surface chemical heterogeneity of polyamide RO membranes: Measurements and implications, *Desalination*. 367 (2015) 154–160. doi:10.1016/j.desal.2015.04.006.
- [24] R.S. Hebbar, A.M. Isloor, A.F. Ismail, *Contact Angle Measurements*, Elsevier B.V., 2017. doi:10.1016/B978-0-444-63776-5.00012-7.
- [25] N. Hilal, A.F.I.T. Matsuura, D. Oatley-Radcliffe, *Front Matter*, 2017. doi:10.1016/b978-0-444-63776-5.01001-9.
- [26] O. Agboola, J. Maree, R. Mbaya, Characterization and performance of nanofiltration membranes, *Environ. Chem. Lett.* 12 (2014) 241–255. doi:10.1007/s10311-014-0457-3.
- [27] D.J. Johnson, D.L. Oatley-Radcliffe, N. Hilal, State of the art review on membrane surface characterisation: Visualisation, verification and quantification of membrane properties, *Desalination*. 434 (2018) 12–36. doi:10.1016/j.desal.2017.03.023.
- [28] D. Johnson, N. Hilal, Characterisation and quantification of membrane surface properties using atomic force microscopy: A comprehensive review, *Desalination*. 356 (2015) 149–164. doi:10.1016/j.desal.2014.08.019.
- [29] A.R. Tehrani-Bagha, Waterproof breathable layers – A review, *Adv. Colloid Interface Sci.* 268 (2019) 114–135. doi:10.1016/j.cis.2019.03.006.
- [30] S.N.S.A. Aziz, M.N.A. Seman, S.M. Saufi, A Review on Surface Characterization Techniques of Polymeric Membrane in Forward Osmosis, *IOP Conf. Ser. Mater. Sci. Eng.* 736 (2020). doi:10.1088/1757-899X/736/5/052026.
- [31] D. Johnson, N. Hilal, Polymer membranes – Fractal characteristics and determination of roughness scaling exponents, *J. Memb. Sci.* 570–571 (2019) 9–22. doi:10.1016/j.memsci.2018.10.024.
- [32] S.R. Holmes-Farley, R.H. Reamey, T.J. McCarthy, J. Deutch, G.M. Whitesides, Acid-base behavior of carboxylic acid groups covalently attached at the surface of polyethylene: The usefulness of contact angle in following the ionization of surface functionality, *Langmuir*. 1 (1985) 725–740. doi:10.1021/la00066a016.
- [33] S.R. Holmes-farley, G.M. Whitesides, Reactivity of Carboxylic Acid and Ester Groups in the Functionalized Interfacial Region of “Polyethylene Carboxylic Acid” (PE-CO<sub>2</sub>H) and Its Derivatives: Differentiation of the Functional Groups into Shallow and Deep Subsets Based on a Comparison of Conta, *Langmuir*. (1987) 62–76.
- [34] S.R. Holmesfarley, C.D. Bain, G.M. Whitesides, Wetting of Functionalized

Polyethylene Film Having Ionizable Organic-Acids and Bases at the Polymer Water Interface - Relations between Functional-Group Polarity, Extent of Ionization, and Contact-Angle with Water, *Langmuir*. 4 (1988) 921–937.

- [35] C.D. Bain, G.M. Whitesides, A Study by Contact Angle of the Acid-Base Behavior of Monolayers Containing  $\omega$ -Mercaptocarboxylic Acids Adsorbed on Gold: An Example of Reactive Spreading, *Langmuir*. 5 (1989) 1370–1378. doi:10.1021/la00090a019.
- [36] R. Schweiss, P.B. Welzel, C. Werner, W. Knoll, Dissociation of surface functional groups and preferential adsorption of ions on self-assembled monolayers assessed by streaming potential and streaming current measurements, *Langmuir*. 17 (2001) 4304–4311. doi:10.1021/la001741g.
- [37] D. Rana, T. Matsuura, Surface Modifications for Antifouling Membranes, *Chem. Rev.* 110 (2010) 2448–2471. doi:10.1021/cr800208y.
- [38] D.J. Miller, D.R. Dreyer, C.W. Bielawski, D.R. Paul, B.D. Freeman, Surface Modification of Water Purification Membranes, *Angew. Chemie - Int. Ed.* 56 (2017) 4662–4711. doi:10.1002/anie.201601509.
- [39] L.T.R. Yuan Y., Contact Angle and Wetting Properties, Springer, Berlin, Heidelberg, 2013.
- [40] K.-Y. Law, H. Zhao, Surface Wetting Characterization, Contact Angle, and Fundamentals, Springer International Publishing, 2016.
- [41] M.F. Ismail, A. Baldygin, T. Willers, P.R. Waghmare, Optical contact angle measurement considering spreading, evaporation and reactive substrate, 2018. doi:10.1002/9781119459996.ch2.
- [42] T. Huhtamäki, X. Tian, J.T. Korhonen, R.H.A. Ras, Surface-wetting characterization using contact-angle measurements, *Nat. Protoc.* 13 (2018) 1521–1538. doi:10.1038/s41596-018-0003-z.
- [43] J.D. Le Roux, D.R. Paul, M. Arendt, Y. Yuan, I. Cabasso, Modification of asymmetric polysulfone membranes by mild surface fluorination Part II. Characterization of the fluorinated surface, *J. Memb. Sci.* 94 (1994) 143–162. doi:10.1016/0376-7388(93)E0154-C.
- [44] W. Zhang, M. Wahlgren, B. Sivik, Membrane Characterization by the Contact Angle Technique: II. Characterization of UF-Membranes and Comparison between the Captive Bubble and Sessile Drop as Methods to obtain Water Contact Angles, *Desalination*. 72 (1989) 263–273. doi:10.1016/0011-9164(89)80011-6.
- [45] Y. Baek, J. Kang, P. Theato, J. Yoon, Measuring hydrophilicity of RO membranes by contact angles via sessile drop and captive bubble method: A comparative study, *Desalination*. 303 (2012) 23–28. doi:10.1016/j.desal.2012.07.006.

- [46] T. Young, An Essay on the Cohesion of Fluids, *Philos. Trans. R. Soc. London.* 95 (1805) 65–87. doi:10.1098/rstl.1805.0005.
- [47] R.N. Wenzel, Resistance of solid surfaces to wetting by water, *J. Ind. Eng. Chem. (Washington, D. C.).* 28 (1936) 988–994. doi:10.1021/ie50320a024.
- [48] R.N. Wenzel, Surface roughness and contact angle, *J. Phys. Colloid Chem.* 53 (1949) 1466–1467. doi:10.1021/j150474a015.
- [49] A.B.D. Cassie, S. Baxter, WETTABILITY OF POROUS SURFACES, *Trans. Faraday Soc.* 40 (1944) 546–551. doi:10.1039/TF9444000546.
- [50] A.B.. B.D. Cassie, Contact angles, *Discuss. Faraday Soc.* 3 (1948) 11–16.
- [51] G. Binnig, H. Rohrer, C. Gerber, E. Weibel, Surface studies by scanning tunneling microscopy, *Phys. Rev. Lett.* 49 (1982) 57–61. doi:10.1103/PhysRevLett.49.57.
- [52] G. Binnig, C.F. Quate, Atomic Force Microscope, *Phys. Rev. Lett.* 56 (1986) 930–933. doi:10.1103/PhysRevLett.56.930.
- [53] J.D. Miller, S. Veeramasuneni, J. Drelich, M.R. Yalamanchili, G. Yamauchi, Effect of roughness as determined by atomic force microscopy on the wetting properties of PTFE thin films, *Polym. Eng. Sci.* 36 (1996) 1849–1855. doi:10.1002/pen.10580.
- [54] P. Samyn, J. Van Erps, H. Thienpont, Relation between optical non-contact profilometry and AFM roughness parameters on coated papers with oil-filled nanoparticles, *Meas. J. Int. Meas. Confed.* 82 (2016) 75–93. doi:10.1016/j.measurement.2015.12.035.
- [55] C.Y. Poon, B. Bhushan, Comparison of surface roughness measurements by stylus profiler, AFM and non-contact optical profiler, *Wear.* 190 (1995) 76–88. doi:10.1016/0043-1648(95)06697-7.
- [56] H.J. Butt, B. Cappella, M. Kappl, Force measurements with the atomic force microscope: Technique, interpretation and applications, *Surf. Sci. Rep.* 59 (2005) 1–152. doi:10.1016/j.surfrep.2005.08.003.
- [57] and X.J. Blunt, Liam, Numerical parameters for characterisation of topography, in: *Adv. Tech. Assess. Surf. Topogr. Dev. a Basis 3D Surf. Texture Stand.*, Elsevier, 2003.
- [58] G.J. Simpson, D.L. Sedin, K.L. Rowlen, Kathy L. Rowlen, K.L. Rowlen, Surface Roughness by Contact versus Tapping Mode Atomic Force Microscopy, *Langmuir.* 15 (1999) 1429–1434. doi:10.1021/la981024a.
- [59] S.J. Fang, S. Haplepete, W. Chen, C.R. Helms, H. Edwards, Analyzing atomic force microscopy images using spectral methods, *J. Appl. Phys.* 82 (1997) 5891–5898. doi:10.1063/1.366489.

- [60] H. Assender, V. Bliznyuk, K. Porfyraakis, How Surface Topography Relates to Materials' properties, *Science* (80-. ). 297 (2002) 973–976.
- [61] A.N. Patel, C. Kranz, (Multi)functional Atomic Force Microscopy Imaging, *Annu. Rev. Anal. Chem.* 11 (2018) 329–350. doi:10.1146/annurev-anchem-061417-125716.
- [62] E.M. V Hoek, S. Bhattacharjee, M. Elimelech, Effect of membrane surface roughness on colloid-membrane DLVO interactions, *Langmuir.* 19 (2003) 4836–4847. doi:10.1021/la027083c.
- [63] D. Johnson, D.L. Oatley-Radcliffe, N. Hilal, *Atomic Force Microscopy (AFM)*, Elsevier B.V., 2017. doi:10.1016/B978-0-444-63776-5.00007-3.
- [64] Mandelbrot B. B., Passoja D. E., Paullay A. J., Fractal character of fracture surfaces of metals, *Nature.* 308 (1984) 721–722.
- [65] M.Y. Victor, N.A. Stelmashenko, and R. Blumenfeld, Fracture surfaces: a critical review of fractal studies and a novel morphological analysis of scanning tunneling microscopy measurements, *Prog. Mater. Sci.* 38 (1994) 425–474. <https://www.theverge.com/2018/3/9/17100518/waymo-self-driving-truck-google-atlanta>.
- [66] T. Onda, S. Shibuichi, N. Satoh, K. Tsujii, Super-Water-Repellent Fractal Surfaces, *Langmuir.* 12 (2002) 2125–2127. doi:10.1021/la950418o.
- [67] K. Tsujii, Fractal Materials and Their Functional Properties, *Polym. J.* 40 (2008) 785–799. doi:10.1295/polymj.pj2008053.
- [68] J.R. Werber, C.O. Osuji, M. Elimelech, Materials for next-generation desalination and water purification membranes, *Nat. Rev. Mater.* 1 (2016). doi:10.1038/natrevmats.2016.18.
- [69] K.H. Choo, C.H. Lee, Understanding membrane fouling in terms of surface free energy changes, *J. Colloid Interface Sci.* 226 (2000) 367–370. doi:10.1006/jcis.2000.6845.
- [70] A.R. Roudman, F.A. Digiano, Surface energy of experimental and commercial nanofiltration membranes: Effects of wetting and natural organic matter fouling, *J. Memb. Sci.* 175 (2000) 61–73. doi:10.1016/S0376-7388(00)00409-9.
- [71] S. Lee, E. Lee, M. Elimelech, S. Hong, Membrane characterization by dynamic hysteresis: Measurements, mechanisms, and implications for membrane fouling, *J. Memb. Sci.* 366 (2011) 17–24. doi:10.1016/j.memsci.2010.09.024.
- [72] Y. Baek, J. Kang, P. Theato, J. Yoon, Q. Li, X. Pan, Z. Qu, X. Zhao, Y. Jin, H. Dai, B. Yang, X. Wang, Measuring hydrophilicity of RO membranes by contact angles via sessile drop and captive bubble method: A comparative

- study, *Desalination*. 303 (2012) 23–28. doi:10.1016/j.desal.2012.07.006.
- [73] Q. Li, X. Pan, Z. Qu, X. Zhao, Y. Jin, H. Dai, B. Yang, X. Wang, Understanding the dependence of contact angles of commercially RO membranes on external conditions and surface features, *Desalination*. 309 (2013) 38–45. doi:10.1016/j.desal.2012.09.007.
- [74] M.J. Rosa, M.N. De Pinho, Membrane surface characterisation by contact angle measurements using the immersed method, *J. Memb. Sci.* 131 (1997) 167–180.
- [75] B. Han, X. Wang, J. Zheng, S. Liang, K. Xiao, J. Yu, Z. Qian, X. Huang, Determination of Surface Energy Parameters of Hydrophilic Porous Membranes via a Corrected Contact Angle Approach, *Langmuir*. 35 (2019) 15009–15016. doi:10.1021/acs.langmuir.9b02508.
- [76] H.J. Butt, R. Berger, W. Steffen, D. Vollmer, S.A.L.L.L. Weber, Adaptive Wetting - Adaptation in Wetting, *Langmuir*. 34 (2018) 11292–11304. doi:10.1021/acs.langmuir.8b01783.
- [77] A. Stammitti-Scarpone, E.J. Acosta, Solid-liquid-liquid wettability and its prediction with surface free energy models, *Adv. Colloid Interface Sci.* 264 (2019) 28–46. doi:10.1016/j.cis.2018.10.003.
- [78] M. Hayatbakhsh, M. Sadrzadeh, D. Pernitsky, S. Bhattacharjee, J. Hajinasiri, Treatment of an in situ oil sands produced water by polymeric membranes, *Desalin. Water Treat.* 57 (2016) 14869–14887.
- [79] C. Duc, A. Vlandas, G.G. Malliaras, V. Senez, Wettability of PEDOT:PSS films, *Soft Matter*. 12 (2016) 5146–5153. doi:10.1039/c6sm00599c.
- [80] R.N. Wenzel, Surface roughness and contact angle, *J. Phys. Colloid Chem.* 53 (1949) 1466–1467. doi:10.1021/j150474a015.
- [81] J. Drelich, Guidelines to measurements of reproducible contact angles using a sessile-drop technique, *Surf. Innov.* 1 (2013) 248–254. doi:10.1680/si.13.00010.
- [82] A. Marmur, Solid-Surface Characterization by Wetting, *Annu. Rev. Mater. Res.* 39 (2009) 473–489. doi:10.1146/annurev.matsci.38.060407.132425.
- [83] A. Marmur, C. Della Volpe, S. Siboni, A. Amirfazli, J.W. Drelich, Contact angles and wettability: towards common and accurate terminology, *Surf. Innov.* 5 (2017) 3–8. doi:10.1680/jsuin.17.00002.
- [84] A. Marmur, A Guide to the Equilibrium Contact Angles Maze, *Contact Angle, Wettability Adhes.* Vol. 6. 6 (2009) 18. doi:doi:10.1201/b12247-3.
- [85] A. Dupré, P. Dupré, and P.D. Dupré, Athanase, *Théorie mécanique de la chaleur*, Gauthier-Villars. (1869).

- [86] J. Berthier, K. Brakke, *The Physics of Microdrops*, Scrivener Publishing, 2012.
- [87] F.M. Fowkes, Determination of Interfacial Tensions, Contact Angles, and Dispersion Forces in Surfaces By Assuming Additivity of Intermolecular Interactions in Surfaces, *J. Phys. Chem.* 66 (1962) 382–382. doi:10.1021/j100808a524.
- [88] F.M. Fowkes, Attractive Forces At Interfaces, *Ind. Eng. Chem.* 56 (1964) 40–52. doi:10.1021/ie50660a008.
- [89] F.M. Fowkes, Donor-acceptor interactions at interfaces, *J. Adhes.* 4 (1972) 155–159. doi:10.1080/00218467208072219.
- [90] W.R. Owens DK, D.K. Owens, R.C. Wendt, R.C. Wendt., Estimation of the Surface Free Energy of Polymers, *J Appl Polym Sci.* 13 (1969) 1741–1747.
- [91] W. Rabel, Einige Aspekte der Benetzungstheorie und ihre Anwendung auf die Untersuchung und Veränderung der Oberflächeneigenschaften von Polymeren, *Farbe Und Lack.* 77 (1971) 997–1005.
- [92] D.H. Kaelble, Dispersion-polar surface tension properties of organic solids, *J. Adhes.* 2.2 (1970) 66–81.
- [93] C.J. van Oss, Development and applications of the interfacial tension between water and organic or biological surfaces, *Colloids Surfaces B Biointerfaces.* 54 (2007) 2–9. doi:10.1016/j.colsurfb.2006.05.024.
- [94] C.J. van Oss, M.K. Chaudhury, R.J. Good, Interfacial Lifshitz—van der Waals and Polar Interactions in Macroscopic Systems, *Chem. Rev.* 88 (1988) 927–941. doi:10.1021/cr00088a006.
- [95] C.. Van Oss, R.. Good, M.. Chaudhury, C.J. Van Oss;Good R.J.;Chaudhury MK, The role of van der Waals forces and hydrogen bonds in “hydrophobic interactions” between biopolymers and low energy surfaces, *Role van Der Waals Forces Hydrog. Bond. “hydrophobic Interact. between Biopolym. Low Energy Surfaces.* 111 (1986) 378–390. doi:10.1016/0021-9797(86)90041-X.
- [96] C.J. van Oss, Acid—base interfacial interactions in aqueous media, *Colloids Surfaces A Physicochem. Eng. Asp.* 78 (1993) 1–49. doi:10.1016/0927-7757(93)80308-2.
- [97] C.J. van Oss, R.J. Good, M.K. Chaudhury, Additive and nonadditive surface tension components and the interpretation of contact angles, *Langmuir.* 4 (1988) 884–891. doi:10.1021/la00082a018.
- [98] C.J. Van Oss, R.F. Giese, The hydrophilicity and hydrophobicity of clay minerals, *Clays Clay Miner.* 43 (1995) 474–477. doi:10.1346/CCMN.1995.0430411.

- [99] C.J. van Oss, M.K. Chaudhury, R.J. Good, Monopolar surfaces, *Adv. Colloid Interface Sci.* 28 (1987) 35–64. doi:10.1016/0001-8686(87)80008-8.
- [100] C.J. Van Oss, C.J. van Oss, C.J. Van Oss, C.J. van Oss, C.J. Van Oss, *Interfacial Forces in Aqueous Media*, 2nd ed., Taylor & Francis Group, 2006.
- [101] P.K.K. Sharma, K. Hanumantha Rao, Analysis of different approaches for evaluation of surface energy of microbial cells by contact angle goniometry, *Adv. Colloid Interface Sci.* 98 (2002) 341–463. doi:10.1016/S0001-8686(02)00004-0.
- [102] D.Y. Kwok, D. Li, A.W. Neumann, L. Y., A.W. Neumann, D. Li, A.W. Neumann, Evaluation of the Lifshitz-van der Waals/Acid-Base Approach To Determine Interfacial Tensions, *Langmuir.* 10 (1994) 1323–1328. doi:10.1021/la00016a057.
- [103] A. Holländer, On the selection of test liquid for the Evaluation of Acid-Base Properties of Solid Surfaces by Contact Angle Goniometry., *J. Coll.* 169 (1995) 493–496.
- [104] W. Wu, R.F. Giese, C.J. Van Oss, Evaluation of the Lifshitz-van der Waals/Acid-Base Approach to Determine Surface Tension Components, *Langmuir.* 11 (1995) 379–382. doi:10.1021/la00001a064.
- [105] C.J. van Oss, *The Properties of Water and their Role in Colloidal and Biological Systems*, Elsevier, 2008. doi:10.1016/S1573-4285(06)80104-3.
- [106] E.A. Vogler, Structure and reactivity of water at biomaterial surfaces, *Adv. Colloid Interface Sci.* 74 (1998) 69–117.
- [107] M. Liu, S. Wang, L. Jiang, Nature-inspired superwettability systems, *Nat. Rev. Mater.* 2 (2017). doi:10.1038/natrevmats.2017.36.
- [108] Y. Tian, L. Jiang, Wetting: Intrinsically robust hydrophobicity, *Nat. Mater.* 12 (2013) 291–292. doi:10.1038/nmat3610.
- [109] C. Guo, S. Wang, H. Liu, L. Feng, Y. Song, L. Jiang, Wettability alteration of polymer surfaces produced by scraping, *J. Adhes. Sci. Technol.* 22 (2008) 395–402. doi:10.1163/156856108X304832.
- [110] S. Wang, K. Liu, X. Yao, L. Jiang, Bioinspired surfaces with superwettability: New insight on theory, design, and applications, *Chem. Rev.* 115 (2015) 8230–8293. doi:10.1021/cr400083y.
- [111] B. Samuel, H. Zhao, K.Y. Law, Study of wetting and adhesion interactions between water and various polymer and superhydrophobic surfaces, *J. Phys. Chem. C.* 115 (2011) 14852–14861. doi:10.1021/jp2032466.
- [112] K.Y. Law, Definitions for hydrophilicity, hydrophobicity, and superhydrophobicity: Getting the basics right, *J. Phys. Chem. Lett.* 5 (2014)



686–688. doi:10.1021/jz402762h.

- [113] S. Zarghami, T. Mohammadi, M. Sadrzadeh, B. Van der Bruggen, B. Van der Bruggen, Superhydrophilic and underwater superoleophobic membranes - A review of synthesis methods, *Prog. Polym. Sci.* 98 (2019) 101166. doi:10.1016/j.progpolymsci.2019.101166.
- [114] S. Zarghami, T. Mohammadi, M. Sadrzadeh, Preparation, characterization and fouling analysis of in-air hydrophilic/underwater oleophobic bio-inspired polydopamine coated PES membranes for oily wastewater treatment, *J. Memb. Sci.* 582 (2019) 402–413. doi:10.1016/j.memsci.2019.04.020.
- [115] S. Zarghami, T. Mohammadi, M. Sadrzadeh, B. Van der Bruggen, Bio-inspired anchoring of amino-functionalized multi-wall carbon nanotubes (N-MWCNTs) onto PES membrane using polydopamine for oily wastewater treatment, *Sci. Total Environ.* 711 (2020) 134951. doi:10.1016/j.scitotenv.2019.134951.
- [116] H. Bellanger, T. Darmanin, E. Taffin De Givenchy, F. Guittard, Chemical and physical pathways for the preparation of superoleophobic surfaces and related wetting theories, *Chem. Rev.* 114 (2014) 2694–2716. doi:10.1021/cr400169m.
- [117] Y.C. Jung, B. Bhushan, Wetting behavior of water and oil droplets in three-phase interfaces for hydrophobicity/philicity and oleophobicity/philicity, *Langmuir.* 25 (2009) 14165–14173. doi:10.1021/la901906h.
- [118] J. Schultz, M. Nardin, Determination of the surface energy of solids by two-liquid phase method, *Mod. Approaches to Wettability.* (1992) 73–100.
- [119] B. Khorshidi, T. Thundat, B.A. Fleck, M. Sadrzadeh, A novel approach toward fabrication of high performance thin film composite polyamide membranes, *Sci. Rep.* 6 (2016) 1–10. doi:10.1038/srep22069.
- [120] S. Yoon, Principle of Membrane Filtration, in: *Membr. Bioreact. Process.*, CRC Press Taylor & Francis Group, 2018: pp. 1–49. doi:10.1201/b18631.
- [121] V. Eric M, E. Menachem, H. Seungkwan, Influence of membrane properties, solution chemistry, and hydrodynamics on colloidal fouling of reverse osmosis and nanofiltration membranes., *J. Memb. Sci.* 188 (2001) 115–128. doi:Doi 10.1016/S0376-7388(01)00376-3.
- [122] S.Y. Kwak, S.G. Jung, S.H. Kim, Structure-motion-performance relationship of flux-enhanced reverse osmosis (RO) membranes composed of aromatic polyamide thin films, *Environ. Sci. Technol.* 35 (2001) 4334–4340. doi:10.1021/es010630g.
- [123] S. Karan, Z. Jiang, A.G. Livingston, Sub-10 nm polyamide nanofilms with ultrafast solvent transport for molecular separation, *Science* (80-. ). 348 (2015) 1347–1351. doi:10.1126/science.aaa5058.

- [124] M.H. Yildirim, D. Stamatialis, M. Wessling, Dimensionally stable Nafion-polyethylene composite membranes for direct methanol fuel cell applications, *J. Memb. Sci.* 321 (2008) 364–372. doi:10.1016/j.memsci.2008.05.013.
- [125] F. Liu, B. Yi, D. Xing, J. Yu, H. Zhang, Nafion/PTFE composite membranes for fuel cell applications, *J. Memb. Sci.* 212 (2003) 213–223. doi:10.1016/S0376-7388(02)00503-3.
- [126] S. Zhao, K. Huang, H. Lin, Impregnated Membranes for Water Purification Using Forward Osmosis, *Ind. Eng. Chem. Res.* 54 (2015) 12354–12366. doi:10.1021/acs.iecr.5b03241.
- [127] M.N. MacGregor-Ramiasa, K. Vasilev, M.N. MacGregor-Ramiasa, Questions and Answers on the Wettability of Nano-Engineered Surfaces, *Adv. Mater. Interfaces.* 4 (2017) 1–24. doi:10.1002/admi.201700381.
- [128] M. Sadrzadeh, J. Hajinasiri, S. Bhattacharjee, D. Pernitsky, Nanofiltration of oil sands boiler feed water: Effect of pH on water flux and organic and dissolved solid rejection, *Sep. Purif. Technol.* 141 (2015) 339–353. doi:10.1016/j.seppur.2014.12.011.
- [129] H. Jacobasch, J. Schurz, Characterization of polymer surfaces by means of electrokinetic measurements, *Prog. Colloid Polym. Sci.* 77 (1988) 40–48.
- [130] M. Elimelech, W.H. Chen, J.J. Waypa, Measuring the zeta (electrokinetic) potential of reverse osmosis membranes by a streaming potential analyzer, *Desalination.* 95 (1994) 269–286.
- [131] R.J. Hunter, *Zeta Potential in Colloid Science, Principals and Applications*, Academic Press, New York, 1981.
- [132] J.N. Israelachvili, *Intermolecular and surface forces*, Third Ed., Academic Press, 2011.
- [133] J.H. Masliyah, S. Bhattacharjee, J.N. Israelachvili, *Electrokinetic and colloid transport phenomena*, 2nd ed., John Wiley & Sons, New York, 2006. doi:10.1002/0471799742.
- [134] B.J. Kirby, E.F. Hasselbrink, Zeta potential of microfluidic substrates: 2. Data for polymers, *Electrophoresis.* 25 (2004) 203–213. doi:10.1002/elps.200305755.
- [135] B.J. Kirby, E.F. Hasselbrink, Zeta potential of microfluidic substrates: 1. Theory, experimental techniques, and effects on separations, *Electrophoresis.* 25 (2004) 187–202. doi:10.1002/elps.200305754.
- [136] D.L. Oatley-Radcliffe, N. Aljohani, P.M. Williams, N. Hilal, *Electrokinetic Phenomena for Membrane Charge*, Elsevier B.V., 2017. doi:10.1016/B978-0-444-63776-5.00018-8.

- [137] A.E. a. E. Childress, M. Elimelech, Effect of solution chemistry on the surface charge of polymeric reverse osmosis and nanofiltration membranes, *J. Memb. Sci.* 119 (1996) 253–268. doi:10.1016/0376-7388(96)00127-5.
- [138] C. Lettmann, D. MoÈckel, E. Staude, Permeation and tangential flow streaming potential measurements for electrokinetic characterization of track-etched microfiltration membranes, *J. Memb. Sci.* 159 (1999) 243–251. doi:10.1016/S0376-7388(99)00067-8.
- [139] M.J. Ariza, J. Benavente, Streaming potential along the surface of polysulfone membranes: A comparative study between two different experimental systems and determination of electrokinetic and adsorption parameters, *J. Memb. Sci.* 190 (2001) 119–132. doi:10.1016/S0376-7388(01)00430-6.
- [140] A. Yaroshchuk, T. Luxbacher, Interpretation of electrokinetic measurements with porous films: Role of electric conductance and streaming current within porous structure, *Langmuir*. 26 (2010) 10882–10889. doi:10.1021/la100777z.
- [141] H.J. Jacobasch, G. Baubock, J. Schurz, Problems and results of zeta-potential measurements on fibers, *Colloid Polym. Sci.* 263 (1985) 3–24.
- [142] M. Mulder, *Basic Principles of Membrane Technology*, Kluwer Academic Publishers, 1996.
- [143] C.C. Wamser, M.I. Gilbert, Detection of Surface Functional Group Asymmetry in Interfacially-Polymerized Films by Contact Angle Titrations, *Langmuir*. 8 (1992) 1608–1614. doi:10.1021/la00042a019.
- [144] T.S. Wong, T. Sun, L. Feng, J. Aizenberg, Interfacial materials with special wettability, *MRS Bull.* 38 (2013) 366–371. doi:10.1557/mrs.2013.99.
- [145] M.D. Firouzjaei, A.A. Shamsabadi, S.A. Aktij, S.F. Seyedpour, M. Sharifian, A. Rahimpour, M.R. Esfahani, M. Ulbricht, M. Soroush, Exploiting Synergetic Effects of Graphene Oxide and a Silver-Based Metal-Organic Framework to Enhance Antifouling and Anti-Biofouling Properties of Thin-Film Nanocomposite Membranes, *ACS Appl. Mater. Interfaces*. 10 (2018) 42967–42978. doi:10.1021/acsami.8b12714.
- [146] A. Bogler, S. Lin, E. Bar-Zeev, Biofouling of membrane distillation, forward osmosis and pressure retarded osmosis: Principles, impacts and future directions, *J. Memb. Sci.* 542 (2017) 378–398. doi:10.1016/j.memsci.2017.08.001.
- [147] R.E. Baier, Surface behaviour of biomaterials: The theta surface for biocompatibility, *J. Mater. Sci. Mater. Med.* 17 (2006) 1057–1062. doi:10.1007/s10856-006-0444-8.
- [148] C. Boo, S. Hong, M. Elimelech, Relating Organic Fouling in Membrane Distillation to Intermolecular Adhesion Forces and Interfacial Surface Energies, *Environ. Sci. Technol.* 52 (2018) 14198–14207.

doi:10.1021/acs.est.8b05768.

- [149] W. Wu, G.H. Nancollas, Interfacial free energies and crystallization in aqueous media, *J. Colloid Interface Sci.* 182 (1996) 365–373. doi:10.1006/jcis.1996.0475.
- [150] L.G. Benning, G.A. Waychunas, Nucleation, Growth, and Aggregation of Mineral Phases: Mechanisms and Kinetic Controls BT - Kinetics of Water-Rock Interaction, *Kinet. Water-Rock Interact.* (2008) 259–333. [http://dx.doi.org/10.1007/978-0-387-73563-4\\_7%5Cnpapers2://publication/doi/10.1007/978-0-387-73563-4\\_7](http://dx.doi.org/10.1007/978-0-387-73563-4_7%5Cnpapers2://publication/doi/10.1007/978-0-387-73563-4_7).
- [151] T. Tong, S. Zhao, C. Boo, S.M. Hashmi, M. Elimelech, Relating Silica Scaling in Reverse Osmosis to Membrane Surface Properties, *Environ. Sci. Technol.* 51 (2017) 4396–4406. doi:10.1021/acs.est.6b06411.
- [152] B. Mi, M. Elimelech, Silica scaling and scaling reversibility in forward osmosis, *Desalination.* 312 (2013) 75–81. doi:10.1016/j.desal.2012.08.034.
- [153] Z. Xiao, H. Guo, H. He, Y. Liu, X. Li, Y. Zhang, H. Yin, A. V. Volkov, T. He, Unprecedented scaling/fouling resistance of omniphobic polyvinylidene fluoride membrane with silica nanoparticle coated micropillars in direct contact membrane distillation, *J. Memb. Sci.* 599 (2020) 117819. doi:10.1016/j.memsci.2020.117819.
- [154] R.R. Choudhury, J.M. Gohil, S. Mohanty, S.K. Nayak, Antifouling, fouling release and antimicrobial materials for surface modification of reverse osmosis and nanofiltration membranes, *J. Mater. Chem. A.* 6 (2018) 313–333. doi:10.1039/c7ta08627j.
- [155] S. Jeon, C.H. Park, S.H. Park, M.G. Shin, H.J. Kim, K.Y. Baek, E.P. Chan, J. Bang, J.H. Lee, Star polymer-assembled thin film composite membranes with high separation performance and low fouling, *J. Memb. Sci.* 555 (2018) 369–378. doi:10.1016/j.memsci.2018.03.075.
- [156] S.H. Maruf, A.R. Greenberg, J. Pellegrino, Y. Ding, Fabrication and characterization of a surface-patterned thin film composite membrane, *J. Memb. Sci.* 452 (2014) 11–19. doi:10.1016/j.memsci.2013.10.017.
- [157] I.M.A. ElSherbiny, A.S.G. Khalil, M. Ulbricht, Tailoring Surface Characteristics of Polyamide Thin-Film Composite Membranes toward Pronounced Switchable Wettability, *Adv. Mater. Interfaces.* 6 (2019) 1–12. doi:10.1002/admi.201801408.
- [158] T.H. Zhang, X.Y. Liu, H.Z. Tian, Y.L. Xiang, How Does a Transient Amorphous Precursor Template Crystallization, *J. Am. Chem. Soc.* 129 (2007) 13520–13526. doi:10.1021/ja073598k.
- [159] C. Huang, Z. Guo, The wettability of gas bubbles: From macro behavior to nano structures to applications, *Nanoscale.* 10 (2018) 19659–19672.

doi:10.1039/c8nr07315e.

- [160] E. Davis, Y. Liu, L. Jiang, Y. Lu, S. Ndao, Wetting characteristics of 3-dimensional nanostructured fractal surfaces, *Appl. Surf. Sci.* 392 (2017) 929–935. doi:10.1016/j.apsusc.2016.09.102.
- [161] M.M. Pendergast, E.M.V. Hoek, A review of water treatment membrane nanotechnologies, *Energy Environ. Sci.* 4 (2011) 1946–1971. doi:10.1039/c0ee00541j.
- [162] A. Lee, J.W. Elam, S.B. Darling, Membrane materials for water purification: Design, development, and application, *Environ. Sci. Water Res. Technol.* 2 (2016) 17–42. doi:10.1039/c5ew00159e.
- [163] Y.-J. Zhao, K.-F. Wu, Z.-J. Wang, L. Zhao, S.-S. Li, Fouling and cleaning of membrane—a literature review, *J. Environ. Sci.* 12 (2000) 241–251. doi:1001-0742(2000)02\_0241-11.
- [164] B. Khorshidi, S.A. Hosseini, G. Ma, M. McGregor, M. Sadrzadeh, Novel nanocomposite polyethersulfone- antimony tin oxide membrane with enhanced thermal, electrical and antifouling properties, *Polymer (Guildf)*. 163 (2019) 48–56. doi:10.1016/J.POLYMER.2018.12.058.
- [165] V. Kochkodan, D.J. Johnson, N. Hilal, Polymeric membranes: Surface modification for minimizing (bio)colloidal fouling, *Adv. Colloid Interface Sci.* 206 (2014) 116–140. doi:10.1016/j.cis.2013.05.005.
- [166] M. Elimelech, X. Zhu, A.E. Childress, S. Hong, Role of membrane surface morphology in colloidal fouling of cellulose acetate and composite aromatic polyamide reverse osmosis membranes, *J. Memb. Sci.* 127 (1997) 101–109.
- [167] P.S. Singh, A.P. Rao, P. Ray, A. Bhattacharya, K. Singh, N.K. Saha, A.V.R. Reddy, Techniques for characterization of polyamide thin film composite membranes, *Desalination*. 282 (2011) 78–86. doi:10.1016/j.desal.2011.04.039.
- [168] H.J. Busscher, A.W.J. van Pelt, P. d. Boer, H.P. d. Jong, J. Arends, The effect of surface roughening of polymers on measured contact angles of liquids, *Colloids and Surfaces*. 9 (1984) 319–331.
- [169] R.J.J. Good, M.K.K. Chaudhury, C. Yeung, C. Yeung., A new approach for determining roughness by means of contact angles on solids, in: *First Int. Congr. Adhes. Sci. Technol., Mittal Festschrift, 1998*: pp. 181–197.
- [170] J.J. Kuna, K. Voitchovsky, C. Singh, H. Jiang, S. Mwenifumbo, P.K. Ghorai, M.M. Stevens, S.C. Glotzer, F. Stellacci, The effect of nanometre-scale structure on interfacial energy, *Nat. Mater.* 8 (2009) 837–842. doi:10.1038/nmat2534.
- [171] K. Voitchovsky, J.J. Kuna, S.A. Contera, E. Tosatti, F. Stellacci, Direct

- mapping of the solid-liquid adhesion energy with subnanometre resolution, *Nat. Nanotechnol.* 5 (2010) 401–405. doi:10.1038/nnano.2010.67.
- [172] M. Taniguchi, G. Belfort, Correcting for Surface Roughness: Advancing and Receding Contact Angles, *Langmuir.* 18 (2002) 6465–6467. doi:10.1021/la020145e.
- [173] J. Tröger, K. Lunkwitz, W. Bürger, J. Troger, K. Lunkwitz, W. Burger, J. Tröger, K. Lunkwitz, W. Bürger, J. Tro, K. Lunkwitz, W. Bu, Determination of the Surface Tension of Microporous Membranes Using Contact Angle Measurements, *J. Colloid Interface Sci.* 286 (1997) 281–286.
- [174] R.J. Good, A Thermodynamic Derivation of Wenzel’s Modification of Young’s Equation for Contact Angles; Together with a Theory of Hysteresis, *J. Am. Chem. Soc.* 74 (1952) 5041–5042. doi:10.1021/ja01140a014.
- [175] B. Khorshidi, T. Thundat, B.A. Fleck, M. Sadrzadeh, Thin film composite polyamide membranes: parametric study on the influence of synthesis conditions, *RSC Adv.* 5 (2015) 54985–54997. doi:10.1039/c5ra08317f.
- [176] B. Khorshidi, I. Biswas, T. Ghosh, T. Thundat, M. Sadrzadeh, Robust fabrication of thin film polyamide-TiO<sub>2</sub> nanocomposite membranes with enhanced thermal stability and anti-biofouling propensity, *Sci. Rep.* 8 (2018) 784. doi:10.1038/s41598-017-18724-w.
- [177] B.N.J. Persson, O. Albohr, U. Tartaglino, A.I. Volokitin, E. Tosatti, On the nature of surface roughness with application to contact mechanics, sealing, rubber friction and adhesion, *J. Phys. Condens. Matter.* 17 (2005). doi:10.1088/0953-8984/17/1/R01.
- [178] O. Coronell, B.J. Mariñas, X. Zhang, D.G. Cahill, Quantification of functional groups and modeling of their ionization behavior in the active layer of FT30 reverse osmosis membrane, *Environ. Sci. Technol.* 42 (2008) 5260–5266. doi:10.1021/es8002712.
- [179] J. Song, S. Rezaee, W. Guo, B. Hernandez, M. Puerto, F.M. Vargas, G.J. Hirasaki, S.L. Biswal, Evaluating physicochemical properties of crude oil as indicators of low-salinity-induced wettability alteration in carbonate minerals, *Sci. Rep.* 10 (2020) 1–16. doi:10.1038/s41598-020-60106-2.
- [180] K. Huang, P. Rowe, C. Chi, V. Sreepal, T. Bohn, K.G. Zhou, Y. Su, E. Prestat, P.B. Pillai, C.T. Cherian, A. Michaelides, R.R. Nair, Cation-controlled wetting properties of vermiculite membranes and its promise for fouling resistant oil–water separation, *Nat. Commun.* 11 (2020) 1–10. doi:10.1038/s41467-020-14854-4.
- [181] J. Drelich, Y.U. Wang, Charge heterogeneity of surfaces: Mapping and effects on surface forces, *Adv. Colloid Interface Sci.* 165 (2011) 91–101. doi:10.1016/j.cis.2010.12.009.

- [182] S. Sinha, H. Jing, H.S. Sachar, S. Das, Role of plasma membrane surface charges in dictating the feasibility of membrane-nanoparticle interactions, *Appl. Phys. Lett.* 111 (2017). doi:10.1063/1.5011208.
- [183] W. Annie, T. Hart, Measurement of  $\zeta$  potential of  $\text{YBa}_2\text{Cu}_3\text{O}_{7-\delta}$  from the adsorption of hydronium ions ( $\text{H}^+$ ,  $\text{OH}^-$ ), *Appl. Phys. Lett.* 60 (1992) 1750. doi:10.1142/s0217984988001326.
- [184] S.M. Neale, The electrical double layer, the electrokinetic potential, and the streaming current, *Trans. Faraday Soc.* 42 (1946) 473–478.
- [185] R. Edelberg, F. Hazel, Streaming Potential Measurements with Phosphors, *J. Electrochem. Soc.* 96 (1949) 13. doi:10.1149/1.2776765.
- [186] G.A. Parks, P.L. De Bruyn, The zero point of charge of oxides, *J. Phys. Chem.* 66 (1962) 967–973. doi:10.1021/j100812a002.
- [187] J. Israelachvili, *Electrostatic Forces between Surfaces in Liquids*, 3rd ed., Academic press, 2011. doi:10.1017/CBO9781107415324.004.
- [188] J.H. Masliyah, S. Bhattacharjee, *Electrokinetic and Colloid Transport Phenomena*, 2005. doi:10.1002/0471799742.
- [189] R.J. Hunter, *Electrokinetics and the zeta potential*, *Found. Colloid Sci.* Oxford Univ. Press. New York. (2001) 373–434.
- [190] H. Horiuchi, A. Nikolov, D.T. Wasan, Calculation of the surface potential and surface charge density by measurement of the three-phase contact angle, *J. Colloid Interface Sci.* 385 (2012) 218–224. doi:10.1016/j.jcis.2012.06.078.
- [191] A. Carre, V. Lacarriere, Study of surface charge properties of minerals and surface-modified substrates by wettability measurements, in: *Contact Angle, Wettability Adhes.*, 2006: pp. 267–280.
- [192] E. McCafferty, J.P. Wightman, Determination of the acid-base properties of metal oxide films and of polymers by contact angle measurements, *J. Adhes. Sci. Technol.* 13 (1999) 1415–1436. doi:10.1163/156856199X00569.
- [193] D.F. Billett, D.B. Hough, R.H. Ottewill, Studies on the contact angle of the charged silver iodide-solution-vapour interface, *J. Electroanal. Chem.* 74 (1976) 107–120. doi:10.1016/S0022-0728(76)80217-3.
- [194] T. Preočanin, A. Selmani, P. Lindqvist-Reis, F. Heberling, N. Kallay, J. Lützenkirchen, Surface charge at Teflon/aqueous solution of potassium chloride interfaces, *Colloids Surfaces A Physicochem. Eng. Asp.* 412 (2012) 120–128. doi:10.1016/j.colsurfa.2012.07.025.
- [195] P.B. Welzel, C. Rauwolf, O. Yudin, K. Grundke, Influence of aqueous electrolytes on the wetting behavior of hydrophobic solid polymers - Low-rate dynamic liquid/fluid contact angle measurements using axisymmetric drop

- shape analysis, *J. Colloid Interface Sci.* 251 (2002) 101–108. doi:10.1006/jcis.2002.8356.
- [196] J. Drelich, J.D. Miller, R.J. Good, The effect of drop (bubble) size on advancing and receding contact angles for heterogeneous and rough solid surfaces as observed with sessile-drop and captive-bubble techniques, *J. Colloid Interface Sci.* 179 (1996) 37–50. doi:10.1006/jcis.1996.0186.
- [197] C. Bourgès-Monnier, M.E.R. Shanahan, Influence of Evaporation on Contact Angle, *Langmuir*. 11 (1995) 2820–2829. doi:10.1021/la00007a076.
- [198] H.Y. Erbil, G. McHale, M.I. Newton, Drop evaporation on solid surfaces: Constant contact angle mode, *Langmuir*. 18 (2002) 2636–2641.
- [199] G. Lippmann, Relations between electrical and capillary phenomena, Diss. Gauthier-Villars. (1875).
- [200] T. Winkler, Determining the surface tension of liquids by measurements on pendant drops, Tech. Note, KRÜSS GmbH. 49 (2010) 1–5.
- [201] F. Hamadi, H. Latrache, M. Zekraoui, M. Ellouali, J. Bengourram, Effect of pH on surface energy of glass and Teflon and theoretical prediction of *Staphylococcus aureus* adhesion, *Mater. Sci. Eng. C*. 29 (2009) 1302–1305. doi:10.1016/j.msec.2008.10.023.
- [202] R. Zimmermann, S. Dukhin, C. Werner, Electrokinetic measurements reveal interracial charge at polymer films caused by simple electrolyte ions, *J. Phys. Chem. B*. 105 (2001) 8544–8549. doi:10.1021/jp004051u.
- [203] J. Drelich, E. Chibowski, D.D. Meng, K. Terpilowski, Hydrophilic and superhydrophilic surfaces and materials, *Soft Matter*. 7 (2011) 9804–9828. doi:10.1039/c1sm05849e.
- [204] L.A. Girifalco, R.J. Good, A theory for the estimation of surface and interfacial energies. I. Derivation and application to interfacial tension, *J. Phys. Chem.* 61 (1957) 904–909. doi:10.1021/j150553a013.
- [205] R.J. Good, L.A. Girifalco, A theory for estimation of surface and interfacial energies. III. Estimation of surface energies of solids from contact angle data, *J. Phys. Chem.* 64 (1960) 561–565. doi:10.1021/j100834a012.
- [206] H. Yasuda, A.K. Sharma, T. Yasuda, Effect of orientation and mobility of polymer molecules at surfaces on contact angle and its hysteresis, *J. Polym. Sci. Polym. Phys. Ed.* 19 (1981) 1285–1291. doi:10.1002/pol.1981.180190901.
- [207] Y.L. Chen, C.A. Helm, J.N. Israelachvili, Molecular mechanisms associated with adhesion and contact angle hysteresis of monolayer surfaces, *J. Phys. Chem.* 95 (1991) 10736–10747. doi:10.1021/j100179a041.



- [208] J. Schultz, A. Carré, C. Mazeau, Formation and rupture of grafted polyethylene/aluminium interfaces, *Int. J. Adhes. Adhes.* 4 (1984) 163–168.
- [209] B. Pan, F. Jones, Z. Huang, Y. Yang, Y. Li, S.H. Hejazi, S. Iglauer, Methane (CH<sub>4</sub>) Wettability of Clay-Coated Quartz at Reservoir Conditions, *Energy and Fuels.* 33 (2019) 788–795. doi:10.1021/acs.energyfuels.8b03536.
- [210] F.E. Bartell, H.J. Osterhof, Determination of the Wettability of a Solid by a Liquid: Relation of Adhesion Tension to Stability of Color Varnish and Lacquer Systems, *Ind. Eng. Chem.* 19 (1927) 1277–1280. doi:10.1021/ie50215a026.
- [211] Y. Tamai, K. Makuuchi, M. Suzuki, Experimental analysis of interfacial forces at the plane surface of solids, *J. Phys. Chem.* 71 (1967) 4176–4179. doi:10.1021/j100872a002.
- [212] A. El-Shimi, E.D. Goddard, Wettability of some low energy surfaces. II. Oils on solids submerged in water, *J. Colloid Interface Sci.* 48 (1974) 249–255. doi:10.1016/0021-9797(74)90159-3.
- [213] Y. Tamai, T. Matsunaga, K. Horiuchi, Surface energy analysis of several organic polymers. Comparison of the two-liquid-contact-angle method with the one-liquid-contact-angle method, *J. Colloid Interface Sci.* 60 (1977) 112–116. doi:10.1016/0021-9797(77)90261-2.
- [214] J. Schultz, K. Tsutsumi, J.-B. Donnet., Surface Properties of High-Energy Solids, *J. Colloid Interface Sci.* 59 (1977) 272–276.
- [215] B.P. Binks, J.H. Clint, Solid wettability from surface energy components: Relevance to pickering emulsions, *Langmuir.* 18 (2002) 1270–1273. doi:10.1021/la011420k.
- [216] K. Trinavee, N.S.K. Gunda, S.K. Mitra, Anomalous Wetting of Underliquid Systems: Oil Drops in Water and Water Drops in Oil, *Langmuir.* 34 (2018) 11695–11705. doi:10.1021/acs.langmuir.8b02569.
- [217] J.N. Israelachvili, M.L. Gee, Contact Angles on Chemically Heterogeneous Surfaces, *Langmuir.* 5 (1989) 288–289. doi:10.1021/la00085a059.
- [218] A. Marmur, Soft contact: Measurement and interpretation of contact angles, *Soft Matter.* 2 (2006) 12–17. doi:10.1039/b514811c.
- [219] E. Ruckenstein, S. V. Gourisankar, Surface restructuring of polymeric solids and its effect on the stability of the polymer-water interface, *J. Colloid Interface Sci.* 109 (1986) 557–566. doi:10.1016/0021-9797(86)90337-1.
- [220] J.N. Israelachvili, Adhesion and Wetting Phenomena, in: *Intermol. Surf. Forces*, 3rd ed., Academic Press, 2015: pp. 419–460.
- [221] D.Y. Kwok, A.W. Neumann, Contact angles and surface energetics, *Prog.*

- Colloid Polym. Sci. 109 (1998) 170–184. doi:10.1007/bfb0118169.
- [222] P. -J Sell, A.W. Neumann, The Surface Tension of Solids, *Angew. Chemie Int. Ed. English*. 5 (1966) 299–307. doi:10.1002/anie.196602991.
- [223] A.W. Neumann, R.J. Good, C.J. Hope, M. Sejpal, An equation-of-state approach to determine surface tensions of low-energy solids from contact angles, *J. Colloid Interface Sci.* 49 (1974) 291–304. doi:10.1016/0021-9797(74)90365-8.
- [224] S. Wu, Calculation of interfacial tension in polymer systems, *J. Polym. Sci. Part C Polym. Symp.* 34 (1971) 19–30. doi:10.1002/polc.5070340105.
- [225] C.L. Yaws, *Viscosity of Liquid- Organic Compounds*, Second Edi, Elsevier Inc., 2014. doi:10.1016/B978-0-323-28658-9/00003-2.
- [226] C.L. Yaws, *Surface Tension – Organic Compounds*, in: *Thermophys. Prop. Chem. Hydrocarb.*, Second Edi, Elsevier Inc., 2014: pp. 718–841. doi:10.1016/B978-0-323-28659-6/00019-7.
- [227] Y. Tian, B. Su, L. Jiang, Interfacial Material System Exhibiting Superwettability, *Adv. Mater.* 26 (2014) 6872–6897. doi:10.1002/adma.201400883.
- [228] J.B. Boreyko, C.H. Chen, Self-propelled dropwise condensate on superhydrophobic surfaces, *Phys. Rev. Lett.* 103 (2009) 2–5. doi:10.1103/PhysRevLett.103.184501.
- [229] R.D. Narhe, D.A. Beysens, Nucleation and growth on a superhydrophobic grooved surface, *Phys. Rev. Lett.* 93 (2004) 1–4. doi:10.1103/PhysRevLett.93.076103.
- [230] J.V. Timonen, M. Latikka, L. Leibler, R.H. Ras, O. Ikkala, Switchable static and dynamic self-assembly of magnetic droplets on superhydrophobic surfaces, *Science* (80-. ). 341 (2013) 253–258. doi:10.7551/mitpress/8876.003.0036.
- [231] M. Schneemilch, W.J.J. Welters, R.A. Hayes, J. Ralston, Electrically induced changes in dynamic wettability, *Langmuir*. 16 (2000) 2924–2927. doi:10.1021/la990524g.
- [232] A.M. Cazabat, F. Heslot, S.M. Troian, P. Carles, Fingering instability of thin spreading, *Nature*. 245 (1990) 118–143. doi:10.1016/0021-9797(80)90501-9.
- [233] M.A. Frysali, S.H. Anastasiadis, Temperature- and/or pH-Responsive Surfaces with Controllable Wettability: From Parahydrophobicity to Superhydrophilicity, *Langmuir*. 33 (2017) 9106–9114. doi:10.1021/acs.langmuir.7b02098.
- [234] S. Goossens, D. Seveno, R. Rioboo, A. Vaillant, J. Conti, J. De Coninck, Can

we predict the spreading of a two-liquid system from the spreading of the corresponding liquid-air systems?, *Langmuir*. 27 (2011) 9866–9872. doi:10.1021/la200439e.

- [235] A. Seshadri, E.C. Forrest, K. Shirvan, Why ionizing radiation enhances surface wettability, *Appl. Surf. Sci.* 514 (2020) 145935. doi:10.1016/j.apsusc.2020.145935.
- [236] X. Jin, A. Jawor, S. Kim, E.M.V. Hoek, Effects of feed water temperature on separation performance and organic fouling of brackish water RO membranes, *Desalination*. 239 (2009) 346–359. doi:10.1016/j.desal.2008.03.026.
- [237] S. Huang, S. Yin, F. Chen, H. Luo, Q. Tang, J. Song, Directional transport of droplets on wettability patterns at high temperature, *Appl. Surf. Sci.* 428 (2018) 432–438. doi:10.1016/j.apsusc.2017.09.158.
- [238] B. White, A. Sarkar, A.M. Kietzig, Fog-harvesting inspired by the *Stenocara* beetle - An analysis of drop collection and removal from biomimetic samples with wetting contrast, *Appl. Surf. Sci.* 284 (2013) 826–836. doi:10.1016/j.apsusc.2013.08.017.
- [239] A. Tosun, H.Y. Erbil, Evaporation rate of PTFE liquid marbles, *Appl. Surf. Sci.* 256 (2009) 1278–1283. doi:10.1016/j.apsusc.2009.10.035.
- [240] M.C. Phillips, A.C. Riddiford, Temperature dependence of contact angles, *Nature*. 205 (1965) 1005–1006. doi:10.1038/2051005b0.
- [241] H. Schonhorn, Dependence of contact angles on temperature: Polar liquids on polyethylene, *Nature*. 210 (1966) 896–897. doi:10.1038/210896a0.
- [242] F.D. Petke, B.R. Ray, Temperature dependence of contact angles of liquids on polymeric solids, *J. Colloid Interface Sci.* 31 (1969) 216–227. doi:10.1016/0021-9797(69)90329-4.
- [243] A. Baszkin, M. Nishino, L. Ter-Minassian-Saraga., Solid-Liquid Adhesion of Oxidized Polyethylene Films. Effect of Temperature on Polar Forces, *J. Colloid Interface Sci.* 54 (1976) 317–328. doi:10.1007/s10499-008-9211-9.
- [244] S.H. Yuk, M.S. Jhon, Temperature dependence of the contact angle at the polymer-water interface, *J. Colloid Interface Sci.* 116 (1987) 25–29. doi:10.1016/0021-9797(87)90093-2.
- [245] A.Y. Aydar, V. Rodriguez-Martinez, B.E. Farkas, Determination and modeling of contact angle of Canola oil and olive oil on a PTFE surface at elevated temperatures using air or steam as surrounding media, *LWT - Food Sci. Technol.* 65 (2016) 304–310. doi:10.1016/j.lwt.2015.08.022.
- [246] S. Ashokkumar, J. Adler-Nissen, P. Moller, Factors affecting the wettability of different surface materials with vegetable oil at high temperatures and its relation to cleanability, *Appl. Surf. Sci.* 263 (2012) 86–94.

doi:10.1016/j.apsusc.2012.09.002.

- [247] M.E. Diaz, M.D. Savage, R.L. Cerro, The effect of temperature on contact angles and wetting transitions for n-alkanes on PTFE, *J. Colloid Interface Sci.* 503 (2017) 159–167. doi:10.1016/j.jcis.2017.05.003.
- [248] F. Villa, M. Marengo, J. De Coninck, A new model to predict the influence of surface temperature on contact angle, *Sci. Rep.* 8 (2018) 1–10. doi:10.1038/s41598-018-24828-8.
- [249] J.W. Song, D.L. Zeng, L.W. Fan, Temperature dependence of contact angles of water on a stainless steel surface at elevated temperatures and pressures: In situ characterization and thermodynamic analysis, *J. Colloid Interface Sci.* 561 (2020) 870–880. doi:10.1016/j.jcis.2019.11.070.
- [250] J. Yong, F. Chen, Q. Yang, J. Huo, X. Hou, Superoleophobic surfaces, *Chem. Soc. Rev.* 46 (2017) 4168–4217. doi:10.1039/c6cs00751a.
- [251] R.Y.Z. Hu, A.T.A. Wang, J.P. Hartnett, Surface tension measurement of aqueous polymer solutions, *Exp. Therm. Fluid Sci.* 4 (1991) 723–729. doi:10.1016/0894-1777(91)90079-7.
- [252] S. Phuntsho, S. Vigneswaran, J. Kandasamy, S. Hong, S. Lee, H.K. Shon, Influence of temperature and temperature difference in the performance of forward osmosis desalination process, *J. Memb. Sci.* 415–416 (2012) 734–744. doi:10.1016/j.memsci.2012.05.065.
- [253] B. Liu, S. Wang, P. Zhao, H. Liang, W. Zhang, J. Crittenden, High-performance polyamide thin-film composite nanofiltration membrane: Role of thermal treatment, *Appl. Surf. Sci.* 435 (2018) 415–423. doi:10.1016/j.apsusc.2017.11.126.
- [254] Y. Zhang, Y. Wan, G. Pan, H. Yan, X. Yao, H. Shi, Y. Tang, X. Wei, Y. Liu, Surface modification of polyamide reverse osmosis membrane with organic-inorganic hybrid material for antifouling, *Appl. Surf. Sci.* 433 (2018) 139–148. doi:10.1016/j.apsusc.2017.10.043.
- [255] Y. Zhao, Z. Zhang, L. Dai, S. Zhang, Preparation of high water flux and antifouling RO membranes using a novel diacyl chloride monomer with a phosphonate group, *J. Memb. Sci.* 536 (2017) 98–107. doi:10.1016/j.memsci.2017.04.039.
- [256] Z. Yan, H. Yang, F. Qu, H. Yu, H. Liang, G. Li, J. Ma, Reverse osmosis brine treatment using direct contact membrane distillation: Effects of feed temperature and velocity, *Desalination.* 423 (2017) 149–156. doi:10.1016/j.desal.2017.09.010.
- [257] V. Vatanpour, N. Zoqi, Surface modification of commercial seawater reverse osmosis membranes by grafting of hydrophilic monomer blended with carboxylated multiwalled carbon nanotubes, *Appl. Surf. Sci.* 396 (2017)

1478–1489. doi:10.1016/j.apsusc.2016.11.195.

- [258] Y. Zhang, Y. Wan, G. Pan, H. Shi, H. Yan, J. Xu, M. Guo, Z. Wang, Y. Liu, Surface modification of polyamide reverse osmosis membrane with sulfonated polyvinyl alcohol for antifouling, *Appl. Surf. Sci.* 419 (2017) 177–187. doi:10.1016/j.apsusc.2017.05.047.
- [259] R. Pang, K. Zhang, A facile and viable approach to fabricate polyamide membranes functionalized with graphene oxide nanosheets, *RSC Adv.* 7 (2017) 53463–53471. doi:10.1039/c7ra11358g.
- [260] C. Dong, Z. Wang, J. Wu, Y. Wang, J. Wang, S. Wang, A green strategy to immobilize silver nanoparticles onto reverse osmosis membrane for enhanced anti-biofouling property, *Desalination.* 401 (2017) 32–41. doi:10.1016/j.desal.2016.06.034.
- [261] I.H. Aljundi, Desalination characteristics of TFN-RO membrane incorporated with ZIF-8 nanoparticles, *Desalination.* 420 (2017) 12–20. doi:10.1016/j.desal.2017.06.020.
- [262] R. Ma, Y.L. Ji, Y.S. Guo, Y.F. Mi, Q.F. An, C.J. Gao, Fabrication of antifouling reverse osmosis membranes by incorporating zwitterionic colloids nanoparticles for brackish water desalination, *Desalination.* 416 (2017) 35–44. doi:10.1016/j.desal.2017.04.016.
- [263] M. Safarpour, V. Vatanpour, A. Khataee, H. Zarrabi, P. Gholami, M.E. Yekavalangi, High flux and fouling resistant reverse osmosis membrane modified with plasma treated natural zeolite, *Desalination.* 411 (2017) 89–100. doi:10.1016/j.desal.2017.02.012.
- [264] R. Pang, K. Zhang, High-flux polyamide reverse osmosis membranes by surface grafting 4-(2-hydroxyethyl)morpholine, *RSC Adv.* 7 (2017) 40705–40710. doi:10.1039/C7RA06486A.
- [265] Y. Wang, Z. Wang, X. Han, J. Wang, S. Wang, Improved flux and anti-biofouling performances of reverse osmosis membrane via surface layer-by-layer assembly, *J. Memb. Sci.* 539 (2017) 403–411. doi:10.1016/j.memsci.2017.06.029.
- [266] F. Shao, C. Xu, W. Ji, H. Dong, Q. Sun, L. Yu, L. Dong, Layer-by-layer self-assembly TiO<sub>2</sub> and graphene oxide on polyamide reverse osmosis membranes with improved membrane durability, *Desalination.* 423 (2017) 21–29. doi:10.1016/j.desal.2017.09.007.
- [267] P. Lu, S. Liang, L. Qiu, Y. Gao, Q. Wang, Thin film nanocomposite forward osmosis membranes based on layered double hydroxide nanoparticles blended substrates, *J. Memb. Sci.* 504 (2016) 196–205. doi:10.1016/j.memsci.2015.12.066.
- [268] S. Surawanvijit, A. Rahardianto, Y. Cohen, An Integrated approach for

characterization of polyamide reverse osmosis membrane degradation due to exposure to free chlorine, *J. Memb. Sci.* 510 (2016) 164–173. doi:10.1016/j.memsci.2016.02.044.

- [269] H. Li, L. Peng, Y. Luo, P. Yu, Enhancement in membrane performances of a commercial polyamide reverse osmosis membrane via surface coating of polydopamine followed by the grafting of polyethylenimine, *RSC Adv.* 5 (2015) 98566–98575. doi:10.1039/c5ra20891b.
- [270] Y. Hu, K. Lu, F. Yan, Y. Shi, P. Yu, S. Yu, S. Li, C. Gao, Enhancing the performance of aromatic polyamide reverse osmosis membrane by surface modification via covalent attachment of polyvinyl alcohol (PVA), *J. Memb. Sci.* 501 (2016) 209–219. doi:10.1016/j.memsci.2015.12.003.
- [271] Z. Mai, V. Butin, M. Rakib, H. Zhu, M. Rabiller-Baudry, E. Couallier, Influence of bulk concentration on the organisation of molecules at a membrane surface and flux decline during reverse osmosis of an anionic surfactant, *J. Memb. Sci.* 499 (2016) 257–268. doi:10.1016/j.memsci.2015.10.012.
- [272] H. Isawi, M.H. El-Sayed, X. Feng, H. Shawky, M.S. Abdel Mottaleb, Surface nanostructuring of thin film composite membranes via grafting polymerization and incorporation of ZnO nanoparticles, *Appl. Surf. Sci.* 385 (2016) 268–281. doi:10.1016/j.apsusc.2016.05.141.
- [273] A. Soroush, W. Ma, Y. Silvino, M.S. Rahaman, Surface modification of thin film composite forward osmosis membrane by silver-decorated graphene-oxide nanosheets, *Environ. Sci. Nano.* 2 (2015) 395–405. doi:10.1039/c5en00086f.
- [274] M. Safarpour, A. Khataee, V. Vatanpour, Thin film nanocomposite reverse osmosis membrane modified by reduced graphene oxide/TiO<sub>2</sub> with improved desalination performance, *J. Memb. Sci.* 489 (2015) 43–54. doi:10.1016/j.memsci.2015.04.010.
- [275] H.D. Raval, P.S. Rana, S. Maiti, A novel high-flux, thin-film composite reverse osmosis membrane modified by chitosan for advanced water treatment, *RSC Adv.* 5 (2015) 6687–6694. doi:10.1039/C4RA12610F.
- [276] J. Duan, Y. Pan, F. Pacheco, E. Litwiller, Z. Lai, I. Pinnau, High-performance polyamide thin-film-nanocomposite reverse osmosis membranes containing hydrophobic zeolitic imidazolate framework-8, *J. Memb. Sci.* 476 (2015) 303–310. doi:10.1016/j.memsci.2014.11.038.
- [277] M. Liu, Q. Chen, L. Wang, S. Yu, C. Gao, Improving fouling resistance and chlorine stability of aromatic polyamide thin-film composite RO membrane by surface grafting of polyvinyl alcohol (PVA), *Desalination.* 367 (2015) 11–20. doi:10.1016/j.desal.2015.03.028.

- [278] H.M. Hegab, Y. Wimalasiri, M. Ginic-Markovic, L. Zou, Improving the fouling resistance of brackish water membranes via surface modification with graphene oxide functionalized chitosan, *Desalination*. 365 (2015) 99–107. doi:10.1016/j.desal.2015.02.029.
- [279] J. Wu, Z. Wang, W. Yan, Y. Wang, J. Wang, S. Wang, Improving the hydrophilicity and fouling resistance of RO membranes by surface immobilization of PVP based on a metal-polyphenol precursor layer, *J. Memb. Sci.* 496 (2015) 58–69. doi:10.1016/j.memsci.2015.08.044.
- [280] J. Duan, E. Litwiller, I. Pinnau, Preparation and water desalination properties of POSS-polyamide nanocomposite reverse osmosis membranes, *J. Memb. Sci.* 473 (2015) 157–164. doi:10.1016/j.memsci.2014.09.022.
- [281] S.H. Woo, J. Park, B.R. Min, Relationship between permeate flux and surface roughness of membranes with similar water contact angle values, *Sep. Purif. Technol.* 146 (2015) 187–191. doi:10.1016/j.seppur.2015.03.048.
- [282] H. Choi, Y. Jung, S. Han, T. Tak, Y.N. Kwon, Surface modification of SWRO membranes using hydroxyl poly(oxyethylene) methacrylate and zwitterionic carboxylated polyethyleneimine, *J. Memb. Sci.* 486 (2015) 97–105. doi:10.1016/j.memsci.2015.03.040.
- [283] G.D. Vilakati, M.C.Y. Wong, E.M. V Hoek, B.B. Mamba, Relating thin film composite membrane performance to support membrane morphology fabricated using lignin additive, *J. Memb. Sci.* 469 (2014) 216–224. doi:10.1016/j.memsci.2014.06.018.
- [284] J. Zhu, N. Guo, Y. Zhang, L. Yu, J. Liu, Preparation and characterization of negatively charged PES nanofiltration membrane by blending with halloysite nanotubes grafted with poly (sodium 4-styrenesulfonate) via surface-initiated ATRP, *J. Memb. Sci.* 465 (2014) 91–99. doi:10.1016/j.memsci.2014.04.016.
- [285] P. Gorgojo, M.F. Jimenez-Solomon, A.G. Livingston, Polyamide thin film composite membranes on cross-linked polyimide supports: IMPROVEMENT of RO performance via activating solvent, *Desalination*. 344 (2014) 181–188. doi:10.1016/j.desal.2014.02.009.
- [286] A.K. Gautam, T.J. Menkhaus, Performance evaluation and fouling analysis for reverse osmosis and nanofiltration membranes during processing of lignocellulosic biomass hydrolysate, *J. Memb. Sci.* 451 (2014) 252–265. doi:10.1016/j.memsci.2013.09.042.
- [287] M.M. Motsa, B.B. Mamba, A. D’Haese, E.M.V. Hoek, A.R.D. Verliefde, Organic fouling in forward osmosis membranes: The role of feed solution chemistry and membrane structural properties, *J. Memb. Sci.* 460 (2014) 99–109. doi:10.1016/j.memsci.2014.02.035.
- [288] J. Wang, H. Sun, X. Gao, C. Gao, Enhancing antibiofouling performance of

Polysulfone (PSf) membrane by photo-grafting of capsaicin derivative and acrylic acid, *Appl. Surf. Sci.* 317 (2014) 210–219. doi:10.1016/j.apsusc.2014.08.102.

- [289] S. Liang, Y. Kang, A. Tiraferri, E.P. Giannelis, X. Huang, M. Elimelech, Highly hydrophilic polyvinylidene fluoride (PVDF) ultrafiltration membranes via postfabrication grafting of surface-tailored silica nanoparticles, *ACS Appl. Mater. Interfaces*. 5 (2013) 6694–6703. doi:10.1021/am401462e.
- [290] M.F. Jimenez-Solomon, P. Gorgojo, M. Munoz-Ibanez, A.G. Livingston, Beneath the surface: Influence of supports on thin film composite membranes by interfacial polymerization for organic solvent nanofiltration, *J. Memb. Sci.* 448 (2013) 102–113. doi:10.1016/j.memsci.2013.06.030.
- [291] S. Jeong, S.J. Kim, L. Hee Kim, M. Seop Shin, S. Vigneswaran, T. Vinh Nguyen, I.S. Kim, Foulant analysis of a reverse osmosis membrane used pretreated seawater, *J. Memb. Sci.* 428 (2013) 434–444. doi:10.1016/j.memsci.2012.11.007.
- [292] B. Liu, C. Chen, T. Li, J. Crittenden, Y. Chen, High performance ultrafiltration membrane composed of PVDF blended with its derivative copolymer PVDF-g-PEGMA, *J. Memb. Sci.* 445 (2013) 66–75. doi:10.1016/j.memsci.2013.05.043.
- [293] A. Tiraferri, Y. Kang, E.P. Giannelis, M. Elimelech, Highly hydrophilic thin-film composite forward osmosis membranes functionalized with surface-tailored nanoparticles, *ACS Appl. Mater. Interfaces*. 4 (2012) 5044–5053. doi:10.1021/am301532g.
- [294] B. SU, T. Wang, Z. Wang, X. Gao, C. Gao, Preparation and performance of dynamic layer-by-layer PDADMAC/PSS nanofiltration membrane, *J. Memb. Sci.* 423–424 (2012) 324–331. doi:10.1016/j.memsci.2012.08.041.
- [295] A. Sotto, A. Boromand, R. Zhang, P. Luis, J.M. Arsuaga, J. Kim, B. Van der Bruggen, Effect of nanoparticle aggregation at low concentrations of TiO<sub>2</sub> on the hydrophilicity, morphology, and fouling resistance of PES-TiO<sub>2</sub> membranes, *J. Colloid Interface Sci.* 363 (2011) 540–550. doi:10.1016/j.jcis.2011.07.089.
- [296] A. Al-Amoudi, P. Williams, A.S. Al-Hobaib, R.W. Lovitt, Cleaning results of new and fouled nanofiltration membrane characterized by contact angle, updated DSPM, flux and salts rejection, *Appl. Surf. Sci.* 254 (2008) 3983–3992. doi:10.1016/j.apsusc.2007.12.052.
- [297] B. Khorshidi, B. Soltannia, T. Thundat, M. Sadrzadeh, Synthesis of thin film composite polyamide membranes: Effect of monohydric and polyhydric alcohol additives in aqueous solution, *J. Memb. Sci.* 523 (2017) 336–345. doi:10.1016/j.memsci.2016.09.062.





# Appendix

## A1.1 Brief literature review on the reported surface properties of TFC membrane

In this section, we present TFC membrane wettability and related parameters reported in the literature (**Table A1.1**). We observe that the majority of the articles reported only contact angle parameter to report the hydrophilicity. A few of them, reported all the parameters required to determine the wettability and hydrophilicity, e.g., contact angle, surface roughness, and surface tension.

Table A1.1: Brief overview of the membrane surface properties performed in the literature

Membrane type	Contact angle measurement technique	Permeation properties		Surface properties			
		Flux (LMH/MPa)	Rejection (%)	Contact angle	Interfacial free energy of interaction	Roughness	Zeta potential
NF [253]	Sessile drop	48 to 136	74% - 95%	48° to 74°		5 to 40 nm	-32.44 mV
RO [254]	Sessile drop	11 to 31	97% - 99%	19° to 77°		16 to 98 nm	-3 mV to -42 mV
RO [255]	Sessile drop	42 to 43	99%	40° to 80°	-101 to -75 mJ/m <sup>2</sup>	57 to 141 nm	
RO [256]	Sessile drop	4.4 to 72	99%	124° to 140°			
RO [257]	Sessile drop	5 to 11	50-95%	30° to 41°			
RO [258]	Sessile drop	17 to 36	98-99%	25° to 64°		15 to 156 nm	-15 to -50 mV
RO [259]	Sessile drop	9 to 56	96-99%	58° to 92°		100 to 110 nm	-18 to -38 mV
RO [260]	Sessile drop	19 to 35	98-99.22%	30° to 55°		50 to 53 nm	
RO [261]	Sessile drop	5 to 10	90-99.4%	33° to 72°			

RO [262]	Sessile drop	19 to 45	85-99%	41° to 90°	-115 to -72 mJ/m <sup>2</sup>	30 to 70 nm	-24 to -29 mV
RO [263]	Sessile drop	19 to 27	95-97%	47° to 65°		34 to 70 nm	
RO [264]	Sessile drop	58 to 80	97.9- 98.6%	82° to 90°		25 to 46 nm	
RO [265]	Sessile drop	27 to 35	99.5%	16° to 47°		63 to 82 nm	
RO [266]	Sessile drop	13 to 45	60 to 95%	30° to 55°		29 to 32 nm	
FO [267]	Sessile drop	18 to 27	97 to 99%	73° to 84°	-79 to 94 mJ/m <sup>2</sup>	79 to 137 nm	
RO [268]	Sessile drop	45 to 55		42° to 55°	-128 to -115 mJ/m <sup>2</sup>	50 to 100 nm	
RO [269]	Sessile drop		95 to 98%	50° to 66°		60 to 80 nm	-40 to 20 mV
RO [270]	Sessile drop	30 to 62	80 to 98%	40° to 60°		96 to 122 nm	-55 to -30 mV
RO [271]	Sessile drop	18 to 24	99%	69° to 88°	Surface tension: 42 to 46 mJ/m <sup>2</sup>		
RO [272]	Sessile drop	~1 to 45	85 to 99%	63° to 71°			
FO [273]	Sessile drop	11		25° to 55°	-120 to -100 mJ/m <sup>2</sup>	25 to 52 nm	-2 to 12 mV
RO [274]	Sessile drop	23 to 34	97 to 99%	44° to 71°		17 to 50 nm	
RO [275]	Sessile drop	14 to 50	84 to 86%	29° to 55°		144 to 276 nm	-37 to -33 mV
RO [276]	Sessile drop	9.5 to 36	96 to 99%	36° to 60°		39 to 46 nm	
RO [277]	Sessile drop	56 to 170	80 to 99%	41° to 60°		78 to 96 nm	-55 to 15 mV
RO [278]	Sessile drop	34 to 44	88 to 96%	19° to 63°		33 to 88 nm	

RO [279]	Sessile drop	19 to 48	98%	14.5° to 59°		43 to 48 nm	-50 to 15 mV
RO [280]	Sessile drop	1.6 to 23	95 to 99%	35° to 73°		29 to 73 nm	
MF [281]	Sessile drop	6500 to 20000		72° to 74°		47 to 166 nm	
RO [23]	Sessile drop	-		72° to 79° Dynamic hysteresis (mN/m): 24 to 29		91 to 97 nm	-21 to -18 mV
RO [282]	Sessile drop	4 to 6	99%	30° to 55°		68 to 74 nm	-30 to 15 mV
FO/RO [283]	Sessile drop	0.0108 to 0.0288	77 to 93%	68° to 108°	-99 to -50 mJ/m <sup>2</sup>		
NF [284]	Sessile drop	75 to 250	75 to 98%	55° to 85°			
RO [285]	Sessile drop	2 to 85	68 to 94%	41° to 70°			-22 to 25 mV
RO/NF [286]	Sessile drop	17 to 26	98 to 99.5%	33° to 64°		9 to 103 nm	
FO [287]	Sessile drop	-		37° to 64°	Interfacial free energy of cohesion: -31 to 26 mJ/m <sup>2</sup>		-4 to 16 mV
MF [288]	Sessile drop	6000 to 11000	70 to 98%	72° to 85°		3 to 7 nm	
RO [73]	Sessile drop	-		53° to 68°		76 to 80 nm	-34 to -14 mV
UF [289]	Sessile drop	142	55 to 95%	17° to 76°	-140 to -78 mJ/m <sup>2</sup>	35 to 55 nm	-20 to 40 mV
UF [290]	Sessile drop	75 to 100	85 to 99%	31° to 74°		1.2 to 4.5 nm	

RO [291]	Sessile drop	6		61° to 120°		56 to 90 nm	-41 to -15 mV
UF [292]	Sessile drop	1000 - 60000		55° to 80°		8 to 16 nm	
FO [293]	Sessile drop	24.6		15° to 100°	-135 to -57 mJ/m <sup>2</sup>	75 to 129 nm	-20 to 35 mV
NF [294]	Sessile drop	30 to 125	15 to 95%	25° to 80°		5 to 18 nm	-46 to 55 mV
RO [295]	Sessile drop	20 to 120	30 to 95%	60° to 75°			-35 to 20 mV
NF [296]	Sessile drop	11 to 165	18 to 97%	25° to 65°			
RO [297]	Sessile drop	8 to 26	97 to 99%	31° to 62°		41 to 160 nm	
RO [119]	Sessile drop	27 to 61	93 to 95%	53° to 81°		49 to 130 nm	

---

## B1.1 Supplementary information on the surface potential quantification

### B1.1.1 Characterizations of surface physical heterogeneity

We performed AFM analysis for the three samples, e.g., BW 30, glass, and polypropylene (scan size  $10\ \mu\text{m} \times 10\ \mu\text{m}$ ). **Table B 1.1** provides the quantitative data for the surface roughness and **Figure B 1.1** depicts the 3D topography of the three samples.

Table B1.1: Roughness parameters from the AFM analysis. SAD is the surface area difference due to the presence of rough features on the surface and was obtained using the Nanoscope Software 1.40.

Sample	Average roughness ( $R_{avg}$ )	RMS roughness ( $R_{rms}$ )	Wenzel roughness-ratio ( $r=1+SAD$ )
Glass	$2.01 \pm 0.5\ \text{nm}$	$3.09 \pm 0.5\ \text{nm}$	$1.002 \pm 0.001$
BW 30	$38 \pm 3\ \text{nm}$	$47 \pm 5\ \text{nm}$	$1.08 \pm 0.05\ \text{nm}$
Polypropylene	$7.75 \pm 0.5\ \text{nm}$	$13.90 \pm 0.8\ \text{nm}$	$1.008 \pm 0.002$

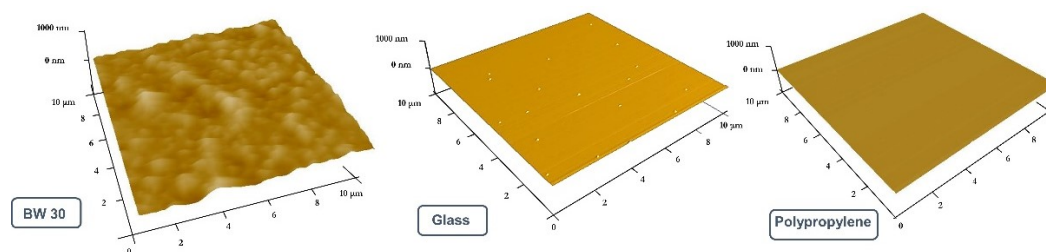


Figure B 1.1: 3D AFM topography of different samples analyzed in this study. We observe nearly uniform surface structure.

### B1.1.2 Evaluation of Gibbs adsorption equation

We assume that the liquid interfacial tension and solid surface tension do not alter due to the variation of pH. This can further allow us to apply combined Gibbs adsorption [189] and Young equation [46] as follows

$$\sigma = \frac{d(\cos \theta_{pH})}{d(pH)} \frac{F\gamma_{DM}}{2.303 RT} \quad (\text{B1.1})$$

where F is the Faraday constant (96500 C.mol<sup>-1</sup>), R is the molar gas constant, T is the system temperature, and  $\gamma_{DM}$  is the interfacial tension between the drop and the surrounding medium.

We can determine the term  $\frac{d(\cos \theta_{pH})}{d(pH)}$  directly from the contact angle titration experiments of the buffered solutions. **Figure B1.2** depicts the sigmoidal relation between the surface wettability  $\cos \theta_{pH}$  and pH. The derivative of the plots leads us to determine the approximate ionization state of the surface.

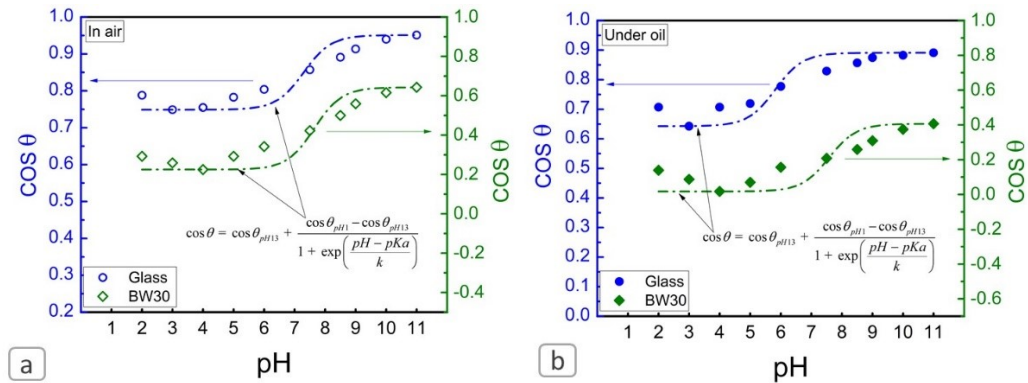


Figure B 1.2: Wettability vs. pH plots of glass, BW 30 samples for (a) in-air, and (b) under-liquid measurements.



## C1.1 Supplementary information for under-liquid wettability analysis

### C1.1.1 Probe liquids used in wettability analysis

Table C 1.1: List of the probe liquids used in wettability analysis. The values of viscosity were calculated using correlations at 20 °C [225,226]

Liquid	Chemical formula	Density (g/mL)	Molecular weight (g/mol)	Viscosity (mPa. s)	Solubility in water (g/L)	Boiling point (°C)
Water	H <sub>2</sub> O	1	18.02	1.002	-	100
1,4-Dibromobutane	C <sub>4</sub> H <sub>8</sub> Br <sub>2</sub>	1.81	215.92	1.91	insoluble	63
Diiodomethane	CH <sub>2</sub> I <sub>2</sub>	3.32	267.84	2.77	1.24	181
1,3-Diiodopropane	C <sub>3</sub> H <sub>6</sub> I <sub>2</sub>	2.58	295.89	5.89	insoluble	111
Diethyl phthalate	C <sub>12</sub> H <sub>14</sub> O <sub>4</sub>	1.12	222.24	12.56	1	298
Di-n-butyl phthalate	C <sub>16</sub> H <sub>22</sub> O <sub>4</sub>	1.04	278.35	3.22	0.4	339
Oleic acid	C <sub>18</sub> H <sub>34</sub> O <sub>2</sub>	0.89	282.47	38.80	insoluble	194
Castor oil	C <sub>57</sub> H <sub>104</sub> O <sub>9</sub>	0.96	933.45	100	insoluble	313

### C1.1.2 Characterizations of surface physical heterogeneity

Table C 1.2: Roughness parameters from the AFM analysis (scan size 10 μm × 10 μm). SAD is the surface area difference due to the presence of rough features on the surface and was obtained using the Nanoscope Software 1.40.

Sample	Average roughness ( $R_{avg}$ )	RMS roughness ( $R_{rms}$ )	Wenzel roughness-ratio ( $r=1+SAD$ )
Glass	2.01±0.5 nm	3.09±0.5 nm	1.002±0.001
PMMA	5.75±0.5 nm	10.90±0.5 nm	1.005±0.001
PTFE	35.00±3.0 nm	44.00±3.0 nm	1.030±0.010

### C1.1.3 Evaluation of previous theoretical models

We evaluated the theoretical framework developed by El-Shimi et al. [212] for predicting the underwater wettability of the solid samples. El-Shimi et al. [212] developed two different theoretical frameworks using the models proposed by Fowkes[88] and Wu[224]. We observed both approaches cannot predict the wettability of polar, as well as, non-polar probe liquids ( $\cos \theta > 1$  for many cases). El-Shimi-Wu (equation C1.1) [212] and El-Shimi-Fowkes [212] (equation C1.2) approaches are as follows:

$$\gamma_{OW} \cos \theta_{OW} = \gamma_W + \gamma_O - \frac{4\gamma_S^D \gamma_W^D}{\gamma_S^D + \gamma_W^D} - \frac{4\gamma_S^P \gamma_W^P}{\gamma_S^P + \gamma_W^P} + \frac{4\gamma_S^D \gamma_O^D}{\gamma_S^D + \gamma_O^D} + \frac{4\gamma_S^P \gamma_O^P}{\gamma_S^P + \gamma_O^P} \quad (C 1.1)$$

$$\gamma_{OW} \cos \theta_{OW} = \gamma_W + \gamma_O - 2\sqrt{\gamma_S^D \gamma_W^D} + 2\sqrt{\gamma_S^D \gamma_O^D} \quad (C 1.2)$$

where  $\theta_{OW}$  is the contact angle between the solid-oil droplet interface in the water medium,  $\gamma_{OW}$ ,  $\gamma_S$ ,  $\gamma_O$ ,  $\gamma_W$  are the interfacial tension of oil-water, solid-air, oil-air, and water-air, respectively. The superscript ‘D’ and ‘P’ denote the dispersive and polar surface tension components. It is to be noted that though all these works used under-liquid contact angle as  $\theta_{OW}$ , the present study represents this as  $\theta_{SWO}$ . **Table C1.3** and **Table C1.4** depict the prediction of underwater wettability for different probe liquids.

Table C 1.3: Theoretical prediction of underwater solid wettability: El-Shimi-Wu approach [212].

Probe liquid	Solid wettability underwater ( $\cos \theta_{SOW}$ )		
	PTFE	Glass	PMMA
Di-n-butyl phthalate	1.95	1.89	1.44
Castor oil	1.96	1.95	1.57
1,3-Diiodopropane	1.09	1.05	0.75
1,4-Dibromobutane	1.3	1.21	0.83
Diethyl phthalate	2.52	2.48	2.02
Diiodomethane	0.93	0.91	0.68
Oleic acid	2.41	2.28	1.8

Table C 1.4: Theoretical prediction of underwater solid wettability: El-Shimi-Fowkes approach [212]

Probe liquid	Solid wettability underwater ( $\cos \theta_{SOW}$ )		
	PTFE	Glass	PMMA
Di-n-butyl phthalate	1.98	2.02	2.05
Castor oil	1.99	2.04	2.07
1,3-Diiodopropane	1.27	1.4	1.49
1,4-Dibromobutane	1.45	1.54	1.62
Diethyl phthalate	1.71	1.73	1.74
Diiodomethane	1.15	1.28	1.39
Oleic acid	2.41	2.42	2.43

Moreover, we also evaluated Bartel-Osterhof equation S3 [117,210] in the case of the PTFE-water interface also.

$$\gamma_{OW} \cos \theta_{OW} = \gamma_{OA} \cos \theta_{OA} - \gamma_{WA} \cos \theta_{WA} \quad (\text{C } 1.3)$$

where  $\theta_{OW}$ ,  $\theta_{OA}$ , and  $\theta_{WA}$  are the contact angle between solid-oil droplet in water medium, solid- oil droplet in air medium, and solid-water droplet in air medium. Table S5 depicts the underwater wettability ( $\cos \theta_{SOW}$ ) of PTFE with

different probe liquids. For all the cases we observe the magnitude of wettability is higher than 1.

Table C 1.5: Theoretical prediction of underwater solid wettability: Bartel-Osterhof equation [117,210]

Probe liquid	Solid wettability underwater ( $\cos \theta_{SOW}$ )
	PTFE
Di-n-butyl phthalate	2.2
Castor oil	2.22
1,3-Diiodopropane	1.37
1,4-Dibromobutane	1.53
Diethyl phthalate	2.84
Diiodomethane	1.22
Oleic acid	2.64

### C1.1.4 Influence of surrounding medium on drop wettability

To analyze the effects of medium surface tension components over polar and non-polar solids we also perform a parametric study using Eq. C1.4.

$$\gamma_{ow}(1 + \cos \theta_{S^*WO}) = 2\gamma_W + 2 \left( \sqrt{\gamma_{S^*}^D \gamma_O^D} + \sqrt{\gamma_{S^*}^P \gamma_O^P} - \sqrt{\gamma_{S^*}^D \gamma_W^D} - \sqrt{\gamma_{S^*}^P \gamma_W^P} - \sqrt{\gamma_O^D \gamma_W^D} - \sqrt{\gamma_O^P \gamma_W^P} \right) \quad (C 1.4)$$

**Figures C 1.1-1.2** depict the impact of medium surface tension components on the wettability of non-polar and polar solids, respectively. We observed from **Figure C1.1a** that the complete wettability region is very large ( $\theta_{S^*MO} = 0^\circ$ ) when the droplet and solid are both non-polar. On the other hand, when the droplet is polar, and the solid is non-polar, even partial wetting ( $\theta_{S^*MO} < 90^\circ$ ) hardly occurs (**Figure C1.1b**).

The effect of the medium surface tension on polar solid samples is shown in **Figure C1.2**. As can be seen in **Figure C1.2a**, achieving partial wetting conditions is almost impractical when the surface is polar, and the droplet is non-polar. Similarly, **Figure C1.2b** shows that a complete wetting scenario would be more likely to happen when the solid and droplet are both polar. It is worth noting that when the medium polarity is very high ( $\gamma_M^P > 35 \text{ mN/m}$ ) and its dispersive surface tension components are very low ( $\gamma_M^D < 5 \text{ mN/m}$ ), the droplet will be at complete non-wetting region ( $\theta_{S^*MO} = 180^\circ$ ). This is because the medium and solid interact more significantly when both are polar, which causes the droplet not to wet the surface even if the droplet is polar.

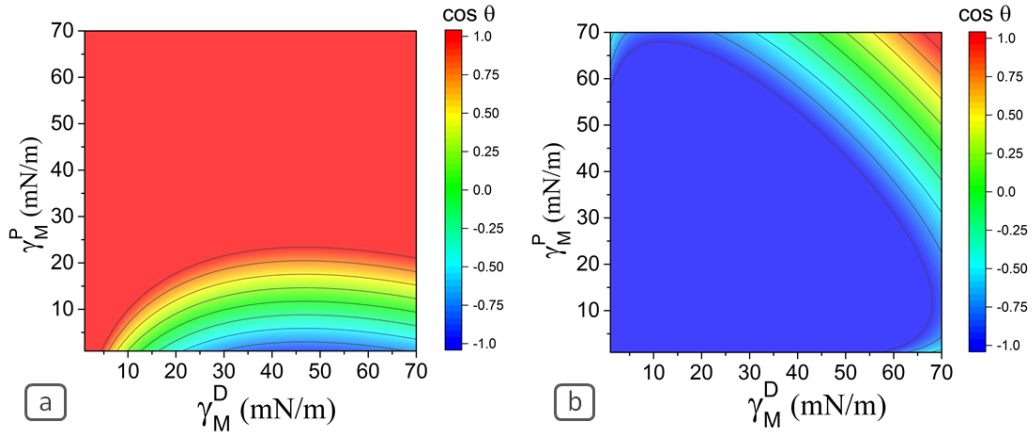


Figure C 1.1: Effects of medium surface tension components on the wettability for non-polar solid, e.g.,  $\gamma_{S^*}^D = 50$  mN/m,  $\gamma_{S^*}^P = 0$  mN/m, and  $\gamma_{OM} = 25$  mN/m, (a)  $\gamma_O^D = 50$  mN/m,  $\gamma_O^P = 0$  mN/m; (b)  $\gamma_O^D = 0$  mN/m,  $\gamma_O^P = 50$  mN/m. The figure indicates that it will be very difficult for a polar liquid (oil) to reach even the partial non-wettability regime when the surface is non-polar. Furthermore, we observed that for a particular solid-droplet configuration it is possible to alter the wettability only by altering the medium surface tension components.

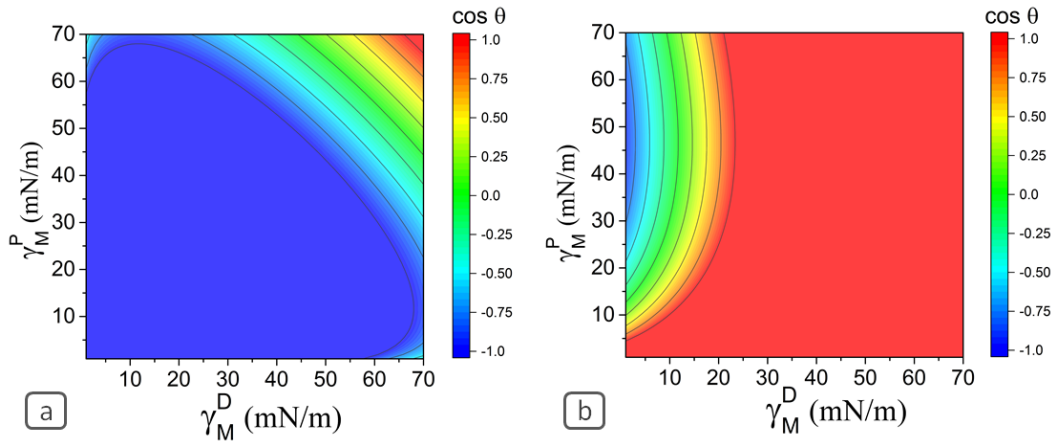


Figure C 1.2: Effects of medium surface tension components on the wettability for polar solid, e.g.,  $\gamma_{S^*}^D = 0$  mN/m,  $\gamma_{S^*}^P = 50$  mN/m, and  $\gamma_{OM} = 25$  mN/m, (a)  $\gamma_O^D = 50$  mN/m,  $\gamma_O^P = 0$  mN/m; (b)  $\gamma_O^D = 0$  mN/m,  $\gamma_O^P = 50$  mN/m. The figure indicates that it will be very difficult for a non-polar oil to reach even the partial non-wettability regime when the surface is highly polar. We also observed that for a particular solid-droplet configuration it is possible to alter the wettability only by altering the medium surface tension components.

### C1.1.5 Evaluation of equation of state (EQS) model [221–223]

Other than the surface tension component (STC) based approach, another approach, i.e., equation of state (EQS) approach is also widely applied to determine the solid surface tension. The EQS model assumes that the interfacial surface tension  $\gamma_{SL}$  depends on the surface tension of the liquid  $\gamma_L$  and solid  $\gamma_S$  only, i.e.,  $\gamma_{SL} = f(\gamma_L, \gamma_S)$ . The general EQS can be written as follows:

$$\gamma_{SL} = \gamma_S + \gamma_L - 2\sqrt{\gamma_S\gamma_L} e^{-\beta(\gamma_L-\gamma_S)^2} \quad (\text{C 1.5})$$

where  $\beta = 0.0001247 (m^2/mJ)^2$

Combining Eq. C1.5 with the Young's equation we get the following equation to determine the surface tension in the air:

$$\gamma_L \cos \theta = -\gamma_L + 2\sqrt{\gamma_S\gamma_L} e^{-\beta(\gamma_L-\gamma_S)^2} \quad (\text{C 1.6})$$

The original EQS has been developed for air medium application. A very recent study [77] further modified the EQS for under-water application as follows:

$$\gamma_{OW} \cos \theta_{S^*WO} = -\gamma_{OW} + 2\sqrt{\gamma_S\gamma_{OW}} e^{-\beta(\gamma_{OW}-\gamma_S)^2} \quad (\text{C 1.7})$$

From **Figure C1.3a**, we calculated the surface tension of PTFE in the air medium using Eq. S6. The outcome (19.7 mN/m) is consistent with our STC based approach obtained data (19.27 mN/m). Interestingly, from **Figure C4.3b** we did not obtain any such trend to determine the PTFE-water surface tension using Eq. C1.7. We further observe two separate regions of polar and non-polar liquids. This observation urges to further modify the EQS approach for under-liquid application.



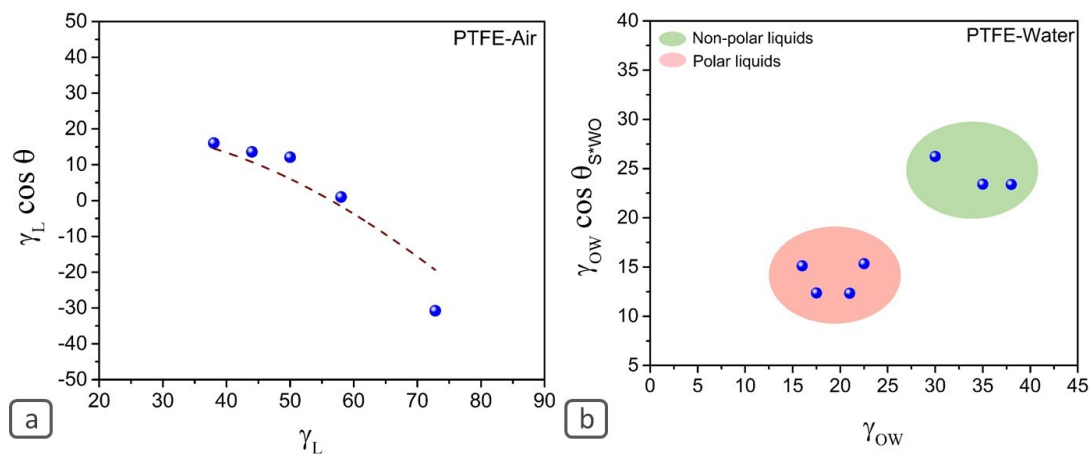


Figure C 1.3:  $\gamma_l \cos \theta$  vs.  $\gamma_l$  for PTFE surface in (a) air and (b) water medium. From the EQS model the surface tension of PTFE is 19.7 mN/m. We observe that PTFE-water interface does not exhibit any trend. Moreover, there exist two distinct regions, polar (red zone) and non-polar (green zone) liquids cases.

## D1.1 Supplementary information for under-liquid wettability analysis

### D1.1.1 Probe liquids used in wettability analysis

Table D 1.1: List of the probe liquids used in wettability analysis. The values of viscosity were calculated using correlations at 20 °C [225,226].

Liquid	Chemical formula	Density (g/mL)	Molecular weight (g/mol)	Viscosity (mPa. s)	Solubility in water (g/L)	Boiling point (°C)
Water	H <sub>2</sub> O	1	18.02	1.002	-	100
Diiodomethane (DIM)	CH <sub>2</sub> I <sub>2</sub>	3.32	267.84	2.77	1.24	181
1,3-Diiodopropane (DIP)	C <sub>3</sub> H <sub>6</sub> I <sub>2</sub>	2.58	295.89	5.89	insoluble	111
Diethyl phthalate (DEP)	C <sub>12</sub> H <sub>14</sub> O <sub>4</sub>	1.12	222.24	12.56	1	298
Di-n-butyl phthalate (DBP)	C <sub>16</sub> H <sub>22</sub> O <sub>4</sub>	1.04	278.35	3.22	0.4	339

## D1.1.2 Characterizations of surface physical heterogeneity

Figure D1.1 shows a qualitative comparison of the 3D and 2D surface features of the samples considered in the present study. We observe homogeneous surface morphology for all the cases.

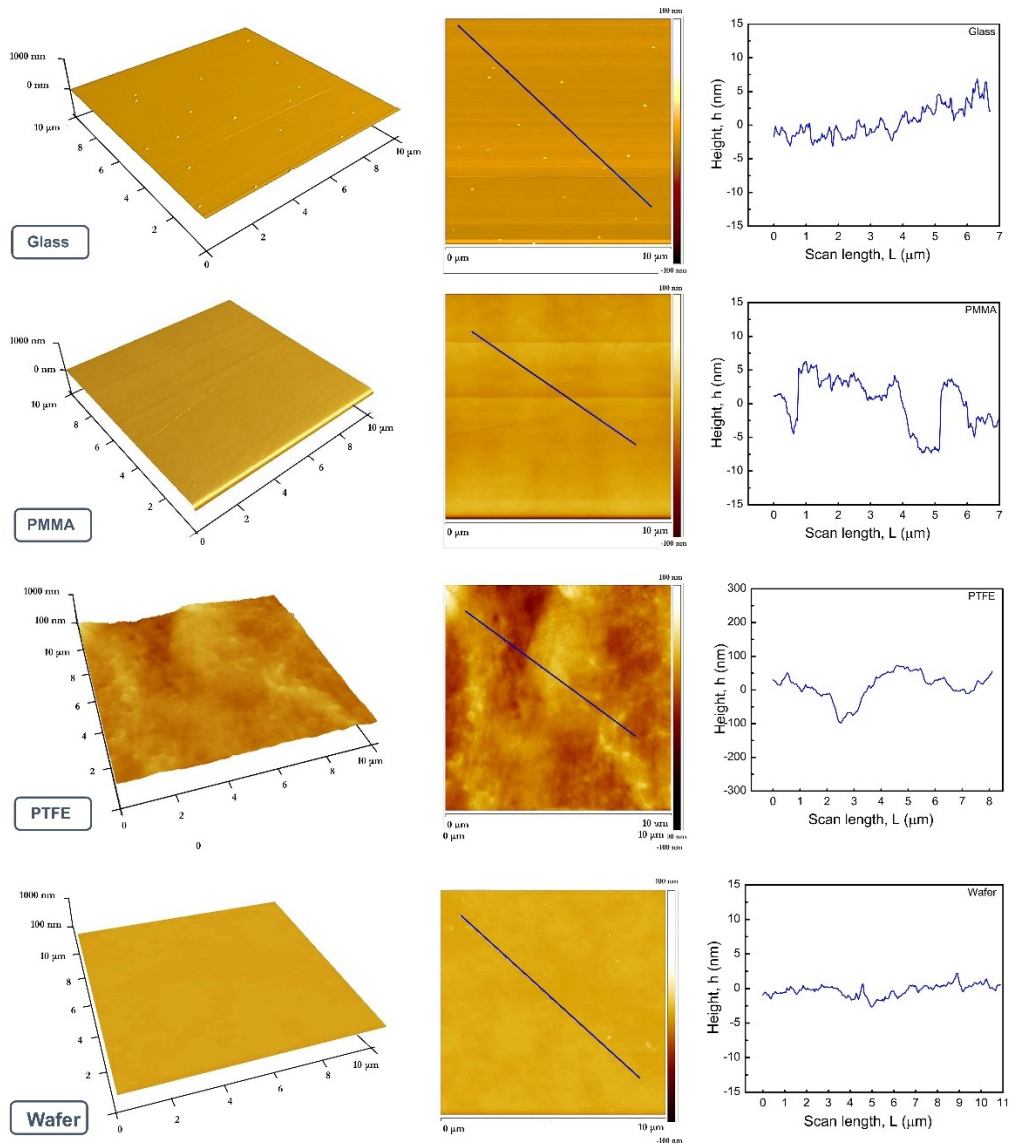


Figure D 1.1: 3D and 2D AFM surface topography of the different samples tested in the present study. All the samples exhibit uniform surface morphology. This allows us to discard the effect of physical heterogeneity over wettability.

### D1.1.3 Evaluation of solid total surface tension at different temperature

We measured the solid total surface tension at different temperatures. **Figure D1.2** depicts that polymeric surfaces exhibited a larger deviation than the average one for all the cases. The temperature averaged surface tensions are plotted as a straight line.

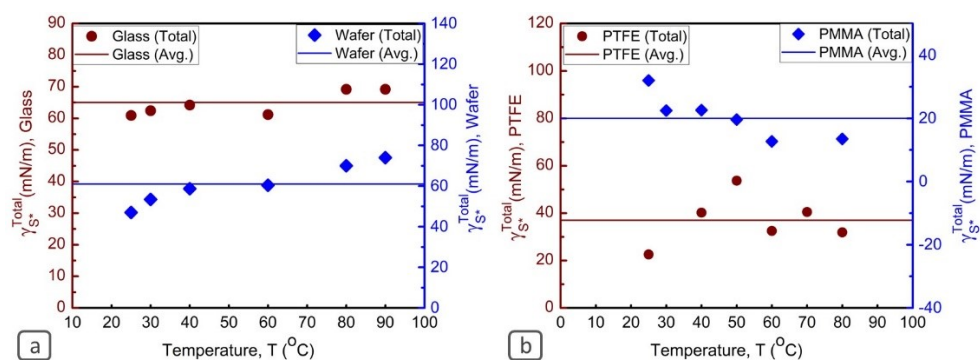


Figure D.1.2: Solid total surface tension at various temperatures, (a) Glass and Wafer, (b) PTFE and PMMA.

### D1.1.4 Effect of temperature on solid-medium interfacial interaction

We measured the solid dispersive and polar interaction with the bulk water at a different temperature which can be calculated by  $\sqrt{\gamma_{S^*}^D \gamma_W^D}$ , and  $\sqrt{\gamma_{S^*}^P \gamma_W^P}$ , respectively (**Figure D1.3**). We observe similar behavior, nearly constant for non-polymeric glass, and wafer (**Figure D1.3 a,b**) surfaces. Conversely, PMMA, and PTFE exhibit a wide variation for both dispersive, and polar interactions. This observation leads us to employ the temperature-dependent surface tension while determining the wettability of the polymers (Eq. D1.2).

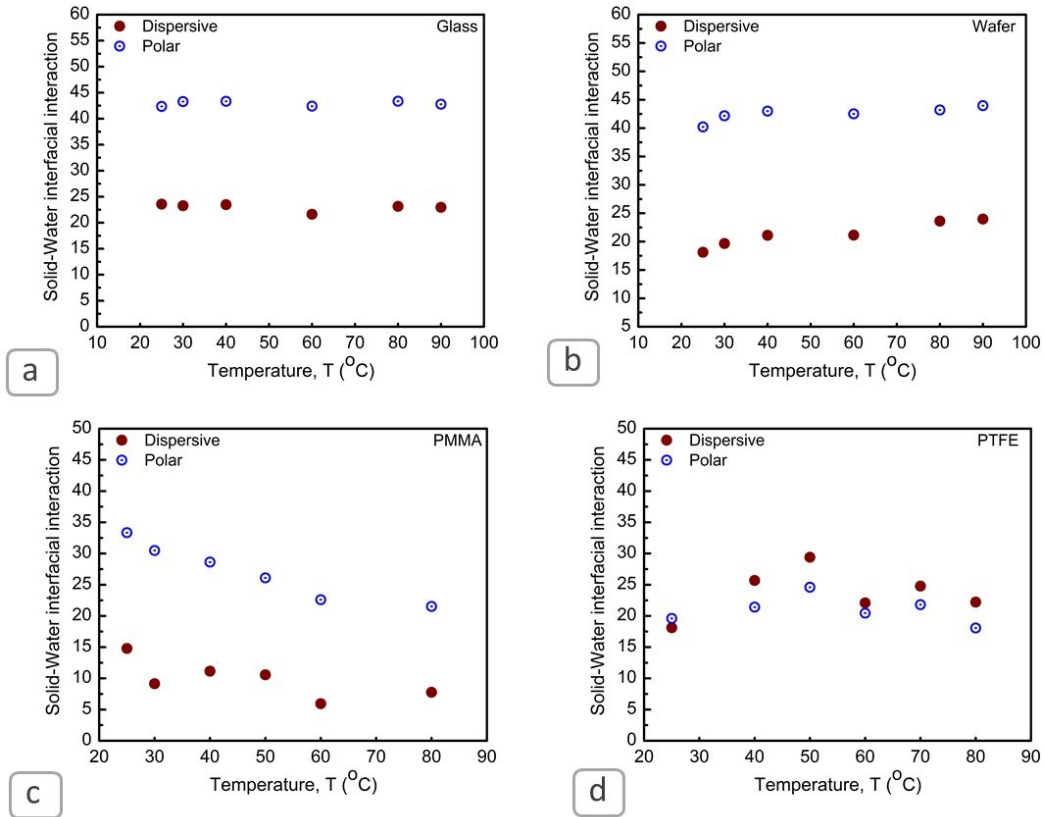


Figure D 1.3: Solid surface interaction with the bulk water medium at different temperatures. We observe nearly constant interaction for (a) glass, and (b) wafer. However, (c) PMMA, and (d) PTFE exhibits a significant variation.

### D1.1.5 Evaluation of previous theoretical models

We evaluated the theoretical framework developed by Yuk et al. [244] for predicting the solid-liquid-liquid wettability at elevated temperatures. Yuk et al. [244] developed their theoretical frameworks (Eq. D 1.1) using the models proposed by Fowkes[88] and Wu[224]. We observed this approach cannot predict the wettability of polar, as well as, non-polar probe liquids ( $\cos \theta > 1$  for many cases).

$$\gamma_{LW} \cos \theta_{S*WD} = \gamma_W - \gamma_D - 2\sqrt{\gamma_S^D \gamma_W^D} + 2\sqrt{\gamma_S^D \gamma_D^D} - \frac{4\gamma_S^P \gamma_W^P}{\gamma_S^P + \gamma_W^P} \quad (\text{D 1.1})$$

where  $\theta_{S*WD}$  is the contact angle between the solid-probe droplet interface in the water medium,  $\gamma_{DW}$ ,  $\gamma_S$ ,  $\gamma_D$ ,  $\gamma_W$  are the interfacial tension of probe drop-water, solid-air, probe drop-air, and water-air, respectively. The superscript ‘D’ and ‘P’ denote the dispersive and polar surface tension components. It is to be noted that though this work used under-liquid contact angle as  $\theta_{DW}$ , the present study represents this as  $\theta_{S*WD}$ . **Table D1.2** depicts the prediction of underwater wettability for different probe liquids.

Table D 1.2 (a): Theoretical prediction of underwater solid wettability: Yuk et al. [244]

Probe liquid	Solid wettability underwater ( $\cos \theta_{S*WD}$ )				
	PTFE				
	25° C	30° C	40° C	60° C	80° C
Di-n-butyl phthalate	-1.47	-1.37	-1.21	-0.97	-0.73
Diethyl phthalate	-2.04	-1.87	-1.59	-1.21	-0.87
1,3-Diiodopropane	-0.94	-0.95	-0.96	-0.99	-1.05
Diiodomethane	-1.0097	-1.02	-1.034	-1.07	-1.12

Table D 1.2 (b): Theoretical prediction of underwater solid wettability: Yuk et al. [244]

Probe liquid	Solid wettability underwater ( $\cos \theta_{S*WD}$ )				
	Silicon wafer				
	25 <sup>o</sup> C	30 <sup>o</sup> C	40 <sup>o</sup> C	60 <sup>o</sup> C	80 <sup>o</sup> C
Di-n-butyl phthalate	-1.2	-1.13	-1.003	-0.82	-0.68
Diethyl phthalate	-1.72	-1.6	-1.35	-1.04	-0.83
1,3-Diiodopropane	-0.92	-0.91	-0.93	-0.95	-0.98
Diiodomethane	-1.01	-1.02	-1.03	-1.06	-1.09

Table D 1.2(c): Theoretical prediction of underwater solid wettability: Yuk et al. [244]

Probe liquid	Solid contact angle underwater, $\theta_{S*WD}$ (deg.)				
	PMMA				
	25 <sup>o</sup> C	30 <sup>o</sup> C	40 <sup>o</sup> C	60 <sup>o</sup> C	80 <sup>o</sup> C
Di-n-butyl phthalate	131	116	104	82	82.50
Diethyl phthalate	176	135	114	85	86
1,3-Diiodopropane	122	120	110	94	93.50
Diiodomethane	130	129	118	102	99

### D1.1.6 Influence of surrounding medium on drop wettability

To analyze the effects of medium surface tension components over polar and non-polar solids we also perform a parametric study using Eq. A5.2.

$$\gamma_{OW}(1 + \cos \theta_{S^*WD}) = 2\gamma_W + 2 \left( \sqrt{\gamma_{S^*}^D \gamma_D^D} + \sqrt{\gamma_{S^*}^P \gamma_D^P} - \sqrt{\gamma_{S^*}^D \gamma_W^D} - \sqrt{\gamma_{S^*}^P \gamma_W^P} - \sqrt{\gamma_D^D \gamma_W^D} - \sqrt{\gamma_D^P \gamma_W^P} \right) \quad (D 1.2)$$

**Figures D1.4-D1.6** further depict the impact of medium temperature over the wettability characteristics between different types of solid surfaces and a polar probe liquid droplet. We observed from **Figure D1.2** that the complete wettability region is difficult to reach for a non-polar solid surface ( $\gamma_{S^*}^D = 50$  mN/m, and  $\gamma_{S^*}^P = 0$  mN/m). Moreover, even the partial wettability will never be achieved at the elevated temperature. We observed similar dependency on temperature for the wettability of polar droplet over a highly polar solid surface ( $\gamma_{S^*}^D = 50$  mN/m, and  $\gamma_{S^*}^P = 50$  mN/m) from **Figure D1.3**.

The effect of the medium temperature on highly polar solid samples is shown in **Figure D1.5**. As can be seen in **Figure D1.5a**, a wide range of wettability region is possible for this case at lower temperatures. Complete wettability can only be observed at a lower temperature (e.g.,  $T=10$  °C, **Figure D1.5a**) when the medium polarity is also low ( $\gamma_M^P < 10$  mN/m). However, **Figure D1.5b** shows that even partial wetting hardly occurs at elevated temperatures. **Figure D1.6** depicts the effects of medium temperature and its interfacial tension variation on the overall wettability of a SLL system when all the involved phases exhibit polarity. To understand the actual effect of temperature on a polar probe droplet wettability ( $\gamma_O^D = 10 - 0.1 \times T$  mN/m, and  $\gamma_O^P = 50 - 0.1 \times T$  mN/m) we theoretically considered highly polar solid surface for this case ( $\gamma_{S^*}^D = 0$  mN/m, and  $\gamma_{S^*}^P = 50$  mN/m). The figure indicates that the underwater solid oleophobicity increases with the increase



of temperature when all the involved phases exhibit a considerable amount of polarity.

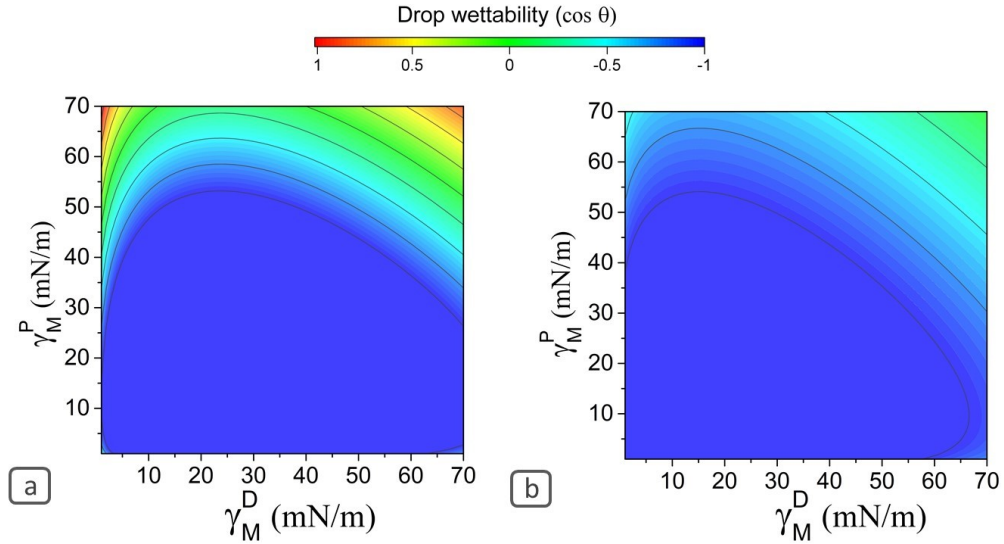


Figure D 1.4: Effects of medium interfacial tension on the solid-liquid-liquid wettability systems and different temperature, (a)  $T=10^\circ\text{C}$ , and (b)  $T=90^\circ\text{C}$  for the following conditions (non-polar solid case):  $\gamma_{S^*}^D = 50\text{ mN/m}$ ,  $\gamma_{S^*}^P = 0\text{ mN/m}$ ,  $\gamma_O^D = 10 - 0.1 \times T\text{ mN/m}$ ,  $\gamma_O^P = 50 - 0.1 \times T\text{ mN/m}$ ,  $\gamma_{OW} = 20 + 0.5 \times T\text{ mN/m}$ . The figure indicates that it will be very difficult for a polar liquid (oil) to reach even the partial non-wettability regime at the elevated temperatures. Furthermore, we observed that for a particular solid-droplet configuration it is possible to alter the wettability only by altering the surrounding medium temperature.

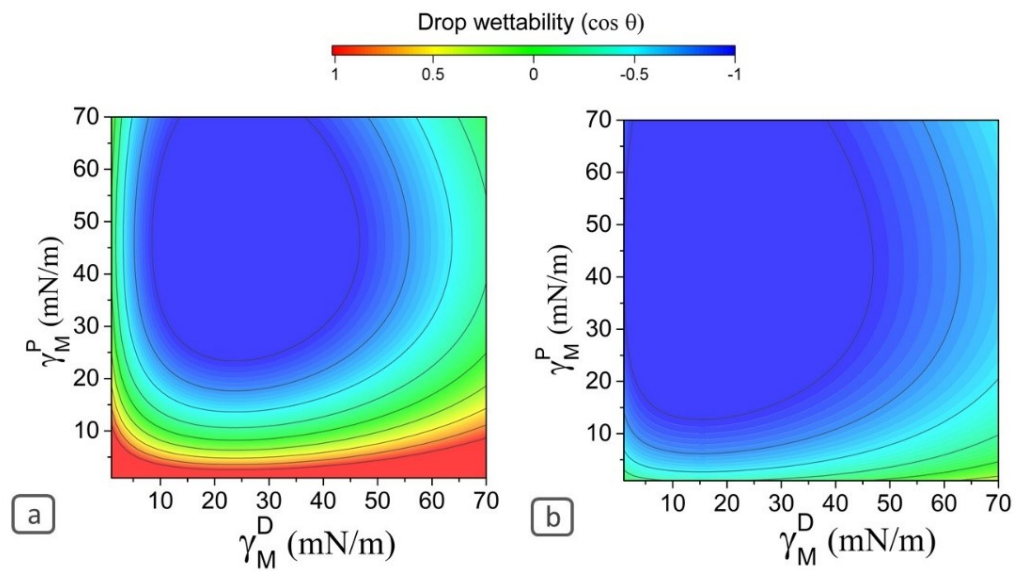


Figure D 1.5: Effects of medium interfacial tension on the solid-liquid-liquid wettability systems at different temperatures, a)  $T=10^{\circ}\text{C}$ , and (b)  $T=90^{\circ}\text{C}$  for the following conditions (high polar and dispersive solid surface tension components case):  $\gamma_{S^*}^D = 50 \text{ mN/m}$ ,  $\gamma_{S^*}^P = 50 \text{ mN/m}$ ,  $\gamma_O^D = 10 - 0.1 \times T \text{ mN/m}$ ,  $\gamma_O^P = 50 - 0.1 \times T \text{ mN/m}$ ,  $\gamma_{OW} = 20 + 0.5 \times T \text{ mN/m}$ . We observe the complete wettability region at lower temperature conditions only.

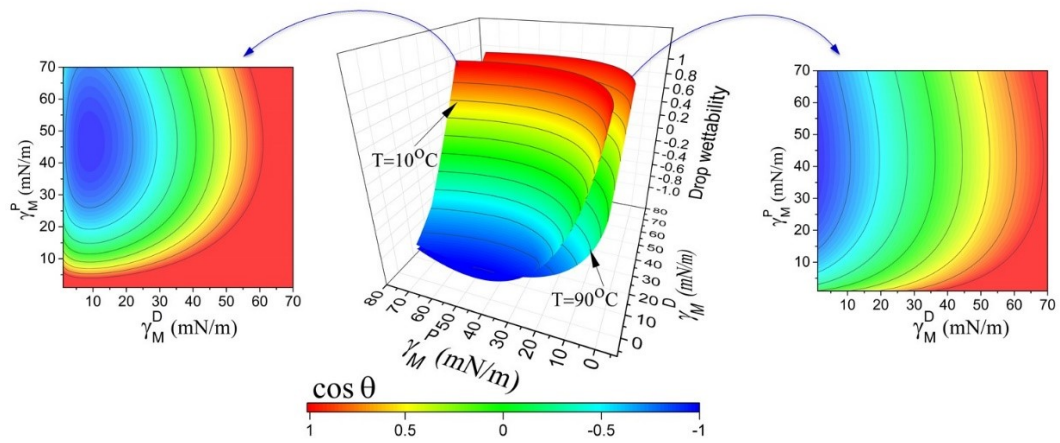


Figure D 1.6: Effects of medium interfacial tension on the solid-liquid-liquid wettability systems and different temperature for the following conditions:  $\gamma_{S^*}^D = 0$  mN/m,  $\gamma_{S^*}^P = 50$  mN/m,  $\gamma_O^D = 10 - 0.1 \times T$  mN/m,  $\gamma_O^P = 50 - 0.1 \times T$  mN/m,  $\gamma_{OW} = 20 + 0.5 \times T$  mN/m.